

**UNIVERSIDAD COMPLUTENSE DE MADRID**

**FACULTAD DE CIENCIAS FÍSICAS**

**DEPARTAMENTO DE FÍSICA APLICADA III**



---

**Contributions to the high frequency  
electronics of MAGIC II Gamma Ray  
Telescope**

---

*Thesis presented by*

**Pedro Antoranz Canales**

For the degree of Doctor of Philosophy  
in the subject of Physics

*Thesis Advisor*

**Dr. José Miguel Miranda Pantoja**

**June 2009, Madrid**



*Para Mere.  
Para Fuencisla.  
Gracias.*

*A mis padres y a mi hermano.  
Por estar ahí incluso cuando yo no estoy.*



## AGRADECIMIENTOS

He dedicado bastante tiempo a reflexionar acerca de cómo empezar esta sección, intentando ser original. Pero cuanto más pienso en ello, más claro está en mi mente: si algo se convierte en estándar, es porque normalmente es la mejor opción. Sin embargo, no sólo los convencionalismos, sino también lo que realmente siento es lo que me ha decidido sobre a quién dar las gracias en primer lugar. A las dos personas que me ‘secuestraron’ y me introdujeron en este mundo de Ciencia. Un mundo lleno de decepciones, de frustraciones y, desgraciadamente, lleno a veces de lágrimas por compañeros que se van. Pero, sin lugar a dudas, un mundo lleno también de satisfacciones, de nuevos descubrimientos y de gente a la que se puede llamar amigo.

Estas dos personas son, por supuesto, mi Director de Tesis, José Miguel Miranda, y la Investigadora Principal del grupo UCM en el experimento MAGIC, María Victoria Fonseca. Gracias.

Según pasaban los años, el ‘Síndrome de Estocolmo’ se hacía cada vez más fuerte, y la lista de gente a la que agradecer su apoyo iba también creciendo.

I want to have a special word on Florian Goebel. A guy to whom we all must be grateful. A life dedicated not only to Science, as proven by MAGIC I and especially by MAGIC II. Also a life dedicated to the people, to the Collaboration human point of view. This is why I want to thank him twice: thank you for making MAGIC possible and better, and thank you for always having a word and a piece of advice when needed.

Una de las primeras personas que me encontré al empezar mi Doctorado fue un divertido italiano, Fabrizio, cuyo laboratorio era un reducto de orden y limpieza hasta que yo entré en escena. Más adelante, Fabrizio decidió dejar Madrid para volver a su ciudad eterna y dedicarse a hacer Ciencia bajo el agua en el proyecto Nemo. Pero al poco de comenzar mi etapa en la Colaboración MAGIC, tuve que hacer mi primer viaje a La Palma para participar en la instalación del Pixel Central. Y, asustado como estaba, tanto Fabrizio como Mariano fueron un gran apoyo. Y así continuaron mientras permanecieron en el grupo. Muchas gracias.

A lo largo de estos años, he trabajado con muchas personas. Pero en el día a día, en la continua y exasperante coexistencia, unos pocos han sufrido mi compañía más que el resto. Y quiero agradecer a los dioses, al destino o como queráis llamarlo por darme los mejores compañeros de despacho que uno podría soñar. Gracias a Igor, a Miguel, a Dani y a Silvia por todas las risas, por

todos los buenos ratos y el apoyo en los momentos de frustración y monotonía. Todo lo que puedo decir es gracias a la gente que ha integrado el grupo durante estos años, oficial y extraoficialmente: Raquel, Marcos, Debanjan, Adolfo, Luispa, Leandro, Valeria, Pablo... y los dos 'seniors' más 'juniors' que he conocido en mi vida, José Luis y Juan Abel.

Being on a shift is one of the most extraordinary things that I have experienced along the years of my PhD. Some times at La Palma, working at night in a so isolated place, I felt like some kind of modern and technological Robinson Crusoe. And as such, I would like to truly thank the many excellent 'Fridays' I have had. I have not only survived, but I also had great times in there because of them. Thank you Dorota and Maxim for escaping a fire with me, thank you Michele for showing me 'El Pinar de la Virgen', thank you Saverio for the good times supporting Barça, thank you to you all, Robert, Roger, Daniela, Thomas...

Gracias al Pibe, a David, a Mariano y a Valentín por todos los descafeinados, sándwiches y mucho más. Que, como diría aquél, no sólo de Ciencia vive el hombre.

Y por último, gracias a todos aquellos a quienes esta tesis os sonará a chino, pero la hojearéis con más cariño que nadie. A mi familia, que se empeña en estar ahí contra viento y marea, y a mis amigos, a veces viento y marea pero siempre chaleco salvavidas.

## TABLE OF CONTENTS

<b>AGRADECIMIENTOS.....</b>	<b>i</b>
<b>TABLE OF CONTENTS.....</b>	<b>iii</b>
<b>LIST OF FIGURES.....</b>	<b>vii</b>
<b>LIST OF TABLES .....</b>	<b>xiii</b>
<b>ABBREVIATIONS.....</b>	<b>xv</b>
<b>Chapter 1 .....</b>	<b>1</b>
<b>Introduction.....</b>	<b>1</b>
1. Gamma-Ray Astronomy History .....	2
1.1. Early days .....	2
1.2. The Satellite Era .....	3
1.3. Ground-based Telescopes .....	4
2. Gamma rays in the atmosphere .....	6
3. Detectors .....	10
4. High frequency, low noise electronics .....	14
5. Structure and Objectives of this Thesis .....	15
6. References.....	17
<b>Chapter 2 .....</b>	<b>19</b>
<b>The MAGIC Telescopes.....</b>	<b>19</b>
1. Introduction .....	21
2. Structure and Drive System.....	22
3. Reflector .....	23
4. Camera.....	25
4.1 Photomultipliers .....	25
4.2 Preamplifier and Optical Transmission .....	27
5. Readout System .....	30
5.1 MAGIC I .....	30
5.2 MAGIC II.....	32
6. Trigger.....	33
6.1 Standard trigger.....	33
6.2 Sum trigger.....	35
7. Analysis .....	36
8. The Central Pixel .....	38
8.1 Motivation .....	38
8.2 The Photodetector .....	39

8.3	The Electro-Optical System.....	40
8.4	The Power Supply .....	43
8.5	The DAQ System and Operation Modes .....	45
8.6	Results: Crab Observations.....	46
9.	Control and Operation of the Telescope .....	49
9.1	Organization of the shifts.....	49
9.2	Telescope operation .....	49
9.3	Participation on the shifts.....	51
10.	References.....	55
<b>Chapter 3.....</b>		<b>59</b>
<b>Wide-band Pulse Generators .....</b>		<b>59</b>
1.	Main Objectives .....	60
2.	Variable Duty Cycle Pulsers based on Schmitt Trigger Inverters.....	63
3.	Symmetric inverter and logical glitch .....	65
4.	Pulse generator with shunt stub .....	66
5.	Sub-nanosecond Pulse Generator based on SRD.....	69
5.1	The Step Recovery Diode .....	69
5.2	SRD pulser design.....	72
6.	References.....	76
<b>Chapter 4.....</b>		<b>79</b>
<b>Wide-band Pulse Generators: Results.....</b>		<b>79</b>
1.	Generator for Photodetector Tests .....	80
1.1	Requirements .....	80
1.2	Design .....	80
1.3	Results.....	81
2.	Generator for MAGIC I Camera Tests.....	83
2.1	Requirements .....	83
2.2	Design .....	83
2.3	Construction.....	86
2.4	Results.....	86
3.	Generator for MAGIC II Receiver Board Tests .....	88
3.1	Requirements .....	88
3.2	Design and construction.....	88
3.3	Results.....	95
4.	References.....	97



<b>Chapter 5</b> .....	<b>99</b>
<b>Pulse amplifiers</b> .....	<b>99</b>
1. Introduction .....	100
2. Flow diagrams and gain definitions .....	101
2.1 Flow Diagram analysis .....	101
2.2 Power gains .....	102
2.3 Voltage gains .....	104
3. Pulse distortion and need for high bandwidths .....	105
4. Stability .....	107
5. Noise .....	109
5.1 Definitions and statistical representation .....	109
5.2 Monte Carlo simulation in the time domain .....	110
6. Dynamic Range / Linearity .....	112
7. Mismatches and ringing .....	113
8. Side effects of dissipative pads .....	115
8.1 Stability improvements .....	115
8.2 Noise increase due to dissipative pads .....	115
9. Software tools .....	117
9.1 MATLAB scripts .....	117
9.2 Spice integration of the models .....	120
10. References .....	121
<b>Chapter 6</b> .....	<b>123</b>
<b>Pulse amplifiers: design and test</b> .....	<b>123</b>
1. Mmics: state of the art .....	124
1.1 Technologies .....	124
1.2 Topology .....	125
2. Fulfilling MAGIC requirements .....	126
2.1 PMT preamplifier .....	126
2.2 Receiver board preamplifier .....	129
3. Practical considerations .....	130
3.1 PCB line studies .....	130
3.2 SMD parasitic modelling .....	132
4. Bias circuit .....	135
5. Frequency-domain response .....	138
5.1 Scattering matrix .....	138
5.2 Stability .....	142
6. Time-domain response .....	145

6.1	Linearity and dynamic range.....	145
6.2	Amplifier behaviour with the photodiode as source .....	146
7.	Noise and sensitivity.....	148
8.	Thermal stability.....	150
8.1	Bias current stability with temperature.....	150
8.2	Influence of temperature on the scattering parameters.....	150
9.	Final tests .....	153
10.	References.....	155
<b>Chapter 7.....</b>		<b>157</b>
<b>Development of a testbench for photodetectors .....</b>		<b>157</b>
1.	Motivation .....	158
2.	LED modelling.....	159
2.1	Circuitual model with high frequency effects .....	159
2.2	Alternative calculations of RS and ideality factors.....	164
2.3	Parameter extraction and results.....	167
3.	Design of the shielding enclosure .....	171
3.1	Shielding considerations .....	171
3.2	Cabling.....	173
3.3	Waveguide below cutoff techniques for optical coupling.....	174
3.4	Shielding effectiveness (SE) of the walls.....	176
4.	Final prototype and measurements.....	177
4.1	Design of the testbench.....	177
4.2	Results.....	178
5.	References.....	183
<b>Chapter 8.....</b>		<b>185</b>
<b>Summary and future prospects.....</b>		<b>185</b>
1.	Main accomplishments.....	186
1.1	Measurements during MAGIC shifts .....	186
1.2	Central pixel electronics .....	186
1.3	Nanosecond range pulse generators .....	187
1.4	Nanosecond range pulse amplifiers .....	187
1.5	High frequency modelling of blue LEDs .....	187
1.6	Evaluation boards and testbenches .....	188
2.	Future work on IACTs: The Čerenkov Telescope Array (CTA) .....	189
2.1	Structure and objectives of CTA.....	189
2.2	Thesis usefulness for CTA.....	191
3.	References.....	193

## LIST OF FIGURES

Figure 1.1 (a) Viktor Hess balloon flight, 1912. (b) Compton Gama-Ray Observatory, launched in 1991. (c) MAGIC I Telescope, inaugurated in 2003. ....	3
Figure 1.2 (a) Diffuse cosmic rays spectrum. (b) Gamma-ray emission of the Crab Nebulae, as seen by different detectors. ....	6
Figure 1.3 (a) Schematic representation of an air shower created by a gamma-ray (left) and a cosmic ray (right). (b) Monte Carlo simulation of air showers with CORSIKA software. ....	7
Figure 1.4 (a) Čerenkov light front. (b) Spectrum of Čerenkov light in atmosphere. ....	8
Figure 1.5 (a) Detection of gamma-ray showers by an IACT. (b) Hillas parameters for the analysis of extended air showers.....	9
Figure 1.6 Energy resolution of modern photodetectors: (a) PMT (b) HPD (c) GAPD.....	13
Figure 2.1 (a) MAGIC Site. (b) MAGIC I and II Telescopes.....	21
Figure 2.2 MAGIC I (a) and II (b) reflectors.....	23
Figure 2.3 (a) Typical muon ring. Isolated muons with energy in excess of 6 GeV create such a geometric figure in the camera, which can be easily reconstructed to calculate the performance of the Telescope. (b) Point Spread Function of the MAGIC Telescope, estimated using muon analysis. The diameter of a MAGIC pixel is 24.5 mm .....	24
Figure 2.4 (a) MAGIC I camera structure. Picture of inner and outer pixels. (b) MAGIC II camera structure. Cluster and PMT with HV base, preamplifier, laser driver and VCSEL. ....	26
Figure 2.5 MAGIC PMT preamplifier: (a) Schematic. (b) Transimpedance gain simulation and response to a pulse. ....	27
Figure 2.6 MAGIC II preamplifier simulation. ....	29
Figure 2.7 High and Low Gain Branches in the receiver board. ....	31
Figure 2.8 (a) Pixel distribution in macrocells for the trigger logic. (b) Tree configuration of the SMART modules of L2T. ....	34
Figure 2.9 Block diagram of the Central Pixel System.....	39
Figure 2.10 (a) Front view of the camera. (b) Backplane of the camera and structural description of the PMT assembly.....	39
Figure 2.11 Schematic of the Central Pixel Transceiver. (a) Modified PMT preamplifier. (b) Transmitter, inside the camera. (c). Receiver, in the Counting House.....	41
Figure 2.12 (a) I-V characteristics of the Honeywell HFE-4050 LED. (b) Dynamic range of the Honeywell HFD-3038-002 PIN photodiode.....	42
Figure 2.13 Dynamic range and bandwidth of the Central Pixel Transceiver. ....	43
Figure 2.14 Central Pixel Power Supply. (a) Schematic. (b) Board. (c) Location in the camera....	44
Figure 2.15 PMT base schematics. ....	45
Figure 2.16 Block diagram of the Central Pixel dedicated PC acquisition. ....	46
Figure 2.17 Light curve of the Crab: (a) Dedicated PC, 20 s. observation. (b) Dedicated PC, 30 s. observation with moderate cloud coverage and moonlight. (c) Dedicated PC, 40 min. observation. (d) FADC, 20 h. observation. ....	47
Figure 2.18 Crab measurements at different wavelengths. The measurements in the optical energy band were made with the central pixel. ....	48

Figure 2.19 Last version of SuperArehucas software. ....50

Figure 3.1 (a) Typical quantum efficiency of MAGIC I PMTs, both coated and uncoated with wavelength shifters, MAGIC II PMTs, an HPD and a GAPD. (b) Relative spectrum of the atmospheric Cerenkov light.....61

Figure 3.2 Critical points where the ns pulse generators are applied for subsystem testing: 1) Combined with a blue light emitter, test of the complete camera transmission. Test of photodetectors in a laboratory testbench. 2) Test of the pixel chain electronics. 3) Test of the optical transceiver and receiver electronics. ....62

Figure 3.3 (a) Hysteresis curve of the 74AC14 HEX inverter. (b) Asymmetric pulse generator...63

Figure 3.4 (a) Schematic of the asymmetric inverter with output buffer.  $R_1=150\text{ k}\Omega$ ,  $R_2= 10\ \Omega$   $C=47\text{ pF}$ ,  $R_b=10\ \Omega$  (b) Simulation.....64

Figure 3.5 (a) Pulse generator based on logical glitches (schematic). (b) Simulation of the voltage on the capacitor, both inputs of the AND gate and the load.....65

Figure 3.6 Schematic of the pulse generator with short-circuited stub and Schottky diode. As a 74AC08 AND gate is used, the pulse polarity is positive. ....67

Figure 3.7 Simulation of the pulse generator of Figure 3.6. ....67

Figure 3.8 Schematic of the pulse generator with short-circuited stub and Schottky diode. As a 74AC00 NAND gate is used, the pulse polarity is negative.....68

Figure 3.9 Simulation of the pulse generator of Figure 3.8.....68

Figure 3.10 Electric field distribution in a SRD during a transit from a forward bias ( $t_1$ ) to a reverse one ( $t_4$ ) .....70

Figure 3.11 Schematic of the SRD pulse generator.....72

Figure 3.12 Pulse generator shaping. Top: Current in the diode ( $I_{SRD}$ ), stub ( $I_{STUB}$ ) and load ( $I_{LOAD}$ ). Bottom: Voltages at the input ( $V_{IN}$ ) and output ( $V_{OUT}$ ) of the SRD. The signals were simulated by removing the Schottky diode from the schematics of Figure 3.11a. ....73

Figure 3.13 Effect of the stub length for a fixed impedance of  $100\ \Omega$  (top) and stub impedance (bottom) for a fixed length of 6 cm on the performance of the generator.....75

Figure 3.14 Comparison between the simulated and measured pulse shape. ....75

Figure 4.1 (a) Pulse generator with output buffer. (b) Generated pulse, measured with the oscilloscope in open circuit (the probe has a resistance of  $1\text{ M}\Omega$  and a capacitance of  $8\text{ pF}$ ).....81

Figure 4.2 Effect of the addition of a series resistant to the LED connected at the output of the pulse generator. ....82

Figure 4.3 Pulsed light detected by the photomultiplier tube.....82

Figure 4.4 Schematics of the pulse generator designed by the author for this thesis, which is presently giving service at MAGIC site. Three stages are observed: pulse generation, ringing reduction by means of attenuator, and power division. ....84

Figure 4.5 (a) Passive attenuator and transmission line schematic. (b) Graphs used for the design of the desired attenuator ( $50\ \Omega$  matched).....85

Figure 4.6 Values of the parameters for a 3 way,  $50\ \Omega$  matched, resistive power splitter with the input coupled. ....85

Figure 4.7 Board layout of the La Palma Pulse Generator. ....86

Figure 4.8 Pulse Generator package.....86

Figure 4.9 Measured pulses at the three different outputs. ....	87
Figure 4.10 Jitter measurements. The standard deviation from the nominal pulse width is only 39 ps. ....	87
Figure 4.11 (a) Picture of the multichannel pulse generator. (b) Design concept of the device. ....	89
Figure 4.12 (a) Schematic, (b) Final layout and (c) waveforms of the power divider. $N$ is the number of outputs. The input pulse was generated with a commercial 50 $\Omega$ waveform synthesizer. ....	90
Figure 4.13 (a) Schematic of the test circuit. (b) Upper graph: dynamic range of Sirenza 7489Z for negative, 4ns wide pulses. Lower graph: noise figure of the 1 stage amplifier board. (c) Scattering parameters and stability. ....	92
Figure 4.14 Schematic (a) and pulse shapes (b) of the two stage power amplifier used in each of the four output channels. ....	93
Figure 4.15 (a) Bias circuit unit for each of the two pairs of VCSELs used in the board. (b) Pulse integrity at VCSEL pins contacts. ....	94
Figure 4.16 Measured pulses at the four different outputs. ....	96
Figure 4.17 Top: pulse width histogram. Bottom: repetition frequency jitter. ....	96
Figure 5.1 (a) Scheme of a pulse amplifier with arbitrary load and source impedances. (b) Flow diagram. ....	102
Figure 5.2 (a) Spectrum of a rectangular pulse for different pulse widths. (b) Effect of an amplifier on the distortion of the output pulse for 3 dB bandwidths of 1 GHz, 300 MHz and 100 MHz. The amplitudes were normalized to the input pulse to better appreciate the amplifier distortion. ....	106
Figure 5.3 Dependence of the pulse noise with the bandwidth. <i>Straight line</i> : input signal. <i>Dashed line</i> : ideal output signal for a noiseless amplifier. <i>Circles</i> : simulated output for a noisy amplifier (BGA616), for a given bandwidth. ....	111
Figure 5.4 Dependence of the pulse noise with amplifier's noise figure. <i>Straight line</i> : input signal. <i>Dashed line</i> : ideal output signal for a noiseless amplifier. <i>Circles</i> : simulated output for a noisy amplifier (BGA616) with a given NF. ....	111
Figure 5.5 Typical performance of an amplifier. Dynamic range, saturation and 1 dB compression point referred to the input are shown. ....	112
Figure 5.6 Effect of the source mismatch on the amplifier output signal. ....	113
Figure 5.7 Effect of an attenuator pad between the mismatched source and amplifier. ....	114
Figure 5.8 Stability of a MMIC amplifier (MSA0886) mounted on coplanar transmission lines and with SMA terminals. The $\kappa$ parameter reveals that the amplifier is unstable without the pad. A 3 dB attenuator makes it unconditionally stable. ....	115
Figure 5.9 Dependence of the BGA616 amplifier output pulse on the pad attenuation. The lower graph on the right shows the dependence of $\sigma'$ and overall gain on the attenuation factor. ....	116
Figure 5.10 (a) Flow diagram of the analysis/simulation software (b) User interface of the program. The rightmost part shows the amplifier characteristics, and the leftmost the time domain response. ....	118
Figure 5.11 Analysis of a 2-stage amplifier obtained from the S matrix. ....	119
Figure 5.12 Simulation of the response to an input pulse. ....	119
Figure 5.13 Device equivalent circuit for integration of the scattering matrix into Spice simulations. ....	120

Figure 6.1 (a), (b) Original figures in S. Darlington patent, 1952 [1]. (c) Darlington configuration of the Infineon BGA616 Gain Block. .... 125

Figure 6.2 Different types of PCB lines: (a) Stripline. (b) Microstrip line. (c) Coplanar line. (d) Coplanar line with ground layer. .... 130

Figure 6.3 Simulation of different 30 mm length PCB transmission lines. *Upper figure*: Reflection coefficient of optimized transmission lines. *Lower figure*: effects of variations in line width in a coplanar (with ground layer) transmission line. .... 131

Figure 6.4 (a) Contribution of the PCB lines to the reflection coefficient. The dashed line includes the effects of MMIC connection pads, much thinner than the lines. (b) Effect in the amplifier performance of via holes close to the coplanar lines. .... 132

Figure 6.5 High frequency parasitic model for inductors (a) and capacitors (b) ..... 133

Figure 6.6 Reflection coefficient for some components. *Dots*: measured; *Line*: simulated. .... 134

Figure 6.7 (a) Amplifier schematic, including the bias circuit and the DC block capacitors. (b) SPICE model of the amplifier (BGA616) (c) APLAC simulation of the  $S_{21}$  of the DC block and bias circuit, including all the parasitics calculated in the previous section. The amplifier has been short-circuited in this simulation. .... 136

Figure 6.8 (a) Response of an amplifier to a -200 mV input pulse. (b) Detail of the pulse tail as a function of the bias inductor value. .... 137

Figure 6.9 (a)  $S_{21}$  of the different analyzed amplifiers. The crosses denote the 3 dB bandwidth. Models noted as 'A' correspond to a standard. Models noted as 'B' correspond to configurations with extended dynamic range. (b) 'A' and 'B' configurations. .... 139

Figure 6.10 Comparison of measured and simulated  $S_{21}$  parameter for BGA616, in order to illustrate the effect of parasitics. .... 141

Figure 6.11 Measured scattering parameters. Models noted as 'A' correspond to a standard. Models noted as 'B' correspond to configurations with extended dynamic range. .... 141

Figure 6.12 Power loss of fabricated prototypes. .... 142

Figure 6.13 Stability parameters of the tested amplifiers. The device is unconditionally stable if  $\kappa > 1$  and  $\Delta < 1$  (or  $U > 1$ ) for every frequency. .... 143

Figure 6.14 Stability circles of the selected amplifiers plotted in the range 50 MHz - 2 GHz. *Upper graphs*: BGA616. *Lower graphs*: SGA4563 (B model). *Left*: source stability circles. *Right*: load stability circles. The center of the Smith chart is stable ..... 144

Figure 6.15 Dynamic range and linearity of several MMICs. Models noted as 'B' correspond to configurations with 3.3 k $\Omega$  feedback resistor for extended dynamic range. .... 145

Figure 6.16 Detailed dynamic range of the receiver photodiode - MMIC set. .... 146

Figure 6.17 BGA 616 response for a 4 ns FWHM, variable amplitude photodiode output pulse. .... 147

Figure 6.18 The 'Y Factor Method' for noise measurement procedure [14]. .... 148

Figure 6.19 Noise figure of the tested MMICs. .... 149

Figure 6.20 Temperature dependence of the BIAS current for BGA616 and SGA4563Z MMICs. .... 151

Figure 6.21 Fluctuation of the BGA616 scattering parameters with temperature variations. The lower graphs represent the power loss due to reflections at the input and at the output of the MMIC. .... 151

Figure 6.22 Influence of temperature variations on the amplifier output. .... 152

Figure 6.23 (a) Complete view of the ‘MONSTER’ receiver board for the MAGIC II telescope. (b) Detail: photodiode connection and pre-amplifying stage consisting on BGA616 MMICs and the corresponding bias network. The buffer amplifier for the readout electronics is also seen. .... 153

Figure 6.24 (a) Setup for the test of the Receiver Board: VCSEL – photodiode – preamplifier connected to a Network Analyzer. (b) Measurement of the scattering parameters. Top left:  $S_{11}$ . Top right:  $S_{12}$ . Bottom left:  $S_{21}$ . Bottom right:  $S_{22}$ . The VCSEL used in these tests had a 75 Ohm input impedance. .... 154

Figure 7.1 Equivalent circuit of the LED. .... 160

Figure 7.2 Measured (symbols) and simulated (line) reflection coefficient of the diode in equilibrium (circles) and with a forward bias of 4.5 V (triangles).  $|r_L|$  for 4.5 V has been divided by 3 in order to differentiate the curves better. The values of the elements used in the simulation are:  $R_j=1371 \Omega$ ,  $C_j=54.92 \text{ pF}$ ,  $R_s=19 \Omega$ ,  $C_p=0.3 \text{ pF}$ ,  $L_p=6.5 \text{ nH}$  (equilibrium), and  $R_j=11.54 \Omega$ ,  $C_j=145 \text{ pF}$ ,  $R_s=19 \Omega$ ,  $C_p=0.3 \text{ pF}$ ,  $L_p=6.5 \text{ nH}$  (bias of 4.5V). .... 162

Figure 7.3  $C$ - $f$  and  $G$ - $f$  curves at 0 V. Total low frequency conductance and capacitance (open circles) and high frequency junction conductance and capacitance (stars). The nonlinear fit shown in the capacitance plot was obtained with  $C_1=77.5 \text{ pF}$ ,  $\tau_1=2.08 \text{ ns}$ ,  $C_2=12 \text{ pF}$ ,  $\tau_2=54.9 \text{ ns}$ ,  $C_j=54.92 \text{ pF}$ . .... 163

Figure 7.4 Measured and simulated I-V curves. Effect of the neglect of the series resistance [curve (a)] and the heating of the device [curve (b)] in LED# 4 are also shown. .... 169

Figure 7.5 Accumulated error of the simulation as a function of  $R_s$  and  $\theta$  (LED # 4). The vertical and horizontal lines indicate the values used in the simulation. This error was calculated as  $\varepsilon_{Acc} = \sum_{K=1}^N \left| \log(I_{meas_K}) - \log(I_{sim_K}) \right|$  where  $N$  is the number of measured IV points,  $I_{meas}$  the measured current and  $I_{sim}$  the simulated one.  $N=101$  in all the measurements presented here. .... 169

Figure 7.6 Measurement of the antenna effect of a MAGIC II PMT pixel with a spectrum analyzer. The photomultiplier and the preamplifier were both unbiased and the Winston cone is used. Similar values were obtained without the Winston cone, and with a backside shielding. .... 172

Figure 7.7 Simulation of the degradation of shielding effectiveness of a wall with a single circular aperture as a function of the diameter. Far field conditions are assumed. .... 172

Figure 7.8 Effective cable connection to a shielded box [25]. .... 173

Figure 7.9 Unshielded wire radiation inside a conductive box [26]. .... 174

Figure 7.10 Attenuation of a cylindrical waveguide in cutoff mode for two different lengths ( $L$ ) and two different dielectric filling permittivities  $\varepsilon_r$ . .... 175

Figure 7.11 Calculation of the SE of a conductive wall. .... 176

Figure 7.12 (a) Box fabricated for the PMT tests. The front side is shown with the detail of the cylindrical waveguide for optical fiber access. (b) Comparison between the signal detected by an unbiased PMT when located outside (top) and inside (bottom) the box. .... 177

Figure 7.13 Measured and simulated pulse waveforms. Pulse measured without blocking C (a) and (b) influence of the blocking C on the measured pulse. .... 179

Figure 7.14 (a) Measured pulse waveforms at the output generator (top) and at the output PMT (bottom). (b) Measurement of the PMT with the conventional technique based on a plastic scintillator. .... 180

Figure 7.15 PMT anode pulse (peak) as a function of the LED polarization. .... 180

List of Figures

---

Figure 7.16 Signal from the PMT when excited with the PicoQuant LED. *Circles*: raw signal. *Line*: averaged.....181

Figure 7.17 Response of a Kingbright L53MBC when mounted on the SRD pulse generator....182

Figure 8.1 CTA layout (a) and projected sensitivity of the CTA Array (b).....190



## LIST OF TABLES

Table 2.1 Characteristics of the MITEL 1A446 PIN photodiode. ....	30
Table 2.2 Sources observed during periods P33, P46 and P59. ....	54
Table 3.1 Polarity of the pulses as a function of the logic gate and the number of amplifiers.....	66
Table 3.2 Typical carrier lifetime for several commercial SRDs.....	70
Table 6.1 Some commercially available devices.....	128
Table 6.2 Basic characteristics of the FR4 laminates.....	130
Table 6.3 Characteristics of some commercially available 100 $\mu$ H inductors.....	133
Table 6.4 Parameterization of the inductor and capacitor models. ....	134
Table 6.5 Component values of the Figure 6.9b. ....	140
Table 6.6 Noise parameters of MMICs. ....	149
Table 7.1 Measured Devices.....	168
Table 7.2 Model Parameters.....	170
Table 8.1 Description of the projected telescopes for CTA .....	190



## ABBREVIATIONS

**AGN** : Active Galaxy Nuclei  
**AMC** : Active Mirror Control  
**APD** : Avalanche PhotoDiode  
**CAD** : Computer Aided Design  
**CCD** : Charge Coupled Device  
**CMOS** : Complementary Metal Oxide Semiconductor  
**CRAB** : Capacitor Ring Analog Board  
**CTA** : Čerenkov Telescope Array  
**DAQ** : Data ACquisition  
**DBR** : Distributed Bragg Reflector  
**DH** : Double Heterostructure  
**DRS** : Domino Ring Sampler  
**DUT** : Device Under Test  
**EM** : ElectroMagnetic  
**EMC** : ElectroMagnetic Compatibility  
**ENR** : Excess Noise Ratio  
**FADC** : Flash Analog-Digital Converter  
**FOV** : Field of View  
**FPGA** : Field-Programmable Gate Array  
**FWHM** : Full Width at Half Maximum  
**GAPD** : Geiger-mode Avalanche PhotoDiode  
**GLAST** : Gamma-ray Large Area Space Telescope  
**GRB** : Gamma Ray Burst  
**GSM** : Global System for Mobile communications  
**HBT** : Heterojunction Bipolar Transistor  
**HPD** : Hybrid PhotoDiode tube  
**IACT** : Imaging Air Čerenkov Telescope  
**LAT** : Large Area Telescope  
**LED** : Light Emitting Diode  
**LUT** : Look Up Table

**MAGIC** : Major Atmospheric Gamma Imaging Cerenkov telescope  
**MESFET** : MEtal Semiconductor Field Effect Transistor  
**MMIC** : Monolithic Microwave Integrated Circuit  
**MPPC** : Multi-Pixel Photon Counter  
**NF** : Noise Figure  
**NSB** : Night Sky Background  
**NTP** : Network Time Protocol  
**OPAMP** : Operational AMPlifier  
**OSO** : Orbiting Solar Observatory  
**PCB** : Printed Circuit Board  
**PMT** : PhotoMultiplier Tube  
**PRF** : Pulse Repetition Frequency  
**PSF** : Point Spread Function  
**PULSAR** : PULSer And Recorder  
**QE** : Quantum Efficiency  
**RFIC** : Radio Frequency Integrated Circuit  
**SE** : Shielding Efficiency  
**SIGMA** : Système d'Imagerie Gamma à Masque Aléatoire  
**Si-PM** : Silicon PhotoMultiplier  
**SMA** : SubMiniature-A connector  
**SMD** : Surface Mount Device  
**SRD** : Step Recovery Diode  
**TDT** : Terrestrial Digital Television  
**TE** : Transversal Electric  
**TEM** : Transversal ElectroMagnetic  
**TM** : Transversal Magnetic  
**TTL** : Transistor-Transistor Logic  
**VCSEL** : Vertical Cavity Surface Emitter Laser  
**VERITAS** : Very Energetic Radiation Imaging Telescope Array System  
**VSWR** : Votage Standing Wave Ratio

# Chapter 1

## Introduction

1. Gamma-Ray Astronomy History
  - 1.1 Early days
  - 1.2 The Satellite Era
  - 1.3 Ground-based Telescopes
2. Gamma rays in the atmosphere
3. Detectors
4. High frequency, low noise electronics
5. Structure and Objectives of this Thesis
6. References

## 1. GAMMA-RAY ASTRONOMY HISTORY

**A**STROPARTICLE Physics is a relatively young Science. For around a century, as it was evolving it gathered experts from different disciplines, as astronomers, particle physicists or cosmologists. But as the energy ranges expanded and particle detection was more and more complicated, the complexity of the detection systems also increased, and Electronics became a priceless partner.

In this chapter, a brief introduction to gamma-ray astronomy and IACT (Imaging Air Čerenkov Telescopes) is done, with special emphasis on the MAGIC Telescope, the project in which the work for this Thesis is framed.

### 1.1. Early days

The first studies on cosmic rays in History were developed by V.F. Hess in 1911, 1912 and 1913, when he was trying to identify an unknown source of ionization. His efforts were aimed to measure the absorption of gamma rays from radium at certain distances from the source, and confirmed that at an altitude of 500 m all the gamma rays coming from ground were almost completely absorbed. The straightforward experiment was to increase altitude, and for that he made several balloon flights in which he carried various (to avoid instrumental errors) electrometers that registered the ionization of the air. Contrarily to his prediction, the amount of ionized particles increased with altitude, what was a demonstration of the existence of an extraterrestrial source of ionization [1].

In 1921, in United States, Millikan examined and confirmed the existence of this ionizing radiation. Due to the high propagation distances, he concluded (later it was proven to be wrong) that the radiation should be high energy gamma-rays. As they were coming from out of Earth, he gave them the name of Cosmic Rays.

J. Clay, in 1927, demonstrated that the radiation is latitude dependent, and so it is influenced by Earth's magnetic field. Combined measurements of cosmic ray flux as a function of latitude and incident direction finally proved that cosmic rays were mainly composed by charged particles.

In early 30's atmospheric showers were discovered. When the cosmic rays interacted with particles in the atmosphere, secondary particles were created which would produce a new interaction. This way, a shower of particles was created by an incident cosmic ray. This opened a brand new field in the study of cosmic rays, and nowadays is the basis of ground-based Čerenkov telescopes.

A special remark must be done on Arturo Duperier Valesa, born in Pedro Bernardo, Ávila (Spain). With the end of the Spanish Civil War, Duperier was removed from his department in Madrid and forced to move to England. In Manchester's University he collaborated with the Nobel Prize M.S. Blackett, becoming one of the most important authorities in Particle Physics. He was proposed for the 1958 Nobel Prize in Physics [2].

In the 40's and 50's, predictions on gamma ray flux were very optimistic. This led to the design of several experiments with balloons and rockets. But the existing instruments were not sensitive enough to detect the actual fluxes, and frequently the results were ruined by too few statistics and experimental uncertainties.

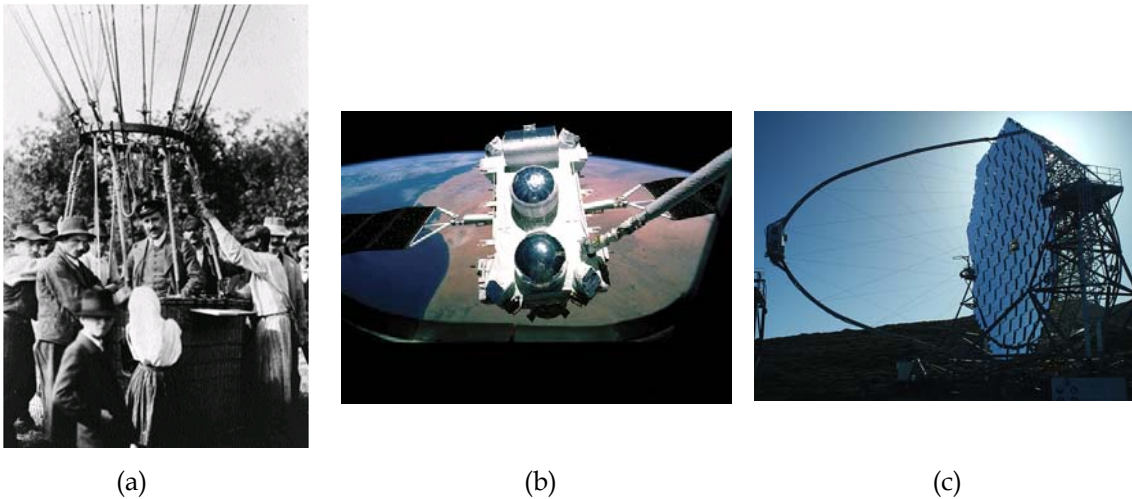


Figure 1.1 (a) Viktor Hess balloon flight, 1912. (b) Compton Gama-Ray Observatory, launched in 1991. (c) MAGIC I Telescope, inaugurated in 2003.

## 1.2. The Satellite Era

In the 60's, a new field was opened, which lasts until present day [3]. With the development of the spatial career, satellites became a feasible tool to support extra-atmospheric instruments for cosmic rays measurements. The number of detected sources rapidly increased.

In 1961, the Explorer XI discovered the first gamma rays outside the atmosphere.

The satellites of Vella Network were initially designed to detect illegal nuclear tests after the Nuclear Test Ban Treaty of 1963. In 1967, they detected the first Gamma Ray Burst in history.

In 1968, the OSO-III (Orbital Solar Observatory) detected at 100 MeV the first gamma rays coming from Milky Way.

In 1972, the OSO-VII discovers spectral lines of annihilation (511 MeV) and neutron capture (2.23 MeV), and nuclear interaction at 4.4 and 6.1 MeV in the solar flares.

At that time, satellites were provided with omnidirectional scintillators with detection ranges between 100 keV and 30 MeV. This way, the diffuse cosmic ray background was discovered. At mid 70's some detailed maps of the Milky Way were produced, but it was not until the 90's when the gamma-ray sources exploration reached its maturity. The French experiment SIGMA (Système d'Imagerie Gamma à Masque Aléatoire), on board of the GRANAT satellite, discovered around 30 sources in the galactic center region emitting in the transition between X and gamma rays (30-1000 keV).

The 'golden age' of space gamma-ray telescopes started with EGRET (Energetic Gamma Ray Experiment Telescope), an instrument aboard the American satellite Compton Gamma Ray Observatory [4]. The observation covered the range between 30 MeV and 30 GeV, and more than 270 sources of gamma ray emission were detected. The number of identified sources is expected to increase even more with the data obtained by the Fermi Gamma-ray Space Telescope (formerly named the Gamma-ray Large Area Space Telescope, or GLAST [5]). This telescope was launched on June 2008 and is expected to produce results shortly.

### **1.3. Ground-based Telescopes**

As early scientists had demonstrated, cosmic rays are attenuated by the atmosphere and the flux is severely reduced at ground level. This was a determining handicap in the study of gamma-ray sources at the Earth's surface. The only way to develop a detector capable to collect information about the gamma ray sources was to deal with the atmospheric showers created by the interaction of the incident radiation with the particles of the atmosphere. But the main difficulty was to distinguish between the showers produced by charged particles (which provide no information about the position of the source due to interaction with magnetic fields) and the showers produced by gamma rays.

This problem was overcome in 1985, when Hillas developed an analysis method to discriminate between both types of phenomena [6]. By the study of the shape of the Čerenkov light produced by a shower, Hillas was able to determine the kind of particle that initiated the interaction in the atmosphere, and thus reject the events produced by charged particles. This led to the



evolution of the IACTs (Imaging Air Čerenkov Telescopes), with bigger and bigger mirrors, more and more sensitive detectors and wider and wider detection energy range.

Whipple was one of the first constructed IACTs, with a 10 m reflector and a detection range between 100 GeV and 10 TeV. In 1989, this experiment produced the first observation of a TeV source, the Crab Nebulae, which has become the standard candle for ground-based Čerenkov telescopes [7].

After Whipple success, several more IACTs have been designed and constructed. Cangaroo in Australia, VERITAS (based in Whipple design) in United States, HESS in Namibia and MAGIC in La Palma (Spain). While Cangaroo, VERITAS and HESS were designed to take advantage of the stereoscopic vision (which leads to a better reconstruction of the impact point and the size of the atmospheric shower), MAGIC Collaboration concentrated in building the biggest and fastest telescope possible [8]. This resulted in a 17 m fast-moving telescope with the best energy threshold up to now (some tens of GeV). MAGIC II telescope is currently in its commissioning period, and together with MAGIC I provides stereoscopic vision, apart from an even lower threshold [9].

With the design of CTA (Čerenkov Telescope Array) a new generation of IACTs is expected. Two different arrays of telescopes, one in the northern hemisphere and other in the southern one will explore galactic and extragalactic sources within an energy range between 10 GeV and 100 TeV. It will work as an observatory, meaning that part of the observation time will be available for astrophysicists outside the international collaboration. This is an important difference with respect to current experiments, which follow a very restrictive policy with the observation data [10].

## 2. GAMMA RAYS IN THE ATMOSPHERE

As was early discovered, cosmic rays consist mainly in charged particles. The flux of these particles depends on their energy, whose range extends from keV to thousands of TeV as can be seen in Figure 1.2a. But no study of the sources can be performed based on charged particles, as they are deflected by magnetic fields and do not provide information about their origin [11].

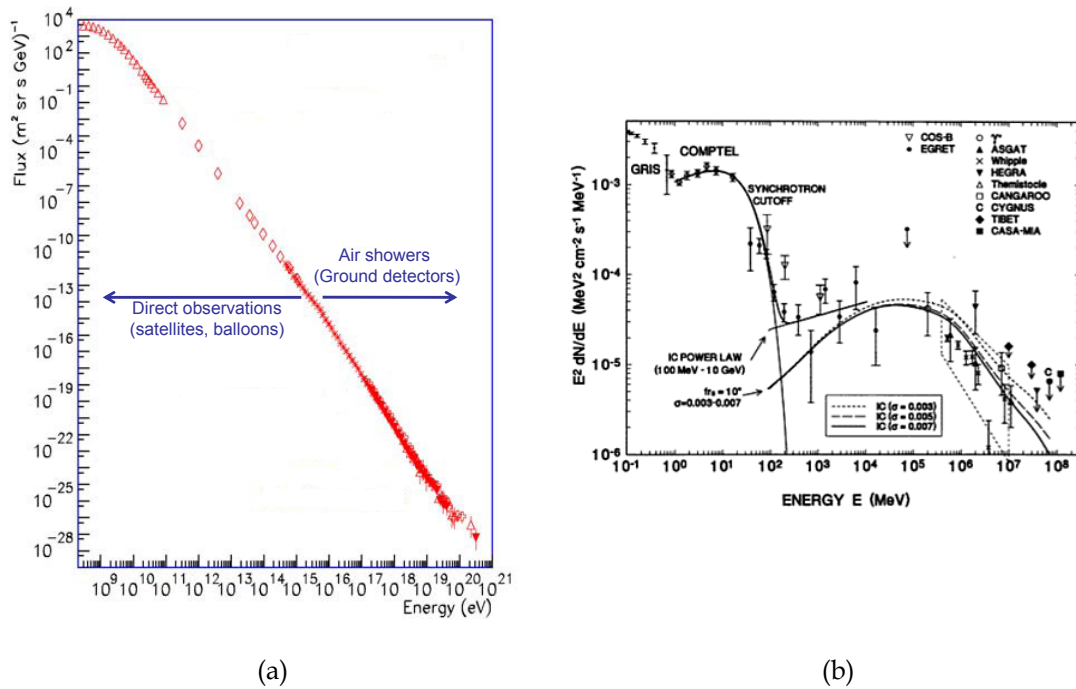


Figure 1.2 (a) Diffuse cosmic rays spectrum [12]. (b) Gamma-ray emission of the Crab Nebulae, as seen by different detectors [13].

Gamma rays, though much less abundant, are not charged and thus they conserve the original trajectory from the source to the detector. Therefore, they became the object of study of astrophysicist devoted to the knowledge of cosmic objects at high energies. Extraterrestrial gamma-rays are classified according to their energy, from Low Energy gamma-rays (100 keV - 10 MeV) to Ultra High Energy gamma-rays (more than 100 TeV). The higher the energy of the photons, the lower the flux is. This is the reason of the limit in the detection range of satellites, because the effective area of an instrument sent to space is much reduced. IACTs have an effective area which depends mainly on the mirror dimension, so particles of higher energy can be analyzed.

Earth's atmosphere is not transparent to gamma-rays. When a gamma-ray penetrates in the atmosphere it starts interaction, creating accelerated secondary particles which produce more interactions. This way, an Extended Air Shower (EAS) is created, as shown in Figure 1.3. The original gamma-ray produces an electron and a positron, and both of them lose a fraction of their energy by Bremsstrahlung creating a new, lower energy gamma-ray that starts again the process. The multiplication continues until the shower reaches a maximum, when the probability of energy loss by ionization and by Bremsstrahlung is the same. The shower finishes when the produced gamma-rays are so low in energy that cannot produce new electron-positron pairs.

It is important to remark that an atmospheric shower can also be initiated by a charged particle. This shower contains no information about the source so it must be discarded. The creation of a method to discriminate both types of shower supposed the birth of ground-based gamma-astronomy; these 'gamma-hadron separation methods' are of extreme importance and subject of hard study [14].

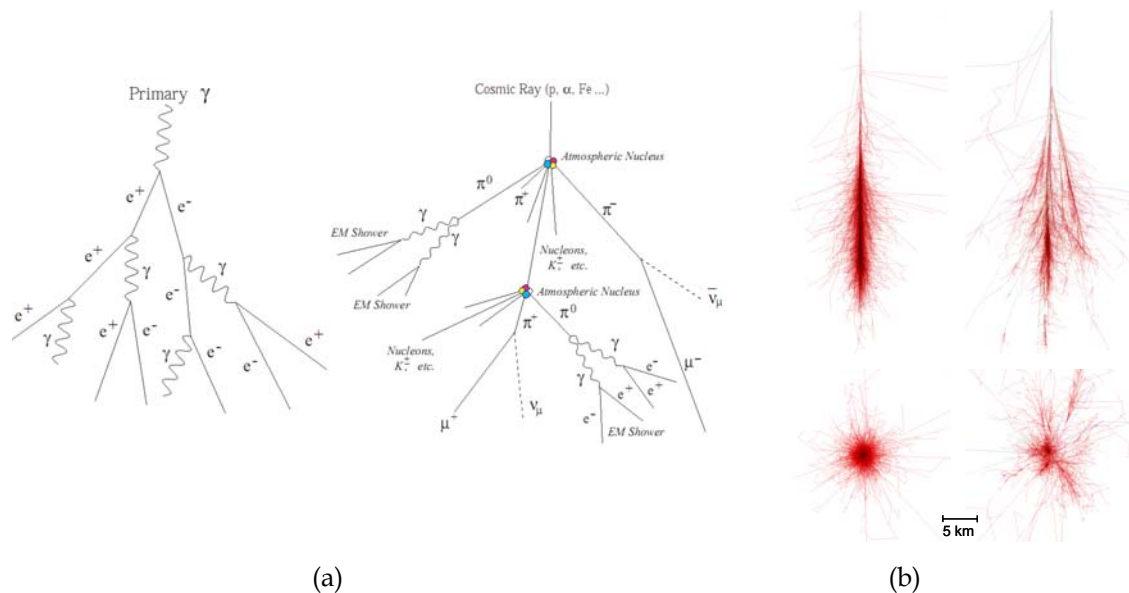


Figure 1.3 (a) Schematic representation of an air shower created by a gamma-ray (left) and a cosmic ray (right) [15]. (b) Monte Carlo simulation of air showers with CORSIKA software [16].

When a charged secondary particle is accelerated beyond the speed of light in the atmosphere, Čerenkov radiation is produced. The propagation angle of the emitted light is given by the velocity of the particle and the refraction index of the atmosphere, as seen in Figure 1.4a.

The intensity of the radiation is proportional to the energy of the particle (up to X-ray wavelengths), but due to attenuation in the atmosphere, the intensity of light peaks in the blue range of the visible spectrum (see Figure 1.4b).

For a gamma ray induced shower, the Čerenkov light intensity is very low (hundreds of photons per square meter) and the duration very short, with a front that lasts between 1 and several ns depending on the particle which originates the shower. To detect a light flash of these characteristics, IACTs must be provided with very sensitive and fast photodetectors. In the next section a brief description of some of these devices will be given.

Typical gamma-ray showers start at 20 km altitude, and have their maximum at 10 km over sea level. The Čerenkov emission angle is  $\sim 1^\circ$  so the radius of the area reached by the light is roughly 120 m. This means that the telescope would detect any shower with an impact parameter (distance between the center of the mirror and the point where the shower would hit the ground) lower than 120 m.

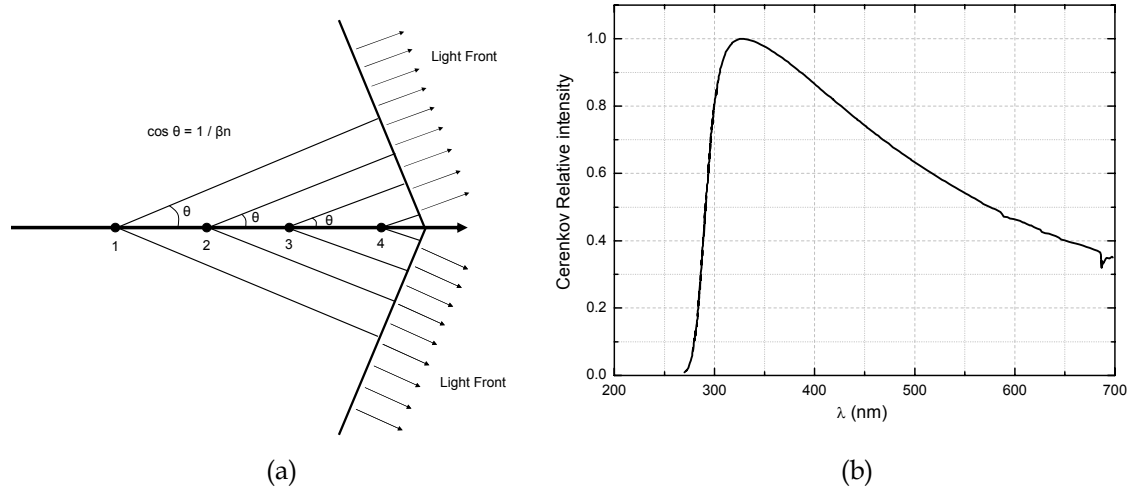


Figure 1.4 (a) Čerenkov light front. (b) Spectrum of Čerenkov light in atmosphere [17].

The light produced by the shower is reflected by the mirror and projected into the camera with elliptic shape (see Figure 1.5a). Analyzing the properties of these ellipses (Hillas parameters) it is possible to extract information about the shower. The main parameters, shown in Figure 1.5b, are the following:

*Length (L)*: longitude of the major semi axis of the ellipse. It gives information about the length of the shower in the atmosphere.

*Width (W)*: longitude of the minor semi axis of the ellipse. It gives information about the width of the shower.

*Orientation angle ( $\alpha$ )*: is the angle between the major axis of the ellipse and the line connecting the center of the ellipse and the center of the camera.

*Size*: quantity of light included in the ellipse. It is usually measured in photoelectrons (phe)

*Nominal distance ( $d$ )*: distance between the center of the ellipse and the center of the camera. Informs about the impact parameter.

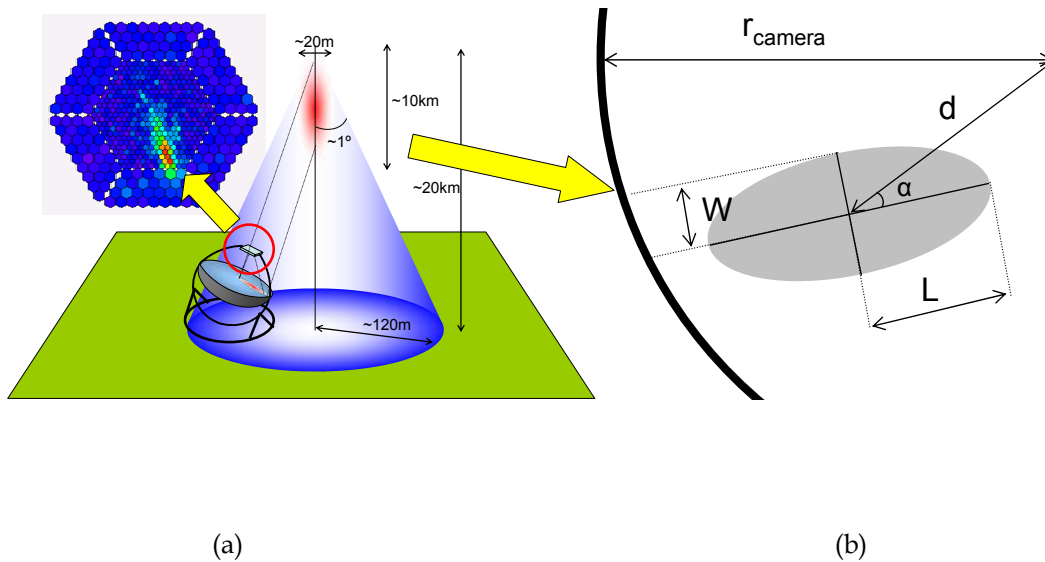


Figure 1.5 (a) Detection of gamma-ray showers by an IACT. (b) Hillas parameters for the analysis of extended air showers.

### 3. DETECTORS

The first instrument used for the detection of cosmic rays was the **electroscope**. This device consists in two parallel gold leafs hanging from an electrode. When some charge is collected by the electrode, it is equally distributed between both leafs and they repel each other. The distance between the gold leafs can be calibrated to measure the amount of charge. Viktor Hess and his contemporary researchers made their balloon experiments with several types of electrometers, and this way they discovered the cosmic origin of the ionizing radiation.

With the introduction of the **cloud chambers** (C.T.R. Wilson, 1911) the first evidences of the trajectory of cosmic ray particles in the atmosphere were detected. Wilson was following the experiments of Aitken, who demonstrated that when a vapour is expanded (and thus its pressure and temperature decrease) the molecules lose energy and condensate around dust particles. Wilson demonstrated that if expansion was further increased, these clouds were created even if the air was filtered and no dust was present. He determined that some 'invisible' particles should exist in the atmosphere, and that these particles were continuously being replaced (clouds kept on appearing even after several expansions and consequent 'dust' removals). He also applied an electric field and condensation disappeared, so he concluded that the particles that produced the condensation were charged ions. Later, Hess discovered that these ions were created by cosmic rays [18].

In late 20's, Geiger and Müller designed the device commonly known as '**Geiger Counter**'. A metal strip was enclosed into a vessel, which was filled with an ionisable gas. A high voltage was applied to the conductor, so when a particle crossed the gas producing ionization, the resulting charged particles were collected and extracted by the metal strip. Although the performance of this device was not good for high energy particles (gas density was low and most cosmic rays passed through without interaction), consequent evolutions provided the scientist the first **coincidence detectors**. Coincidence technique allowed for the first time to detect two particles in a time window and to observe their coherence with respect to their common origin, or to detect an ionizing particle which passes at least two counters.

The introduction of the **photomultiplier tube (PMT)** was one of the most important milestones in experimental particle physics. Since its invention in the mid 30's it has been continuously evolved and widely used, and still nowadays is the common light detector in all IACT experiments. The PMT consists in a vacuum tube with a photocathode (material with low work function) and an anode used to extract the current. Several electrodes (dynodes) are placed along the tube between cathode and anode.

A high potential ( $\sim -1$  kV) is applied to a photocathode, and by means of a voltage divider decreasing voltage values are applied to the dynodes. When a photon hits the cathode, there is some probability that one electron of the cathode is released, and accelerated towards the next dynode, in which electron multiplication is produced. This process is repeated in every dynode, resulting in an overall multiplication factor that can vary from  $10^3$ - $10^4$  in 'ancient' PMTs [19] to  $3 \cdot 10^7$  in the newest models.

One of the most important features of PMTs is the quantum efficiency (Q.E.), i.e., the probability of an incident photon to produce an electron in the photocathode. The higher this probability, the better the performance as detector. PMTs can be designed to peak this efficiency in the blue region of the spectrum, to match the characteristics of Čerenkov light.

The time resolution of PMTs is dominated by statistics (poissonian distribution of the emission at the dynodes, transition time of the electrons along the tube...) but is as low as several ns [20]. The newest models perform less than 2 ns FWHM.

The second half of the 20th century supposed a revolution in Electronics, due to the huge advances in Solid State Physics. The creation of PN junction soon led to the design of new gamma-ray **detectors based in Silicon and Germanium**. The incident photon creates electron/hole pairs in the semiconductor, which are accelerated and collected by the ohmic contacts [21].

One of the best features of solid state devices is their detection efficiency. As there is very low probability that an incident high energy particle does not produce any pair in the sensitive region of the semiconductor, this efficiency is close to 100%. If the sensitive region is thicker than the range of the incident particle, the device will also perform a very good linearity. Dividing the junction into several strips, it is also possible to create position-sensitive detectors. A good example is the Large Area Telescope (LAT) on board of the GLAST satellite: a tracker consisting on 18 silicon-strip detectors reads out both  $x$  and  $y$  coordinates of the incident particle.

Silicon detectors, though, have several drawbacks that made them easily overcome by new detectors in ground-based gamma-ray astronomy. For example, the increase of the detection area implies to enlarge the capacity of the junction and so a worsening of the time response. There is also an important dependence of the performance with temperature; cooling is recommendable to decrease the noise.

Silicon diodes can be constructed in such a way that, when a given reverse bias is reached, any pair produced by an incident photon is accelerated and creates a carrier avalanche. Such devices are known as **Avalanche Photodiodes (APD)**. This process provides the diode with a multiplication factor ( $M$ , which

depends on the bias). Internal amplification makes the device less sensitive to noise, and therefore a suitable detector for small signals. The sensitivity, though, is lower than that of photomultipliers, being necessary at least 20 photons to produce an acceptable S/N ratio.

APDs have some drawbacks, though. Shot noise increases with gain. For lower values of internal amplification, device's noise is dominated by thermal noise, but as the gain increases the shot noise becomes dominant. Temperature is also an important factor, as it has a big influence on the gain, so compensation circuits have to be implemented to assure the constant gain of the device [22].

A further step is to combine the advantages of PMTs and solid state devices. This way, the **hybrid photon detector (HPD)** was born. A vacuum tube with a high Q.E. photocathode (more than 50% in the visible range for the newest designs) is biased at voltages of several kV. The generated photoelectrons are accelerated and focused on an APD. This way, two stages of amplification are applied: the first one due to acceleration and impact on the semiconductor, and the second due to avalanche in the diode. Combined multiplication factors of  $5 \cdot 10^4$  can be achieved. These devices have much better energy resolution, sensitivity and Q.E. than PMTs. The detection area is much bigger than that of solid state devices, and the time response is at least comparable to any other photodetector ( $\sim 2$  ns FWHM). The main drawbacks, though, are the ageing of the photocathode, high rates of afterpulses<sup>1</sup>, dark counts, temperature dependence or handling of high voltages (isolation, sparks...) [23]

In the last years, a very important effort has been done on these detectors. MAGIC II camera will include several clusters of HPDs in next steps of development [24] [25].

A novel detector has been introduced in recent years, mainly developed by Russian researchers. The basic idea is to operate an APD slightly over breakdown voltage in Geiger mode, that means, any incident photon produces the breakdown of the device, and so a fixed amount of charge is released. When the current in the diode is high enough, a series quenching resistor produces a voltage drop in the diode bias and stops the breakdown. When several of these so-called cells are connected in parallel, the dynamic range of the detector is equal to the number of cells. These detectors have been named in many ways depending on the geometry or use: Geiger mode APDs (GAPDs), Silicon Photomultipliers (Si-PM), Multi Pixel Photon Counters (MPPC)...

---

<sup>1</sup> An afterpulse is a random pulse produced when an ion present in the tube, due to the non-perfect vacuum, is accelerated towards the APD producing a signal several times higher than the one produced by a photoelectron. It can also be produced by the light emitted by a recombination in the semiconductor when hitting back the photocathode.



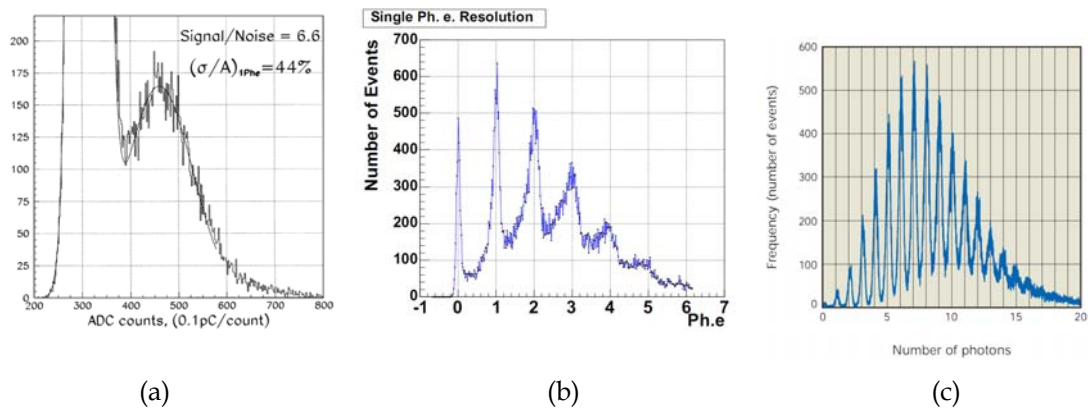


Figure 1.6 Energy resolution of modern photodetectors: (a) PMT [26] (b) HPD [27] (c) GAPD [28]

Some important features of these devices are:

- High energy resolution (much better even than that of a HPD).
- Very high sensitivity, performing single photon counting.
- High gain ( $10^5$  -  $10^7$ ).
- Dynamic range equal to the number of cells. The area of the device is increased in newer models, so this parameter is to be evolved.
- Easy manipulation (at difference with HPDs or PMTs, GAPDs can be biased at daylight without risk).

And some drawbacks:

- Small detection areas (this will be improved in future).
- High dark count rate (improved with cooling).
- Optical crosstalk between pixels.

Several tests have been performed with these devices. In MAGIC Telescope, 4 PMTs were replaced by GAPDs integrated in the data acquisition. The results were convincing, so further efforts are being done to incorporate these detectors in Čerenkov Telescopes [29] [30].

All of the photodetectors mentioned in this section are able to resolve single photons. This detection is usually made by means of a measurement plot called Single Photoelectron Resolution. Figure 1.6 shows an example of a single photoelectron response plot of different devices which were considered as photodetectors for MAGIC cameras. This plot is a charge histogram which can be observed with the aid of a fast oscilloscope. In order to see the resolution of the signals due to different photon numbers on the scope, a low light level, pulsed LED must be used. The LED should be suitable for use with a pulse generator which can generate a pulse width of 5 – 20 ns to give the best results.

## 4. HIGH FREQUENCY, LOW NOISE ELECTRONICS

The objective of IACTs is to study gamma-ray sources through the analysis of the Čerenkov light flashes produced by the electromagnetic air showers. The characteristics of these flashes, unfortunately, are not compatible with comfortable, standard tested electronics.

The low flux of the source as compared with the night sky background and other source of noise make specially critic the electronics noise performance. This is the reason of the development of internally amplified detectors such as PMTs, HPDs or GAPDs. As can be inferred from the Friis equation for the noise factor,

$$F_{sys} = F_1 + \frac{F_2 - 1}{G_1} + \frac{F_3 - 1}{G_1 G_2} + \dots + \frac{F_n - 1}{G_1 G_2 \dots G_{n-1}} \quad (1.1)$$

the first amplification stage is critical, and must have the best noise performance. But it must be pointed out that the Friis equation provides information on how the signal to noise ratio is degraded. This information is relevant, but not sufficient to fix the sensitivity specifications of each component belonging to the pixel chain. In fact, Friis equation could be used to argument that for detection with a GAPD, PMT or HPD it is unnecessary to use a low noise amplifier due to the fact that these photodetectors have enough gain. However, these devices could provide useful output signals in pulsed mode which are of the order of one hundred microvolts in  $50 \Omega$  loads. A ns pulse amplifier can generate similar or higher equivalent input noise voltages. For this reason attention has been paid in this thesis to the simulation in the time domain of the noise voltages generated by the amplifiers.

From the detection of the signal to the acquisition there are several stages of amplification, transmission and reception. Every device in the chain has a characteristic bandwidth, and must be chosen carefully not to degrade the total bandwidth of the system. Čerenkov pulses typically last 1 – 3 ns, so bandwidths higher than 500-700 MHz are desirable. Very wide dynamic range (up to 60 dB) is also recommendable, in order to better resolve the shower images. This implies the use of state of the art amplifiers, transceivers and digitizers. In next chapter MAGIC Telescope subsystems will be explained.

In the design, construction and test of any device it is important to provide conditions and signals as similar to the working ones as possible. With this goal in mind, it is very important to have in the lab tools to emulate Čerenkov pulses, and this implies the design of blue light pulse generators in the range of nanoseconds. For simulation, accurate models of pulsers and diodes are desirable. These topics are also addressed in this thesis.

## 5. STRUCTURE AND OBJECTIVES OF THIS THESIS

This Thesis is focused on the work developed in the frame of the MAGIC Collaboration, mainly in High Frequency Electronics for MAGIC I and II Telescopes. The main achievements during the PhD. period have been the following:

- Learning of the operation tasks of the MAGIC I Telescope. Participation in training periods and observation shifts.
- Design of low noise, low jitter pulse generators. The purpose of these devices is the testing of the analog transmission of the MAGIC I Telescope. A dedicated pulse generator was developed for the testing of the MAGIC II Telescope receiver boards. This generator feeds Vertical Cavity Surface Emitting Lasers (VCSELs) similar to that of MAGIC II camera in order to emulate operation conditions. Pulses of 1 ns FWHM and 4 V amplitude were obtained in order to fulfil the laser dynamic range.
- Design, production and test of broadband (up to 1 GHz), low noise and high dynamic range amplifiers. These amplifiers are integrated in the MAGIC II Telescope receiver boards, after the photodiodes which detect the signal transmitted from the telescope camera. Test of preamplifiers for the camera pixels.
- Based in previous designs, modelling and construction of a prototype of pulsed light emitter based on high speed blue LEDs. This prototype generates signals similar to the ones received by the Telescope, with the purpose of testing camera pixels.
- Setup of a testbench for time response and single photoelectron counting of the PMT and HPD used in the camera of MAGIC II Telescope and solid state detectors for future IACTs telescopes.

This work is exposed in the present Thesis, with the following structure:

In Chapter 1, a brief introduction to Gamma-Ray Astronomy is made, with special emphasis in the evolution of cosmic ray detectors. Extended air showers and Imaging Technique for ground-based telescopes are described.

Chapter 2 briefly describes the main subsystems of the MAGIC I and II Telescopes, and the work developed for one of the detectors of the MAGIC I Telescope: The Central Pixel. The photosensor, the transceiver and power supply are detailed in this chapter. Some results of optical observation on the Crab Nebula are also reported.

Chapter 3 presents the description and simulation of some models of pulse generator in the order of nanoseconds. One of these generators is currently being used in the test of the transmission chain of the pixels of the MAGIC I Camera. Another model was specifically designed for the test of the receiver boards of the MAGIC II Telescope. In Chapter 4 results on these generators are reported.

In Chapter 5 a theoretical approach to pulse amplifiers is made, with emphasis in the development of dedicated software for amplifier analysis and simulation.

Chapter 6 is devoted to the experimental work with these amplifiers. Some practical considerations are studied in detail: printed circuit performance, via holes for grounding, state of the art of MMIC and Surface Mount Devices (SMD), amplifier bias, etc. The performance of the most suitable amplifiers for MAGIC requirements is analyzed (bandwidth, gain, stability, noise, ringing, linearity, temperature stability...)

In Chapter 7, a study is made on pulsed light sources. An electrical model for GaN/SiC blue light emitting diodes is proposed, with which the describing parameters of the LED are obtained. A study of the properties of the photosensor testbenches is done.

In last Chapter, a summary of the main goals and conclusions achieved with this Thesis are presented.

## 6. REFERENCES

- [1] Elliot H., Sekido Yataro. *Early history of cosmic ray studies : personal reminiscences with old photographs*. D. Reidel Publishing Company, 1985.
- [2] González de Posada F., Bru Villaseca L. *Arturo Duperier: Mártir y Mito de la Ciencia Española*. Diputación Provincial de Ávila - Institución Gran Duque de Alba, Ávila, 1996
- [3] Volker Schönfelder, *The Universe in Gamma Rays*. Springer, 2001
- [4] Fichtel, C. E. et al. *The first energetic gamma-ray experiment telescope (EGRET) source catalog*. The Astrophysical Journey Supplement Series, 94:551-581, 1994 October.
- [5] W.B. Atwood et al. *Design and initial tests of the Tracker-converter of the Gamma-ray Large Area Space Telescope*. Astroparticle Physics 28 (2007) 422-434
- [6] A.M. Hillas, Proc. 19th ICRC, La Jolla 3 (1985) 445.
- [7] Weekes, et al. *Observation of TeV gamma rays from the Crab nebula using the atmospheric Cherenkov imaging technique*. 1989 Astrophysics J. 342, 379.
- [8] Barrio, J.A., et al. *The MAGIC Telescope Design report*. MPI Institute Report MPI-PhE/98-5, March 1998
- [9] C.Baixeras et al. *MAGIC Phase II*. 29th International Cosmic Ray Conference Pune (2005) 00, 101-104
- [10] *CTA Proposal to the European ESFRI sub-committee*. [http://www.cta-observatory.org/CTA\\_ESFRI\\_prop.pdf](http://www.cta-observatory.org/CTA_ESFRI_prop.pdf)
- [11] T. Stanev, *High Energy Cosmic Rays*, Springer, 2004
- [12] <http://astroparticle.uchicago.edu/sciam1.eps>
- [13] O. C. de Jager, A. K. Harding, P. F. Michelson, H. I. Nel, P. L. Nolan, P. Sreekumar, and D. J. Thompson. *Gamma-Ray Observations of the Crab Nebula: A Study of the Synchro-Compton Spectrum*. Ap. J., 457:253+, January 1996.
- [14] R.K. Bock, A. Chilingarian, M. Gaug, F. Hakl, T. Hengstebeck, M.Jirina, J. Klaschka, E. Kotrc, P. Savick, S. Towers, A. Vaiciulis, W. Wittek. *Methods for multidimensional event classification: a case study using images from a Cherenkov gamma-ray telescope*. Nuclear Instruments and Methods in Physics Research A 516 (2004) 511-528.
- [15] R. De los Reyes, *Search for gamma-ray emission from pulsars with the MAGIC telescope: sensitivity studies, data check and data analysis*. PhD Thesis, UCM 2008.
- [16] F. Schmidt. *Corsika shower images*, 2005.
- [17] M. Döring, K. Bernlöhr, G. Hermann, W. Hofmann, and H. Lampeitl. *Measurement of the Cherenkov light spectrum and of the polarization with the HEGRA-IACT-system*. Proceeding of the 27<sup>th</sup> ICRC. Hamburg (Germany), 2001.
- [18] N. N. Das Gupta, S. K. Ghosh. *A report on the Wilson Cloud Chamber and its application in Physics*. Reviews of Modern Physics, Volume 18 Number 2 April 1946.
- [19] B.K.Lubsandorzhev. *On the history of photomultiplier tube invention*. arXiv:physics/0601159v1
- [20] *Photomultiplier Tubes: Basics and Applications*. 3rd edition, 2007. Hamamatsu Photonics K.K.

- 
- [21] W.R. Leo, *Techniques for Nuclear and Particle Physics Experiments*, Second Revised Edition 1994. Springer Verlag.
- [22] *Characteristics and use of Si-APD (Avalanche Photodiode)*. Hamamatsu Photonics K.K.
- [23] C. D'Ambrosio, H. Leutz. *Hybrid Photon Detectors*. Nuclear Instruments and Methods in Physics Research A. 501 (2003) 463-498.
- [24] T.Y. Saito, E. Bernardini, D. Bose, M.V. Fonseca, E. Lorenz, K. Mannheim, R. Mirzoyan, R. Orito, T. Schweizer, M. Shayduk, M. Teshima. *Very High Q.E. HPDs with a GaAsP photocathode for the MAGIC Telescope Project*. Preprint submitted to Elsevier, 28 August 2008.
- [25] Ferenc D., Lorenz E., Mirzoyan R. A "LEGO" Hybrid Photon Detector - assembled from standard mass-produced vacuum components. Nuclear Instruments and Methods in Physics Research A, Volume 442, Number 1, 11 March 2000 , pp. 124-127(4)
- [26] A. Ostankov, D. Paneque, E. Lorenz, M. Martinez, R. Mirzoyan. *A study of the new hemispherical 6-dynodes PMT from electron tubes*. Nuclear Instruments and Methods in Physics Research A. Volume 442, Issues 1-3, 11 March 2000, Pages 117-123.
- [27] Takayuki Saito, Masaaki Hayashida, Razmik Mirzoyan, Thomas Schweizer, Maxim Shayduk, Eckart Lorenz Maria Victoria Fonseca Karl Manheim *Favorable properties of HPD R9792U-40 for the MAGIC telescope project*. Proceedings of the International Workshop on New Photon-Detectors PD07, 2007
- [28] *MPPC. Multi-pixel Photon Counter*. Hamamatsu Photonics K.K. 2008.
- [29] A. N. Otte, I. Britvich, A. Biland, F. Goebel, E. Lorenz, F. Pauss, D. Renker, U. Röser, T. Schweizer. *Detection of Cherenkov light from air showers with Geiger-APDs*. Proceedings of the 30<sup>th</sup> International Cosmic Ray Conference, Mérida (Mexico) 2007.
- [30] A. Biland, I. Britvich. E. Lorenz, N. Otte, F. Pauss, D. Renker, S. Ritt, U. Roesner, M. Scheebeli. *First detection of air shower Cherenkov light by Geigermode-Avalanche Photodiodes*. Nuclear Instruments and Methods in Physic Research A 595 (2008) 165-168.

# Chapter 2

## The MAGIC Telescopes

1. Introduction
2. Structure and Drive System
3. Reflector
4. Camera
  - 4.1 Photomultipliers
    - I. Preamplifiers and Optical Transmission
5. Readout System
  - 5.1 MAGIC I
  - 5.2 MAGIC II
6. Trigger
  - 6.1 Standard Trigger
    - I. Level 0 Trigger (L0T)
    - II. Level 1 Trigger (L1T)
    - III. Level 2 Trigger (L2T)
  - 6.2 Sum Trigger
7. Analysis
8. The Central Pixel
  - 8.1 Motivation
  - 8.2 The Photodetector
  - 8.3 The Electro-Optical System
  - 8.4 The Power Supply
  - 8.5 The DAQ System and Operation Modes
  - 8.6 Results: Crab Observations
9. Control and Operation of the Telescope

9.1 Organization of the shifts

9.2 Operation of the Telescope

10. References



## 1. INTRODUCTION

MAGIC I and II Telescopes are the most innovative detectors devoted to the study of Very High Energy gamma-rays from astrophysical sources. The telescopes are optimized to perform Čerenkov light detection from extended air showers in the range between some tens of GeV and tens of TeV. They make use of the Imaging Atmospheric Čerenkov Technique. The short light flashes are reflected by a 17 m Ø parabolic, tessellated high reflectivity mirror and focused into the camera.

Figure 2.1 shows two pictures of the MAGIC Telescopes. MAGIC I Camera is composed of 577 high speed, high quantum efficiency photomultipliers. The data is transmitted via optical fiber to the Flash-ADC located in the Control House, which is shown in Figure 2.1a. The overall bandwidth of the system is ~350 MHz, allowing a precise digitization of the incident pulses. In MAGIC II the camera contains more than a thousand pixels, and the bandwidth has been extended to above 500 MHz. The digitization is performed by a state of the art DAQ system consisting of a dedicated chip called 'DOMINO'. This AD conversion is performed basically by means of a capacitor array. The whole structure is able to point to any place in the sky in less than 40 seconds, which makes it the fastest existing Čerenkov Telescope.

The location of the Experiment is El Roque de los Muchachos, in the Canary Island of La Palma, Spain. It is placed at 2200 m altitude, in the observational site of the Instituto Astrofísico de Canarias [1]. The high altitude makes this place an exceptional location for air shower observation; the luminous contamination is minimal, and the Telescope is closer to the production of the showers than in other locations.



(a)

(b)

Figure 2.1 (a) MAGIC Site. (b) MAGIC I and II Telescopes.

## 2. STRUCTURE AND DRIVE SYSTEM

One of the main features of MAGIC Telescopes is their lightness. By reducing at maximum the weight of the components it is possible to optimize the response time of the system, and to aim rapidly to the source. This is of special relevance in the case of Gamma Ray Bursts (GRB). When a burst is detected by a satellite an automatic routine of the Central Control (that can be aborted by operators) interrupts the current observation source and points to the GRB in  $\sim 30$  s.

The frame of MAGIC I Telescope is built with carbon fiber and epoxy (CFR) tubular pipes in a lattice structure. The total weigh of the Telescope is  $\sim 72$  tons. This structure is lighter than conventional steel or aluminium structures implemented in other IACTs. However, a deformation due to the weight of the camera and reflector is produced. The camera is supported by an aluminium arc secured by steel cables. A Bending Model has been implemented in order to calibrate and correct the deformation of the structure [2].

The whole Telescope is mounted on a 20 m diameter rail, which allows rotation in azimuth by means of two commercial servo-motors ( $-90^\circ$  to  $318^\circ$ ). The reflector and camera move in declination ( $+100^\circ$  to  $-70^\circ$ ). For the control of the orientation shaft-encoders with 14 bits resolution are used, providing an angular resolution of a fifth of a camera pixel ( $\sim 1'$ ). At the end of both azimuth and elevation ranges, end switches are installed. Once the end switch is activated by a movement beyond the accessible range of the Telescope, a fast deceleration of the drive motors is started.

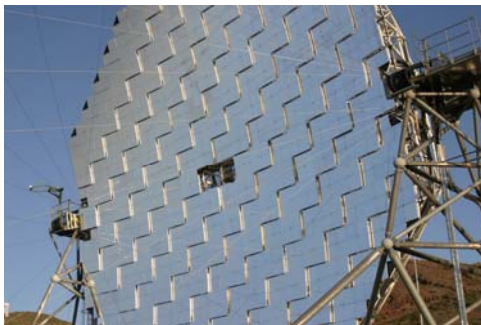
A CCD camera mounted in the center of the reflector registers continuously the sky and a LED system installed in the Telescope camera. The identification of the background stars (by means of the so called Star Guider System) and the position with respect to the LEDs allows the monitoring of the drive system performance [3].

MAGIC II carbon-fiber epoxy frame and drive system are very similar to the first telescope ones, with minor improvements. The documentation on these subsystems of the second telescope is still under development.

### 3. REFLECTOR

MAGIC I and II mirrors have a diameter of 17 m and a surface of approximately 240 m<sup>2</sup>. In order to optimize the timing of the signal, a parabolic design has been used. This arrangement minimizes the arrival time spread for the photons of an incoming plane front signal. This is of special relevance due to the short duration of the Čerenkov flashes, and reduces the influence of the Night Sky Background (NSB) photons. A spherical reflector was also considered but finally discarded. It showed high spherical aberrations as compared with parabolic reflector, which performs negligible aberrations for on-axis incidence and a slight coma with increasing incidence angle [4].

Both MAGIC I and II reflectors are tessellated structures, as shown in Figure 2.2. All the small mirrors have spherical curvature with radius equal to that of the paraboloid at the mirror center, and normal equal to the normal of the reflector in that point. This tessellation might introduce some more aberrations if the mirrors are not perfectly aligned, but this effect is controlled by means of a very accurate Active Mirror Control (AMC) [5].



(a)



(b)

Figure 2.2 MAGIC I (a) and II (b) reflectors.

MAGIC I reflector is composed of 964 small mirrors of 2.45 m<sup>2</sup>. In order to reduce the total weight special materials were used. The back layer is built in aluminium, and the front one in AlMgSi 1 alloy. In between both, an aluminium honeycomb gives the mechanical robustness. The front layer is polished to maximize reflectivity and mechanically manipulated to provide it the corresponding radius. A heating printed circuit below this layer avoids the freezing of the panels. The measured reflectivity of the mirrors is higher than 85% for the operating wavelengths (300 - 600 nm)

The movement of the reflector structure can produce a misalignment of the mirrors, especially when the telescope moves in elevation. The Active Mirror Control also fixes these misalignments. The mirrors are disposed in panels, in groups of four per panel. These panels can be moved by means of actuators in the corners. In the center of the panels, a laser points to the center of the Telescope camera, and a CCD camera reads the position of the laser spot. Via software, the AMC analyzes the spot pattern and moves the actuators until the CCD camera confirms that every panel has recovered the correct position.

An important figure of merit of the reflector is the Point Spread Function (PSF). The PSF is defined as the distribution of photons from a point object on the focal plane of a telescope, and can be fitted to a gaussian distribution with  $\sigma < 0.05^\circ$ , that means half the field of view of a camera pixel. It can be calculated by two methods: pointing the telescope to a star and analyzing pictures captured by a dedicated CCD camera, or reconstructing the camera pattern for muon incidence (see Figure 2.3)

MAGIC II reflector clones the main characteristics of MAGIC I. There are, though, some design differences. Instead of panels of 4 mirrors, 0.985 m side mirrors are used, with a central hole to host the AMC laser and actuators in the back. Two techniques have been used to build the reflecting surface. The outer mirrors are built with aluminized glass, while the inner ones are built with AlMgSi 1 as in MAGIC I. The glass-aluminium mirrors are easier to produce, lighter and have higher reflectivity, but are more sensitive to ageing [6].

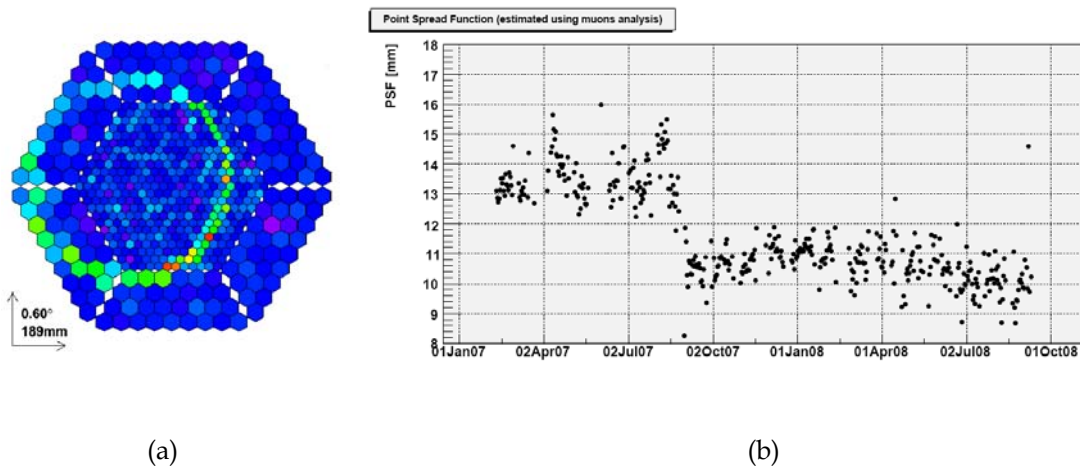


Figure 2.3 (a) Typical muon ring. Isolated muons with energy in excess of 6 GeV create such a geometric figure in the camera, which can be easily reconstructed to calculate the performance of the Telescope. (b) Point Spread Function of the MAGIC Telescope, estimated using muon analysis. The diameter of a MAGIC pixel is 24.5 mm [7]

## 4. CAMERA

MAGIC I camera is placed on the focal plane of the Telescope, at 17 m from the reflector center. It is supported by a single aluminium arc and steel wires. The camera frame encloses the photodetectors, preamplifiers, lasers and laser drivers and the Central Pixel PMT, supply and transmitter. The total weight of the camera is ~500 kg.

### 4.1 Photomultipliers

MAGIC I camera front is composed of 577 photomultipliers arranged in two different patterns, as shown in Figure 2.4. The 397 inner pixels are Electron Tubes ET9116A with 1" diameter and 0.1° field of view (FOV). The 180 outer pixels are Electron Tubes ET9117A with 1.5" diameter and 0.2° FOV. The total FOV of the camera is ~3.5°.

The PMT hemispherical bialkali photocathode is optimized for the blue region of the spectrum, and the nominal Q.E. peaks 25% at 350 nm wavelength. A special lacquer has been applied to increase this value up to 30%. Incident photons are scattered in this layer, increasing the probability of releasing an electron in the photocathode. On top of each PMT a Winston cone is used in order to maximize the detecting area of the camera [8].

Gain is chosen to be low, not to suffer damages for high anode currents due to accidental light incidence. The PMT has only 6 dynodes, for an overall multiplication factor of  $\sim 2 \cdot 10^4$  at operation voltages ( $\sim 1.1$  kV). Single photoelectron resolution above the noise pedestal is possible, as shown in Figure 1.6a.

Dynamic range of the PMT covers all possible event sizes, from a single photoelectron to the biggest showers of several hundreds of photoelectrons per pixel.

The linearity of the tube highly relies on the bias circuit. The basic configuration is a resistive divider which provides the operation voltage to each dynode. For high anode currents, though, a voltage drop is produced in the last resistors of the divider (the closest to the anode), deriving in a decrease of the overall gain. To avoid this effect, active loads have been applied to the last dynode stages of the PMT [9].

The time-domain response of PMT is among the fastest of all the actual detectors, with a PWHM of 2-3 ns that makes it capable to detect without distortion the fast Čerenkov pulses originated by gamma-ray showers.

MAGIC II camera has a different design, as shown in Figure 2.4b. Although the size and FOV is the same than MAGIC I, the number of pixels is increased to 1039 identical PMTs, allowing a bigger trigger region. The pixels are grouped in clusters of seven units. These clusters can be extracted independently, increasing the modularity of the system. Every cluster includes the PMTs, preamplifiers, transmitters, control electronics and test pulse generators. A big cooling plate is in contact with every cluster to refrigerate and reduce noise and instability of the VCSELs. Another feature of the camera is that the high voltage for the PMTs is produced inside the camera, independently for each pixel, by means of a Cockcroft-Walton generator. This feature avoids the need to transport the HV through the 170 m long cables [10].

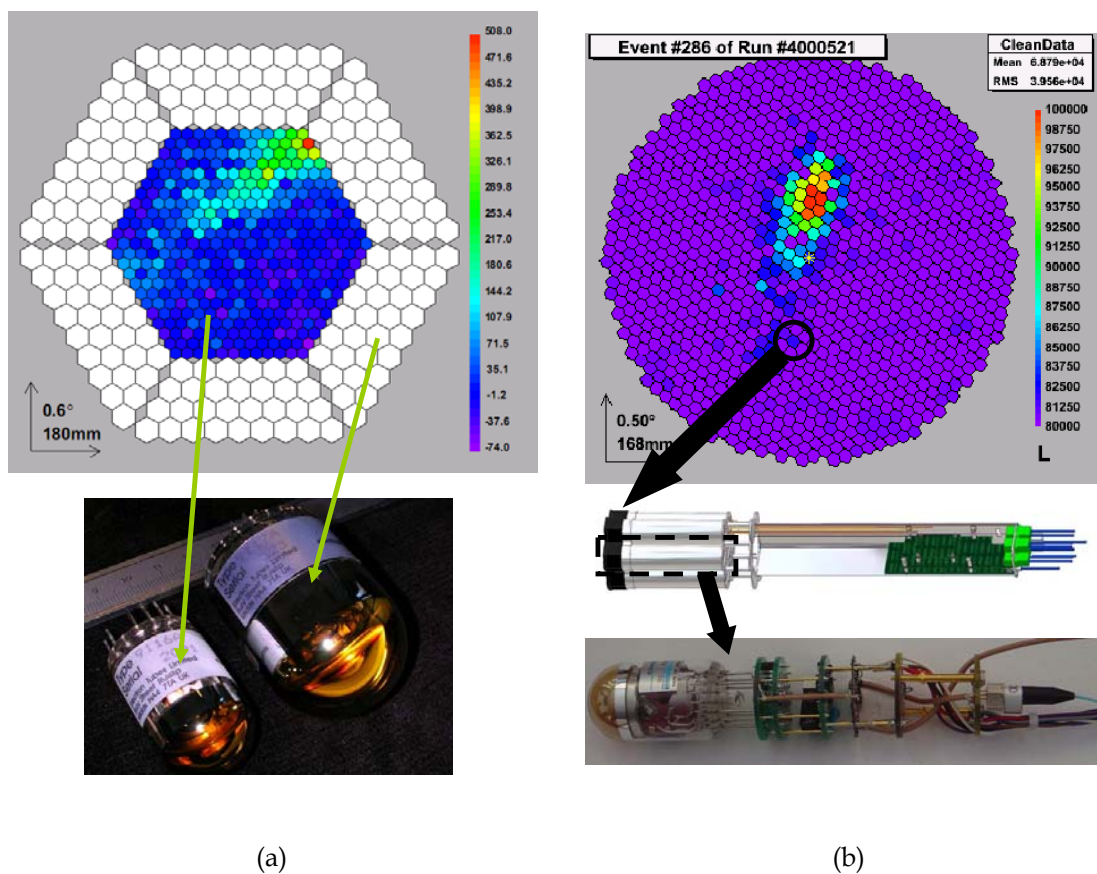


Figure 2.4 (a) MAGIC I camera structure. Picture of inner and outer pixels. (b) MAGIC II camera structure. Cluster and PMT with HV base, preamplifier, laser driver and VCSEL.

The chosen PMT for the MAGIC II camera is a Hamamatsu R10408, with roughly the same electrical characteristics of ET9116B but an increased Q.E. (35% [11]). It is planned to replace several of the clusters with HPDs, which



outperform PMTs in Q.E. (up to 50%) and increase the sensitivity of the Telescope.

A low frequency amplifier in the base of the PMT reads the anode DC current. This value is transmitted to the Central Control, where the PMT gain can be reduced (or even switched off) to avoid damages.

## 4.2 Preamplifier and Optical Transmission

As seen in section 1.4, Friis equation (Eq. 1.1) states that the first amplification stage is the most important in terms of noise. The closer to the detector it is, the lower the noise that will be introduced. For this reason, a low noise high frequency transimpedance preamplifier is placed at the base of the PMT.

In MAGIC I camera, the preamplifier performs 400 MHz bandwidth and  $\sim 400 \Omega$  transimpedance gain (Figure 2.5). The dynamic range is  $\sim 56$  dB.

Optical data transmission has several advantages over the electric one. The optical fibers are lighter than the coaxial cable, and pulse distortion and attenuation through the 170 m between the camera and the receiver boards is much lower. The probability of capturing electromagnetic noise (from the Telescope motors, for example) or electrical crosstalk is also cancelled by using fibers. Multimode, 50/120  $\mu\text{m}$  core/cladding and 170 m longitude optical fibers were used [12].

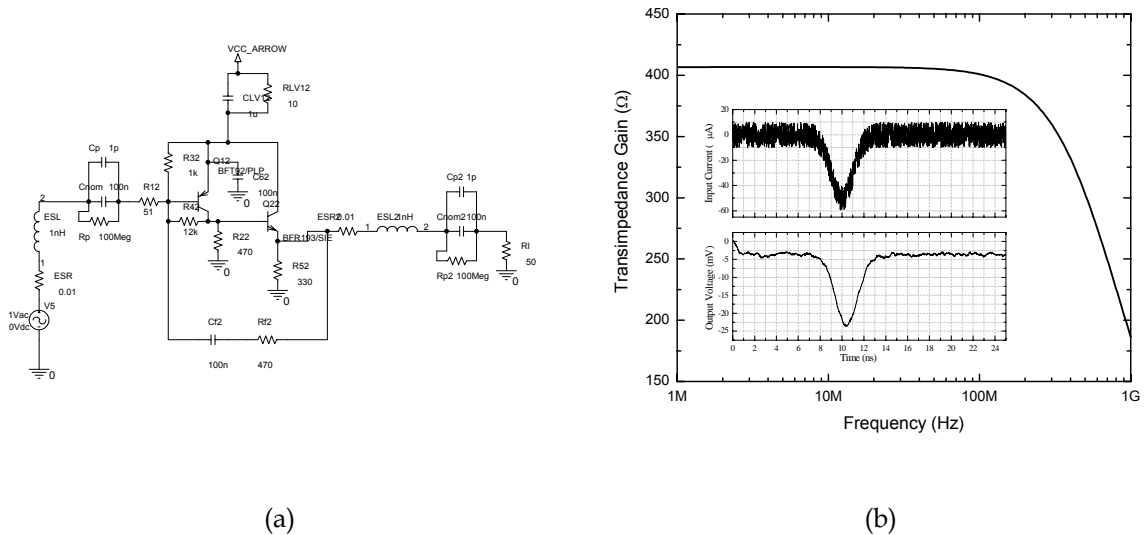


Figure 2.5 MAGIC PMT preamplifier: (a) Schematic. (b) Transimpedance gain simulation and response to a pulse.

A driver circuit transmits the signal to the VCSELs. This driver consists of a transconductance amplifier which biases the laser at 6 mA DC. This biasing keeps the laser permanently in its linear mode. The signal is added by the driver to this DC level.

In VCSELs, the confinement is produced perpendicular to the junction. The distance between the reflectors of the Fabry-Perot cavity is lower than in lateral emission devices. As the probability for a photon to produce stimulated emission decreases with the distance, to increase efficiency they must have highly reflective mirrors. The high reflectivity is achieved by means of distributed Bragg reflectors (DBRs). These reflectors consist in successive layers of dielectric and semiconductor with different refraction index. The high number of necessary layers increases the internal resistance of the device with respect to lateral emission devices.

The main advantage of vertical emission devices is the low power consumption, as the threshold current (the lower current needed for laser effect) is much lower than in lateral emission devices. It has been proved that lower currents produce less fluctuations in the height and width of the transmitted pulses [13], [14]. VCSELs also perform a high stability in I-V characteristics.

The model used in MAGIC I Telescope is the Honeywell HFE4080-321. Some of the features of this model are:

- Peak wavelength: 850 nm @  $I_{bias} = 12$  mA.
- 25  $\Omega$  impedance. This value is quite high as compared with other laser types. This simplifies the matching between laser and drive circuit.
- Rise and fall times in the order of 100 ps.
- Low beam divergence,  $\sim 15^\circ$ . This improves the coupling with optical fiber.
- High dynamic range, up to 100-200 mA for low duty cycle pulses.

Even though these devices are widely available, MAGIC has been the first Project which used them for analog transmission. Further details can be found in Paneque Thesis [13].

In MAGIC II camera a different approach has been taken. Instead of a transimpedance amplifier based on discrete components, a Monolithic Microwave Integrated Circuit (MMIC) gain block has been used. The output current of the PMT is converted into voltage pulses at the input of the pre-amplifier stage. Figure 2.6 shows a simulation of the scattering parameters of the MAGIC II camera preamplifier. This simulation was made with the software tools indicated in Chapter 5. The chosen model (a SiGe Sirenza SGA-5586Z)



performs an excellent  $50\ \Omega$  input and output impedance and a very low noise figure of 3 dB. The bias circuit has been designed to present a bandwidth from 100 kHz to 800 MHz with 1 dB flatness. The gain and the dynamic range fit the requirements imposed by the PMT output and the VCSEL: 1 photon incidence on the PMT means  $\sim 160\ \mu\text{V}$  pulse amplitude at the input of the amplifier, which is amplified 25.5 dB to be resolvable over the VCSEL's noise. The dynamic range of 60 dB adapts to the input voltage range of the VCSEL.

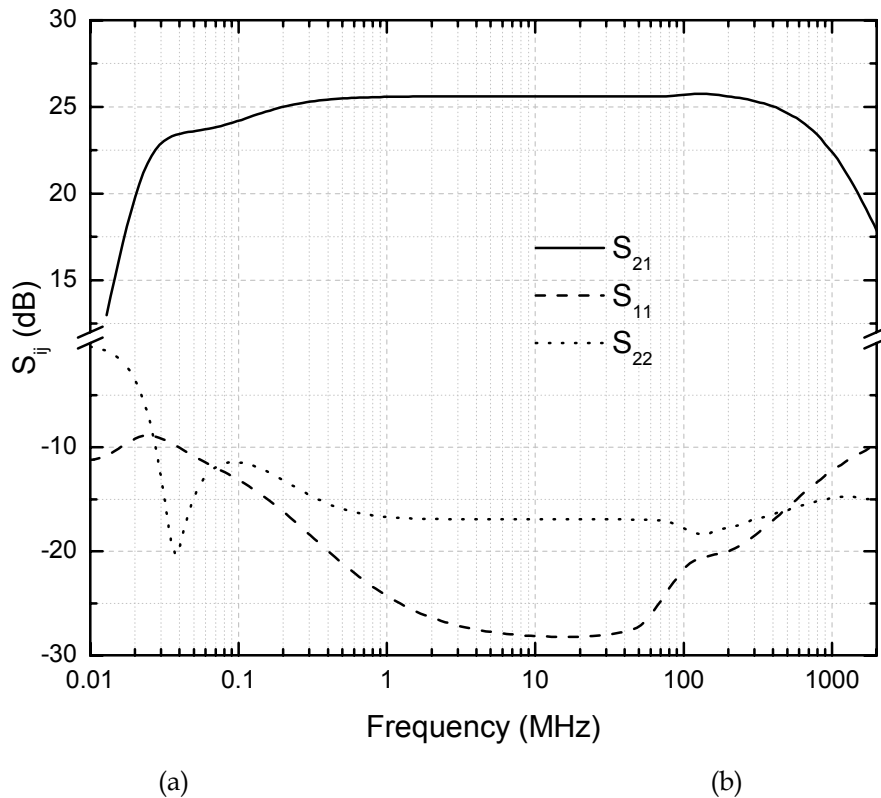


Figure 2.6 MAGIC II preamplifier simulation.

## 5. READOUT SYSTEM

### 5.1 MAGIC I

MAGIC I Telescope readout has recently been upgraded. The former system, operating from 2003 to 2007 is first described, and later an outline of the new multiplexed system will be given.

In the receiver boards, optical reception is performed by GaAs PIN photodiodes (MITEL 1A446), with the characteristics shown in Table 2.1.

PEAK WAVELENGTH (nm)	SPECTRAL SENSITIVITY (A/W)	CAPACITANCE @ 3.3-5V (pF)	RISE TIME (ns)	FALL TIME (ns)	BANDWIDTH (GHz)
850	0.45	1	0.4	0.2	1

Table 2.1 Characteristics of the MITEL 1A446 PIN photodiode.

These devices feature a very low input capacitance when reverse biased. The 1 GHz bandwidth makes them suitable for the optical-electrical conversion. The signal is amplified by a high frequency transimpedance amplifier.

As will be explained later, the digitizing of the signal is done by an 8 bit, 300 MHz FADC. This implies that the sampling rate of the AD converter is 3.3 ns. The fastest detected pulses are in that range, so the signal must not be directly sampled because there is a probability that the pulses are not detected by the system. In order to avoid this, the pulse is stretched to 6 ns, assuring that there is, at least, one sampling point for the fastest pulses. As the sampling rate follows a uniform distribution, for periods of 3.3 ns the obtained resolution is better than 1 ns ( $3.3/\sqrt{12}$ ).

In order to increase the resolution of the data acquisition, the pulse is divided by a splitter into two different branches, as shown in Figure 2.7. In the so-called high gain branch, the signal is amplified by a factor of 10. In the low gain branch, the signal is not amplified but delayed 50 ns. If the high gain branch signal exceeds a given threshold (set by the control software), an ultra fast GaAs diode commutes between branches, being both of them digitized by the FADC. This procedure increases the overall signal resolution.

The FADCs are distributed in 19 crates, each of them contains 4 base boards of 8 FADCs. This gives a total of 608 channels. The FADC bandwidth is 500 MHz, although in MAGIC they operated at 300 MHz with 8 bit resolution [15].

Since February 2007 the DAQ of MAGIC I was upgraded with a new 10 bit, 2 GS/s multiplexed FADC [16]. The goal of this DAC is to fulfil the duty cycle of the converter with several multiplexed channels. This way, for a trigger frequency of  $\sim 1$  kHz and pulses not longer than a few ns, it is possible to read 16 channels consecutively for every trigger event. The channels are adequately delayed by optical fibers.

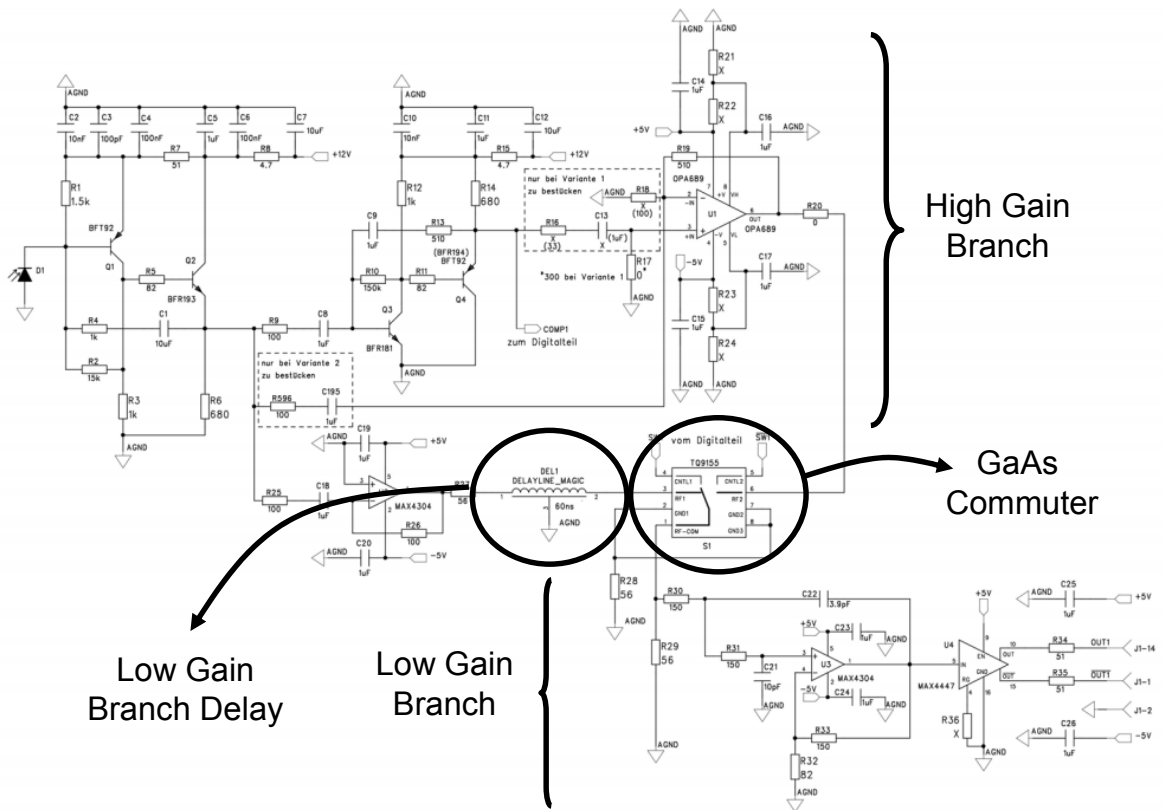


Figure 2.7 High and Low Gain Branches in the receiver board.

The signal is splitted to feed both the trigger logic and the FADC. The ultra-fast multiplexers assign one time slot to each channel, reserving some time between slots for the switching noise of the multiplexer not to affect the signal.

Mux-FADC bandwidth is 700 MHz, which produces an improvement in the pulse resolution, from 6.3 ns FWHM in former FADC to 3.2 ns in multiplexed

ones. In these new models no stretcher is needed, so the integration time for a pulse is lower and the resulting noise decreases in a 40%.

## 5.2 MAGIC II

An analog sampler based on CMOS technology has been developed for the readout of MAGIC II. The name is DOMINO Ring Sampler (DRS), due to the analogy of the system with the ancient tile game [17].

The analog part of the sampler consists of an internal ring buffer of 1024 cells. These cells (basically capacitors for charge storage) are sequentially activated by a 2 GHz frequency, <200 ps jitter clock signal called 'Domino Wave'. The sampling window is then 500 ps. The stored charge is digitized by an external high resolution ADC (12 bits) which operates at 40 MHz frequency.

This analog sampler is contained in a mezzanine board called CRAB (Capacitor Ring Analog Board). A PULSAR board (18 in total) hosts 4 CRAB boards to integrate up to 80 channels of acquisition and several more for trigger and monitor purposes. In the PULSAR board three FPGA are responsible of the data management.

## 6. TRIGGER

### 6.1 Standard trigger

There are three trigger levels in each MAGIC Telescope [18]. The first level (level L0T) consists in a discriminator. The second level (L1T) relates the fast coincidences in the firing of several next neighbour pixels. The third level (L2T), the most complex, identifies known patterns in the images of the camera. Only the inner part (not all the pixels) of the camera contributes to the L1T and L2T trigger. A fourth trigger level (L3T) was recently developed to identify the events detected simultaneously by both telescopes, but it will be omitted in this discussion since it is still under development.

#### I. Level 0 Trigger (L0T)

This trigger level is implemented in every pixel of the camera, at the receiver stage. The signal is splitted and introduced both in the data acquisition and in the trigger logic, where it is discriminated with a threshold set by control software. The pulse is then stretched to 6 ns PWHM.

For the control of this trigger level it is necessary the use of digital-analog converters (DACs), because the software produces digital levels. For every discriminator there is an 8 bit resolution DAC. The control software fixes the number of counts that determine the threshold. The DAC converts these counts to a DC signal which is compared with the pulse from the camera preamplifier.

The DAC makes 9 counts for every mV DC. The threshold is typically set in 36 DAC counts, so the L0T triggers for pulses bigger than 4 mV.

#### II. Level 1 Trigger (L1T)

For the trigger logic, the inner pixels of the camera are distributed in 19 overlapped hexagonal cells. Each cell includes 36 PMTs, as shown in Figure 2.8a.

This trigger level detects the fast coincidences (2–5 ns) of  $n$  next neighbour pixels (usually  $n=4$ ). These  $n$  pixels must be close packed, i.e. a pixel contributes to the trigger only if at least two next neighbours are fired. This way a first discrimination between muon and gamma shower can be done. The typical rate of this trigger level is  $\sim 2$  kHz.

The hardware for this logic is implemented in each of the 19 macrocells, and operates with LOT discriminator pulses.

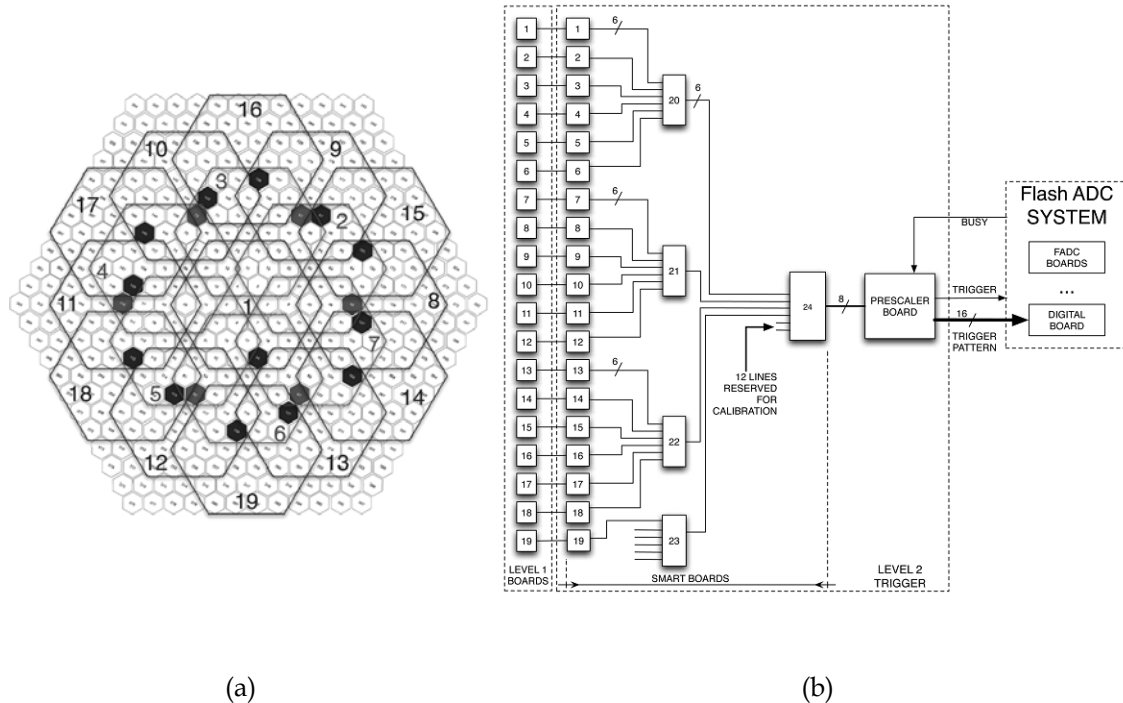


Figure 2.8 (a) Pixel distribution in macrocells for the trigger logic. (b) Tree configuration of the SMART modules of L2T [18].

### III. Level 2 Trigger (L2T)

In this level, images in the trigger region of the camera image are compared with several look-up-tables (LUT) to identify patterns. The hardware implementation consists in programmable SMART modules. Every module has 36 inputs and 6 outputs, and internal LUTs of 4096 bytes. The inputs are compared with the contents of the LUTs and the result is codified in 6 bits words at the output of the module.

There are 24 SMART modules in a tree configuration. The first stage has 19 modules, one for each macrocell of the camera. In the second stage 4 modules are used, and 1 in the third (see Figure 2.8b)

The maximum rate the FADC can stand without losing information is 1 kHz, so a prescaler must be used to reduce the trigger rate by means of a counter (0-65535). There is a second prescaler able to admit trigger rates up to 1 MHz,

communicated with the FADCs by an independent line. Typical rates of L2T are around 200 Hz.

## 6.2 Sum trigger

A new trigger design was installed in MAGIC I in 2007-2008. This new system, called Sum Trigger, lowers the energy threshold of the Telescope to 25 GeV [19].

Instead of analyzing patterns, the Sum Trigger divides the camera in sectors and adds the signal of all the PMTs of the sector. This way, a shower incidence would produce an increase in the signal over the noise.

The main problem of this method comes from the intrinsic noise of the PMTs. For values in excess of 6 photoelectrons, the rate of afterpulses is much higher than the rate of Čerenkov light or NSB. Because of this, most of the trigger events are due to accidentals.

This effect can be reduced if any PMT signal higher than certain value is clipped. This reduces the total signal for a sector and increases sensitivity. It was proved by simulations that the optimum value to do the clipping was 6.2 photoelectrons.

For the chosen integration window (2.6 ns), the pileup due to NSB is minimum and will not produce the clipping of the signal. The trigger region is divided into 24 overlapping cells of 18 pixels each, and defines a donut-like zone in the center of the camera optimized for low energy sensitivity (10-20 GeV). The SumTrigger threshold is set to 27 phe, corresponding to 7-9 standard deviations of the NSB noise.

The Sum Trigger has been used in the observation during 2008, resulting in the detection of pulsed gamma ray emission from Crab above 25 GeV and providing 9 times more effective collection area at that energy than the standard trigger.

## 7. ANALYSIS

The basic observation conditions of the Telescope included in the analysis procedures are [7]:

- **Observation mode:** in *on-off mode*, data is first taken pointing directly to the source (*on data*). Later, background data is taken pointing to an 'empty' region of the space with similar characteristics (*off data*). These off-data is used to suppress the background from the source.

In *wobble mode*, the Telescope points close to the source within a small angle ( $\Delta\beta$ ). There are two wobble positions ( $+\Delta\beta$  and  $-\Delta\beta$ ) and every 20 minutes the position is exchanged. A careful selection of  $\Delta\beta$  along the horizontal axis or the camera produces an anti-position for each wobble position. This provides good background estimation.

- **Pedestal:** special data runs are taken to estimate the pedestal of the camera every hour. During data taking, pedestals are taken with 5 Hz frequency. This provides information about stars present in the field of view and about the camera position.
- **Trigger conditions:** the trigger settings include factors as thresholds for the pixels in L0T, number of next neighbours in L1T, coincidence gate for fired pixels or the suppression of pixels triggered by light from stars on the field of view.

The analysis mainly depends on the pointing direction of the Telescope, the position of the source in the camera, the pedestal fluctuation and the configuration of the PMTs (thresholds, high voltages...). These dependences will determine the cuts in the data for source/background and gamma/hadron separation, or the effective collection area.

The most common separation technique in MAGIC is the 'Random Forest', in which decision trees are used. Using Monte Carlo simulations, every event is given a hadronness coefficient, which expresses the probability of being a hadron or a gamma shower. With cuts in this parameter it is possible to perform the background suppression.

In order to obtain the absolute flux from a source, several tasks must be done. A simplified list of them is:



1. *Tasks related with pixels:*

- Remove noise and pedestal: calculation of the mean, fluctuations and errors of the pedestal and electronic noise.
- Determine the conversion factor. This is obtained from the 'F factor', which relates the charge on the FADCs with the actual number of photons incident on the camera. By means of the calibration files, and the interleaved calibration (pulse trains from LEDs that illuminate the camera with 25Hz frequency), it is possible to determine the variation with temperature, humidity...
- Determine the relative arrival time of the photon bunch. All the arrival times are related to that of pixel 2, close to the camera center. This way, timing discrepancies due to detector geometry and electronic delays are considered.

2. *Tasks related with events:*

- Determine the position of the source and the orientation of the starfield in the camera.
- Obtain the absolute time from the GPS and Rubidium Clock.
- Check if the event produced a trigger.
- Clean the image (remove from analysis pixels not included in the shower image). This is done by an algorithm that takes into account the charge of the pixel and its neighbours, and the relative arrival times [20]
- Calculate Hillas parameters of the images.
- Discriminate the signal events from the background. The standard methods are Random Forest or Dynamical Cuts [21].
- Estimate the energy of the shower using Random Forest.

3. *Final calculations:*

- Determine the statistical significance of the signal events over background events. [22]
- Determine the unfolded source spectral energy distribution [23].
- Determine the integral flux
- Draw the lightcurve.

## 8. THE CENTRAL PIXEL

### 8.1 Motivation

The main purpose of the Central Pixel is to analyze the slow variation of the optical flux of different types of sources [24]. The simultaneous observation in the optical and gamma-ray regimes can provide real-time ephemeris for periodicity search in gamma-rays. This task is performed by a dedicated PMT, placed in the very center of the camera. When on-axis observation, the light of the source is reflected into this position, and the slow variations of the intensity are transmitted to a dedicated DAQ system and to the standard MAGIC DAQ.

The MAGIC Telescope has been designed specifically to maximize the sensitivity to cosmic gamma-rays between 50 GeV and several TeV. The mirror and the camera have been optimized for these observations. That means that the position of the camera has been shifted  $\sim 3$  cm from the focus, to observe the maxima of the atmospheric showers, at 10 km above the telescope. Because of this defocusing respect to infinity and the misaligning of the mirrors (the so-called Point Spread Function or PSF,  $\sim 0.05^\circ$  when focusing the mirror to infinity), not all the light coming from a point source is collected by the Central Pixel. The light of the night sky background, however, is isotropically distributed, so is not affected by the defocusing and contributes to decrease the signal to noise ratio of the source and the necessary time of observation.

The 934 mirrors of the parabolic reflector are adapted in radius according to their position, and are equipped with mechanical actuators to improve the focusing on the shower maxima. Due to cost reasons, their reflectivity is not as high as in optical telescopes. All these factors result in a decrease of the signal to noise ratio, and thus in the importance of a low-noise electro-optical system.

Most of the objects to be observed with the Central Pixel emit at frequencies between 1 Hz (Blazars) and 1 kHz (pulsars and Gamma Ray Bursts). The characteristic emission frequency of the Crab Pulsar is  $\sim 30$  Hz. These values fix the 3 dB bandwidth of the readout system of the Central Pixel (1 Hz - 1 kHz). The slow variation of the PMT anode current must be integrated, and the resulting value transmitted through an electro-optical transceiver to the data acquisition system.

Figure 2.9 shows the block diagram of the central pixel. The PMT is followed by a DC coupled amplifier which feeds two different channels. The first one is used to monitor the DC levels. The second one transmits the pulsed signals to the counting house via an optical transceiver.

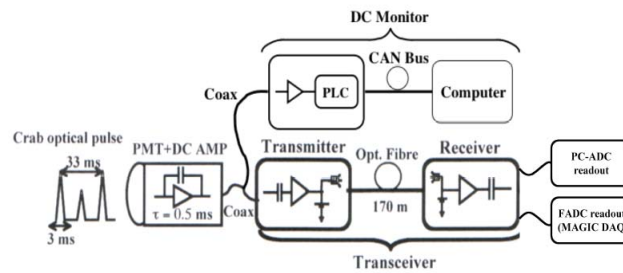


Figure 2.9 Block diagram of the Central Pixel System.

## 8.2 The Photodetector

The photodetector used in the Central Pixel is a standard MAGIC inner pixel (ET 9116) described in Section 4.1. Besides the logical camera integration simplicities, this device presents a feature that makes it ideal for the optical observation of the Crab Pulsar: having only 6 dynodes and thus a gain of only 20.000 for a 1100 V polarization, it is very robust against high levels of night sky background. As will be shown in Section 8.6, it was possible to measure the Crab light curve even in moon-observation conditions.

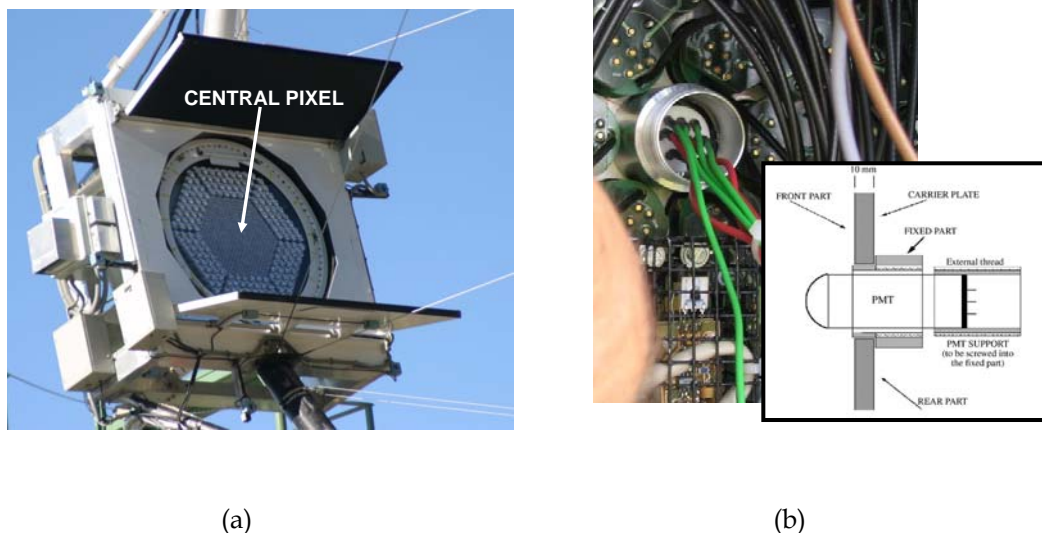


Figure 2.10 (a) Front view of the camera. (b) Backplane of the camera and structural description of the PMT assembly.

The PMT is inserted into the camera plate or motherboard, as shown in Figure 2.10. This board hosts all the Telescope pixels; a hole was left empty in order to integrate the central one. A special screwed tube fixes the PMT into the hole, allowing the access for replacement from the back part of the camera (the rest of the pixels must be accessed from the front part, which is a far more complex operation). A removable connector for the PMT base contains all the power and signal cables.

### 8.3 The Electro-Optical System

The structure of the data transmission chain of the Central Pixel is basically the same used for the standard camera pixel. This implies a huge simplification in the design, installation and compatibility with the existing hardware and data acquisition of the Telescope. The communication between the camera and the Counting House maintains the original design with a 170 m long optical fibers (step index multimode, 50/125  $\mu\text{m}$  core/cladding).

Some changes with respect to the standard pixels have been done, in order to fulfil the requirements for the optical observation of the Crab lightcurve:

- The bandwidth of the system must be reduced. The original 230 MHz go far beyond the needs for the observation of signals in the order of Hz and introduces a lot of unnecessary noise.
- The gain must be stable within a strict range.
- Low noise amplifiers must be used. Increasing the S/N ratio of the signal the observation time can be noticeably reduced.
- DC signal must be filtered. This way the night sky background is removed from the data and only the signal from the Crab is digitized.

Figure 2.11 shows the final schematic of the Central Pixel Transceiver. The signal of the ET9116A photomultiplier is driven into a standard MAGIC preamplifier. The integration time constant of the pre-amp has been adapted to low frequency operation (0.15 ms, 1.06 kHz) by replacing the feedback capacitor. This value sets the transceiver high frequency cutoff.

As no high frequency transmission is needed, it is desirable to replace the standard pixel VCSEL by a LED as electro-optical converter. This way the noise is reduced, and the stability of the system with variations of the temperature is

increased. A large dynamic range LED (Honeywell HFE 4050-014) was chosen to drive the optical fiber. Figure 2.11c shows the schematic of the receiver, placed in the Counting House. A PIN photodiode with preamplifier (Honeywell HFD 3038-002) produces the opto-electrical conversion.

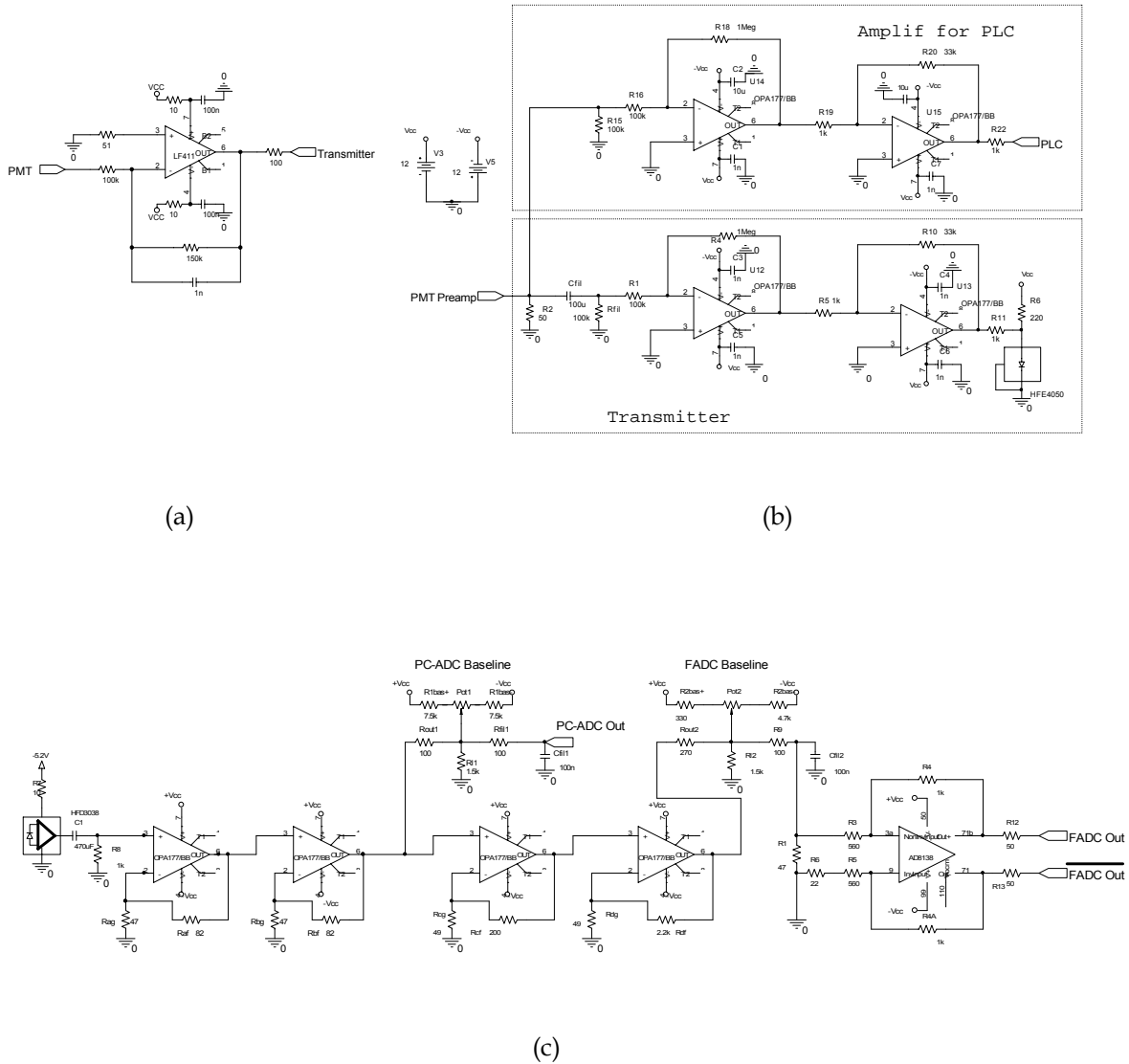


Figure 2.11 Schematic of the Central Pixel Transceiver. (a) Modified PMT preamplifier. (b) Transmitter, inside the camera. (c). Receiver, in the Counting House.

Figure 2.12a shows the measured I-V curve of the diode, and the equivalent model used for simulation. The operation point of the diode was set to 40 mA in order to permanently work in the linear region and maximize the dynamic range. The LED is driven by a two-stage amplifier. An ultra-low drift, ultra-low offset op-amp (Burr-Brown OPA277) is used in order to minimize the effects of the camera temperature on the system gain. The camera temperature in normal operation conditions is stable within 35-40 °C; the gain fluctuations for this range are lower than 2%. The input voltage noise density of the amplifier is 8 nV/ $\sqrt{\text{Hz}}$ .

A high pass filter at the input sets the 3 dB cut-off at 0.8 Hz, enough to observe the Crab light variations and reject the DC of the NSB.

An analog input of the commercial Programmable Logic Controller (PLC) (type Modicon TSX Micro) is used to transmit the DC level of the PMT to the Central Control. This way the NSB and the correct operation of the system can be monitored. If the DC current at the PMT anode is too high the Central Pixel supply can be disconnected and this way avoid system damages.

Figure 2.12b shows the dynamic range of the photodiode as a function of the voltage applied to the transmitter LED.

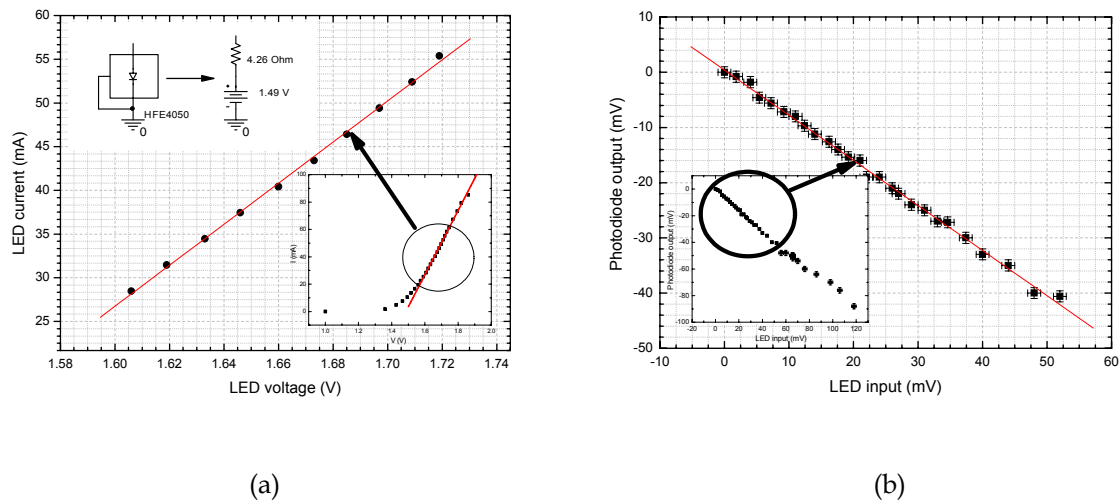


Figure 2.12 (a) I-V characteristics of the Honeywell HFE-4050 LED. (b) Dynamic range of the Honeywell HFD-3038-002 PIN photodiode

As will be explained in next section, two types of data acquisition are used. The dynamic range and the baseline of the input signal and different for each of them, so two different stages of amplification and offset control are used. The first one feeds the PC-ADC data acquisition and the second one the modified MAGIC FADC. The FADC input is differential, so an AD8138 differential amplifier is used to convert the signal into a balanced one.

The same op-amps of the transmitter are used in the receivers (Burr-Brown OPA277), so the ultra-low drift ensures gain fluctuations lower than 3% of the nominal value for a temperature variation between 25 and 30 °C.

Figure 2.13 shows the bandwidth of the transceiver (excluding the modified MAGIC preamplifier). The low frequency cut-off is determined by the input low pass filter of the receiver in 0.8 Hz, and the high frequency one by the output high pass filter.

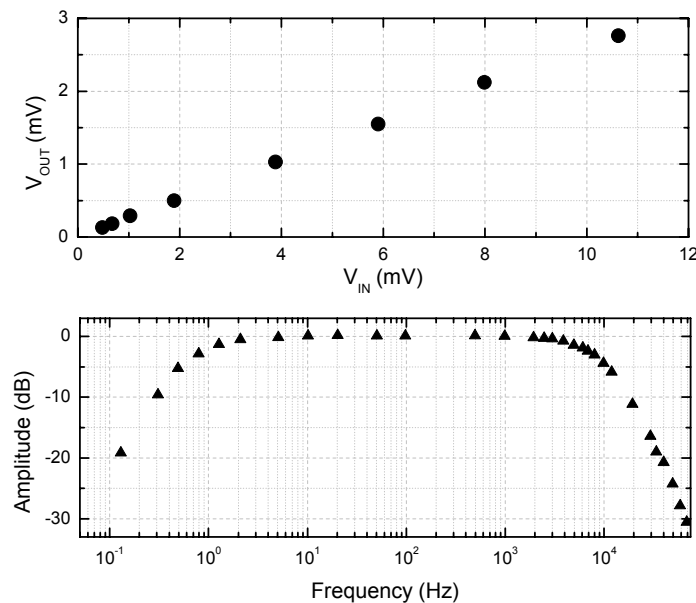
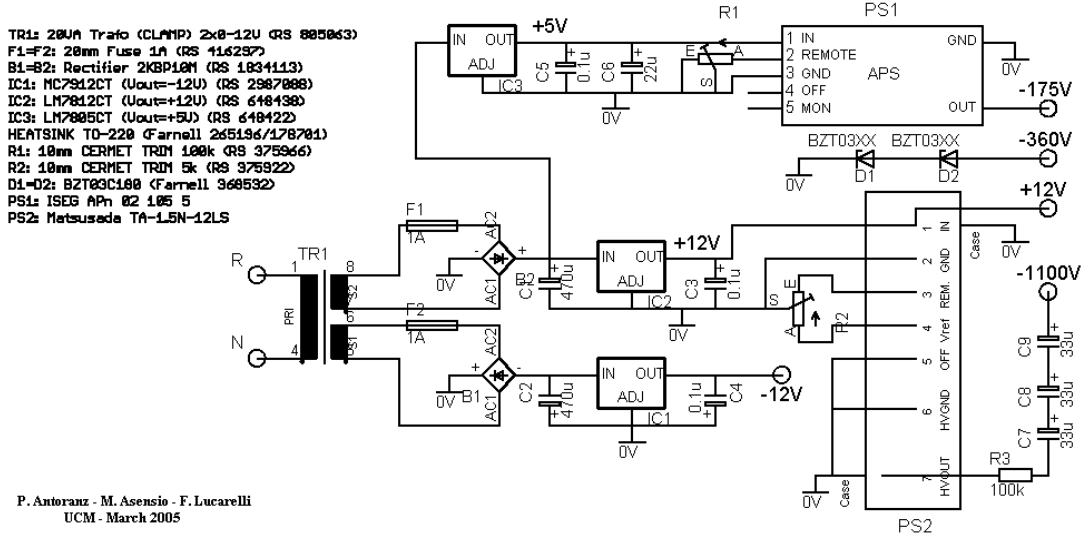


Figure 2.13 Dynamic range and bandwidth of the Central Pixel Transceiver.

## 8.4 The Power Supply

The Central Pixel Power Supply is designed to operate independently from the rest of the Camera electronics. A special board, which includes high voltage for the PMT (-1100 V, -360 V, -175 V) and low voltage for the transceiver (12 V, -12 V, -5.2 V) was developed. Figure 2.14 shows the schematic and a picture of the board and the cabinet in which it was installed. The whole Central Pixel Power Supply is fixed in a water-tight cabinet attached to the Telescope Camera. The total weigh is lower than 2 kg and does not affect the telescope performance or weight balance.

Central pixel and optical transmitter power supplies



(a)



(b)



(c)

Figure 2.14 Central Pixel Power Supply. (a) Schematic. (b) Board. (c) Location in the camera.

Figure 2.15 shows the PMT base schematics. A 220 V line available at the telescope camera feeds the board. A transformer, rectifiers, filters and regulators provide the DC level to the transceiver electronics. A high voltage power supply (Matsusada TA-1.5N) provides the high voltage to the PMT cathode, and an Iseg HV module (APn 02 105 5) sets the active load for the last dynodes.



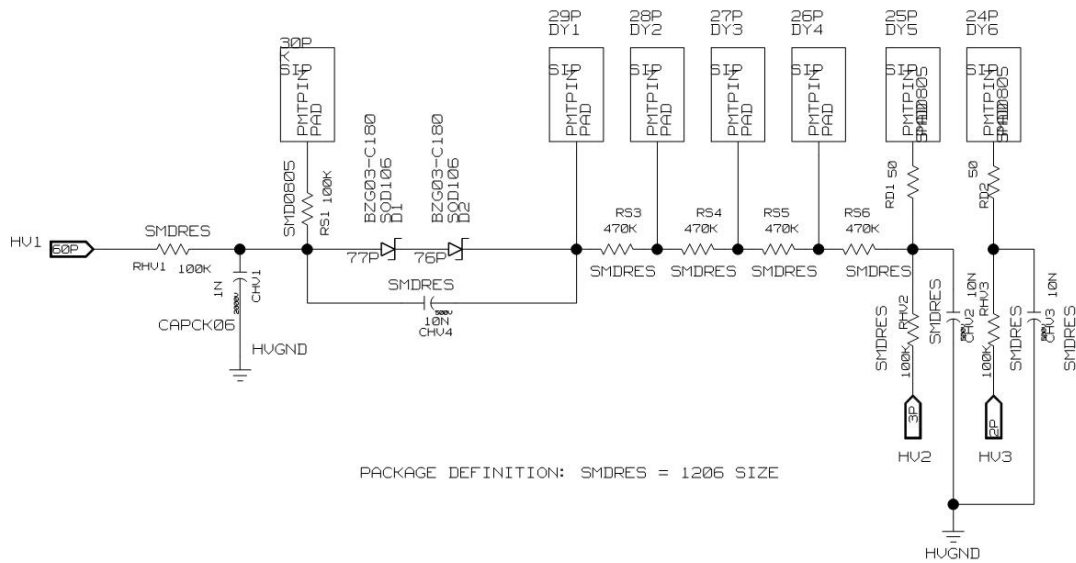


Figure 2.15 PMT base schematics.

## 8.5 The DAQ System and Operation Modes

### I. Dedicated PC

The first stage of the receiver is directly fed into a dedicated PC running under Linux by means of a wide SCSI cable. A software controlled ADC card (National Instruments PCI-6034E) samples continuously the data with 16-bits resolution. The acquisition rate can be set within a range between 1 and 20 kHz. The actual operating rate, described in Figure 2.16, makes use of the MAGIC Timing System: a Rubidium Clock, synchronized with a GPS, generates a 5 MHz sinusoidal signal. This signal is fed into the 'sub-second module' (used to improve the time resolution of the data up to microseconds), where it is converted to TTL logic and driven into an internal frequency divider. The resulting 20 kHz square signal is used by the PC-ADC card as sampling frequency.

It is necessary to correlate data from different observations. For this purpose, an absolute time is set by the Network Time Protocol (NTP) of the PC with millisecond precision. To improve this precision, a pulse from the Rubidium Clock (1 Hz, 20  $\mu$ s wide) is used. As the ADC sampling rate is too low to resolve these pulses, a JK flip-flop inside the receiver module is used to generate a 0.5 Hz clock signal that is stored together with the data and the NTP absolute time.

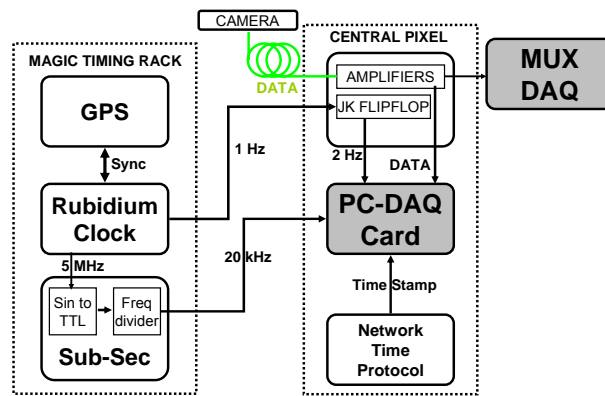


Figure 2.16 Block diagram of the Central Pixel dedicated PC acquisition.

## II. MAGIC FADC

Another readout system is also implemented. The differential output of the second stage of the receiver is driven into a standard MAGIC FADC module. This module, originally designed to record extremely fast Čerenkov pulses, has been modified by the Max Plank Institute group to work with signals below 10 kHz. The FADC starts acquisition, as the rest of the FADCs in the telescope, when a trigger event is produced. The rate of events is 200 Hz on average in normal observation, and up to 1 kHz with the recently installed Sum Trigger.

The sensitivity of this method is lower than the PC-ADC one. While the dedicated PC samples with 20 kHz rate, the FADC has a variable sampling frequency that depends on the observation rate. But when data is scaled to observation duty cycle, the sensitivity of both systems is comparable.

The main advantage of the FADC DAQ is the total integration in the standard MAGIC readout. This way the Central Pixel data is available for analyzers with the same time-stamp than the Čerenkov events, and can lead to detect possible coincidences in gamma-optical emission.

### 8.6 Results: Crab Observations

As the Crab optical pulses are embedded in noise, it is not possible a direct inspection of the signal. The absolute time is transformed into an inertial reference frame, for which the Solar Barycentre System (SBS) is used. The signal is folded for frequencies around the expected Crab rotational period (obtained from the Jodrell Bank Observatory radio ephemeris), which results into a set of phaseograms. These phaseograms are tested against a uniform distribution with

several statistic tests to determine the exact Crab period. Then the lightcurve is produced for that frequency.

At the end of 2005 all the system, including modified FADC and absolute time stamp was already installed. From December 2005 to February 2006, 2 months data were taken and analyzed. Figure 2.17c shows the lightcurve obtained from 20 h observation with the FADC, and Figure 2.17d shows the lightcurve for 40 min observation with dedicated PC (phase is chosen to be 0 at the maximum intensity of the lightcurve measured for the radio band). The significance of 40 min of data recorded by PC is better than 20 h of FADC data, but when scaled to de acquisition duty cycle the sensitivity is comparable.

As obtained by calculations [24], 20 seconds of observation should be enough to obtain a  $5\sigma$  peak in the lightcurve. This can be seen in Figure 2.17, where the lightcurve has been obtained for 24 seconds normal observation (a) and 30 seconds of moderate cloud coverage and moonlight illumination (b).

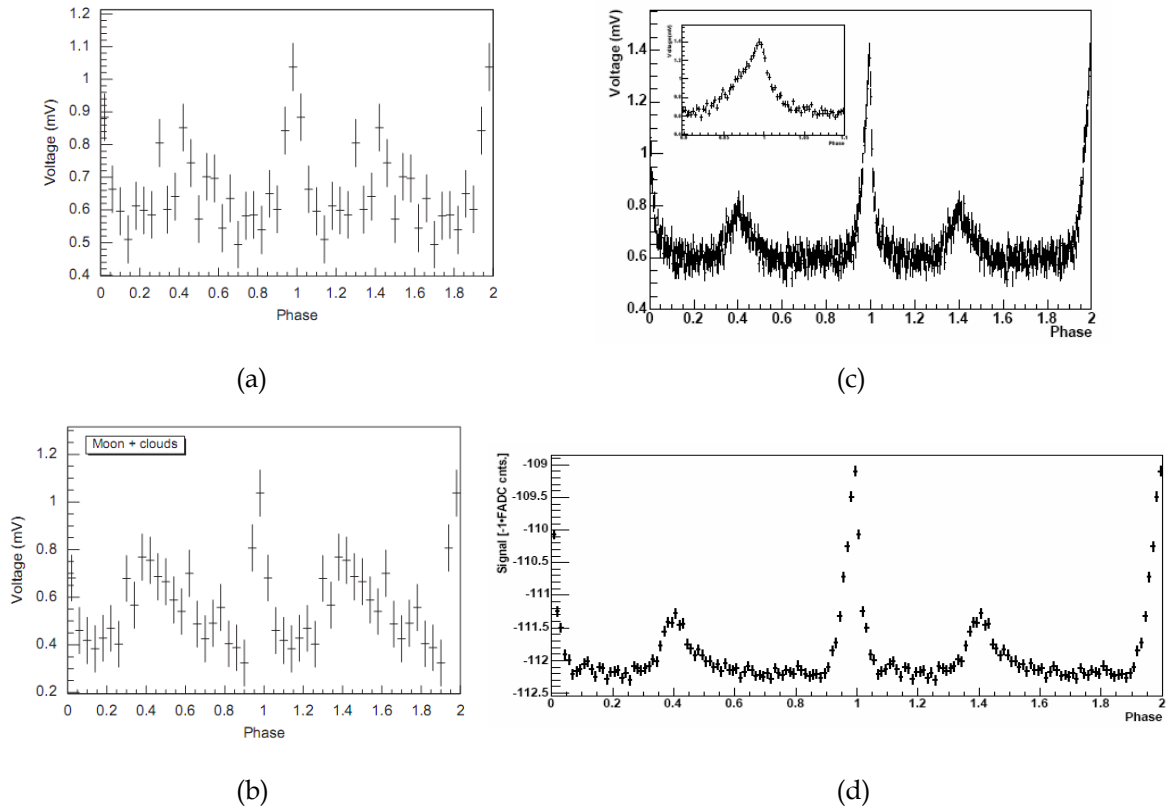


Figure 2.17 Light curve of the Crab: (a) Dedicated PC, 20 s. observation. (b) Dedicated PC, 30 s. observation with moderate cloud coverage and moonlight. (c) Dedicated PC, 40 min. observation. (d) FADC, 20 h. observation.

Although Crab optical observation has already been reported [25], MAGIC approach presents several advantages. The Central Pixel can be used to measure

fast optical variations with excellent time precision, not only for the Crab Pulsar but for flaring Active Galaxy Nuclei (AGNs) (Mrk 421, 501...) and X-ray binary systems (AE Aquarii). Moreover, inverting the procedure, the Crab rotational period can be used to periodically test the precision of MAGIC Telescope timing system.

One fundamental question about pulsars concerns the mechanism of their pulsed electromagnetic emission. The MAGIC collaboration observed the Crab pulsar between October 2007 and February 2008, obtaining 22.3 hours of good-quality data, and detected pulsed emission above 25 GeV. By optimizing the electronic trigger, the threshold of the telescope was reduced to 25 GeV. In this configuration, pulsed gamma-rays from the Crab pulsar were detected and compared with optical measurements made with the central pixel, as well as with independent measurements made by Energetic Gamma Ray Experiment Telescope (EGRET), an instrument installed in a NASA satellite with a measuring range between 20 MeV and 30 GeV. Figure 2.18 shows the results [26].

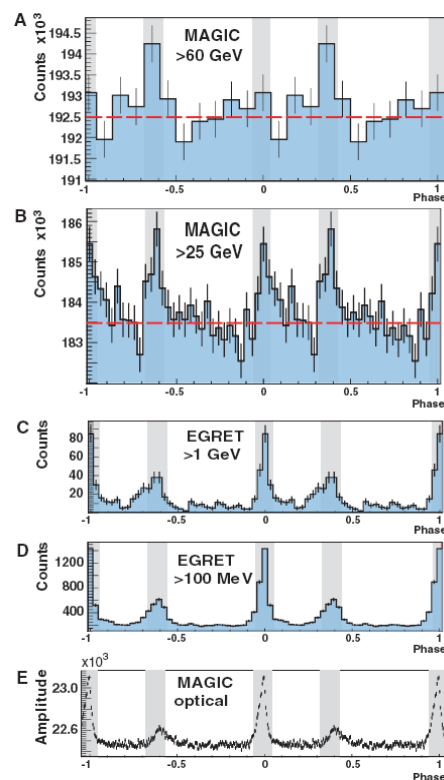


Figure 2.18 Crab measurements at different wavelengths. The measurements in the optical energy band were made with the central pixel.

## 9. CONTROL AND OPERATION OF THE TELESCOPE

### 9.1 Organization of the shifts

The data taking at La Palma is organized on shifts. Each shift lasts for 3.5 weeks centered around the new moon nights of each month. The shift crew consists of two operators, a shift leader and a deputy shift leader, who must stay on site for the whole shift. The shift leader is an experienced person with the responsibility of training the operators and the deputy shift leader on the telescope subsystems. More details on the exact duties of these positions are explained in the Safety Rules document of the collaboration [27].

Interaction with the authors of the operation manuals or the persons appointed as responsables of the corresponding subsystem is addressed through a dedicated `magic_online` distribution list. The operators find what astronomical objects they must observe every night in the source schedule. These objects are defined well in advance to the shift by the 'Time Allocation Committee (TAC)', also called Physics Programme Committee.

### 9.2 Telescope operation

MAGIC telescope subsystems are detailed in two manuals: the Datataking Operations Manual (DOM) [28] and the whole Technical Operations Manual (TOM) [29]. The Central Control (CC) software is called Superarehucas and it is written in Labview. Figure 2.19 shows the main panel of this software in its last version. Superarehucas enables the operation of all the control subsystems in the MAGIC telescopes. All the functionalities in these subsystems (DAQ, Drive, Camera, Calibration, Trigger...) needed to take data are coordinated by this software. Operators do not usually work with most of the program interfaces running in the subsystem computers, which are reserved for debugging purposes, special functions or emergency operation.

The recommended time to start working on the night shift is two hours before astronomical sunset, which takes place one hour after the sun or the moon goes down over the horizon; the high voltage for the PMTs is switched on in advance enough (two hours) for the voltage levels to be stabilized when the data taking starts. Low voltage electronics is switched on one hour before data taking. Observation is only possible if the following conditions are fulfilled:

- Wind speed < 40 km/h
- Humidity < 90%
- Average PMT current < 7  $\mu\text{A}$  (mainly moon observations)
- Individual PMT current < 20  $\mu\text{A}$
- Zenith angle > 1.5°

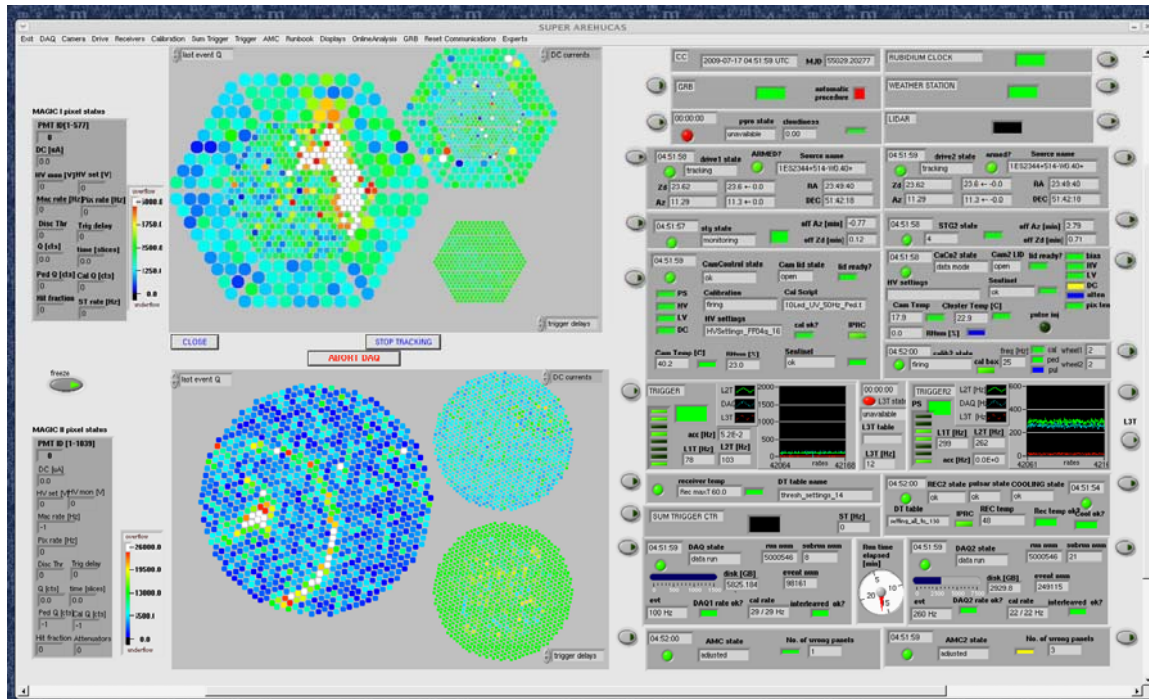


Figure 2.19 Last version of SuperArehucas software.

The first two limits are monitored by the ‘Sentinel’ of the camera control. The camera lids close by themselves if the limits are surpassed. The telescope operation for data taking has a startup sequence in which the protocols establish a verification of the weather, a verification of the subsystems and a warming up period of more than one hour.

The default way of datataking is the wobble mode, already defined in Section 7. In this operating mode the telescope is pointed to a fixed sky position, which is usually 0.4° away from the source position. There are commonly two wobble positions for each source with fixed Right Ascension (RA) and Declination (Dec) chosen in such a way that the source position is between them. During the observation the wobble positions should be exchanged frequently enough so that very similar observation conditions (weather as well as zenith angle) for both positions can be achieved. In the second operation mode (ON-OFF), the measurements are made by periodically pointing and mispointing the telescope from the source under observation.

### 9.3 Participation on the shifts

During the period of this thesis the author participated in a technical shift in September of 2004 by working on the installation of the MAGIC I central pixel. In addition, he made three shifts as operator: P33 (September 2005), P46 (September 2006) and P59 (October 2007). Table 2.2 shows a summary of the sources measured during these periods. Even though the data is mostly taken during dark night, another possibility exists: if the moon is in the sky but it is not very bright, the so called 'Moon Data' is taken. The source must be then as far in the sky from the moon as possible. This data is of worse quality (the background light is obviously higher).

As it can be seen, each shift provides information on typically between 10 to 15 sources. Among them it is worth to mention the following ones:

- Crab [26], [30]. The Crab Nebula (catalogue designations M1, NGC 1952, Taurus A) is a supernova remnant and pulsar wind nebula in the constellation of Taurus. The nebula corresponds to a bright supernova recorded by Chinese and Arab astronomers in 1054. At the center of the nebula lies the Crab Pulsar, a rotating neutron star, which emits pulses of radiation from gamma rays to radio waves with a spin rate of 30.2 Hz. At X-ray and gamma-ray energies above 30 KeV, the Crab is generally the strongest persistent source in the sky, and therefore it is generally used as a reference for different telescope calibration procedures.
- 1ES 1959+650 [31], [32]. This object is a blazar. Blazars are a class of AGN with collimated plasma outflows (jets) directed along the line of sight. The jets give rise to a continuum emission extending from the radio to X-rays, sometimes even into the MeV and GeV/TeV energy range. The 1ES 1959+650 is one of the blazars detected so far in the GeV/TeV energy range with ground based Čerenkov telescopes.
- 1ES 2344+514 [33]. This source is another blazar. It was observed for 32 hr in total, distributed over 27 days between 2005 August and the first days of 2006 January.
- BL Lac [34], [35]. BL Lacertae objects (BL Lac for short) exhibit no emission lines but have a strong continuum stretching from RF through X-ray frequencies. They can exhibit strong variability in the emissions. The name remains from an original mis-identification of the prototype of such galaxies as a variable star in our own galaxy that was named BL Lacertae.
- Cassiopeia A [36]. This object is a prominent shell type supernova remnant and a bright source of synchrotron radiation observed at radio

frequencies and in the X-ray band. The remnant results from the youngest known Galactic supernova, whose explosion took place around 1680. It was observed with the MAGIC telescope between July 2006 and January 2007 for a total time of 47 hours.

- Cygnus-X1 [37]. Cygnus X-1 was discovered as an X-ray source 30 years ago. It is a binary system with a black hole, and gamma ray emission was detected by MAGIC for a total observation time of 40 hours along 26 nights, from June to November of 2006.
- LSI +61 303 [38], [39]. LSI +61 303 object is identified as a Microquasar. Microquasars are X-ray binary systems with relativistic radio-emitting jets. Unlike their extragalactic relatives, the quasars, many of which have been detected as TeV gamma-ray emitters, only one TeV microquasar had been discovered so far. This binary system is located at a distance of  $\sim 2$  kpc and is composed of a compact object of unknown nature (neutron star or black hole) orbiting a Be star in a highly eccentric orbit. MAGIC has reported the discovery of very high energy (VHE,  $>100$  GeV) gamma-ray emission from it. This high energy emission was found to be variable, and as such constitutes the first reported detection of variability at VHE gamma-rays in a microquasar. A first campaign was made between October 2005 and March 2006, with 54 hours of observation, which covered a total of 6 orbits. A second campaign of 112 hours was made between September and December of 2006.
- MKN 501 [40], [41]. MKN 501 is an AGN. This source is particularly relevant because it has been used to report a possible evidence of the Theory of Quantum Gravity, which demands a revision of the Relativity Theory. Models of Quantum Gravity naturally contain quantum fluctuations of the gravitational vacuum, and lead to predictions of an energy-dependent velocity for electromagnetic waves. In other words, gammas of different energy produced simultaneously in an extragalactic object, arrive on Earth at different times due to their propagation through the gravitational vacuum. Gamma telescopes like MAGIC are suitable instruments to measure these effects. They provide sensitivity to large expected time delays between gammas in a wide range of energies. Also, any time delay effect must be studied over a wide range of redshifts, in order to disentangle any Quantum Gravity effect from source-dependent time delay emission effects. For this reason, a large number of sources at different redshifts and different characteristics must be detected and measured with precision. A low-energy threshold and high-sensitivity detector has clear advantages. MKN501 was measured during several shifts for a total observation time of 21 hours.



- TeV J2032+42 [42]. This is an unidentified source. It was first detected by MAGIC during a campaign of 80 hours of observation between 2005 and 2006.
- GRBs [43], [44]. GRB are sudden, intense flashes of gamma-rays. They are detected at the rate of about once a day; and while they are on, they outshine every other gamma-ray source in the sky. GRBs seen in the gamma ray domain last between a fractions of a second and minutes; the X-ray emission typically runs on a scale of days, and the optical one even on a scale of weeks. Multiwavelength observations of GRBs have been made made possible by fast distribution of the information coming mainly from satellites, in real time.

Table 2.2 Sources observed during periods P33, P46 and P59.

P33	Observation Time [min]		P46	Observation Time [min]		P59	Observation Time [min]	
	Source	No Moon		Moon	Source		No Moon	Moon
1ES0120+34	594	6	1ES 0229+200	274	0	Mrk 501	51	7
1ES2344+51	318	414		261			73	20
AE-Aqr	1006	11	1ES 1959+650	33	50	1ES 1959+650	76	115
BL Lac	152			87	36		66	122
Crab	344		1ES 2344+514	20	18	Cyg X1	351	
GRBs	366	18		10	10		357	
HESS1834	378		3EG J2021+3716	79	110	BL Lac	372	
PSRB1957+20	315			162			367	
PSRJ0205+64	559	47	BL Lac	221	1	Tycho	368	457
W44	253			226			365	456
			Cas-A	19	372	M 42	61	126
				6	403		22	142
			Crab	169		Crab	373	13
				173			360	
				749	25	ES 0158+003	73	5
			Cyg-X1	602			681	
				582			719	
			GRB0609-17	18		RXS J044127.8	211	1
							228	
			GRB0609-26		23	Crab-SUM	364	
			LSI +61	975	254	OffCrab14-SUM	102	
				954	266			
			Mkn501	47	32			
				52	37			
			PSR J0218	131				
			PSR B1951+32	566	2			
			TeV J2032+42	101	198			
				77	199			

## 10. REFERENCES

- 
- [1] Barrio, J.A., et al. *The MAGIC Telescope Design report*. MPI Institute Report MPI-PhE/98-5, March 1998.
  - [2] E. Lorenz. *Status of the 17 m Ø MAGIC Telescope*. *New Astronomy Reviews* 48 (2004) 339–344.
  - [3] T. Bretz, D. Dorner, R. M. Wagner, P. Sawallisch. *The drive system of the Major Atmospheric Gamma-ray Imaging Cherenkov Telescope*. arXiv:0810.4593v1 [astro-ph]
  - [4] Albert Schliesser, Razmick Mirzoyan. *Wide-field prime-focus imaging atmospheric Cherenkov telescopes: A systematic study*. *Astroparticle Physics* 24 (2005) 382–390
  - [5] Markus Garczarczyk. *First Observations of the GRB Prompt and Early Afterglow Emission Phase at ~ 100 GeV Energy Regime with the 17 m Diameter MAGIC Imaging Atmospheric Cherenkov Telescope*. PhD Thesis, Universität Rostock, 2006.
  - [6] C. Schultz. *Novel All-Aluminium Mirrors of the MAGIC Telescope Project and Low Light Level Silicon Photo-Multiplier Sensors for Future Telescopes*. Diploma Thesis, Fachhochschule München, 2008.
  - [7] Igor Oya. *Análisis de fuentes con el Telescopio MAGIC*. Diploma Thesis, Universidad Complutense de Madrid, 2006.
  - [8] D. Paneque, H. J. Gebauer, E. Lorenz, M. Martinez, K. Mase, R. Mirzoyan, A. Ostankov and T. Schweizer. *A method to enhance the sensitivity of photomultipliers for air Cherenkov telescopes*. *Nuclear Instruments and Methods in Physics Research A*. Volume 504, Issues 1-3, 21 May 2003, Pages 109-115.
  - [9] Philips Photonics. *Photomultiplier Tubes: principles & applications*. 1994.
  - [10] C.C. Hsu, A. Dettlaff, D. Fink, F. Goebel, W. Haberer, J. Hose, R. Maier, R. Mirzoyan, W. Pimpl, O. Reimann, A. Rudert, P. Sawallisch, J. Schlammer, S. Schmidl, A. Stipp, M. Teshima for the MAGIC Collaboration. *The Camera of the MAGIC-II Telescope*. arXiv:0709.2474v1 [astro-ph]
  - [11] Ching-Cheng Hsu. *PMT Characterization for MAGIC II Telescope*. *Proceedings of the 10th ICATPP Conference on Astroparticle, Particle, Space Physics, Detectors and Medical Applications 2007*.
  - [12] E. Lorenz, R. Maier, T.S. Tran, P. Weissbach. *A fast, large dynamic range analog signal transfer system based on optical fibers*. *Nuclear Instruments and Methods in Physics Research A* 461 (2001) 517–520
  - [13] D. Paneque. *The Magic Telescope: development of new technologies and first observations*. PhD thesis, Technical University Munich, 2004
  - [14] J. Zapatero. *Characterization of laser diodes for the new Optical Links of the MAGIC II Telescope*. Diploma Thesis, Universitat Autònoma de Barcelona, 2006
  - [15] Florian Goebel, Jose Antonio Coarasa, Ralf Stiehler and Sergei Volkov for the MAGIC collaboration. *The Data Acquisition of the MAGIC Telescope*. 28th International Cosmic Ray Conference, 2003

- [16] H. Bartko, F. Goebel, R. Mirzoyan, W. Pimpl, M. Teshima. *Tests of a prototype multiplexed fiber-optic ultra-fast FADC data acquisition system for the MAGIC telescope*. Nuclear Instruments and Methods in Physics Research A 548 (2005) 464–486
- [17] M. Bitossi, R. Cecchi, R. Paoletti, R. Pegna, N. Turini, M. Barcelò, J. M. Illa. *The Data Acquisition System of the MAGIC-II Telescope*. IEEE International Workshop on Intelligent Data Acquisition and Advanced Computing Systems: Technology and Applications Dortmund, (Germany) 2007.
- [18] R. Paoletti, R. Cecchi, D. Corti, F. Dazzi, M. Mariotti, R. Pegna, and N. Turini. *The Trigger System of the MAGIC Telescope*. IEEE TRANSACTIONS ON NUCLEAR SCIENCE, VOL. 54, NO. 2, APRIL 2007
- [19] M. Rissi, N. Otte, T. Schweizer, M. Shayduk for the MAGIC Collaboration. *A new trigger provides lower energy threshold for the MAGIC Cherenkov Telescope*. Proceedings of the IEEE NSS-MIC 2008, Dresden
- [20] E. Aliu et al. (MAGIC Collaboration). *Improving the performance of the single-dish Cherenkov telescope MAGIC through the use of signal timing*. Astropart. Phys. 30 (2009) 293
- [21] J. Albert et al. *Implementation of the Random Forest Method for the Imaging Atmospheric Cherenkov Telescope MAGIC*. Nucl. Instr. Meth. A 588, 424 (2008).
- [22] Ti-pei Li, Yu-quian Ma, *Analysis methods for results in gamma-ray Astronomy*. Astrophysical Journal, Part 1, vol. 272, Sept. 1, 1983, p. 317-324
- [23] T. Bretz and the MAGIC collaboration, *Standard Analysis for the MAGIC Telescope*, 29th International Cosmic Ray Conference, Pune (2005) 00, 101–106
- [24] F. Lucarelli, J.A. Barrio, P. Antoranz, M. Asensio, M. Camara, J.L. Contreras, M.V. Fonseca, M. Lopez, J.M. Miranda, I. Oya, R. de los Reyes, R. Firpo, N. Sidro, F. Goebel, E. Lorenz, N. Otte, *The central pixel of the MAGIC telescope for optical observations*. Nuclear Instruments and Methods in Physics Research A 589 (2008) 415–424
- [25] J.W. Percival et al, *The Crab pulsar in the visible and ultraviolet with 20 microsecond effective time resolution*. Astrophysics J. 407 (1993) 207
- [26] E. Aliu et al. (MAGIC Collaboration). *Observation of Pulsed  $\gamma$ -Rays Above 25 GeV From the Crab Pulsar with MAGIC*, SCIENCE, vol. 322, pp. 1221-1224 (2008)
- [27] J. Cortina, *Safety and Health Rules at the MAGIC Site*, MAGIC internal publication, May 2009
- [28] J. Cortina, R. Zanin, *MAGIC Datataking Operations Manual (DOM)*, MAGIC-TDAS 08-05
- [29] MAGIC Collaboration, *Technical Operations Manual (TOM)*, 2009
- [30] E. Aliu et al. (MAGIC Collaboration). *VHE gamma-Ray Observation of the Crab Nebula and its Pulsar with the MAGIC Telescope*, Astrophysical Journal, vol 674 (2), pp. 1037-1055, (2008)
- [31] J. Albert et al. (MAGIC Collaboration). *Observation of VHE gamma-ray emission from the Active Galactic Nucleus 1ES1959+650 using the MAGIC telescope*, Astrophysical Journal, vol 639, pp. 761– 765 (2006)
- [32] J. Albert et al. (MAGIC Collaboration). *Simultaneous multiwavelength observations of the blazar 1ES 1959+650 at a low TeV flux*, Astrophysical Journal, in press.
- [33] J. Albert et al. (MAGIC Collaboration). *Observation of very high energy gamma-rays from the AGN 1ES 2344+514 in low emission state with the magic telescope*, Astrophysical Journal, vol 662, pp. 892–899 (2007).

- [34] J. Albert et al. (MAGIC Collaboration). *Systematic search for VHE gamma-ray emission from X-ray-bright high-frequency BL Lac objects*, *Astrophysical Journal*, 681(2), pp. 944-953 (2008).
- [35] J. Albert et al. (MAGIC Collaboration). *Discovery of very high energy gamma-ray emission from the low-frequency-peaked BL Lac object BL Lacertae*, *Astrophysical Journal*, vol 666, pp. L17-L20 (2007).
- [36] J. Albert et al. (MAGIC Collaboration). *Observation of VHE  $\gamma$ -rays from Cassiopeia A with the MAGIC telescope*, *Astronomy and Astrophysics*, vol 474, pp. 937-940 (2007).
- [37] J. Albert et al. (MAGIC Collaboration). *Very High Energy Gamma-Ray Radiation From The Stellar-Mass Black Hole Cygnus X-1*, *Astrophysical Journal*, vol 665, pp. L51-L54 (2007).
- [38] J. Albert et al. (MAGIC Collaboration). *Variable Very High-Energy gamma ray emission from the microquasar LSI +61 313*, *SCIENCE*, vol 312, pp. 1771-1773 (2006).
- [39] J. Albert et al. (MAGIC Collaboration). *Multiwavelength (Radio, X-ray, and gamma-ray) observations of the gamma-ray binary LS I +61 303*, *Astrophysical Journal*, 684(2), pp. 1351-1358 (2008).
- [40] J. Albert et al. (MAGIC Collaboration). John Ellis, N.E. Mavromatos, D.V. Nanopoulos, A.S. Sakharov, E.K.G. Sarkisyan, *Probing quantum gravity using photons from a flare of the active galactic nucleus Markarian 501 observed by the MAGIC telescope*, *Physics Letters B*, vol 668 (4) pp. 253-257 (2008).
- [41] J. Albert et al. (MAGIC Collaboration). *Variable Very High Energy [gamma]-Ray Emission from Markarian 501*, *Astrophysical Journal*, vol 669, pp. 862-880 (2007).
- [42] J. Albert et al. (MAGIC Collaboration). *MAGIC Observations of the unidentified gamma-ray source TEV J2032+4130*, *Astrophysical Journal*, vol 675, pp. L25-L29, (2008).
- [43] J. Albert et al. (MAGIC Collaboration). *Flux Upper Limit on Gamma-Ray Emission by GRB 050713a from MAGIC Telescope Observations*, *Astrophysical Journal*, vol 641, pgs. L9-L12 (2006).
- [44] J. Albert et al. (MAGIC Collaboration). *MAGIC upper limits on the high energy emission from GRBs*, *Astrophysical Journal*, vol 667, pp. 358-366 (2007).



# Chapter 3

## Wide-band Pulse Generators

1. Main Objectives
2. Variable Duty Cycle Pulsers based on Schmitt Trigger Inverters
3. Symmetric inverter and logical glitch
4. Pulse generator with shunt stub
5. Sub-nanosecond pulse generator based on SRD
  - 5.1 The Step Recovery Diode
  - 5.2 SRD pulser design
6. References

## 1. MAIN OBJECTIVES

THE need for compact pulse generators able to provide clean pulses in the ns range emerged soon within the MAGIC collaboration. Nanosecond pulse generators started to become popular with the development of Time Domain Reflectometry techniques [1], [2]. The analog part of the MAGIC Telescope acquisition chain must process Čerenkov light pulses with widths ranging between one and four ns, and amplitudes ranging from tens of microvolts to four volts for a 50  $\Omega$  load. Each one of the 577 PMT-preamplifier-VCSEL blocks in the camera of the MAGIC I Telescope must transmit these pulses along more than 170 m of optical fiber to the receivers located in the control room, with an overall bandwidth of 400 MHz [3]. The camera of the MAGIC II Telescope includes more than one thousand of these blocks, and the analog bandwidth has been increased up to 1 GHz [4]. There are three essential tasks to fulfill:

### 1) Design of evaluation devices for diagnostics of pixel electronics.

A pulse generator with the characteristics of the PMT-preamplifier block is very helpful for pixel chain fault diagnostics, since it makes possible a fast and convenient discrimination between optical link and photodetector electronic failures. Therefore, it was necessary to design, fabricate and test different dedicated pulse generators with precise specifications for this purpose.

### 2) Design of a testbench for photodetector testing.

MAGIC specific needs demand stringent requirements to the photodetectors in terms of quantum efficiency in the blue and UV range, as well as noise, bandwidth and reliability. A proper characterization of possible candidates to become camera photodetectors (as the PMTs, HPDs and GAPDs tested in the frame of the MAGIC Telescope Project) requires a number of different tests, namely:

- a) Bandwidth and pulse shape integrity
- b) Afterpulsing
- c) Noise
- d) Single photoelectron response

In all these tests it is necessary to excite the photodetector to be measured with ns pulses of blue/UV light. In principle, this can be accomplished by using two different sources: a) laser and b) LEDs.



By the time of the MAGIC II fabrication a bulky laser pulser was available at the faculty of Physics of the UCM which was able to provide ultra-short (100 ps PWHM), large dynamic range and highly monochromatic (405 nm) light pulses, with no options to increase the pulse width up to the ns range. On the other hand, by this time the LED industry was evolving very rapidly and supplied inexpensive LED devices suitable for the generation of blue and UV light pulses in the ns range with good characteristics to simulate the light flashes produced by the atmospheric showers. Figure 3.1 shows the quantum efficiency of some of the photodetectors to be tested (a) and the relative intensity distribution of the atmospheric Cerenkov light (b). The light pulses incident at the photodetectors use to be of very low intensity and are far from being monochromatic. A LED pulser is able to provide stable weak signals of moderate monochromaticity which resemble with good fidelity the light flashes to be measured within the UV/blue wavelength range.

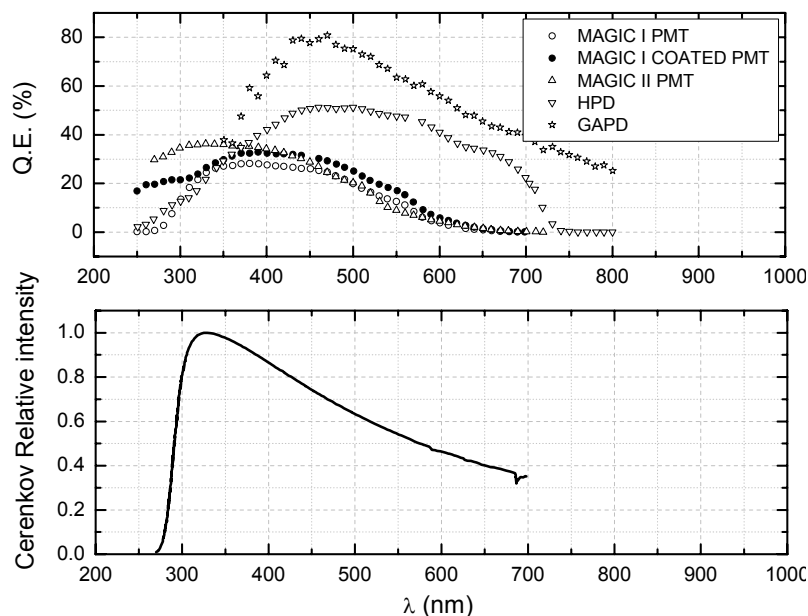


Figure 3.1 (a) Typical quantum efficiency of MAGIC I PMTs, both coated and uncoated with wavelength shifters [5], MAGIC II PMTs [6], an HPD [7] and a GAPD [8]. (b) Relative spectrum of the atmospheric Cerenkov light [9]

### 3) Design of a testbench for optical transmission testing

The nanosecond pulse generators presented in this thesis are also suitable for making diagnostics of the optical transmission links. In both MAGIC I and II telescopes, the optical links are able to transmit analog signals with a very high bandwidth and dynamic range, making the design of the pulsers to be used as testers very challenging.

Figure 3.2 shows the test points for the three applications mentioned above. The most critical issues to address in the design are the following ones:

- a) Pulse width. It must be of the order of 1 ns.
- b) Peak amplitude. In excess of 3.5 V. This is particularly critical in applications 2 and 3. Blue LEDs need a turn on voltage in excess of 3 V and at least 23 mA. VCSELs have a very high dynamic range, and provide an excellent linearity up to pulses with peak amplitudes of 4 V.
- c) Jitter. As low as possible, in order to avoid an overestimation of device under test jitter. In addition, a low jitter generator will be useful to detect possible faults in contacts or interconnections.
- d) Noise. It should be low enough to be able to provide pulses with peak amplitudes of 100  $\mu$ V without severe noise pollution.
- e) Impedance sensitivity. Another particularly critical issue for applications 2 and 3, where the loads for the pulser (a LED and a VCSEL, respectively) exhibit significant impedance changes between the ON and OFF state.
- f) Matched to 50  $\Omega$ . This is also particularly critical for applications 2 and 3, where broadband matching is not possible without signal loss, and therefore severe risk of ringing exists.

This Chapter is divided in Sections corresponding to the different topologies studied for the design of pulse generators. The basic component is the Schmitt Trigger inverter, which is used as initial stage in all the designs due to the fast rise and fall time of the generated flanks. Sections 2, 3, 4 and 5 are devoted to the study of different types of pulse width reduction techniques.

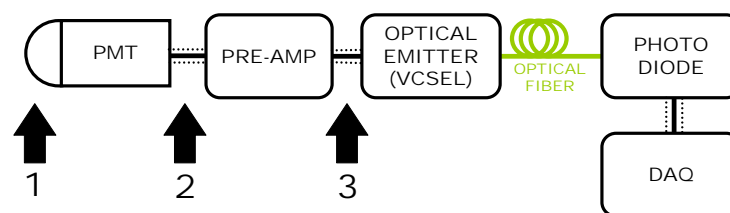


Figure 3.2 Critical points where the ns pulse generators are applied for subsystem testing: 1) Combined with a blue light emitter, test of the complete camera transmission. Test of photodetectors in a laboratory testbench. 2) Test of the pixel chain electronics. 3) Test of the optical transceiver and receiver electronics.

## 2. VARIABLE DUTY CYCLE PULSERS BASED ON SCHMITT TRIGGER INVERTERS

The theoretical basis of the first pulse generator presented in this thesis lays on the hysteresis behaviour of the Schmitt Trigger inverter. Figure 2.3 shows the hysteresis curve of a hexadecimal inverter and the schematics of a pulse generator based on this device. The asymmetry in the feedback network makes possible the generation of pulses with tunable frequency and duty cycle.

The generator works as follows: the input capacitor is initially discharged, so the logic at the input of the inverter is 0 and at the output is 1. At this point, the capacitor charges through R1 (the diode is in OFF mode). Once the voltage of the capacitor reaches  $V_{IH}$ , the output turns to 0 and the capacitor discharges through the parallel of R1 and R2 (the diode is in ON mode). When the voltage of the capacitor reaches  $V_{IL}$ , the output changes to 1. This process is repeated once and again while the inverter is biased. The frequency of the pulser can be controlled by means of the charge time constant ( $R1C$ ), and the pulse width with the value of R2.

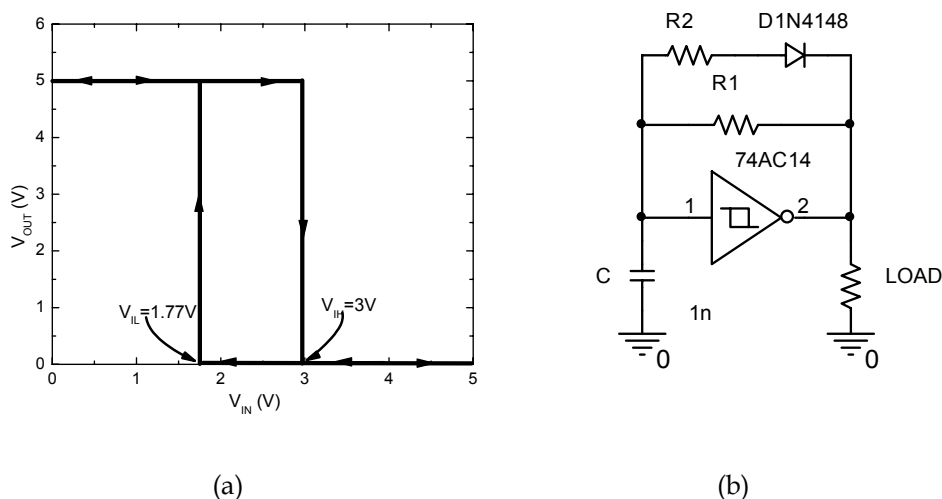
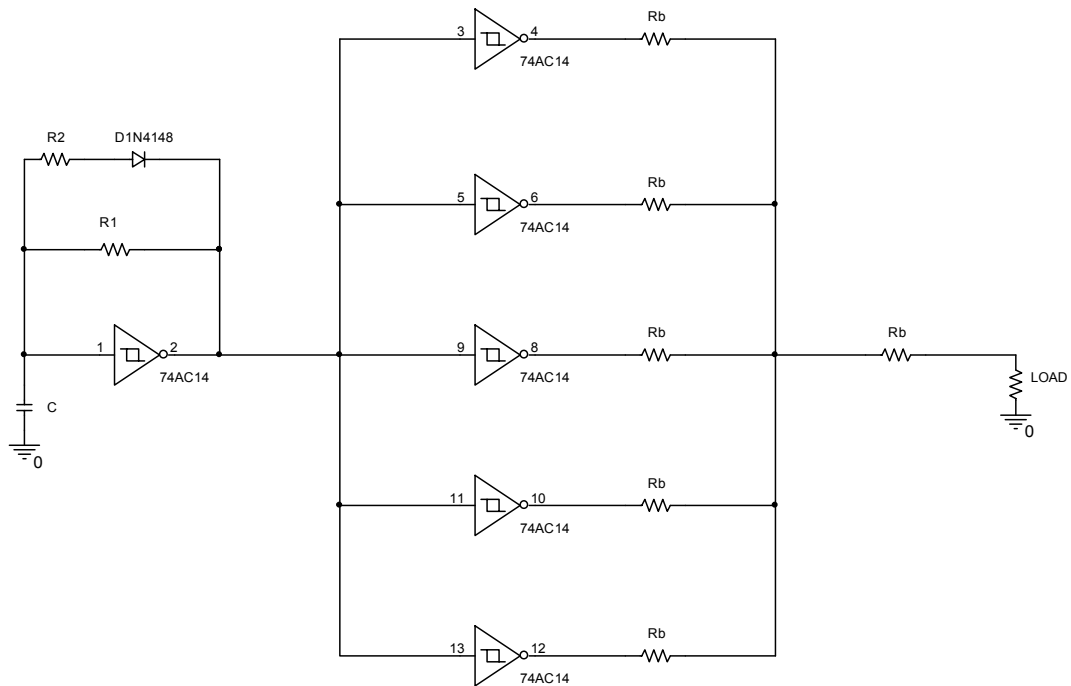


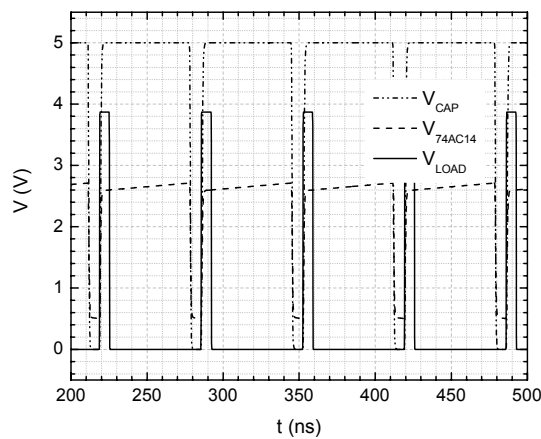
Figure 3.3 (a) Hysteresis curve of the 74AC14 HEX inverter. (b) Asymmetric pulse generator.

The time response of the system is of special relevance, that is, the rise and fall flanks of the pulse must be as sharp as possible. Among all the variety of Schmitt Triggers commercially available, one of the fastest belongs to the CMOS family (74AC14) [10]. This technology fits well to the present purposes, as the power consumption is minimized (the quiescent supply current of the device is very small, no more than a few  $\mu\text{A}$ ), the edge transitions are approximately symmetrical and have a duration of less than 2 ns. 74ACT14 inverters were also

tested, but the flanks of the resulting pulse presented more ringing and were discarded. Figure 3.4 shows the schematics and simulation of the first prototype of a 10 ns pulse generator designed for the MAGIC project. It is a modified version of a popular compact pulser for time domain reflectometry [11]



(a)



(b)

Figure 3.4 (a) Schematic of the asymmetric inverter with output buffer.  $R_1=150\text{ k}\Omega$ ,  $R_2=10\text{ }\Omega$ ,  $C=47\text{ pF}$ ,  $R_b=10\text{ }\Omega$  (b) Simulation.

### 3. SYMMETRIC INVERTER AND LOGICAL GLITCH

A second design of a pulse generator was developed based on digital logic and the usually undesired gate delays and glitches. Again, the 74AC14 block is used, this time to produce a square signal that feeds the next stage of the design (the asymmetric feedback network is replaced by a single resistor, thus obtaining similar paths for the charge and discharge of the capacitor).

Figure 3.5 shows the schematics of the pulse generator. The square wave is fed into a second inverter, and both signals ( $Q$  and  $\bar{Q}$ ) into a 74AC08 AND gate [12]. The 'AND' function of a square wave and its inverted would be a logical zero, but as a certain delay exists in the propagation of the signal through the gates, a *glitch* will occur at the output of the AND gate as shown in Figure 3.5b. This produces an output pulse, with an ideal amplitude of  $V_{CC}$  (logic gate bias), and a width that equals the delay of the inverter gate, typically 2-4 ns. The actual pulse is, nevertheless, determined by the rise and fall time of the inverter. Both of them are around 2 ns, so the output pulse will be slightly smaller than  $V_{CC}$ .

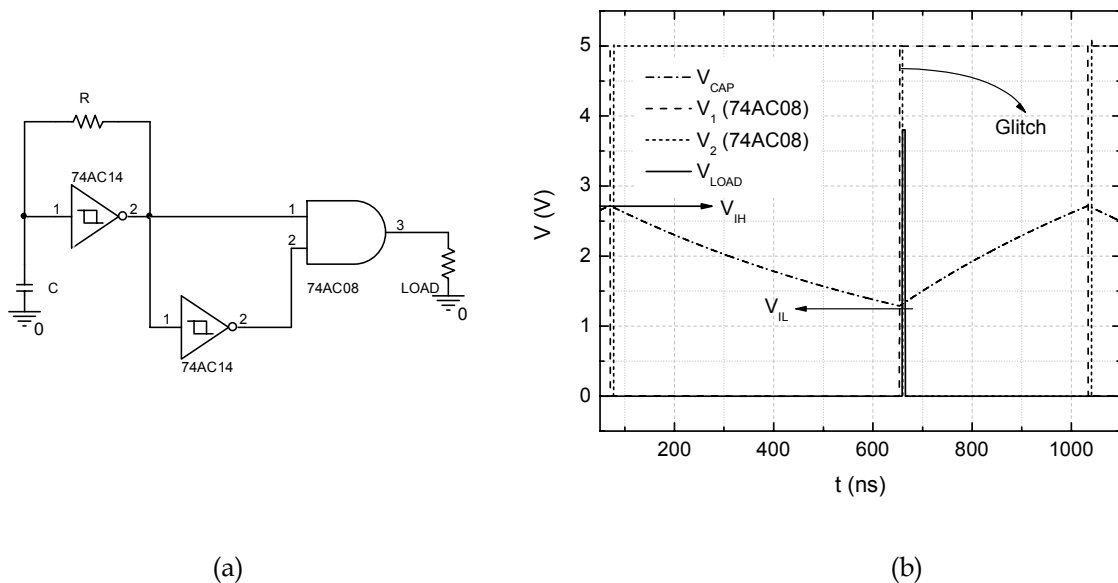


Figure 3.5 (a) Pulse generator based on logical glitches (schematic). (b) Simulation of the voltage on the capacitor, both inputs of the AND gate and the load.

#### 4. PULSE GENERATOR WITH SHUNT STUB

All the previous pulse generator designs have a clear bottleneck in the rise and fall time of the devices. Their logic gates have a typical rise time of  $\sim 2$  ns, so the minimum pulse width, if a pulse height of more than 3 V is needed, will be therefore limited to these values.

According to the type of gate (74AC00 or 74AC08) and the number of MMIC blocks used, the polarity of the output pulse is shown in Table 3.1. Although the most desirable configuration is a positive output, in some occasions it is interesting to have a negative one. Some examples are the simulation of the output of several photodetectors which provide negative output on working conditions [13], [14].

Logic Gate	Num of phase inversions	Output Pulse
AND	0 or 2	Positive
AND	1	Negative
NAND + DC block	0 or 2	Negative
NAND + DC block	1	Positive

Table 3.1 Polarity of the pulses as a function of the logic gate and the number of amplifiers.

In order to reduce the pulse width, time-domain reflectometry topologies were implemented. These topologies are based on the fact that if a short circuited stub is placed at the output of the generator, the reflected signal will interfere with the incident one and as a result an effective pulse width reduction is obtained [15]. Figures 3.6 and 3.7 show the design and simulation of a positive pulse generator based in this technique. Negative pulses due to the reflected signal can be cancelled by means of a Schottky diode.

If the AND gate is replaced by a NAND one (74AC00), and a DC block capacitor is placed as shown in Figure 3.8, the polarity of the output pulse can be inverted. The resulting simulation is depicted in Figure 3.9. It must be pointed out that these simulations were made by assuming that a pure TEM coaxial line is used. It is however more practical to use planar transmission lines, which do not transmit pure TEM modes and therefore cannot be simulated as a coaxial cable. In the next section this issue is discussed in detail.

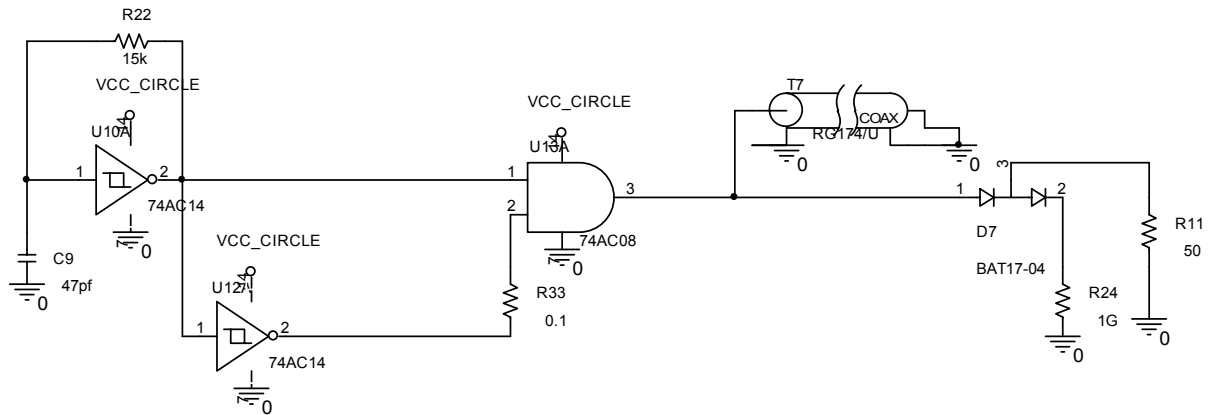


Figure 3.6 Schematic of the pulse generator with short-circuited stub and Schottky diode. As a 74AC08 AND gate is used, the pulse polarity is positive.

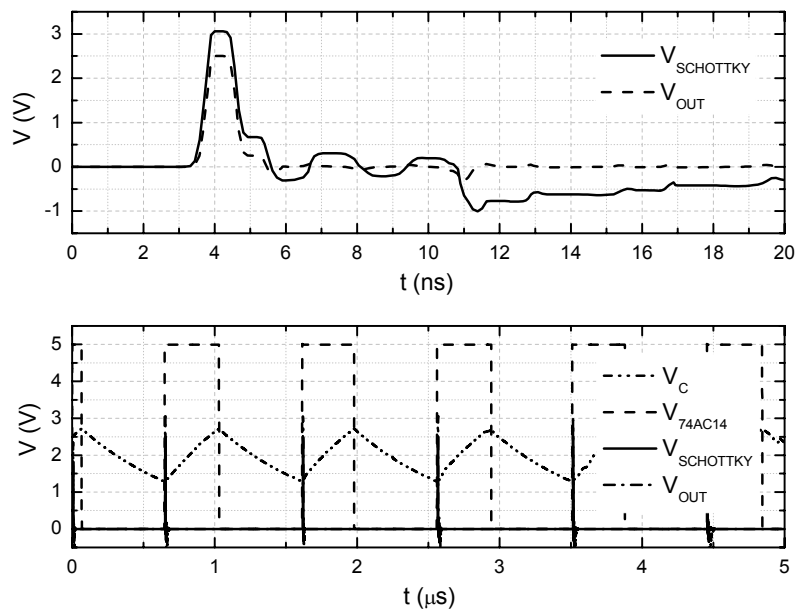


Figure 3.7 Simulation of the pulse generator of Figure 3.6.

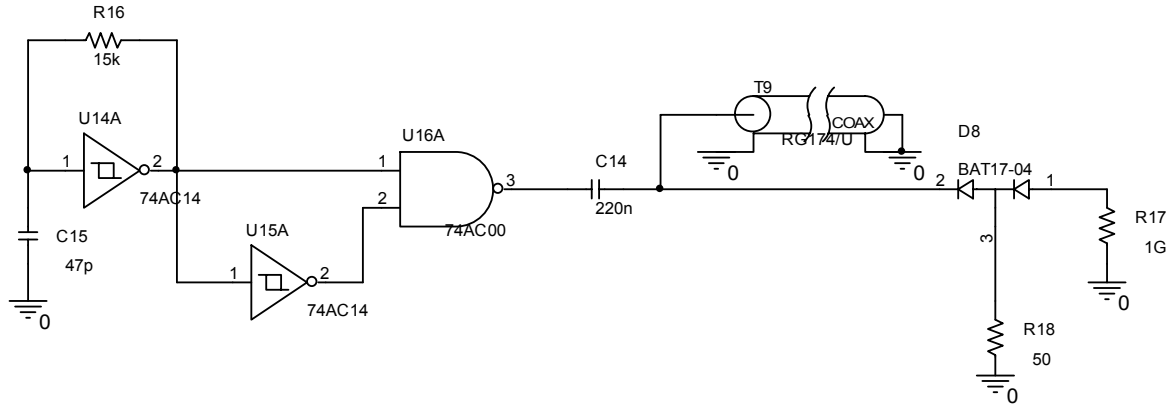


Figure 3.8 Schematic of the pulse generator with short-circuited stub and Schottky diode. As a 74AC00 NAND gate is used, the pulse polarity is negative.

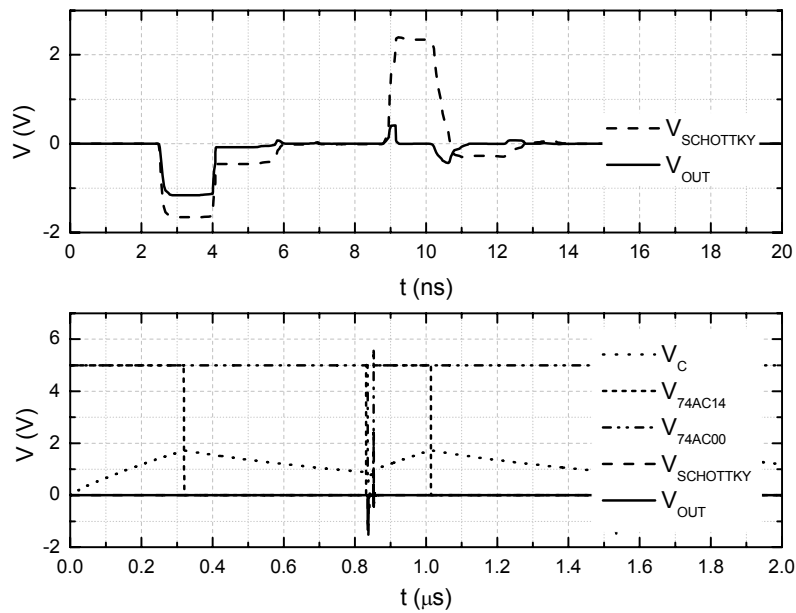


Figure 3.9 Simulation of the pulse generator of Figure 3.8.



## 5. SUB-NANOSECOND PULSE GENERATOR BASED ON SRD

The rise and fall times of the previous models imposed a limitation in the generated pulse width. With the increased bandwidth of MAGIC II Telescope, newer models with faster specification were demanded. Concretely, for the testing of the new receiver boards performed at the IFAE, the optimum performance of the pulse generator set by the Engineers was 1.3 ns PWHM and amplitude in excess of 4 V. Other features such as low noise and low jitter, as well as minimum ringing were also desirable.

These specifications are not easy to meet. The availability of commercial key components imposes some constraints to the figures of merit that can be achieved without relevant difficulties. Integrated SMD pulse generators are commercially available and can easily supply 5 V pulses to 50  $\Omega$  loads, but the corresponding widths hardly go below 5 ns.

A different approach was then taken. In Chapter 4 an extensive description of the complete pulse generator is done; the core and most important part of this device, though, is the SRD pulse generator which will be described in detail in this Section.

### 5.1 The Step Recovery Diode

Step Recovery Diodes (SRD) are P-I-N junction devices whose dynamic characteristics make them ideal to develop ultra-wideband RF devices such as frequency multipliers [16], sampling mixers [17], Phase Locked-Loops (PLL) [18], and different pulse generators. Among them it is worth to mention the monocycle pulsers of Tzyh-Ghuang et al. [19], and Han et al. [20], the ambipolar pulse generator of Jianping Lai et al. [21], the FET pulser of Han et al. [22], and the picosecond range pulser of Lee and Nguyen [23]. An excellent study of these devices and applications to pulse generators can be found in the doctoral thesis of M. J. Chudobiak [24].

SRDs are fabricated with a quite narrow intrinsic region, and with very abrupt n and p doping distributions surrounding the intrinsic part. Figure 3.10 shows the electric field distribution in the *i* region of the SRD during a transient from a forward bias to a reverse one. When the junction is forward biased, there is a strong accumulation of carriers at the *i* layer. Since this layer is very narrow, all the charge injected by a forward bias is stored close to the junctions. If a constant charging current is applied, the charge continuity equation states:

$$i(t) = \frac{dQ}{dt} + \frac{Q}{\tau} \quad \text{for } (Q > 0) \quad (3.1)$$

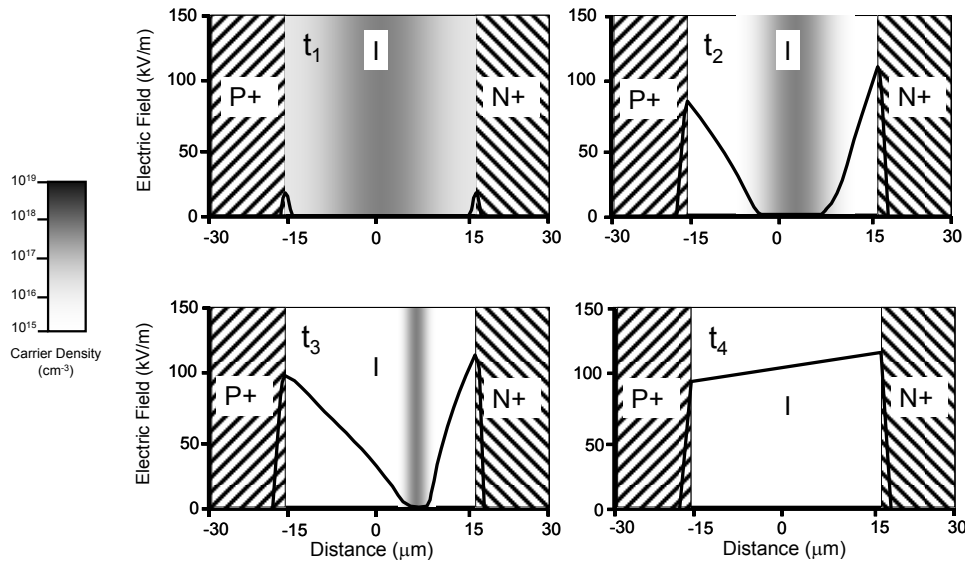


Figure 3.10 Electric field distribution in a SRD during a transit from a forward bias ( $t_1$ ) to a reverse one ( $t_4$ ) [25].

Where  $i$  is the total instantaneous diode current,  $Q$  the charge stored at the junction and  $\tau$  the minority carrier lifetime of diode. Then, the injected charge is given by the expression:

$$Q_F = I_F \tau (1 - e^{-t_F/\tau}) \quad (3.2)$$

Where  $Q_F$  is the stored charge from forward current,  $I_F$  the forward charging current and  $\tau_F$  the instantaneous time at which  $Q_F$  is calculated. If  $t_F$  is long compared to  $\tau$  then:

$$Q_F \approx I_F \tau \quad (3.3)$$

Table 3.2 shows the carrier lifetime of some state of the art SRDs.

SRD model	Carrier lifetime, $\tau$ (ns)
ASI ASRD 800 Series	10 – 100
AEROFLEX METELICS MMD Series	4 – 100
MPulse MP Series	15 – 120

Table 3.2 Typical carrier lifetime for several commercial SRDs.

When the switching to reverse bias starts, the carriers start to deplete from the i layer, and an electric field starts to grow from the junctions [26], [27]. As a result, a reverse current is induced. When the i layer is about to be depleted from carriers (this is called the 'punch through' situation), an abrupt increase of the electric field occurs. This field strongly reduces the time needed to obtain a full depletion. In terms of currents, one can therefore identify three successive states:

1. The current initially corresponds to the one of a conventional forward biased diode.
2. During the depletion a high reverse current exists until punch through occurs. The amount of injected and stored charge when forward-biased with finite recombination time, determines the impedance of the diode when reverse biased. If the charge is removed by a constant current, the time required will be:

$$\frac{t_S}{\tau} = \ln \left( 1 + \frac{I_F (1 - e^{-t_F/\tau})}{I_R} \right) \quad (3.4)$$

And, in case of  $t_F \gg \tau$  :

$$\frac{t_S}{\tau} \approx \ln \left( 1 + \frac{I_F}{I_R} \right) \quad (3.5)$$

Furthermore, in many applications the reverse current is much higher than the direct one, so:

$$\frac{t_S}{\tau} \approx \frac{I_F}{I_R} \quad (3.6)$$

3. A fast transition to the normal negligible reverse saturation current takes place when the depletion is finished.

This behaviour of the current will clearly be seen in the next section, where the simulation of the prototype is described.

The simulation of the SRD dynamic characteristics has been the subject of intense research [28], [29]. The charge depletion after punch-through is so fast that its modelling poses severe numerical difficulties. However, we will show in the next section that a simplified model compatible with commercial CAD software provides a reasonable accuracy for ns range pulsers.

## 5.2 SRD pulser design

Figure 3.11 shows the schematic of the proposed pulse generator. A low bandwidth pulser is applied to the series SRD. During the positive part of the pulse the diode is under forward bias, and the carriers are stored into the intrinsic region. The amount of stored charge, and thus the time-characteristics of the low and high state transitions of the diode, can be controlled by means of the time and amplitude of the forward bias.

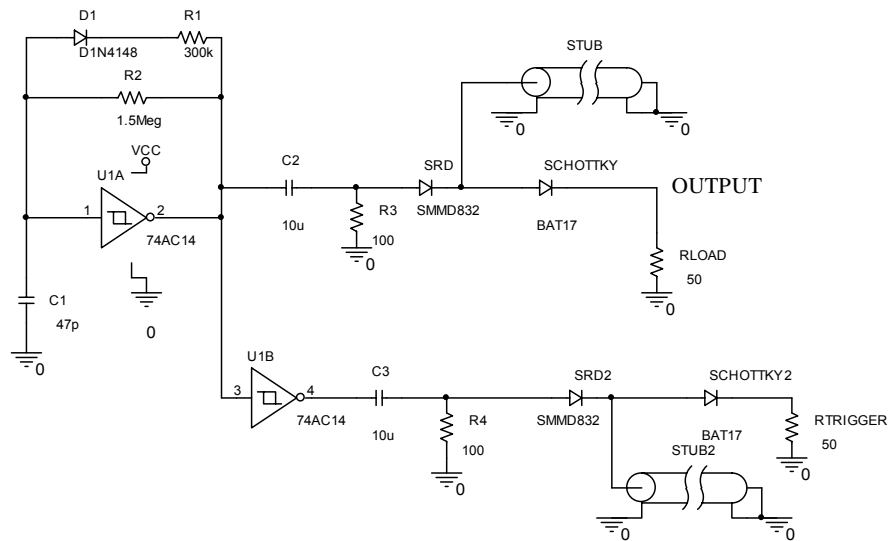


Figure 3.11 Schematic of the SRD pulser generator.

The low bandwidth pulser (tens of nanoseconds) is used to feed the pulse-shortening circuit, which consists of an SRD, a shunt stub terminated in short-circuit and a Schottky diode. This generator is based on the Schmitt-Trigger inverter with asymmetric feedback described in Section 2.

The charge and discharge of the input capacitor controls the input and output states of the inverter. When the capacitor is charged, the logic input is 1, and the output is 0. At this point, the capacitor discharges through the parallel of  $R_1$  and  $R_2$ , as the diode is in ON mode.

When the states are inverted, the capacitor charges through  $R_2$ , so that the diode is in OFF mode. This way, both the repetition frequency and the pulse width of the low bandwidth pulser can be adjusted. A high value capacitor filters the DC component of the signal, so that its duty cycle determines the high and low voltages applied to the pulse shortening circuit. An accurate adjustment is of special relevance, so the charge and discharge times of the SRD and the

voltage levels have a direct influence on the stored charge and so in the output pulse shape. The repetition frequency was set to 20 KHz and the voltage levels to 1 V and -2 V.

The pulse-shortening stage works as follows (see Figure 3.12). While the SRD (dashed line) is forward biased, the current corresponding to that voltage charges the intrinsic region of the junction. When reverse bias is applied the diode starts to discharge. A shunt, short-circuited stub (dotted line) sinks all the current provided by the SRD. But at high frequencies the electrical length of the stub is not negligible, and there is a delay in the signal propagation towards the short circuit. This delay makes the current in the load to be the difference between the one provided by the diode and the one sunk in the stub. According to this, a negative and a positive pulse are produced in the flank of the current signal.

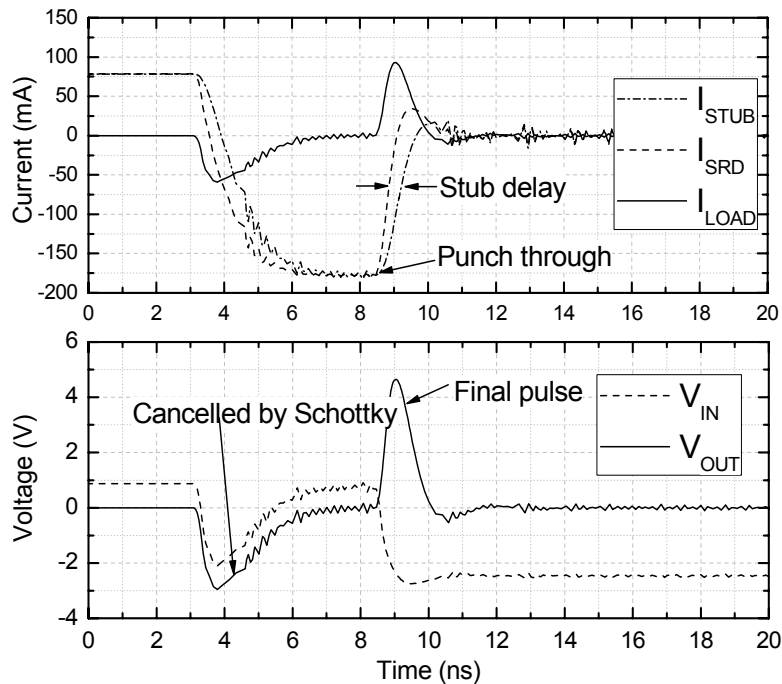


Figure 3.12 Pulse generator shaping. Top: Current in the diode ( $I_{SRD}$ ), stub ( $I_{STUB}$ ) and load ( $I_{LOAD}$ ). Bottom: Voltages at the input ( $V_{IN}$ ) and output ( $V_{OUT}$ ) of the SRD. The signals were simulated by removing the Schottky diode from the schematics of Figure 3.11a.

The negative pulse is cancelled by means of a series Schottky diode (BAT17), and the positive one is driven to the load. This cancellation is made at the expense of reducing in  $\sim 200$  mV the pulse amplitude. The simulation was made by removing the Schottky diode in order to visualize the negative pulse

cancelled by this diode. The SRD used in this design was an Aeroflex-Metelics SMMD832 [30] with a transition time of 70 ps, carrier lifetime of 12 ns and a junction capacitance of 0.6 pF.

The pulse shape depends, apart from the SRD charge time, on the time delay of the stub and its impedance. An accurate modelling of the stub is critical to obtain a good simulation of the pulse width and amplitude. The stub designed for the pulser presented here was a coplanar line terminated in a via hole. This line transmits the pulse as a quasi-Transverse Electromagnetic Mode (quasi-TEM) with an associated effective permittivity and characteristic impedance which were both simulated with APLAC software.

The results of the simulation made with APLAC were then applied to model the equivalent TEM transmission line parameters in the pulse generator simulation. The simulation of the overall circuit was made with a recent version of ORCAD, which includes models of standard (coaxial) transmission lines. These models can be defined by either the physical geometry or by means of the electrical length and the characteristic impedance. This last option was the one selected in this work, since it enabled us to directly make use of the more accurate APLAC models for non TEM transmission lines.

In order to combine the benefits of both programs, ORCAD and APLAC, an optimization was first made with APLAC to obtain the phase constant and characteristic impedance of a short-circuited coplanar line. A model for the via hole was also considered in the simulation. Once the proper parameters were obtained, a fictitious equivalent TEM line with the calculated  $Z_0$  and  $\lambda_{\text{eff}}$  calculated by APLAC was included in the ORCAD simulation of the pulse generator.

Figure 3.13 shows the dependence of the stub impedance and length on the pulse shape and amplitude. In this simulation, the previously described approach was followed. The final values of the simulated coplanar line were 112 mm length, 1 mm width, and 0.5 mm gap between line and ground plane. The substrate was a FR4 laminate, with  $\epsilon_r=4.5$ , substrate thickness of 1.57 mm and metallization thickness of 36  $\mu\text{m}$ .

The modelling of an equivalent fictitious TEM line with the parameters obtained by APLAC provided an excellent agreement between theory and measurements. This is shown in Figure 3.14, where a comparison between the measured pulse and two simulations (one including coplanar line and the other assuming an equivalent coaxial line with a pure TEM mode) is made for the prototype of Figure 3.11.

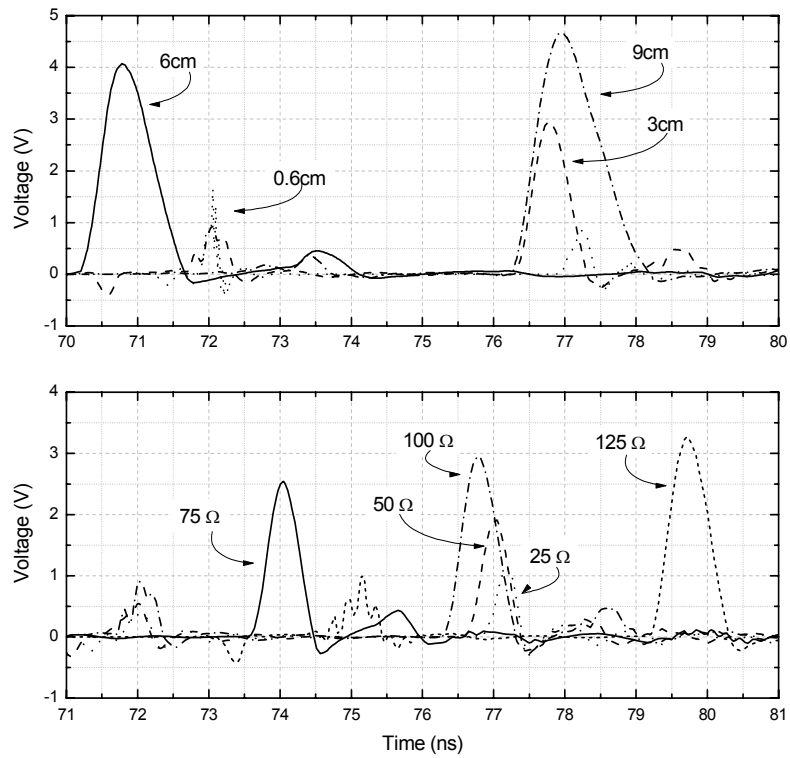


Figure 3.13 Effect of the stub length for a fixed impedance of 100 Ω (top) and stub impedance (bottom) for a fixed length of 6 cm on the performance of the generator.

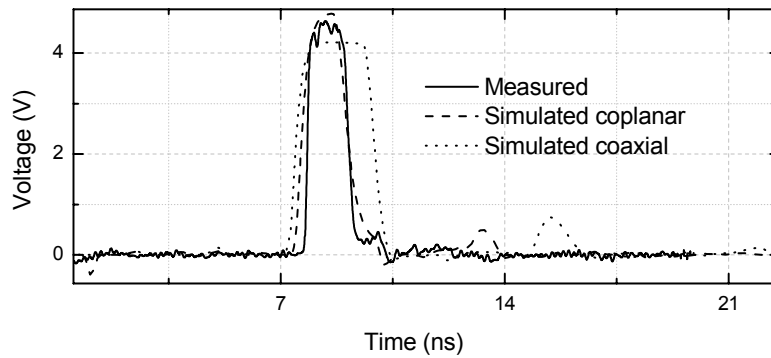


Figure 3.14 Comparison between the simulated and measured pulse shape.

## 6. REFERENCES

- [1] United States Patent N° 7,206,703 B1. Papageorgiou et al. *System and method for testing packaged devices using time domain reflectometry.*
- [2] United States Patent N° 7,245,129 B2. Daniel Wajcer et al. *Apparatus for and method of cable diagnostics utilizing time domain reflectometry.*
- [3] Juan Cortina (for the MAGIC Collaboration). *Status and first results of the MAGIC Telescope.* Astrophysics and Space Science, Volume 297, Numbers 1-4 / junio de 2005
- [4] C.C. Hsu et al. *The Camera of the MAGIC-II Telescope.* 30<sup>th</sup> International Cosmic Ray Conference, Sept 2007, Mérida (Mexico)
- [5] D. Paneque, H. J. Gebauer, E. Lorenz, M. Martinez, K. Mase, R. Mirzoyan, A. Ostankov and T. Schweizer. *A method to enhance the sensitivity of photomultipliers for air Cherenkov telescopes.* NIM A, Volume 504, Issues 1-3, 21 May 2003, Pages 109-115
- [6] Ching-Cheng Hsu. *PMT Characterization for MAGIC II Telescope.* Proceedings WSPC, October 2007
- [7] M.Hayashida, J.Hose, M.Laatiaoui, E.Lorenz, R.Mirzoyan, M.Teshima, A.Fukasawa, Y.Hotta, M.Errando and M.Martinez. *Development of HPDs with an 18-mm-diameter GaAsP photo cathode for the MAGIC-II project.* 29th International Cosmic Ray Conference Pune (2005) 5, 183-186
- [8] D. Renker. *Geiger-mode avalanche photodiodes, history, properties and problems HPD.* NIM A, 567 (2006) 48-56
- [9] M. Döring, K. Bernlöhr, G. Hermann, W. Hofmann, and H. Lampeitl. *Measurement of the Cherenkov light spectrum and of the polarization with the HEGRA-IACT-system.* ICRC 2001
- [10] 74AC14 and 74ACT14 datasheet. <http://www.fairchildsemi.com/ds/74/74AC14.pdf>
- [11] *Build your own cable radar,* Electronic Design, October 1998, <http://electronicdesign.com/Articles/ArticleID/6260/6260.html>. Also in T. Engdahl *Time domain reflectometer,* <http://www.epanorama.net/circuits/tdr.html>
- [12] 74AC08 and 74ACT08 datasheet. <http://www.fairchildsemi.com/ds/74/74ACT08.pdf>
- [13] F. Lucarelli, M. Camara, P. Antoranz, J.M. Miranda, M. Asensio. *Testbench to characterize pixels of the Major Atmospheric Gamma-ray Imaging Cherenkov (MAGIC) telescope.* Opt. Eng., Vol. 45, 084003 (2006)
- [14] D. Renker. *Geiger-mode avalanche photodiodes, history, properties and problems.* Nuclear Instruments and Methods in Physics Research A 567 (2006) 48-56
- [15] David M. Pozar, *Microwave Engineering,* 2nd edition, John Wiley and Sons, (1998)
- [16] Jian Zhang, Antti V. Räsänen, *Computer aided design of Step Recovery Diodes frequency multipliers,* IEEE Transaction on Microwave Theory and Techniques, VOL 44. No 12, December 1996
- [17] Jeongwoo Han, Cam Nguyen, *Coupled-Slotline-Hybrid Sampling Mixer Integrated with Step-Recovery-Diode Pulse Generator for UWB Applications,* IEEE Transactions on Microwave Theory and Techniques, VOL. 53, No. 6, June 2005



- [18] Teng K.H., Linton D., Humphrey D., *Microwave phase-locked loop circuit development and efficiency improvement*, High Frequency Postgraduate Student Colloquium 2003. ISBN: 0-7803-8123-8
- [19] Tzyh-Ghuang Ma, Chin-Jay Wu, Po-Kai Cheng, Chin-Feng Chou, *Ultrawideband Monocycle Pulse Generator with Dual Resistive Loaded Shunt Stubs*, Microwave and Optical Technology Letters Volume 49, Issue 2, pp. 459-462
- [20] Jianping Lai, Qing Hao, Jingzhao She and Zhenghe Feng, *A Low Cost Trigger Frequency Alterable Ultra-Wide Band Ambipolar Pulses Generator*, International Conference on Microwave and Millimeter Wave Technology, Nanjing, P.R. China, April 2008. VOL. 1, pp 216-219
- [21] Jeongwoo Han, Cam Nguyen, *A new Ultra-Wideband, Ultra-Short Monocycle Pulse Generator With reduced Ringing*, IEEE Microwave and Wireless Components Letters, June 2002, VOL. 12, No. 6
- [22] Jeong-Woo Han, Meng Miao, Cam Nguyen, *Recent development of SRD and FET based sub-nanosecond pulse generators for ultra-wideband communications*, IEEE Topical Conference on Wireless Communication Technology, Oct. 2003. 15-17 pp 441-442
- [23] J.S. Lee and C. Nguyen, *Uniplanar picosecond pulse generator using step-recovery diode*, Electronics Letters, 12th April 2001 VOL. 37 No. 8
- [24] M.J. Chudobiak, D.J. Walkey, *Subnanosecond 300V diffused step recovery diode*, IEEE Electronics Letters 1st August 1996 VOL. 32, No. 16.
- [25] M.J. Chudobiak, *New Approaches For Designing High Voltage, High Current Silicon Step Recovery Diodes for Pulse Sharpening Applications*. PhD Thesis.  
<http://www.avtechpulse.com/papers/thesis/>
- [26] *Pulse and Waveform Generation with Step Recovery Diodes*. HP Application Note 918.
- [27] K.L.Kotzebue. *A Circuit Model of the Step-Recovery Diode*. Proceedings of the IEEE, October 1965.
- [28] Zhou Jianming, Gao Xiaowei, Fei Yuanchun. *A new CAD model of step recovery diode and generation of UWB signals*. IEICE Electronics Express Vol. 3 (2006) , No. 24 pp.534-539
- [29] I. McGregor, E. Wasige, I. Thayne. *Step Recovery Diode Look-Up Model with Bi-Phase Wavelet Generator*. Proceedings of Asia-Pacific Microwave Conference 2007
- [30] Aeroflex-Metelics SMMD832 Datasheet, [www.aeroflex-metelics.com](http://www.aeroflex-metelics.com)



# Chapter 4

## Wide-band Pulse Generators: Results

1. Generator for Photodetector Tests
  - 1.1. Requirements
  - 1.2. Design
  - 1.3. Results
2. Generator for MAGIC I Camera Tests
  - 2.1. Requirements
  - 2.2. Design
  - 2.3. Construction
  - 2.4. Results
3. Generator for MAGIC II Receiver Boards Tests
  - 3.1. Requirements
  - 3.2. Design and construction
    - I. Pulse generation stage
    - II. Amplification stage
    - III. Attenuators
    - IV. VCSEL biasing
    - V. DC regulation
  - 3.3. Results
4. References

## 1. GENERATOR FOR PHOTODETECTOR TESTS

### 1.1 Requirements

**D**URING the work developed for this Thesis, several pulse generators were designed, constructed and tested. The first group of pulsers was devoted to the test of photodetectors, as part of a testbench which included a black box with  $\mu$ -metal walls to avoid electromagnetic and optical interferences and different bases for photosensor biasing [1].

The pulse generators proved to be very useful and reliable when connected to blue LED; the limitations in the pulse width are determined by the time response of the diodes. Most of the blue LEDs developed up to now present rise and fall times that do not match the pulse generator performance; however, new models are coming to the market with improved time response [2].

Blue LEDs have quite high threshold voltages in comparison with other LEDs (typically more than 2.5 V). This implies that the peak voltage applied by the pulse generator must be higher than this threshold in order to switch the LED on. This is the most restrictive requirement in the design. Pulse width was not considered a critical issue in the present design, as the LEDs available at that moment had a quite slow time response. Faster generators are described in following sections.

### 1.2 Design

Figure 4.1a shows the schematic of the generator, based on the Schmitt Trigger inverter with output buffer described in Chapter 3.

The output impedance of the generator is designed to be  $50\ \Omega$  matched. The convenience of implementing a matching network to couple the output impedance of the system to the input impedance of the blue LED will be discussed later. The resulting pulse is shown in Figure 4.1b. It has been sampled with an oscilloscope probe with a  $1\ \text{M}\Omega$  resistance and an  $8\ \text{pF}$  capacitance, so it could be considered as an open circuit and the pulse as the one that will excite the LED. It can be seen the effect of discontinuities: some ringing is produced, which causes the pulse to be higher than expected. The effect of the LED when connected at the output, and its relation with the observed distortion of the signal will be studied straightforward.

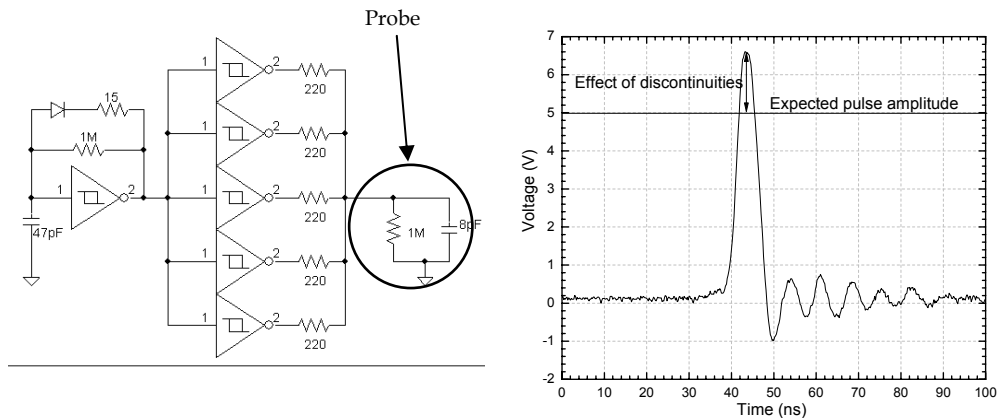


Figure 4.1 (a) Pulse generator with output buffer. (b) Generated pulse, measured with the oscilloscope in open circuit (the probe has a resistance of 1 M $\Omega$  and a capacitance of 8 pF).

Once the LED has been analysed [3], the input impedance presented to the applied pulse can be estimated. Classical procedures of impedance matching based on narrow band reactive elements cannot be applied to couple a LED to a pulse generator due to two main reasons: a) the pulse signal has a wide frequency bandwidth, and b) the LED impedance is bias-dependent. However, dissipative coupling networks can reduce reflections and therefore ringing at the expense of a slight signal loss. In this case a trimmer series resistance could be placed at the output of the generator and in series with the diode.

Surface Mount Devices (SMD) have been used in the final implementation, so the size and weight of the generator are extremely reduced. This makes it suitable for the use inside the black box or other reduced testbench. Only two types of active devices (the inverters and a diode) are necessary and the working conditions (temperature, bias...) are always below the recommended maximum. Therefore, the lifetime expected is the one provided by the device manufacturer, making the complete system very reliable.

### 1.3 Results

Figure 4.2 shows the pulse shape measured at the diode pins, for three values of the series resistance mentioned in Section 1.2. The signal loss can be considered acceptable for coupling resistances below 20  $\Omega$ . Above this value, the peak voltage applied to the LED is too close to its threshold voltage. However, the observed residual ringing levels are far below the LED turn on voltage, as one could expect from the simulation, and therefore they are not replicated in the optical signal. Consequently, no matching networks were considered necessary for the tested devices.

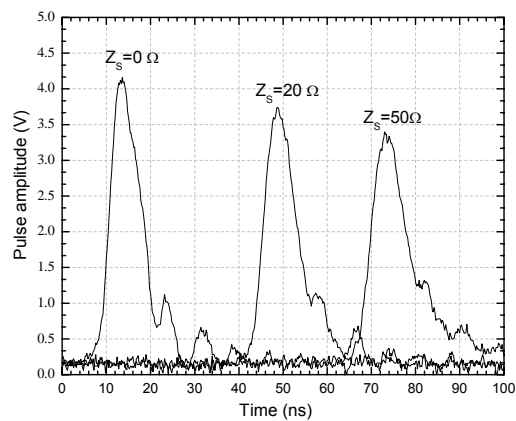


Figure 4.2 Effect of the addition of a series resistant to the LED connected at the output of the pulse generator.

The generator-pulse chain is biased and placed inside the black box (1 x 0.5 x 0.5 m) used to test the sensors. The device used to characterize the optical response of the generator was a photomultiplier (Hamamatsu EMI9116) [4] which is already installed in the MAGIC II camera.

It is known that the photomultiplier response is very fast ( $\sim 2.5$  ns FWHM) [5], so the generated light pulse must induce a clear and well shaped pulse in the detector, whose rise and fall time correspond to the rise and fall time of the light intensity of the LED.

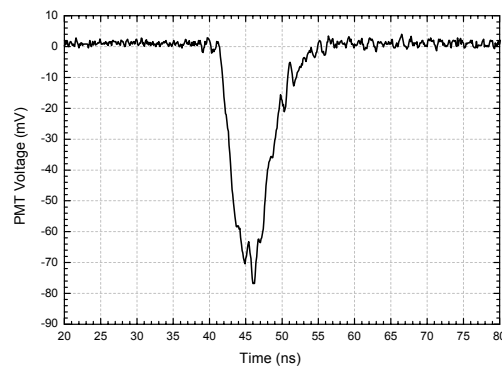


Figure 4.3 Pulsed light detected by the photomultiplier tube

The noise produced by the pulse generator plays a marginal role in this particular case. None of the blue LEDs is turned on until the bias reaches about 2.5 V, so the noise coming from the devices, and even the ringing produced by the discontinuities are not optically transmitted to the detectors. Therefore, the only noise to care about in real working conditions is the one due to the intrinsic characteristics of the detector, and the one produced by the sky background

## 2. GENERATOR FOR MAGIC I CAMERA TESTS

### 2.1 Requirements

A relevant task in the maintenance of the MAGIC I Telescope camera is the test of the VCSELs, the optical link and the receiver boards. These tests can be simplified with the aid of a compact device able to emulate the signals supplied by the PMT-preamp set to the VCSELs when the camera is illuminated by Čerenkov pulse radiation. These signals produce an ‘artificial camera event’ when at least three next neighbour pixels are simultaneously fired, as established by the trigger logic. Three identical pulses are therefore needed, and must be perfectly synchronized in order to reach the trigger within the same time window. The timing of the signal is thus a very important issue in the data acquisition of the Telescope. Consequently, a very low jitter is imposed to the design, both in the pulse width and in the repetition frequency.

The duration of the pulses to be generated is determined by the characteristics of the Čerenkov light and the PMT response. Taking into account these issues, a FWHM of  $\sim 2$  ns has been chosen as the key design specification. The amplitude of the pulses is set by the amount of photons incident on the PMT cathode and the gain of both the photomultiplier and the preamplifier in the base of the PMT. This is within the range of 1 mV - 1 V at the preamplifier output. To fully cover this range, three outputs were implemented, with amplitudes of 2 mV, 20 mV and 700 mV. Finally, the pulse repetition frequency should be close to the rate of events under real-world operating conditions, which is around 200 Hz with the standard MAGIC trigger.

The main characteristics demanded for this pulse generator are summarized in the following list:

- Pulse width:  $\sim 2$  ns.
- Pulse amplitudes: 2 mV, 20 mV, 700 mV.
- Channels: three, each one with three different reference amplitudes.
- Pulse repetition frequency:  $\sim 200$  Hz.
- Low noise, low jitter.

### 2.2 Design

The pulse generator is clearly divided in three separate stages. The complete schematic can be seen in Figure 4.4. In the first stage, the pulse is generated. To accomplish all the requirements in pulse width and repetition frequency, the

pulse generator based in logical glitches described in Chapter 3 was implemented. This configuration performs 2 ns width pulses, with amplitude in excess of 4 V. Three generators are constructed, one for each of the desired output amplitudes.

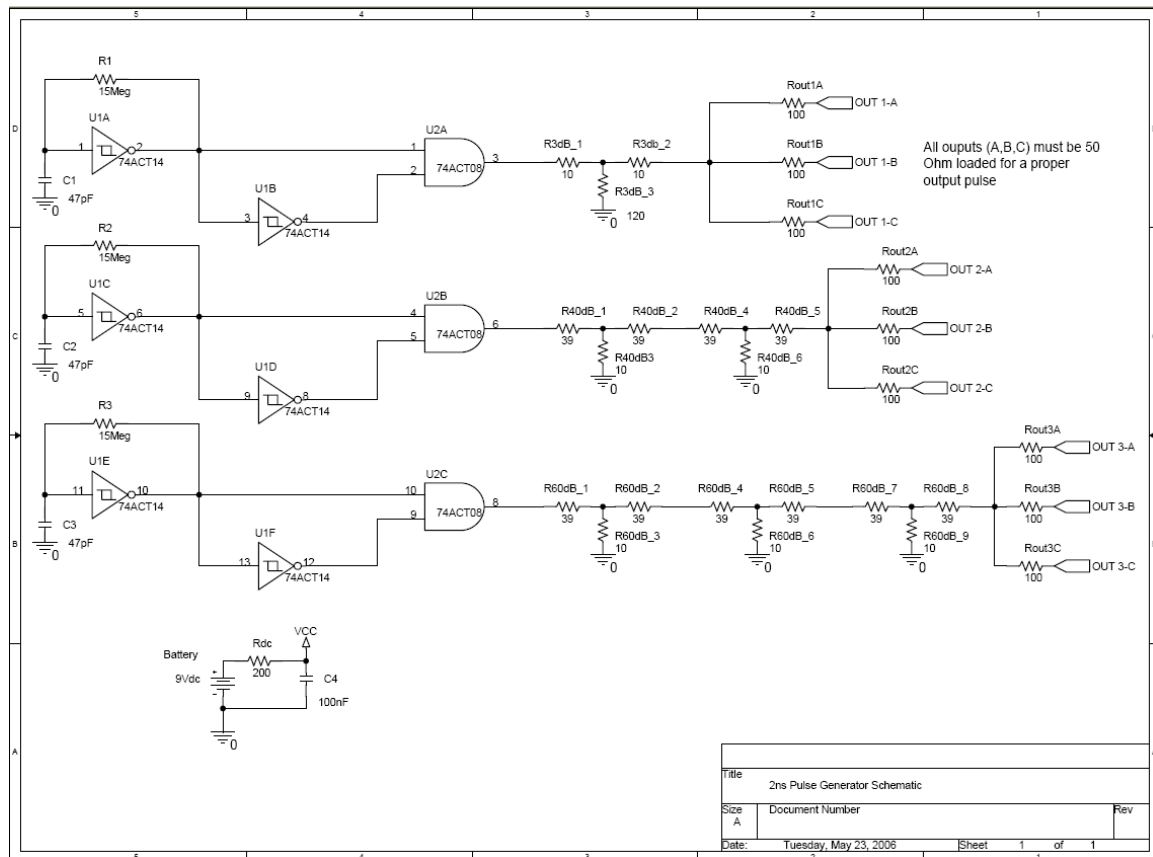


Figure 4.4 Schematics of the pulse generator designed by the author for this thesis, which is presently giving service at MAGIC site. Three stages are observed: pulse generation, ringing reduction by means of attenuator, and power division.

In the second stage, the pulse is adapted to the final amplitude by means of 50  $\Omega$  passive attenuators designed to provide simultaneously the desired output level and the necessary impedance matching to the input of the VCSEL drive circuit. Taking into account that the transmission lines have a characteristic impedance of 50  $\Omega$ , the typical attenuation network can be implemented and synthesized as shown in Figure 4.5a. The resistances are chosen for the attenuator to be matched at both ports and to provide the desired attenuation as shown in Figure 4.5b. For a given value of the attenuation, the lower graph sets the value of  $R$ , and the upper graph sets  $Z$  for that  $R$ .

The main disadvantages of the use of resistive pads are the obvious power consumption and the unavoidable introduction of noise in the signal. On the



other hand, the advantages are an extremely easy design and implementation, not needing external bias and control as active elements do.

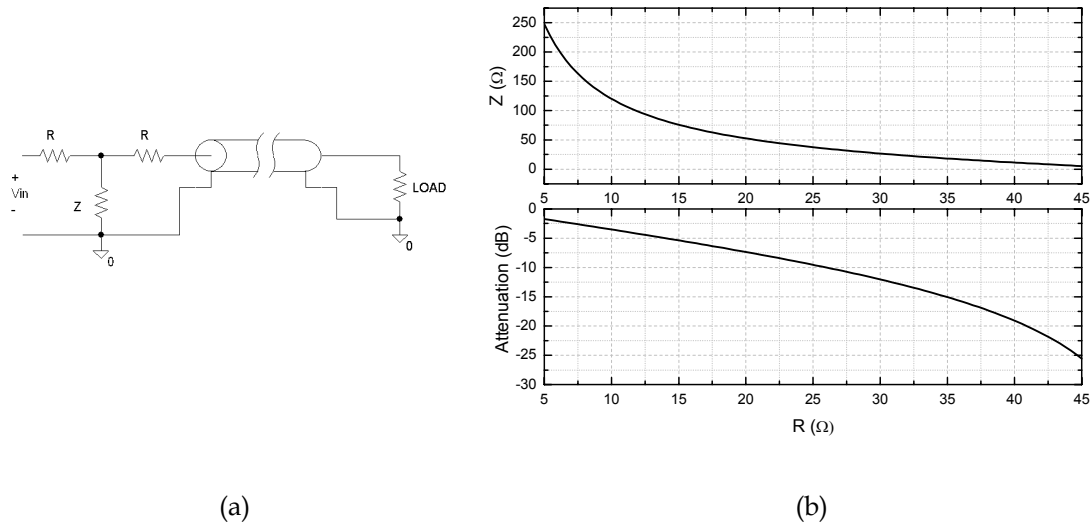


Figure 4.5 (a) Passive attenuator and transmission line schematic. (b) Graphs used for the design of the desired attenuator (50 Ω matched).

After the resistive power splitters three identical outputs are obtained for every channel. The line coming from the attenuator must be splitted into other three, each one with an impedance that provides 50 Ω when viewed from the input port. Figure 4.6 shows the power delivered to each of the three loads ( $P_1$ ,  $P_2$  and  $P_3$  in Figure), which is 1/9 of the input power and the losses in the resistances are 2/3 of the initially available signal power. It must be pointed out that the design shown in Figure 4.6 leaves the outputs mismatched. In order to couple them an additional resistor is needed at the output, and the values of the resistances must be different (see Section 3.2).

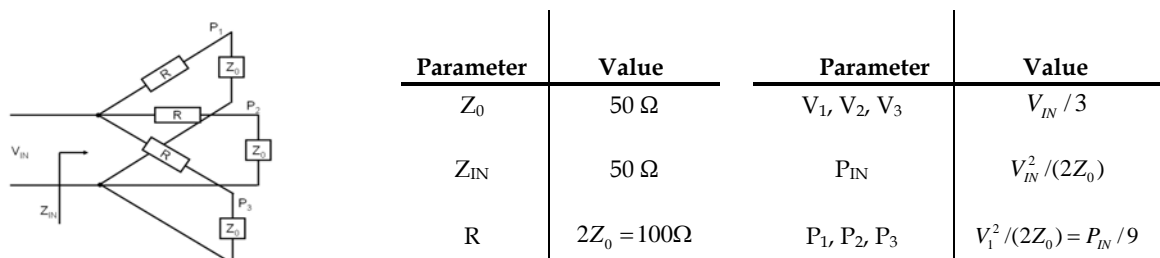


Figure 4.6 Values of the parameters for a 3 way, 50 Ω matched, resistive power splitter with the input coupled.

## 2.3 Construction

The layout of the pulse generator has been developed using ORCAD software (Capture CIS and Layout Plus) and is shown in Figure 4.7.

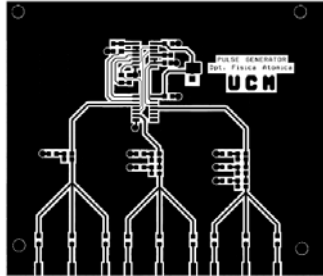


Figure 4.7 Board layout of the La Palma Pulse Generator.

All the outputs are in the rear part of the box, divided into three sets of three identical outputs. The connectors used are 50  $\Omega$  coaxial female subminiature-A connectors (SMA), as shown in Figure 4.8.



Figure 4.8 Pulse Generator package.

## 2.4 Results

Once the pulse generators were assembled, the outputs were tested and analyzed using a 6 GHz, 20 GSa/s digital oscilloscope (AGILENT infiniium 5855A DS8).

Figure 4.9 shows the actual generated pulses. For a given set of outputs, the three channels are correctly synchronized, which is crucial due to the narrow time window imposed to pixel coincidence (around 4 nanoseconds). The noise is well below the sensitivity of both the oscilloscope and the data acquisition subsystem of the telescope.

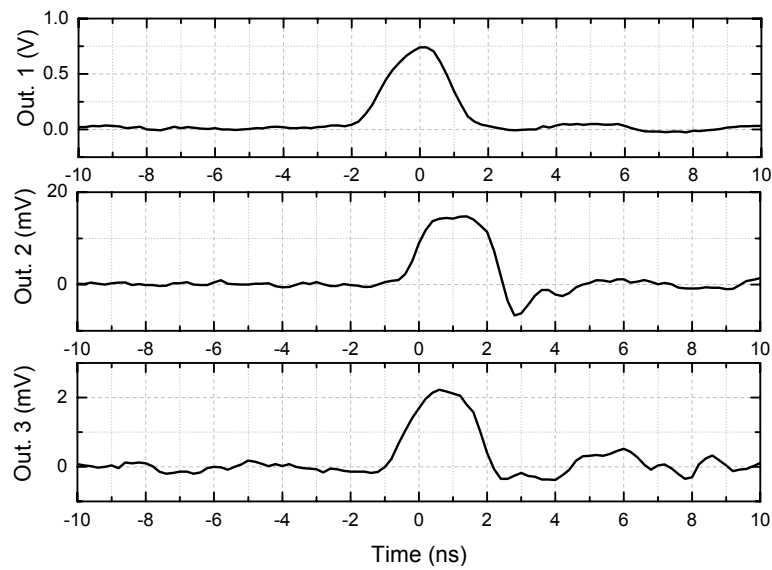


Figure 4.9 Measured pulses at the three different outputs.

The jitter on the pulse width has also been measured and it is shown in Figure 4.10. Setting the trigger of the oscilloscope on the rising flank of the pulse, a histogram is made at the same voltage level of the falling flank of the pulse. These measurements prove that the pulse is very stable, with standard deviation of the pulse width of only 39 ps. It must be commented that a 'phantom state' on the pulse width appears as a consequence of glitches, with probability lower than 8%.

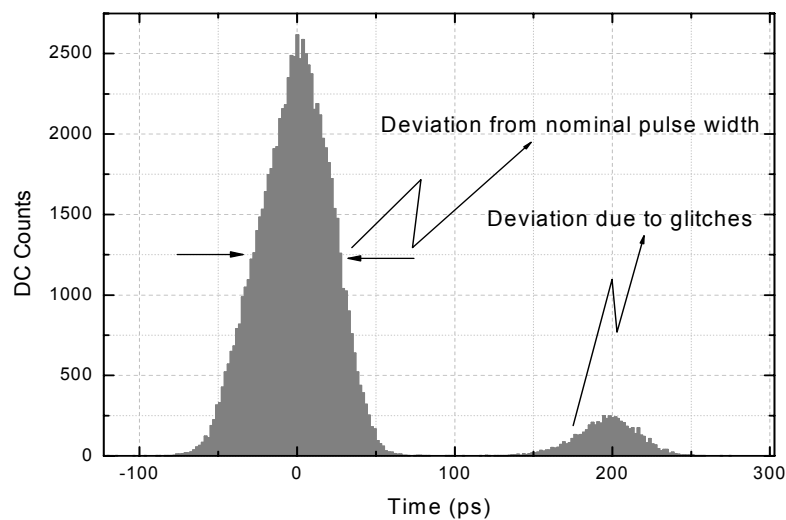


Figure 4.10 Jitter measurements. The standard deviation from the nominal pulse width is only 39 ps.

### **3. GENERATOR FOR MAGIC II RECEIVER BOARD TESTS**

#### **3.1 Requirements**

A much more challenging pulse generator was developed as requested by the MAGIC II receiver board designers of the IFAE group. The aim of this model was the test of these boards. As the overall bandwidth was increased with respect to the previous camera, faster devices were needed in order to test the limits of the signal transmission and acquisition.

A number of commercial pulse generators are presently available in the market. But as the pulse width is reduced, the difficulty of generating amplitudes of several volts increases. In addition, these generators are mainly intended to drive perfect resistive loads. The compact and cost effective commercial models are not well prepared to directly feed devices like LEDs or lasers, which exhibit noticeable impedance changes between their ON and OFF states. The issue of the generator sensitivity to load impedance changes is generally addressed by either inserting an attenuator or a broadband buffer amplifier between generator and load.

A custom-made generator is therefore of critical relevance in terms of cost and efficiency. The main specifications requested by IFAE Engineers were a PWHM of 1.3 ns, amplitude in excess of 4 V to cover all the dynamic range and low noise and jitter.

#### **3.2 Design and construction**

##### **I. Pulse generation stage**

Figure 4.11b shows an overall diagram of pulse generator. The first stage, as commented in Chapter 3, consists on a generator based on a Step Recovery Diode. The number of different channels to be tested in the MAGIC II Receiver Boards demanded the need for multiple generator outputs; finally a compromise between the number of outputs and the complexity of the design was achieved, and four channels were implemented. This requirement immediately led to the decision of using amplification and power division. In Section 4 a detailed description of the power dividers is done.

The RF attenuators are necessary to minimize pulse distortion and ringing, which mostly occur at the output of the pulser and the input of the amplifiers.

They also limit the amplitude levels at the amplifier inputs to avoid their saturation. An even number of amplifying stages preserves the polarity of the SRD pulser signals, since the best MMICs found for this application had a gain with a 180° phase shift, but the output needed for this work was positive.

The constitutive parts of the prototype (SRD pulser, power divider and amplifiers) were mounted in different boards and tested separately. The interconnections were made via SMA connectors and RG174 coaxial cables, and the RF paths were kept identical for all four channels. In order to accomplish this, it was necessary to design a power divider with a vertical input.

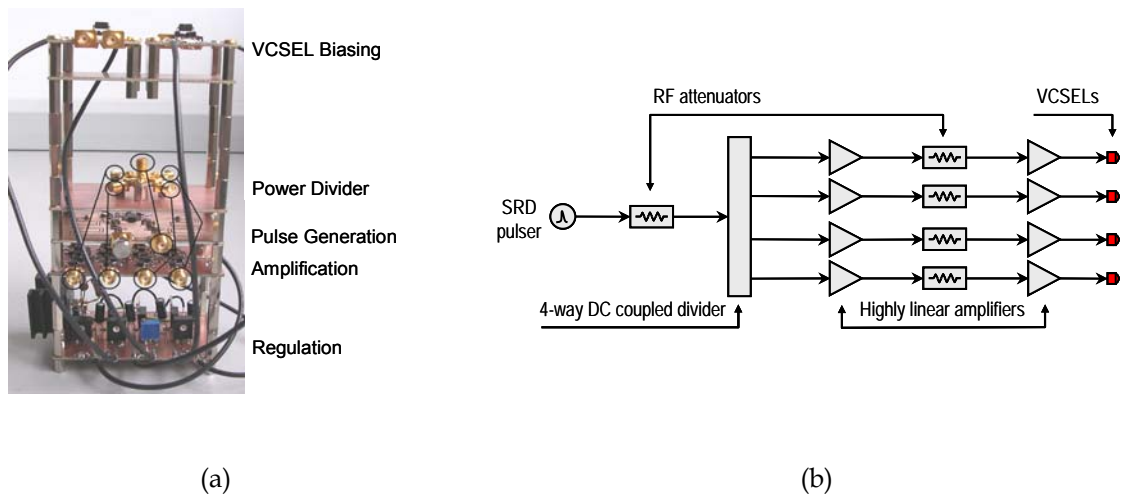


Figure 4.11 (a) Picture of the multichannel pulse generator. (b) Design concept of the device.

One of the main issues to address in the design of broadband power dividers is the minimization of the junction reactive parasitics, which are sources of mismatches and therefore pulse ringing. This minimization can efficiently be accomplished by minimizing the final size and maximizing the symmetry of the design. Figures 4.12a and b show the schematics and final layout of the designed 4-way power divider for the second pulse generator, respectively. In this case all the ports (input and outputs) are coupled to 50 Ω.

The input resistance  $R_0$  was mounted vertically inside a via hole opened in the board. This enables a compact design with all four outputs being perpendicular each other. The discrepancies in dB between the measured and theoretical (12.04 dB) insertion losses were less than 1% (the insertion loss of an N output power divider is given by (4.1)).

$$IL = 10 \log \left( \frac{1}{N^2} \right) \quad (4.1)$$

Figure 4.12c shows the measured output waveforms, which are fully free from any ringing. In this measurement, a reference gaussian pulse of 4 ns width was applied to the input using a commercial 240 MHz bandwidth waveform generator (model Tektronix AFG3252).

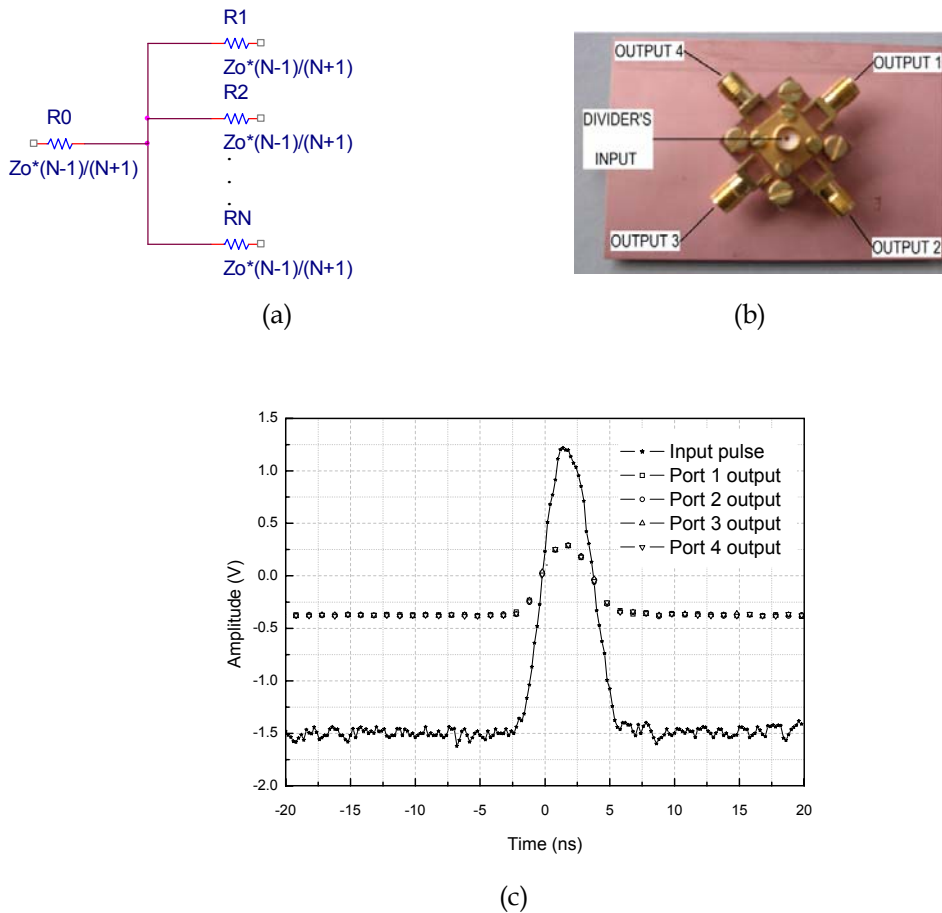


Figure 4.12 (a) Schematic, (b) Final layout and (c) waveforms of the power divider.  $N$  is the number of outputs. The input pulse was generated with a commercial  $50\ \Omega$  waveform synthesizer.

The minimization of the cabling length was achieved by mounting the boards in a vertical arrangement, just like the pixel electronics of the MAGIC I and II cameras. With this arrangement the prototype is reasonably compact and free from long printed transmission lines, which could distort the pulses and make the prototype less robust against interferences. In addition, the four pulses at each channel are nominally identical and reach simultaneously the VCSELs, without any noticeable delay among them.

Pulse generators relying on Step Recovery Diodes produce pulse amplitudes in excess of 4 V, as described in Chapter 3. As power dividers were needed to produce multiple synchronized outputs with a single generator, it is unavoidable the use of wideband, high dynamic range amplifiers to recover the initial amplitude. In Chapter 5 and 6 a detailed explanation of several amplifiers can be found. In this chapter only a brief description of the used MMIC is done.

## II. Amplification stage

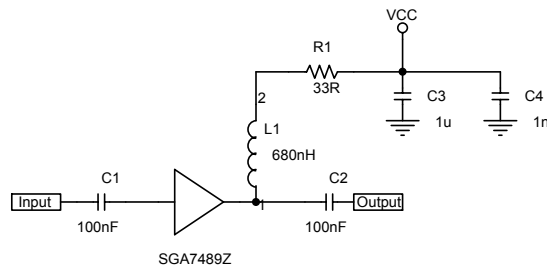
In the selection of the amplifier three parameters were of special relevance: noise figure, dynamic range and bandwidth. Due to the short length of the pulse, an amplifier with bandwidth from DC to at least 1 GHz was needed. The MMIC gain blocks basically consist of an inverting Darlington couple. This configuration yields to a 180° gain phase shift. Therefore, in order to have a positive output with a positive input two MMICs in cascade are needed. According to the Friis equation, the noise of the system is dominated by the input stage. The dynamic range is dominated by the output one. Several commercial amplifiers were studied in order to choose the one which fulfils the mentioned requirements.

The selected model, Sirenza 7489Z [6], is a low cost commercially available MMIC amplifier based on SiGe HBT technology, with 1 mm emitter Darlington configuration. This MMIC features 23 dB gain, 2.8 dB of noise figure and 1 dB compression point of 22.4 dBm at 850 MHz. The 3 dB bandwidth is 1 GHz. The MMIC was first mounted as a single stage amplifier on a FR4 substrate for test purposes. It was tested on the bias circuit detailed in Figure 4.13a. Figure 4.13b shows the measured values of the dynamic range in pulsed mode and the noise figure. The scattering and stability parameters are shown in Figure 4.13c [7].

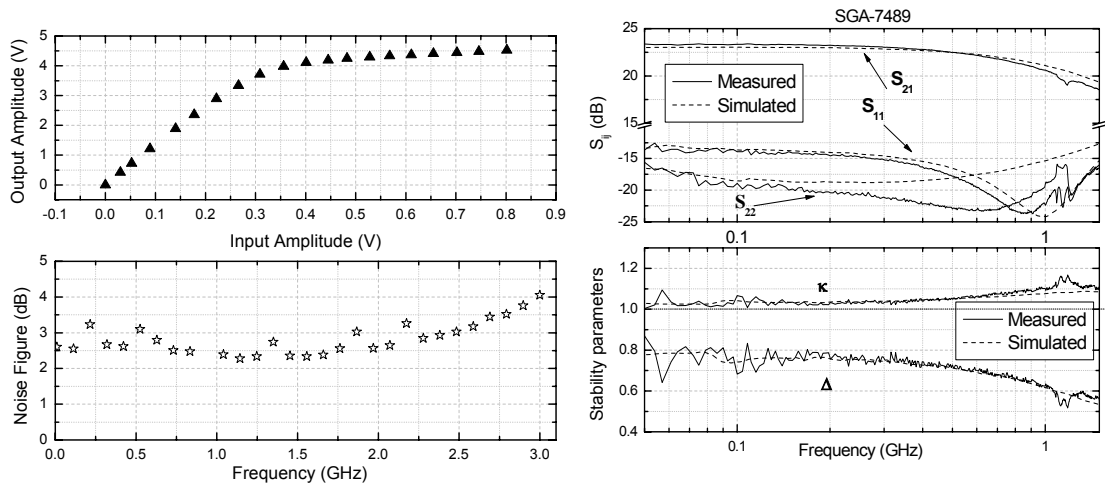
The dynamic range measurements were made with a sequence of 4 ns PWHM pulses of 1 MHz pulse repetition frequency. According to these measurements, the 22.4 dBm of 1 dB compression points yields to maximum saturation voltages of around 4.5 V. It is rather difficult to find in the market at the present moment RF MMIC amplifiers able to provide this range of linearity. The noise figure was measured with the noise measurement personality of the spectrum analyzer Agilent E4402B and the Agilent 346A calibrated noise source. Some spikes are shown in the noise figure curve, which are not attributed to the amplifier but to external interferences. Despite them the noise figure of the mounted amplifier is fairly close to the one claimed by the MMIC manufacturer.

The simulation of the S parameters includes all the bias network and blocking capacitor parasitics, and it was made with APLAC software. The S parameter datasheet of the 7489Z is provided by the manufacturer. The stability

factors show that the amplifier is unconditionally stable ( $\kappa > 1$  and  $|\Delta| < 1$ ) in the whole range of frequencies. On the other hand, the low values of  $S_{11}$  and  $S_{22}$  show an excellent match to 50  $\Omega$ . Finally, no significant resonances are observed in the gain factor ( $S_{21}$ ).



(a)



(b)

(c)

Figure 4.13 (a) Schematic of the test circuit. (b) Upper graph: dynamic range of Sirenza 7489Z for negative, 4ns wide pulses. Lower graph: noise figure of the 1 stage amplifier board. (c) Scattering parameters and stability.

Once the single stage was tested we proceeded with a two stage design. The corresponding schematic is shown in Figure 4.14a. The second stage includes a feedback resistor to avoid saturation. Although this reduces the overall gain of the amplifier block, the present design already achieves the highest pulse voltages that can be obtained without saturating the two MMIC gain blocks.



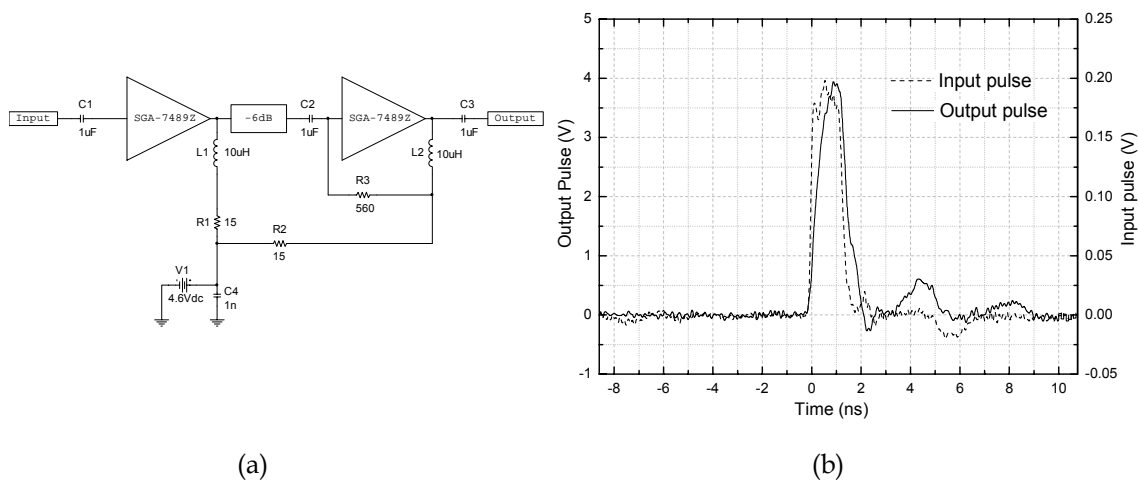


Figure 4.14 Schematic (a) and pulse shapes (b) of the two stage power amplifier used in each of the four output channels.

### III. Attenuators

The attenuator between stages is an integrated 6 dB pad supplied by Minicircuits [8]. An alternative design based on discrete resistors was also studied, as explained in next Section, but the low cost and high integration of Minicircuits devices turned out to be the most suitable solution. This pad prevents both saturation and distortion at the second stage, and avoids ringing between the different modules and stages.

Measurements on the prototype showed -20 dB of ringing level at the input (see dashed line of Figure 4.14b). This ringing level is excellent in comparison with those found in recently published pulsers [9][10].

### IV. VCSEL biasing

Figure 4.15a shows the bias network designed to drive the VCSELs with a stabilized DC current. The topology is inspired in an improved version of the classical Howland constant current source [11], which is nicely described by Rafiei-Naeini and McCann in [12], and was proposed by the Max Planck Institute for the MAGIC II camera. In our design we include one operational amplifier (OPAMP) to drive only two VCSELs, which are modelled by 50  $\Omega$  resistors. Therefore, we need two bias circuits. This approach has been followed in order to make use of low noise precision amplifiers, which are not able to drive the relatively large amount of current demanded by four lasers. The source labelled

as  $V_{control}$  enables the tuning of the VCSEL current. The topology is designed to provide a stable VCSEL current  $I_{VCSEL}$  given by

$$I_{VCSEL} = \frac{V_{CONTROL}}{2R_{BIAS}} \quad (4.2)$$

The OPAMP is an OP27 low noise precision amplifier featuring a low  $1/f$  noise corner with an input equivalent noise voltage of  $3.5 \text{ nV}/\sqrt{\text{Hz}}$  at  $10 \text{ Hz}$  [13]. The low frequency noise injected to the VCSELs is thus minimized. Although this amplifier nominally works with bipolar biasing, a proper operation with an unipolar one was verified for DC. The possible distortion in the AC signal amplification is not relevant for this current source design.

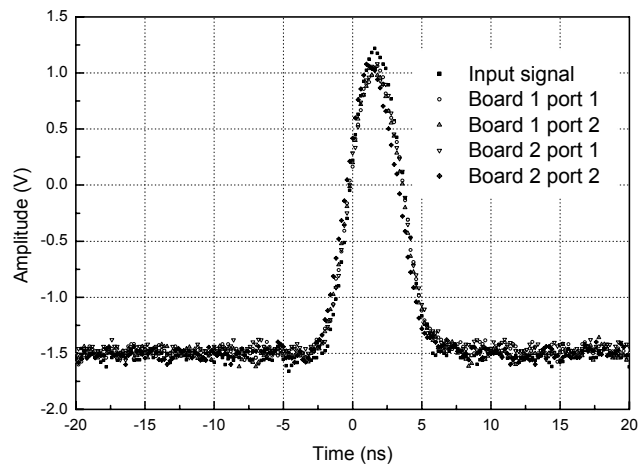
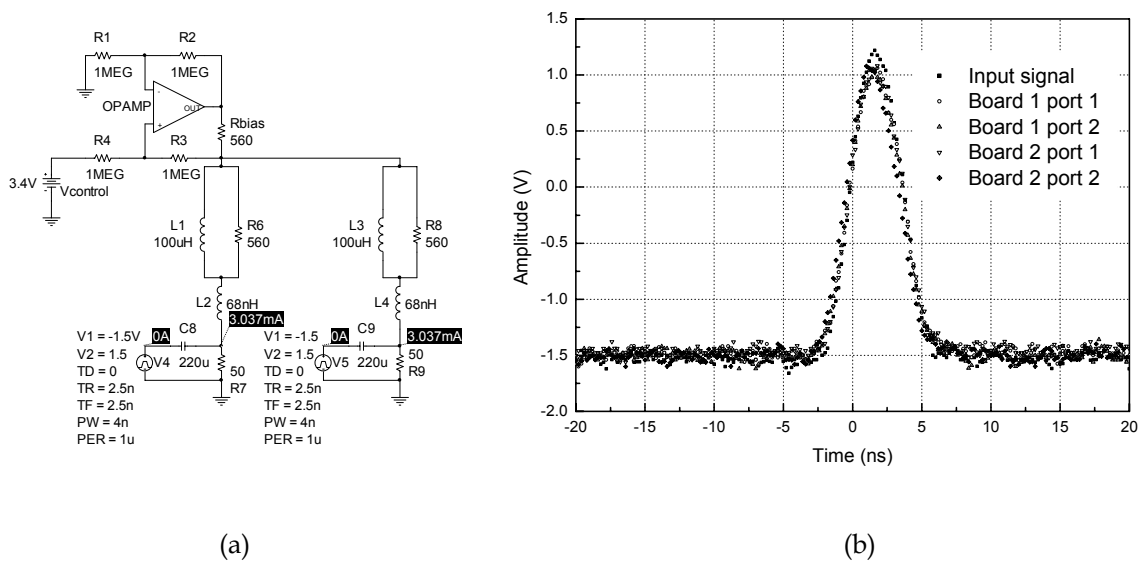


Figure 4.15 (a) Bias circuit unit for each of the two pairs of VCSELs used in the board. (b) Pulse integrity at VCSEL pins contacts.

In order to effectively block the pulse signal path to this bias circuit an inductive filtering implemented by  $L_1$ ,  $R_6$  and  $L_2$  is applied. One filter per channel is needed to prevent crosstalk between the DC paths of the lasers. Resistor  $R_6$  effectively reduces the resonant quality factor of  $L_1$ . This enables the use of fairly high inductances without pulse distortion due to resonant effects. Other filtering topologies were also tried (i.e. by using a capacitor between terminal 2 of  $L_2$  and ground) but the one shown here demonstrated the best behaviour in terms of pulse shape integrity. Figure 4.15b shows an example of the signals measured at the four VCSEL signal ports. As it can be seen, the signals are free from ringing.

## V. DC Regulation

The DC regulation design strategy paid special attention to the noise performance. Many voltage regulators are important sources of noise, including voltage spikes from switching circuits and high  $1/f$  noise from references which can exceed one microvolt per root-hertz. Three-terminal regulators use to generate hundreds of nV per root-hertz of white noise. Switching regulators and DC to DC converters may have switching products of the order of millivolts which cover an unfairly wide range of frequencies.

Different procedures have been suggested to reduce the noise of DC regulation circuits. For instance, a large-value inductor combined with a capacitor or a clean-up regulator inserted between the noisy regulator and load. Other alternatives have been suggested to remove the undesired noise without directly handling the supply's high current [14].

The regulation board features bias circuits for the pulse generator, amplification and VCSEL boards which have highly selective filters to avoid pulse distortion. On the other hand, the power consumption is not a critical issue for this application. Therefore the optimum choice for this case is a resistive three terminal regulation. The design proposed here makes use of four LM317 regulators to provide the four voltages needed: 10 V and 3.7 V for the VCSEL board, 4.6 V for the amplification board and finally 5.5 V for the pulse generator. All of them are fed by 12 V.

### 3.3 Results

Figure 4.16 shows the output pulses injected into the VCSEL inputs. The peak amplitude of 4 V is achieved at the four channels without noticeable delays among them. The pulse width is 1.3 ns. The secondary peaks of 0.5 and 0.25 V were generated at the amplifier output as shown before, and are identical at all the channels. Therefore, they can be helpful to calibrate the saturation of the receivers by direct comparison with the detected amplitude of the main peak, without the need for using variable pulse amplitudes.

A timing analysis has been made to the four outputs of the pulse generator. The measured jitter for the pulse width is only 6.32 ps, and the jitter for the pulse repetition frequency is 23.5 ns, as shown in Figure 4.17.

The pulse generator does not introduce significant noise to the system; the spectrum of the scope input was analyzed both with a matched load and with the pulse generator. There was no increase in the white noise, nor any new peak in the spectrum.

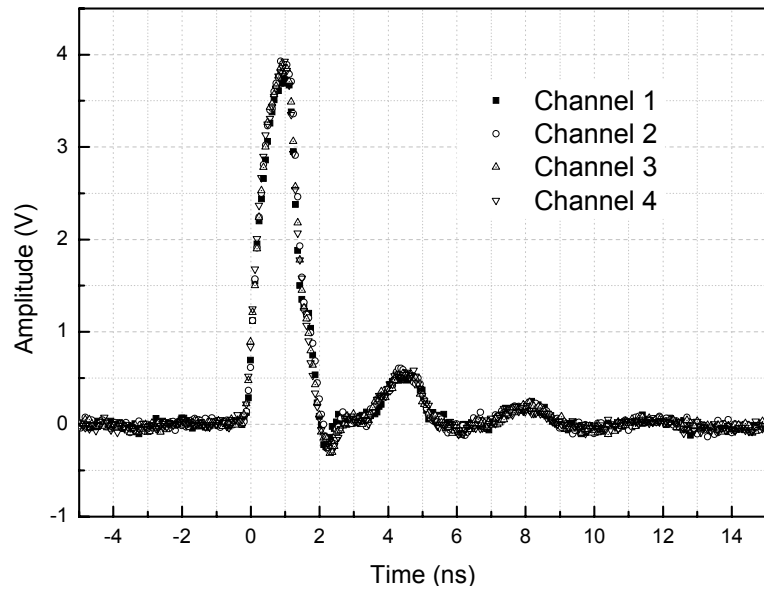


Figure 4.16 Measured pulses at the four different outputs.

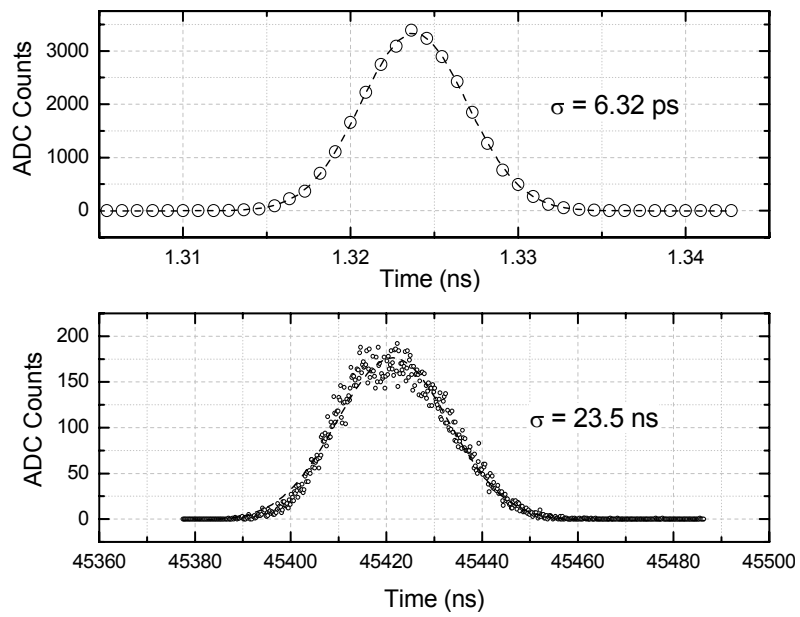


Figure 4.17 Top: pulse width histogram. Bottom: repetition frequency jitter.

## 4. REFERENCES

- 
- [1] F. Lucarelli, R. Bueno, J.M. Miranda, M. Asensio, M. V. Fonseca. *Banco de test para la caracterización de los píxeles del Telescopio MAGIC*. Proceedings of the XIX URSI, September 2004, Barcelona (Spain)
  - [2] *2009 LED Catalogue*, <http://www.nichia.com/product/led.html>.
  - [3] P.Antoranz, J.M.Miranda, J.L.Sebastián, M.Cámara, M.V.Fonseca, *High frequency modeling of GaN/SiC blue light emitting diodes*, J. Appl. Phys. 97, 096107 (2005)
  - [4] *PMT Handbook (Complete)*, HAMAMATSU.  
[http://sales.hamamatsu.com/assets/applications/ETD/pmt\\_handbook/pmt\\_handbook\\_complete.pdf](http://sales.hamamatsu.com/assets/applications/ETD/pmt_handbook/pmt_handbook_complete.pdf)
  - [5] A. Ostankov, D. Paneque, E. Lorenz, M. Martinez and R. Mirzoyan. *A study of the new hemispherical 6-dynodes PMT from electron tubes*. NIM A, VOL 442, Issues 1-3, 11 March 2000, Pages 117-123
  - [6] Sirenza 7489Z Datasheet, [www.sirenza.com](http://www.sirenza.com)
  - [7] David M. Pozar, *Microwave Engineering*, 2nd edition, John Wiley and Sons, (1998)
  - [8] Minicircuits LFCN-6000 LP Filters Datasheet, [www.minicircuits.com](http://www.minicircuits.com)
  - [9] Jeongwoo Han, Cam Nguyen, *A new Ultra-Wideband, Ultra-Short Monocycle Pulse Generator With reduced Ringing*, IEEE Microwave and Wireless Components Letters, June 2002, VOL. 12, No. 6
  - [10] Jeong-Woo Han, Meng Miao, Cam Nguyen, *Recent development of SRD and FET based sub-nanosecond pulse generators for ultra-wideband communications*, IEEE Topical Conference on Wireless Communication Technology, Oct. 2003. 15-17 pp 441-442
  - [11] S. Franco, *Design with Operational Amplifiers and Analog Integrated Circuits*, 2<sup>nd</sup> ed., New York, McGraw-Hill, 1998.
  - [12] Rafiei-Naeini, M., McCann, H. *Low-noise current excitation sub-system for medical EIT*, Physiol. Meas. 29 (2008) S173-S184
  - [13] Analog Devices. *OP27 Datasheet*, [www.analog.com](http://www.analog.com).
  - [14] *Finesse Voltage Regulator Noise!*, Wenzel Assoc.,  
<http://www.wenzel.com/documents/finesse.html>



# Chapter 5

## Pulse amplifiers

1. Introduction
2. Flow diagrams and gain definitions
  - 2.1. Flow diagram analysis
  - 2.2. Power gains
  - 2.3. Voltage gains
3. Pulse distortion and need for high bandwidths
4. Stability
5. Noise
  - 5.1. Definitions and statistical representation
  - 5.2. Monte Carlo simulation in the time domain
6. Dynamic range / linearity
7. Mismatches and ringing
8. Side effects of dissipative pads
  - 8.1. Stability improvements
  - 8.2. Noise increase
9. Software tools
  - 9.1. MATLAB scripts
  - 9.2. Spice integration of the models
10. References

## 1. INTRODUCTION

MAGIC II telescope requires amplifiers with demanding specifications in both the camera and the counting house receivers. Nanosecond pulses have a wide spectrum, which varies from DC to frequencies of several hundreds of MHz. Distortion of these pulses during their processing is therefore relatively easy, especially when amplification is made. The needs for detecting low level signals also require an amplifier with a reasonably low noise figure. In addition, the device must also be stable for all the frequencies and impedances involved in nominal operation, in order to prevent self-oscillations which could easily produce errors in both the calibration and measurement processes. The ability to amplify both small and relatively large pulses is also required, so special care must be taken in the dynamic range figures.

Finally practical considerations force to pay attention to other specifications such as the reliability, and the sensitivity to both biasing voltage and temperature drifts. Furthermore, since the amplification must be made pixel by pixel the layout must occupy a small area and consume a reasonably low power, and the prototypes must be simple enough to be affordable and with repeatable characteristics when fabricated in large quantities.

The experience gained by the MAGIC collaboration during the fabrication of the first telescope amplifiers was not too helpful for the design of the amplifiers for the second telescope. MAGIC I makes use of transistor-based amplifiers with bandwidths of 300 MHz, but it soon became clear that the bandwidth of the second telescope should be increased considerably.

In the 2006 meeting of the collaboration in Aschau some researchers defended to use the same design of MAGIC I amplifiers and simply change their transistors by others which were faster. But at the Department of Applied Physics III a different approach was defended and finally accepted for the design of MAGIC II amplifiers. This approach is based on using integrated SiGe Darlington monolithic gain blocks. These MMICs were developed and optimized by different companies which already were well established in the market of radar and mobile communications. Their figures of merit in terms of size, repeatability, power consumption, noise and dynamic range were therefore difficult to beat.

In this chapter, a brief overview of the fundamental concepts related to high frequency amplifiers is first given, and then the tools developed for the design and analysis of these circuits are described. Next chapter will deal with the measurements of implemented prototypes.



## 2. FLOW DIAGRAMS AND GAIN DEFINITIONS

### 2.1 Flow Diagram analysis

Signal flow diagrams are a powerful tool in the analysis of multi-port high frequency devices and are well known by microwave engineers [1]. These diagrams facilitate the unification of the low frequency formalism, based on voltages and currents, with the high frequency one, based on the S parameters. This unification is particularly important in pulse amplifiers, where both high frequency and low frequency components are present in the signal.

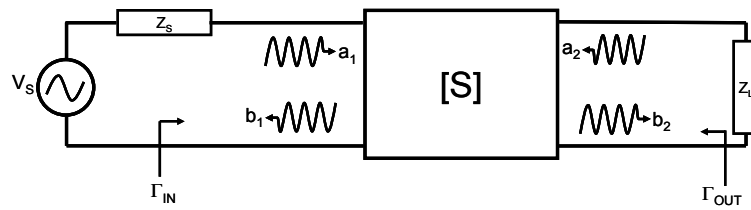
For the purposes of this thesis, the flow diagrams are used to calculate the voltage gain in terms of the S parameters, which can be measured directly. This voltage gain can then be applied to estimate the peak pulse gain, which can be measured in the time domain with the aid of a wide band oscilloscope.

There are two alternative methods to analyze high frequency circuits based on flow diagrams. The simplest one, called **decomposition**, takes advantage of the clear resemblance of this representation with the elemental circuit theory [1]. The second method, called **Mason's Rule** [2] is a more powerful technique that can also be applied to the analysis of feedback control systems. Although less intuitive than decomposition, it can be much more easily implemented in CAD systems.

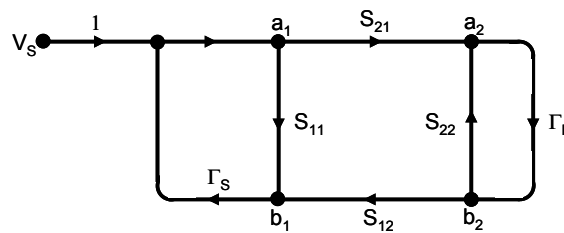
Flow diagram analysis is regularly used to calculate the ratio between either two voltages or currents at the nodes or branches of a high frequency circuit. The main interests of this technique lies in the fact that it provides direct information on reflection losses at any circuit port. It also facilitates the calculation of voltage or current gains by giving analytical expressions for them in terms of magnitudes which can be measured at high frequencies with vectorial network analyzers, such as the S parameters and the reflection coefficients.

Figure 5.1 shows the general representation of a pulse amplifier (a) and the flow diagram used for the analysis (b). Arbitrary source and load impedances are included. Each node is defined by a voltage wave, whereas each branch is defined by a quotient of waves. Each port of the network is represented by two waves: the incoming one is represented by the letter  $a$ , whereas the reflected one is represented by  $b$ .

A branch is a directed path between an  $a$ -node and a  $b$ -node, representing the signal flow from node  $b$  to node  $a$ . Every branch has an associated S parameter or reflection coefficient. Once a network is represented in signal flow form, it is relatively easy to solve for the ratio of any combination of wave amplitudes.



(a)



(b)

Figure 5.1 (a) Scheme of a pulse amplifier with arbitrary load and source impedances. (b) Flow diagram.

## 2.2 Power gains

Different types of power gain are defined in high frequency network theory [3]. This fact uses to be the source of confusions. The **transducer power gain** is defined as the ratio of the power delivered to the load to the power available from the source. It depends on not only the scattering matrix of the amplifier, but also the load and source impedances.

For a full characterization of a two port network, the transducer gain gives more information than any other one. It can be derived from the flow diagram theory described in the previous section,

$$G_T = \frac{|S_{21}|^2 (1 - |\Gamma_L|^2)(1 - |\Gamma_S|^2)}{|(1 - S_{22}\Gamma_L)(1 - S_{11}\Gamma_S) - S_{12}S_{21}\Gamma_L\Gamma_S|^2} \quad (5.1)$$

Where

$$\Gamma_L = \frac{Z_L - Z_0}{Z_L + Z_0} \quad (5.2)$$

$$\Gamma_S = \frac{Z_S - Z_0}{Z_L + Z_0} \quad (5.3)$$

Being  $Z_0$  the reference impedance of 50  $\Omega$ . For the particular case of conjugate matching at the amplifier output the transducer gain becomes the **available gain**, defined as the ratio of the power available from the two-port network to the power available from the source. The available gain can be expressed as:

$$G_A = \frac{|S_{21}|^2 (1 - |\Gamma_S|^2)}{|1 - S_{11}\Gamma_S|^2 (1 - |\Gamma_{OUT}|^2)} \quad (5.4a)$$

Where  $\Gamma_{OUT}$  is the reflection coefficient seen at the amplifier output, as shown in Figure 5.1a. It depends only on the S parameters and the source impedance, and it can be calculated from the flow diagrams:

$$\Gamma_{OUT} = S_{22} + \frac{S_{21}S_{12}\Gamma_S}{1 - S_{11}\Gamma_S} \quad (5.4b)$$

Similarly, the so called operating power gain or simply the **power gain** is defined as the ratio of the power dissipated in the load to the power delivered to the input of the amplifier.

The power gain depends only on the S parameters and the load impedance, and equals to the transducer gain when input conjugate matching conditions exist. It must be pointed out that no reflection (i.e. null reflection coefficient) does not necessarily imply maximum transfer of power (i.e. complex conjugate matching). However, this is usually the case in coaxial transmission line systems since the characteristic impedance (50  $\Omega$ ) uses to be real. The power gain is given by

$$G_P = \frac{|S_{21}|^2 (1 - |\Gamma_L|^2)}{|1 - S_{22}\Gamma_L|^2 (1 - |\Gamma_{IN}|^2)} \quad (5.5a)$$

Where

$$\Gamma_{IN} = S_{11} + \frac{S_{21}S_{12}\Gamma_L}{1 - S_{22}\Gamma_L} \quad (5.5b)$$

### 2.3 Voltage gains

The operating and transducer voltage gains can be defined in an analogous manner. They can be obtained from the flow diagram of Figure 5.1 in a straightforward way. The **operating voltage gain** is, by definition, a quotient of total voltages. These voltages are obtained by adding the incident and reflected voltage waves at both input and output ports. Therefore,

$$G_v = \frac{a_2 + b_2}{a_1 + b_1} \quad (5.6)$$

Or in a similar way,

$$G_V = \frac{a_2/V_s + b_2/V_s}{a_1/V_s + b_1/V_s} \quad (5.7)$$

Mason rules can then be used to estimate independently each quotient, which yields to

$$G_V = \frac{S_{21}(1 + \Gamma_L)}{(1 - S_{22}\Gamma_L)(1 + S_{11}) + S_{21}S_{12}\Gamma_L} \quad (5.8)$$

If the source impedance is also considered, then the **voltage transducer gain** can be derived. In this case

$$G_{VT} = \frac{a_2 + b_2}{V_s} \quad (5.9)$$

Which yields

$$G_{VT} = \frac{S_{21}(1 + \Gamma_L)}{1 - (S_{11}\Gamma_s + S_{22}\Gamma_L + S_{21}\Gamma_L\Gamma_s S_{12}) + S_{11}S_{22}\Gamma_L\Gamma_s} \quad (5.10)$$

The equations (5-9) and (5.10) were the ones used in the software described in Section 9. The voltage gains enable the estimation of the peak pulse gain, but in order to do so it is necessary to work in the time domain via the standard linear system theory and the inverse Fourier transform. These equations can therefore be used to estimate the influence of mismatches on the peak pulse voltages.

### 3. PULSE DISTORTION AND NEED FOR HIGH BANDWIDTHS

The optimum bandwidth of MAGIC telescopes has been the subject of intense debate within the collaboration, and this debate has recently emerged again with the design study phase of the Čerenkov Telescope Array (CTA) observatory. The development of high frequency electronics demands for CAD tools and instrumentation which are significantly more complex and costly, and for an expertise which is difficult to find.

Figure 5.2 shows a simple simulation of a square pulse characteristic frequencies by means of the Fast Fourier transform (a) and the distortion experienced by a pulse when passing through an unity gain amplifier with different 3 dB bandwidths (b). As a rule of thumb it can be assumed that for an amplifier of bandwidth  $B$  the resulting pulse rise time will be around  $0.35/B$ .

It must be pointed out that the limitations on the amplifier bandwidth do not affect only to the pulse shape integrity but also to the pulse delay. According to the circuit theory, the transit time through a two port network becomes higher when the bandwidth of the network becomes narrower and the gain drop more pronounced.

When dealing with only one amplifier the delay due to transit time effects can be considered repeatable and therefore susceptible to be corrected by software. However, in real world operation a number of pixels are working simultaneously, and the information on the pulse arrival times is significant. In fact, the image projected to the telescope camera is used to discriminate the desired signals from the undesired ones, as it was explained in Chapter 2.

A good precision in the measurement of the signal arrival times allows to take maximum benefit from the gamma-hadron rejection by means of the timing characteristics. Therefore, there is a strong need of well defined pulse arrival times, and the timing equalization between pixels becomes considerably more complicated when the transmission bandwidths are reduced.

It must be pointed out that the use of subsystems with a bandwidth of 1 GHz does not result into a full system of 1 GHz when cascading all of them. If the system has  $N$  components the 3-dB bandwidth decreases as  $N$  increases. This decrease is strongly dependent on the frequency dependence of each subsystem gain. For the simple case of  $N$  identical subsystems with bandwidth  $B$  and gain given by  $G_0B/(s+B)$  the total bandwidth of the system is  $B\sqrt{2^{1/N}-1}$ . Three stages would be enough, in this case, to reduce the bandwidth in around 50%.

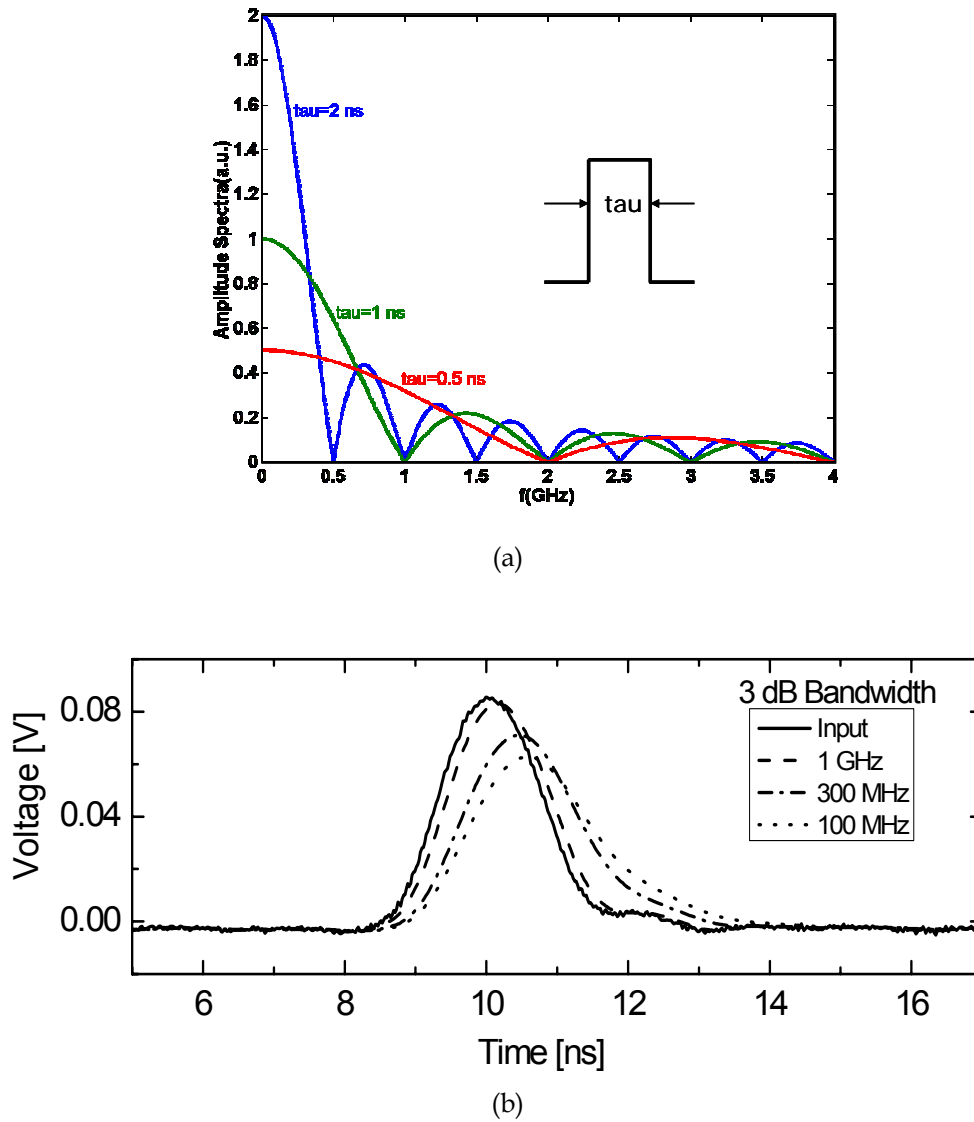


Figure 5.2 (a) Spectrum of a rectangular pulse for different pulse widths. (b) Effect of an amplifier on the distortion of the output pulse for 3 dB bandwidths of 1 GHz, 300 MHz and 100 MHz. The amplitudes were normalized to the input pulse to better appreciate the amplifier distortion.

## 4. STABILITY

The stability of a high frequency amplifier is a well known critical issue. An amplifier is stable when both the input and output reflection coefficients are passive, i.e. they satisfy:

$$\begin{aligned} |\Gamma_{IN}| &< 1 \\ |\Gamma_{OUT}| &< 1 \end{aligned} \quad (5.11)$$

Several methods are known to determine whether an amplifier is stable or not. The most popular one is based on the analysis of the **stability circles** [4]. These circles are defined as the loci in the  $\Gamma_L$  (or  $\Gamma_S$ ) plane for which  $|\Gamma_{IN}|=1$  (or  $|\Gamma_{OUT}|=1$ ). The stability circles then define the boundaries between stable and potentially unstable regions of  $\Gamma_S$  and  $\Gamma_L$ . Any impedance inside these circles will derive into amplifier oscillations.

From these conditions for the reflection coefficients, it is possible to derive the equations for the load (L) and source (S) stability circles:

$$C_L = \frac{(S_{22} - \Delta S_{11}^*)^*}{|S_{22}|^2 - |\Delta|^2} \quad (5.12a)$$

$$R_L = \left| \frac{S_{12} S_{21}}{|S_{22}|^2 - |\Delta|^2} \right| \quad (5.12b)$$

$$C_S = \frac{(S_{11} - \Delta S_{22}^*)^*}{|S_{11}|^2 - |\Delta|^2} \quad (5.12c)$$

$$R_S = \left| \frac{S_{12} S_{21}}{|S_{11}|^2 - |\Delta|^2} \right| \quad (5.12d)$$

Where

$$\Delta = S_{11} S_{22} - S_{12} S_{21} \quad (5.13)$$

is the determinant of the scattering matrix.

It must be pointed out that all the scattering parameters depend on the frequency, and therefore the stability will also depend on it. It is necessary to study the stability of the amplifier as a function of the frequency.

It is also possible to study the stability of the amplifier without tracing the circles, by means of the **stability coefficients,  $\kappa$  and  $\Delta$**  [5], [6]. For the amplifier to be unconditionally stable, the following conditions must be satisfied:

$$\left. \begin{array}{l} \kappa > 1 \\ |\Delta| < 1 \end{array} \right\} \quad (5.14a)$$

where  $|\Delta|$  is the scattering matrix determinant expressed in (5.13) and  $\kappa$  is:

$$\kappa = \frac{1 - |S_{11}|^2 - |S_{22}|^2 + |\Delta|^2}{2|S_{12}S_{21}|} \quad (5.14b)$$

Work reported in 1992 by Edwards and Shynski [7] detailed a single stability parameter,  $u$ , to characterize amplifier stability and prove that the condition  $U > 1$  is necessary and sufficient for unconditional amplifier stability. This parameter is given by

$$U = \frac{1 - |S_{11}|^2}{|S_{22} - S_{11}^* \Delta| + |S_{21}S_{12}|} \quad (5.15)$$

Unconditional stability is particularly important when the amplifiers are connected to sources or loads which exhibit strong variations of the impedance during nominal operation. This is in fact the case for both the camera and the receiver amplifiers.

The PMTs have an impedance that depends on the amount of incident light, and therefore in normal operating conditions important impedance changes should be expected. In addition the VCSELs used in the optical transmission have different impedances for the ON and OFF states, a fact that becomes important when detecting large pulses, which can modify the device bias point. The same argument can be applied to the receiver board solid state photodetectors.

Furthermore, conditionally stable amplifiers use to exhibit large voltage standing wave ratios when the impedances are close to the unstable areas. Large reflections in pulse processing can be the origin of ringing. This point is addressed in Section 7 of this chapter.



## 5. NOISE

### 5.1 Definitions and statistical representation

The **noise factor**  $F$  of any two port network is defined as [8], [9]

$$F = \frac{S_i/N_i}{S_o/N_o} = \frac{S_i/N_i}{GS_i/(N_a + GN_i)} = \frac{N_a + GN_i}{GN_i} \quad (5.16)$$

where  $S_i/N_i$ ,  $S_o/N_o$  are the input and output signal to noise ratios, respectively,  $G$  is the network available power gain, and the input noise power is calculated by assuming that the noise is thermal at the reference temperature of 290 K.  $F$  is called **noise figure** ( $NF$ ) when expressed in dB.

Usual values of noise figures for narrow band low noise amplifiers with center frequencies in the range of 1 GHz are between 0.5 and 1 dB. However, in pulse amplifiers with 1 GHz bandwidth this factor can hardly be less than 2.5 dB, even if they are not DC coupled. This is due to the fact that the main noise contribution from a high frequency amplifier is thermal and therefore its spectrum is white [10], [11].

DC coupled amplifiers could give considerably large values of the noise figure due to non-thermal contributions which have  $1/f^\alpha$  spectrum, with  $\alpha$  close to unity. In this case values of 15 dB are not uncommon and are considered by manufacturers as low noise figures. The noise behaviour of the amplifier use to be specified in this case by an input equivalent noise voltage density  $v_{amp}$ , generally expressed in units of  $nV/\sqrt{Hz}$ . This parameter is related to the noise figure through the following equation,

$$F = 1 + \frac{v_{amp}^2}{v_{Z_0}^2} = 1 + \frac{v_{amp}^2}{kT_0Z_0} \quad (5.17)$$

where  $v_{Z_0}$  is the **available** (not generated) **noise voltage density** corresponding to the characteristic impedance at the reference temperature of  $T_0=290$  K, which for a  $50 \Omega$  resistor is  $0.45 \text{ nV}/\sqrt{Hz}$ .

Thermal noise is of gaussian nature. The **normalized standard deviation of the probability density function of the voltage noise** generated by an amplifier is given by

$$\sigma = \sqrt{\frac{kT_eBG}{2}} \quad (5.18)$$

Where the equivalent noise temperature  $T_e$  represents the temperature at the input of the network that would produce an available noise power equivalent to the one generated by the amplifier,  $T_e = T_o(F - 1)$ .

## 5.2 Monte Carlo simulation in the time domain

A Monte Carlo based simulation has been performed in order to evaluate, in the time domain, the influence of the amplifier noise on the sensitivity in pulse detection. This simulation builds up a time domain representation of the amplifier output pulse polluted with noise. Noise contributions come from both the input signal (if specified) and the amplifier noise. The key input data for the simulation are the noise factor and the scattering parameters of the amplifier. These data are usually provided by the manufacturers of the active devices [12] [13], or can be measured in a laboratory with a microwave noise meter and a vectorial network analyzer.

The simulation is based on the hypothesis that the dominant noise source is additive, white and gaussian, as it is in the case of thermal noise. The noise voltages can be generated by a gaussian random number estimator with a normalized  $\sigma$  given by the Equation 5.18. The waveforms can be then constructed by estimating the noiseless output pulse in the time domain with standard linear system theory and the inverse Fourier transform of the transducer voltage gain estimated in Section 2.3. The time domain noise voltages estimated by the random number generators are then added to the noiseless pulse.

As can be seen in (5.18), the three parameters that contribute to increase the amplifier output noise are temperature, bandwidth and noise figure. The influence of the bandwidth on the sensitivity has been investigated by applying filters to the amplifier transducer gain, whereas the influence of the noise factor was studied by changing the corresponding  $\sigma$  [14].

Figure 5.3 illustrates the dependence of the amplifier output pulse noise with the bandwidth. An ideal filter with the specified bandwidth has been used in the simulations. High bandwidth increases the system noise, while low bandwidth can distort the pulse shape. In the simulations, a NF of 3 dB has been used for the amplifier and the scattering matrix corresponds to a BGA616 Gain Block MMIC.

Finally, Figure 5.4 shows the dependence of the output pulse noise with the NF of the amplifier. This factor is assumed to be variable while the scattering parameters are kept constant. The bandwidth used in the simulations is 3 GHz. In all the simulations, noiseless input pulses have intentionally been used, in order to better visualize the contributions of the amplifier noise.

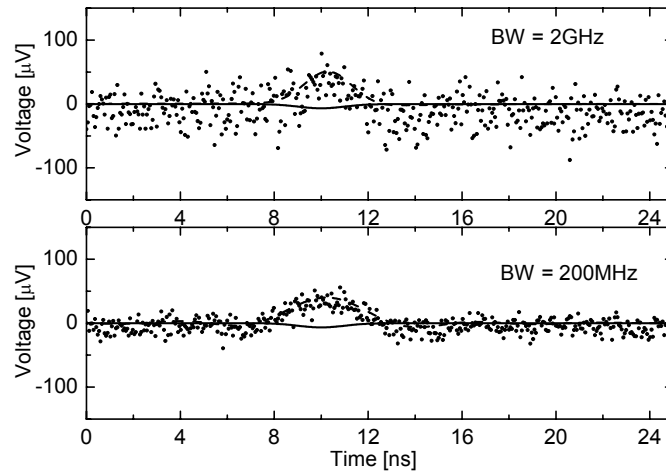


Figure 5.3 Dependence of the pulse noise with the bandwidth. *Straight line*: input signal. *Dashed line*: ideal output signal for a noiseless amplifier. *Circles*: simulated output for a noisy amplifier (BGA616), for a given bandwidth.

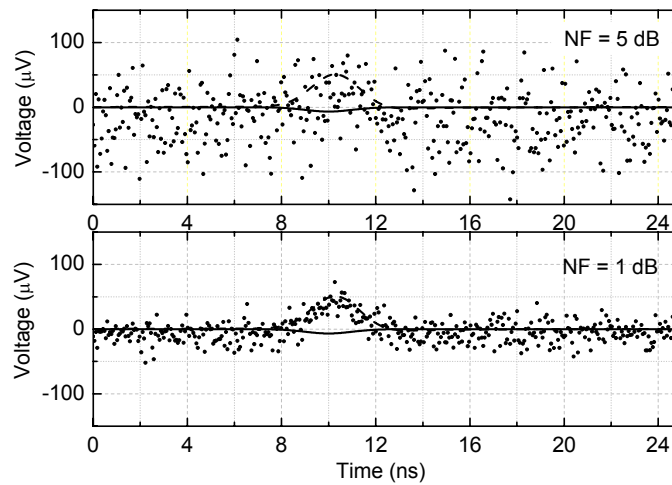


Figure 5.4 Dependence of the pulse noise with amplifier's noise figure. *Straight line*: input signal. *Dashed line*: ideal output signal for a noiseless amplifier. *Circles*: simulated output for a noisy amplifier (BGA616) with a given NF.

## 6. DYNAMIC RANGE/LINEARITY

Figure 5.5 shows the typical performance of a generic amplifier in terms of its dynamic range. For low input signals, the sensitivity is determined by the intrinsic noise of the amplifier. If the pulse to be amplified is below this 'noise floor', it will not be detectable. This is the case of the photomultipliers of the MAGIC telescope camera. Their sensitivity is so high that they can even resolve single photons. In this case very weak currents are obtained at the output. In next chapter further information about dynamic range and linearity of tested amplifiers is shown.

The maximum pulse that the amplifier is capable to process without distortion is generally limited by the end of the linear region, when the device enters into saturation. In case that the amplification curve is perfectly characterized, it is possible to correct the saturation effect by software and extend the dynamic range of the amplifier.

In most cases the end of the linear region is determined by the 1 dB compression point. However, it must be pointed out that in pulsed mode operation it is possible to have an extended useful linearity range which lies far beyond the nominal 1 dB compression point. With the prototypes designed with this thesis it was possible to amplify without noticeable distortion ns range pulses with MHz repetition frequencies up to amplitudes of 4 V, using gain blocks with a nominal 1 dB compression point referred to the output of 22 dBm at 1 GHz.

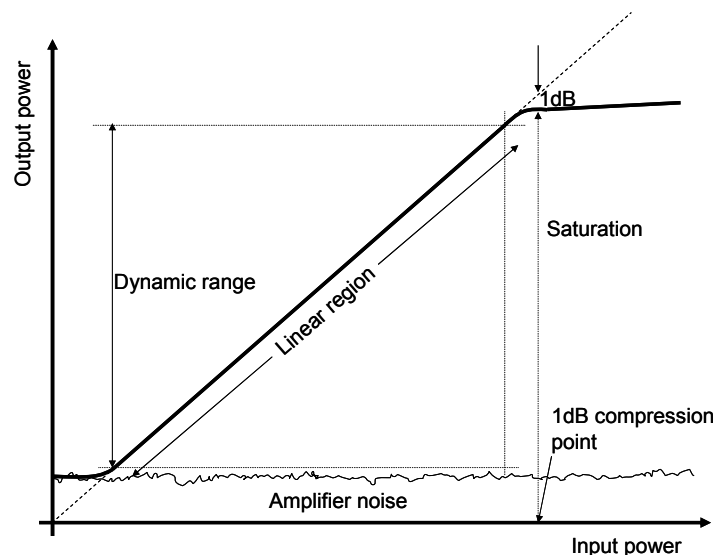


Figure 5.5 Typical performance of an amplifier. Dynamic range, saturation and 1 dB compression point referred to the input are shown.

## 7. MISMATCHES AND RINGING

Not only insufficient bandwidth can cause distortion. Mismatches between the amplifier ports and either the source or load are of special relevance. They are responsible for the generation of phantom secondary pulses, pulse shape distortion and signal loss. In this section, a simulation based on the scattering parameter analysis, which is able to accurately predict the time domain pulse shape coming out the amplifier is presented.

The influence of mismatches between the source and the amplifier input has been analyzed. Figure 5.6 illustrates an example where these effects can be observed: the mismatch was simulated by means of a standard pulse amplifier which feeds a mismatched RC load ( $|\Gamma_L|=0.8$ ). Similar  $\Gamma$  are usual in biased PMTs under dark conditions.

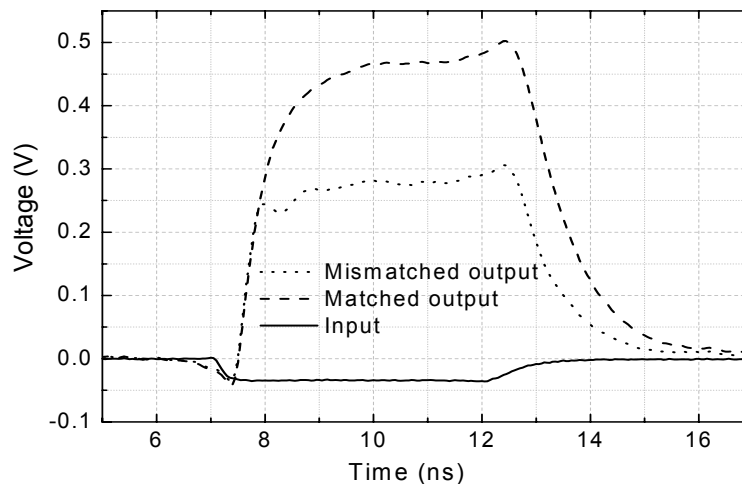


Figure 5.6 Effect of the source mismatch on the amplifier output signal.

Secondary (echo) pulses are also obtained due to mismatches. This problem is commonly addressed by following two different approaches:

1) Use of an amplifier where the input reflection coefficient is low. This needs to be done at the expense of noise figure increase, since minimum noise and optimum broadband coupling cannot be obtained simultaneously [3].

2) **Use of a dissipative pad between an amplifier with moderate reflection losses and the source.** It can be implemented with a T resistive network or with an integrated SMD attenuator.

The second option is easier for the applications considered in this thesis. With the pad we relax the demands for low  $S_{11}$  in the amplifier design and there is no loss in bandwidth. In addition, the amplitude of pulse echoes is attenuated

and the stability is improved. However, a price must be paid in terms of sensitivity.

A dissipative pad with an attenuation factor  $A$  reduces the voltage standing wave ratio (VSWR) in a fairly broad band of frequencies [15]. As a result, the ratio true-pulse-peak-voltage/secondary-pulse-peak-voltage increases by a factor of  $A^{1/2}$ . The final VSWR (VSWR') is related to the original one (VSWR) by

$$VSWR' = \frac{VSWR(A+1) + A - 1}{VSWR(A-1) + A + 1} \quad (5.22)$$

Figure 5.7 shows a simulation of the amplifier output pulse on the attenuation factor of the dissipative pad. Due to mismatches between source (a photomultiplier) and amplifier, a secondary pulse is produced. The pad tends to attenuate this echoed pulse. The bandwidth considered for the simulation is 3 GHz, and the amplifier noise figure is 3 dB.

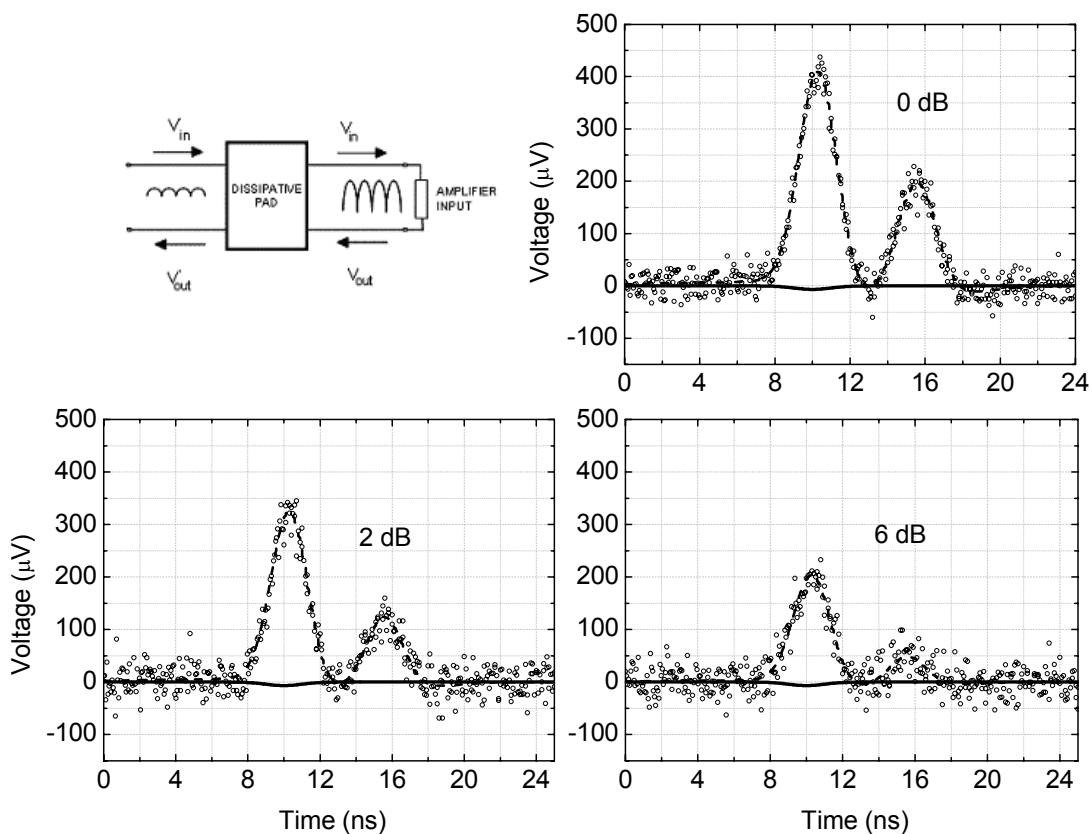


Figure 5.7 Effect of an attenuator pad between the mismatched source and amplifier.

## 8. SIDE EFFECTS OF DISSIPATIVE PADS

### 8.1 Stability improvements

The insertion of a dissipative pad between the amplifier and either its source or its load can also help to prevent oscillations. This is due to the fact that the pad tends to make the impedances seen by the amplifier closer to a  $50\ \Omega$  resistor. These impedances used to be located in the stability zone of the amplifier. This effect is illustrated in Figure 5.8, which shows an example of the stability parameters measured for a monolithic pulse amplifier. Without any dissipative pad, this device is potentially unstable within the operating frequency band, since  $\kappa < 1$  below 100 MHz and above 1.5 GHz. When the pad is added, the system becomes unconditionally stable at all the frequencies.

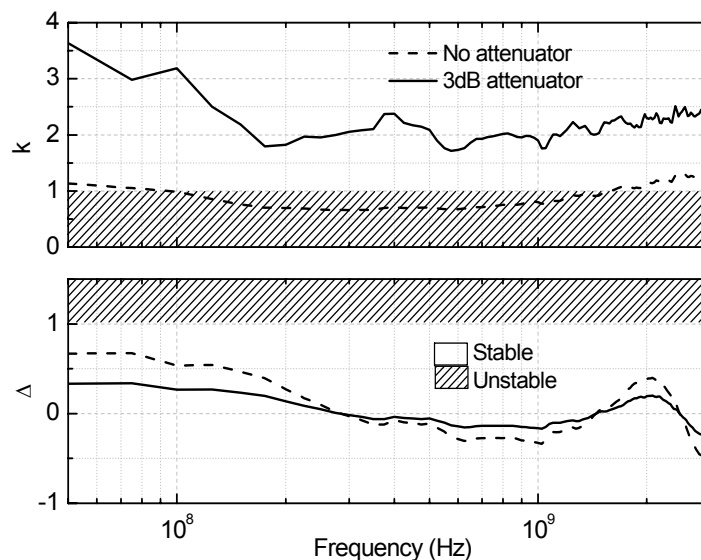


Figure 5.8 Stability of a MMIC amplifier (MSA0886) mounted on coplanar transmission lines and with SMA terminals. The  $\kappa$  parameter reveals that the amplifier is unstable without the pad. A 3 dB attenuator makes it unconditionally stable.

### 8.2 Noise increase due to dissipative pads

The equivalent temperature  $T_{e,pad}$  of a dissipative pad with attenuation factor  $A$  is

$$T_{e,pad} = (A - 1)T \quad (5.23)$$

where  $T$  is the physical temperature of the pad. If this pad is connected to an amplifier input with gain  $G$  and equivalent temperature  $T_{e,amp}$  the overall equivalent noise temperature is given by the Friis equation,

$$T_{e,total} = T_{e,pad} + AT_{e,amp} \quad (5.24)$$

The new normalized standard deviation of the probability density function of the voltage noise generated by the amplifier and the pad is therefore

$$\sigma' = \sqrt{\frac{kB[T(A-1) + AT_{e,amp}]}{2A}} \quad (5.25)$$

Figure 5.9 shows an example of the dependence of both pulse and noise amplitude with the variation of the attenuation  $A$ . It is noticeable that the increment of  $\sigma'$  with  $A$  is weak for practical purposes. The noise figure for the simulation was 3 dB, as specified by the manufacturer. The bandwidth was chosen intentionally as 3 GHz in order to test an almost worst-case situation for the pad in a ns pulse detection scenario.

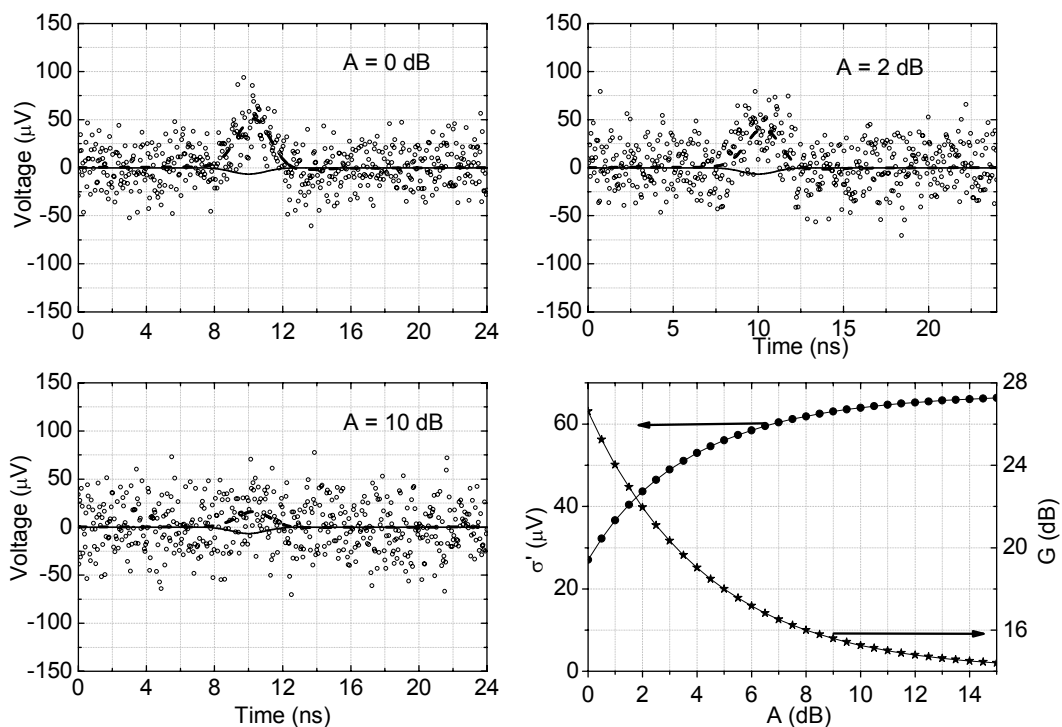


Figure 5.9 Dependence of the BGA616 amplifier output pulse on the pad attenuation. The lower graph on the right shows the dependence of  $\sigma'$  and overall gain on the attenuation factor.



## 9. SOFTWARE TOOLS

### 9.1 MATLAB scripts

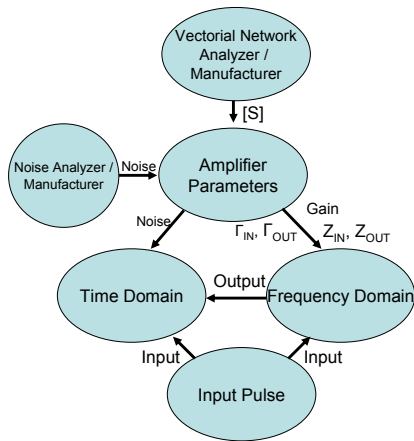
Several MATLAB based simulation scripts have been developed to simulate the behaviour of an amplifier in the time domain for a given input signal. These tools have been divided in two stages:

1. **Analysis:** the analytic part of the software provides information about the frequency domain characteristics of the amplifier. The program makes use of the amplifier and source parameters. With a vectorial network analyzer, the scattering matrix of the amplifier and the reflection coefficient of the source are measured in the frequency domain. Most of the manufacturers provide these values within the device datasheet. From these parameters, it is straightforward to determine characteristics as input and output impedances or power and voltage gains. The analytical expressions for these gains are obtained by using the Mason's Rule and signal flow diagram theory described in Section 2. It is also possible to determine the stability of the amplifier applying the  $\kappa$ - $\Delta$  analysis.
2. **Simulation:** the program is also designed to analyze the amplifier output for a given set of input data, including mismatch effects and noise pollution described in Sections 5 and 7. These data are:
  - a. Sampled input signal, which can be measured in the time domain with a digitizing oscilloscope, or be software-created
  - b. Ambient temperature
  - c. Amplifier noise figure
  - d. System bandwidth.

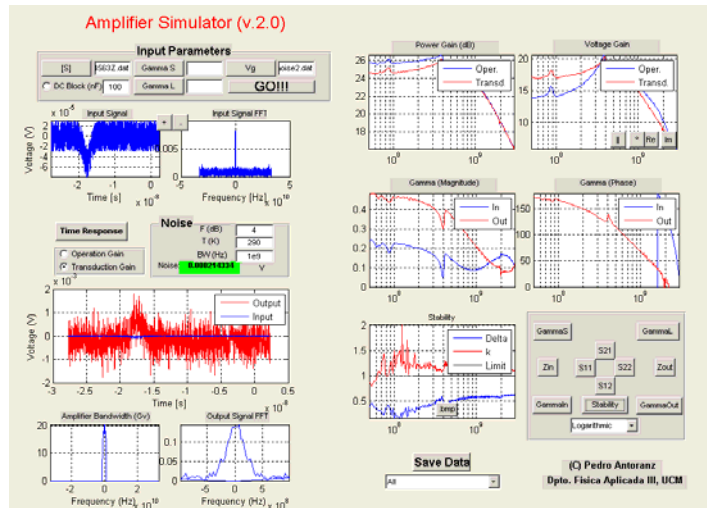
The easiest way to determine the amplifier response to a given input is to work in the frequency domain. The FFT of the input signal is multiplied by the voltage gain of the amplifier (an interpolation algorithm takes charge of fitting the number of points of these two functions). To cover the complete spectrum of the input signal, the voltage gain must also be expanded to the negative frequencies region; this is done by taking the complex conjugate of the values for positive frequencies. This way, the spectral components of the output signal are obtained. With this information, it is possible to analyze the

harmonic distortion of the pulse. By means of the IFFT, the output signal is converted into time-domain and the amplifier output is obtained.

The noise added by the amplifier, and therefore the system sensitivity is calculated from the NF, the ambient temperature and the bandwidth of the system.



(a)



(b)

Figure 5.10 (a) Flow diagram of the analysis/simulation software (b) User interface of the program. The rightmost part shows the amplifier characteristics, and the leftmost the time domain response.

The operation of the software is illustrated in the following example. A two-stage amplifier was constructed, consisting in two cascaded Infineon BGA616 MMICs (this device will be described in detail in next Chapter). By means of a Network Analyzer and a Noise Analyzer both the scattering parameters and the noise figure were obtained. It is also possible to use the data provided by manufacturer.

Figure 5.11 shows the analysis of the device performed from the scattering parameters. Stability, voltage gain, or input and output impedances can be obtained.

In Figure 5.12, the simulation of the response to an input pulsed signal is shown. Both simulated and measured outputs are displayed, showing great agreement and the accuracy of the simulation. Only a slight difference in the delay of the transmitted pulse is appreciated.

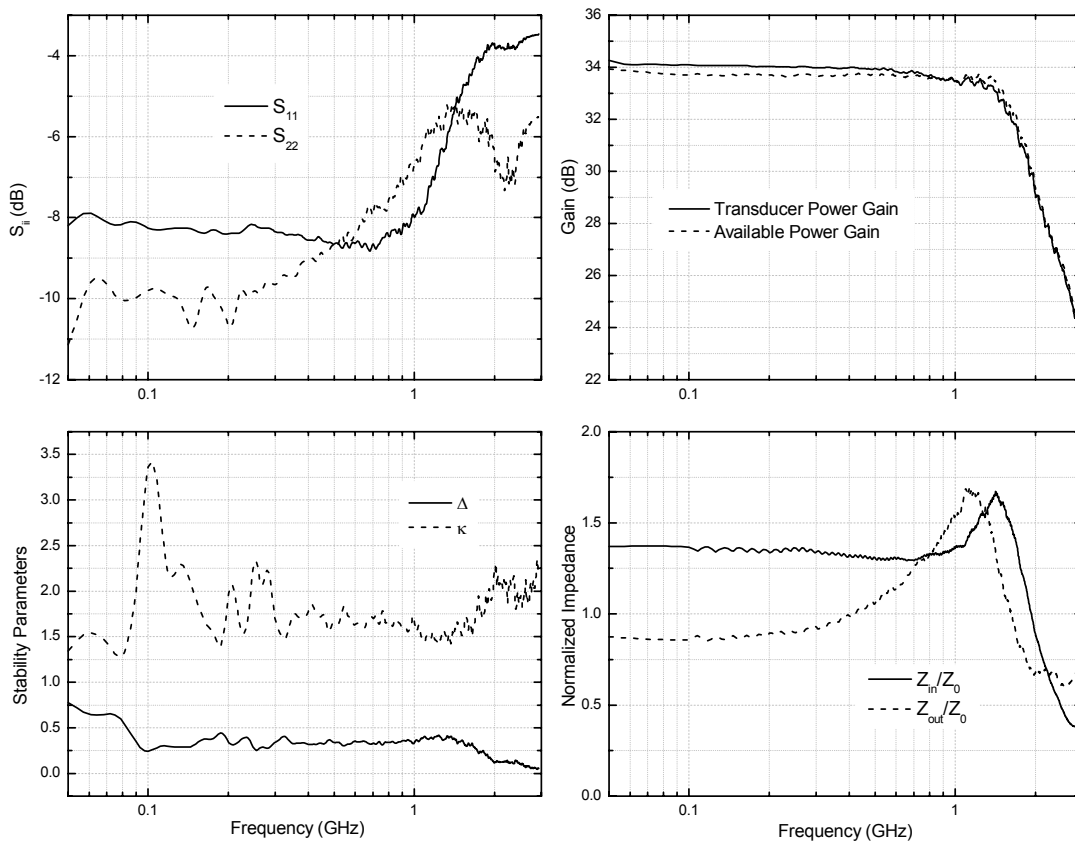


Figure 5.11 Analysis of a 2-stage amplifier obtained from the S matrix.

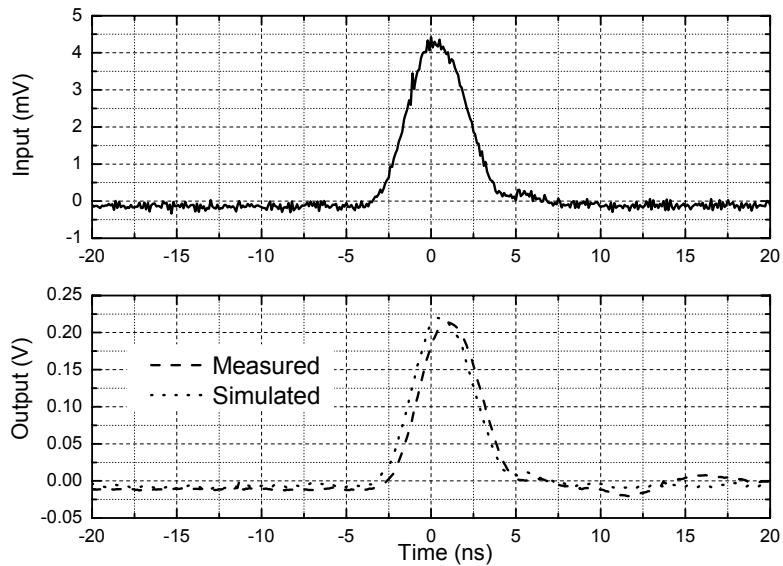


Figure 5.12 Simulation of the response to an input pulse.

An important feature of this analysis and simulation software is its independence with respect to other software packages. The simulation routines can be easily exported and utilized.

## 9.2 Spice integration of the models

Conventional CAD tools can hardly integrate in a straightforward way the scattering parameters when a new device model is created. In most cases, specific software as APLAC, or self-made MATLAB scripts are enough to perform the simulations, but it is always very useful to dispose of Spice circuitual models of the amplifiers. Recent versions of ORCAD permit, as well, to easily generate mask for the PCB production from the layouts associated to the components.

It is therefore useful to have a method to quickly integrate measurements from the Network Analyzer into Spice circuits [16]. This can be easily done by means of an equivalent circuit for the device, in which dependent voltage supplies represent the scattering parameters and their frequency dependence. Figure 5.13 shows an implementation of the mentioned circuit, in which the characteristic impedance is  $50\ \Omega$ . Nodes 1 and 2 represent the device ports, and node 3 is common for the input and the output, and is ground connected. The control voltage of  $E_{ij}$  supplies is applied in nodes 4 and 5, and the response of these supplies is determined by means of a table obtain from the S parameters.

With a MATLAB based graphic interface, the measured scattering parameters are introduced, and a file for the Spice library (ModelName.lib) is generated. In this file the whole circuit is contained. If this model is associated to a Spice component symbol, the component is ready to be integrated into simulations.

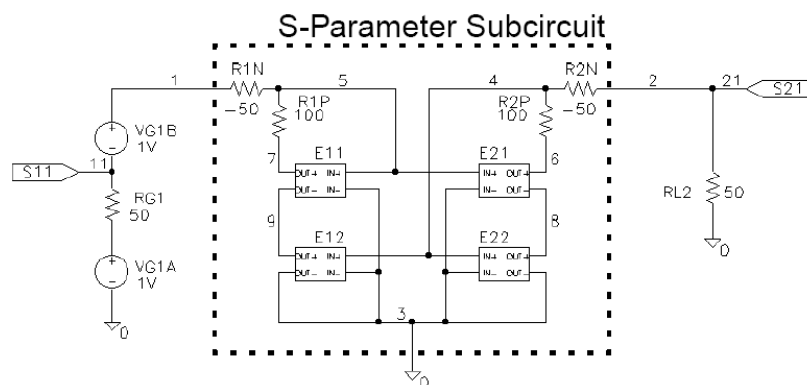


Figure 5.13 Device equivalent circuit for integration of the scattering matrix into Spice simulations.

## 10. REFERENCES

- 
- [1] D.M. Pozar, *Microwave Engineering*, 2nd Edition, 1998. Addison Wesley. Cap 5.
  - [2] S. J. Mason, *Feedback theory - Further properties of signal flow graphs*, Proc. IRE 44 (1956), 920-926.
  - [3] D.M. Pozar, *Microwave Engineering*, 2nd Edition, 1998. Addison Wesley. Cap 11.
  - [4] G. Gonzalez, *Microwave Transistor Amplifiers Analysis and Design*, Prentice Hall (1984).
  - [5] J. M. Rollett, *Stability and power gain invariants of linear two-ports*, IRE Trans. Circuit Theory, vol. 9 num. 3 (1962), 29-32.
  - [6] D. Woods, *Reappraisal of the unconditional stability criteria for active 2-port networks in terms of S parameters*, IEEE Trans. Circuits Syst., vol. 23, (1976) 73-81.
  - [7] M.L. Edwards and J.H. Sinsky, *A new criterion for linear 2-port stability using a single geometrically derived parameter*, IEEE Transactions on Microwave Theory & Techniques, Vol. 40, No. 12, pp. 2303-2311, December 1992.
  - [8] *Fundamentals of RF and Microwave Noise Figure Measurements*, Agilent Application Note 57-1
  - [9] *Description of the Noise Performance of Amplifiers and Receiving Systems*, Sponsored by IRE subcommittee 7.9 on Noise, Proc. Of the IEEE, March, 1963, pp 436-442
  - [10] J. Johnson, *Thermal Agitation of Electricity in Conductors*, Phys. Rev. 32, 97 (1928)
  - [11] H. Nyquist, *Thermal Agitation of Electric Charge in Conductors*, Phys. Rev. 32, 110 (1928)
  - [12] Infineon Technologies, *BGA616, Silicon-Germanium Broadband MMIC Amplifier*, Preliminary datasheet, Apr. 2003.
  - [13] Agilent Technologies, *MSA0886 Datasheet*, (1997).
  - [14] P.Antoranz, M.V.Fonseca, M.Asensio, J.A.Barrio, M.Cámara, J.L.Contreras, R.de los Reyes, M.López, J.M.Miranda, I.Oya for the MAGIC Collaboration, *Noise-Bandwidth Tradeoff in the Design of the Pixel Preamplifiers for the MAGIC II Telescope Camera*, proceedings of the 20<sup>th</sup> European Cosmic Ray Symposium, Lisbon 2006.
  - [15] J.M. Miranda, J.L. Sebastián, M. Sierra, J. Margineda, *Ingeniería de Microondas y Técnicas Experimentales*, Ed. Pearson, 2002, pp 208.
  - [16] *Create S-parameters circuits for Microwave and RF Applications*. Microsim Application Note.



# Chapter 6

## Pulse amplifiers: design and test

1. MMICS: state of the art
  - 1.1 Technologies
  - 1.2 Topology
2. Fulfilling MAGIC requirements
  - 2.1 PMT preamplifier
  - 2.2 Receiver board preamplifier
3. Practical considerations
  - 3.1 PCB line studies
  - 3.2 SMD parasitic modelling
4. Bias circuit
5. Frequency-domain response
  - 5.1 Scattering matrix
  - 5.2 Stability
6. Time-domain response
  - 6.1 Linearity and dynamic range
  - 6.2 Amplifier behaviour with the photodiode as source
7. Noise and sensitivity
8. Thermal stability
  - 8.1 Bias current stability with temperature
  - 8.2 Influence of temperature on the scattering matrix
9. Final tests
10. References

## 1. MMICS: STATE OF THE ART

### 1.1 Technologies

SINCE the second half of 20<sup>th</sup> century, society has experienced an exponential technological growth. The number of 'gadgets' and tools, for both professional and leisure use has increased beyond the imaginable. Together with the constant evolution of informatics, recent decades have assisted to a huge boom in telecommunications.

As the laptops, mobile phones or GPS receivers became more and more powerful and compact, integrated circuits became smaller and smaller. In this scaling process, one of the most important features has been achieved by Monolithic Microwave Integrated Circuits (MMICs). These devices, with bandwidth up to tens of GHz, rapidly replaced the 'traditional' amplifiers based on discrete transistors. As all the components were built in the same wafer, mass production and high integration levels were easier to perform. Moreover, main amplifier features as noise, stability or impedance matching improved with this technology.

MMIC and RFIC (Radio Frequency Integrated Circuits) technological trends have suffered several changes and advances along the years. Depending on the desired features for the amplifier, different technologies are preferred [1].

The first developed MMICs and RFICs were based in GaAs technology. Heterojunction Bipolar Transistors (HBT) were common in the 90's, though their poor performance as power amplifiers relegated them as compared with InGaP amplifiers, which offer also better linearity. Gallium Arsenide technology is still used in MESFETs (metal semiconductor field effect transistors) mainly in switches and classic RF circuits due to their good noise performance.

Ternary III-V compounds were soon proved to offer better features. For general purpose amplifier, HBT InGaP gain blocks still provide the best performance. For high sensitivity devices such as GPS and mobiles, InGaAs pHEMT (pseudomorphic high electron mobility transistor) amplifiers have become very used due to their low noise and high dynamic range. Gallium nitride (GaN) technology is also being developed. These devices allow greater integration for power applications.

The main drawback of all these technology is the high cost per unit area and the limitations in the integration this implies.

Silicon-germanium (SiGe) technology came as a straightforward evolution of silicon devices. With no important increase in fabrication complexity, SiGe



amplifiers provide much higher bandwidths than former silicon ones. This is the preferred technology for high integration, low GHz frequency range devices such as fiber optic communications or automotive sensors.

For the most highly integrated, low cost devices, RF CMOS technology is becoming more and more popular, especially for digital systems as computer processors.

## 1.2 Topology

By far, the most used configuration in MMIC gain blocks is the Darlington Pair [2]. This configuration is widely used in bipolar technology, because it increases the current gain and the input resistance of a classic bipolar transistor. This is achieved by connecting both collectors together, and exciting the base of the second stage with the emitter of the first one, as shown in Figure 6.1.

This Darlington Pair can be modified in order to improve the performance [3]. For example, in Figure 6.1c, the resistors provide independent bias point to each amplifier, and reduce the time needed to turn off the amplifier. The operation point of the transistors can be adjusted by means of the resistor values. If an 'external' resistor is added in parallel with the internal feedback, the total value of the feedback resistor is reduced, and the dynamic range of the amplifier increases. This resistor, though, must be carefully chosen because it can affect the overall stability of the system. Another drawback of the original Darlington Configuration is that the switching speed of the amplifier is limited. The base current of the second amplifier cannot be actively inhibited by the first amplifier; this turns into a slow switching off of the device. To reduce this effect, the second transistor often has a base resistor of a few hundred ohms (see Figure 6.1c).

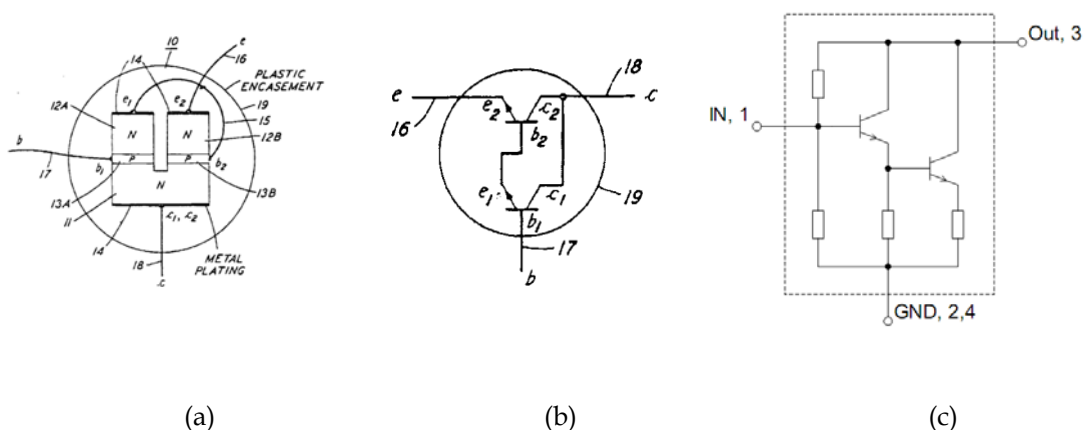


Figure 6.1 (a), (b) Original figures in S. Darlington patent, 1952 [3]. (c) Darlington configuration of the Infineon BGA616 Gain Block.

## 2. FULFILLING MAGIC REQUIREMENTS

There are two critical preamplifiers in the MAGIC II telescope pixel chain, as described in Chapter 2. The first one is located after the PMT inside the camera. Several prototypes were designed and tested in this thesis, and the final design was fixed by the engineers responsible for the camera construction. The second one amplifies the signal from the PIN photodiodes located at the receiver boards. The design presented in this thesis could be integrated without modifications in the final version of these boards.

In this section, the main characteristics to be fulfilled by these amplifiers are described.

### 2.1 PMT preamplifier

The PMT preamplifier must satisfy several conditions, imposed by the characteristics of the photomultiplier signal, the noise of the system and the VCSEL which transmit the signal through the optical fiber.

#### **Bandwidth**

The Cerenkov pulses at the PMT anode have a typical FWHM of 1-3 ns [4]. The amplifier must transmit this signal with minor or no distortion of the pulse; in any case the area of the amplified pulse must not vary more than 1% respect to the area of the input signal.

The bandwidth of the total pixel chain was agreed by the collaboration to be at least 500 MHz, with 200 ps pulse risetime. The total bandwidth is determined by all the cascaded components, so in order to not to reduce this value below 500 MHz, an amplifier bandwidth close to 1 GHz is suggested.

The lower frequency cutoff is determined by the resolvable time between pulses. The pulse tail (and therefore the minimum distance between pulses without producing pile-up) depends on the lowest frequencies and on the bias circuit. Typical repetition rates are ~300 kHz.

#### **Sensitivity and gain**

The gain of the amplifier is determined by the minimum signal provided by the PMT and by the system noise.

The minimum detectable signal is 1 photoelectron (phe). If the typical gain of the PMT is ~20.000 [5] and the dispersion of electrons due to the dynode

emission and the transmission through the tube is  $\sim 1$  ns, the anode current can be roughly approximated to a square pulse of 1 ns and amplitude:

$$I = 20.000 \times (1.602 \times 10^{-19}) C / (10^{-9}) s = 3.204 \times 10^{-6} A \quad (6.1)$$

If the input impedance of the amplifier is  $50 \Omega$ , the minimum sensitivity required for the amplifier would be  $\sim 160 \mu V$  for this load. This implies that the selected MMIC must have a very low noise figure. This is one of the most restrictive conditions in the amplifier selection.

The initial requirements suggested the gain of the amplifier to be enough to increase the signal level a factor of 6 above the system noise. This noise is determined by the VCSEL input, where a noise of  $\sim 2$  mV was measured (for no input signal) [6]. The gain should then be:

$$12mV / 0.160mV = 75 = 37dB \quad (6.2)$$

To achieve such a high gain presented two main problems: no single-stage amplifier offered these values, so a two stage amplifier was needed, with all the complications this implied. And the dynamic range of the system was compromised, because so high gains produced too big amplitudes at the amplifier output for the highest input pulses, with which the VCSELs could not deal without entering saturation.

A compromise was then achieved between sensitivity and dynamic range, and a gain of  $\sim 22$  dB is obtained. This yield to a sensitivity of  $\sim 1$  mV or 6 photoelectrons.

### **Dynamic range**

To optimize the shower detection, it is desirable to maximize the dynamic range. The maximum signal the VCSEL can transmit without saturation is  $\sim 4$  V. If a dynamic range of 60 dB is required, then the minimum signal applied to the VCSEL will be 2 mV. For a PMT output of  $160 \mu V$ , the amplifier gain must be  $\sim 23$  dB.

At the beginning of the work which conducted to this thesis it was difficult to find suitable amplifiers of high gain and dynamic range. But the MMIC market evolved very fast during the last years and careful attention was paid to the last novelties in the field of highly linear RF amplifiers. In addition, it is possible to modify the operating point of the amplifiers to improve the dynamic range, although at the expenses of increasing the power consumption and the risk of degrading stability.

## Noise

The previous calculations have been done without considering amplifier's noise. As the noise power is added in quadrature, the intrinsic noise of the amplifier should only be taken into account if it is comparable with the noise of the system.

Table 6.1 shows a summary of the most suitable commercially available amplifiers found to date. As can be seen in these specifications, all inspected amplifiers have noise figures below 4 dB. This noise figure gives an equivalent input noise voltage of  $\sim 200 \mu\text{V}$  for a  $50 \Omega$  load and 1 GHz bandwidth.

Model	Manuf.	G (dB)	BW (GHz)	P1dB (dBm)	NF (dB)	V <sub>CC</sub> (V)	V <sub>D</sub> * (V)	I <sub>CC</sub> (mA)	Tech.
ABA54563	Avago	23	3.5	16.1	$\sim 4$	5	5	79	Si
BGA616	Infineon	18.5@1GHz	2.7	18	2.90	5	4.5	80	Si-Ge
BGA614	Infineon	18.5@1GHz	2.4	12	2.30	5	3	80	Si-Ge
GALI-51	Minicir.	16.1@1GHz	4	16.5	3.5		4.5	65	InGaP
GALI-74	Minicir.	21.8@1GHz	1	18.3@1GHz	2.7	7-15	4.8	80	InGaP
HELA-10	Minicir.	12	0.05-1	30	3.5	12	-	525	-
SGA4563	Sirenza	25.6@850MHz	$\sim 0.8$	15.0@850MHz	2.4@1950MHz	5	3.6	45	Si-Ge
SGA4586	Sirenza	24@850MHz	$\sim 0.8$	16.5@850MHz	1.9@1950MHz	5	3.6	45	Si-Ge
SGA7489	Sirenza	22.4@850MHz	$\sim 1.3$	22.4@850MHz	3.3@1950MHz	7-12	5	115	Si-Ge

\*V<sub>CC</sub> = bias voltage.

\*V<sub>D</sub> = voltage at the bias pin.

Table 6.1 Some commercially available devices.

## Integration

PMT preamplifiers must be integrated into the photomultiplier base; this means that the layout of the printed circuit must be 1" diameter. This is a quite important constraint: the number of components and the size must be strictly controlled. A single stage amplifier is again preferred over a two stages amplifier. As the number of gain blocks increases, also does the number of components of the bias network and the integration in a small circuit is more complicated.

It is also desirable a maximum homogeneity in the power supply. Both the PMTs and the VCSELs are 5 V biased, so amplifiers with this voltage requirements are preferred. This reduces the number of cables to power up the units, with the consequent reduction in cost, infrastructure and risk of failure.

As all the studied amplifiers have inverting configuration, the number of stages is a determining factor in the signal polarity. PMT pulses are negative; VCSELs can admit both positive and negative pulses, depending on the pin

configuration. If VCSEL input polarity is negative, however, a -5 V extra power supply is needed. This is another reason favouring single-stage amplifiers.

The power consumption is another important constrain in the design of the amplifier. As more than a thousand pixels will work simultaneously, a high amount of consumed power will translate in an important increase of the camera temperature. The camera cooling system is designed to dissipate 2 kW, so a safety limit was set at 1 kW for the whole bunch of amplifiers [6]. For a 5 V bias, this means that the maximum allowed current per amplifier is 120 mA. As will be shown in next sections, this current is enough for all the tested models.

It is also advisable to provide the amplifier input with a discharge path for possible high charge accumulations in the PMT anode. This path must be a high impedance one for the signal bandwidth but practically a short-circuit for discharges.

All of the MMIC shown in Table 6.1 are cheap enough (~1 U.S.\$) to allow their integration in large batches of electronic boards, as is the case of the pixels or the receiver boards of the MAGIC II telescope.

## 2.2 Receiver board preamplifier

The preamplifier placed in the receiver boards, after the PIN photodiode, must fulfil basically the same requirements that the PMT one. However, for the gain and the dynamic range different criteria must be followed. Tests on the photodiode (1A446 OECA-ST100C [7]) showed an output dynamic range between 250  $\mu$ V and 200 mV. For lower levels the signal is masked by noise, and higher levels produce saturation.

The engineers responsible of receiver boards development requested a maximum pulse amplitude of 1.5 V. Higher amplitudes would saturate the next receiver stages. These parameters led to the following requirements for the amplifiers:

- Amplifier gain of 7.5 (17.5 dB).
- Dynamic range of 58 dB (from 1.8 mV to 1.5 V).
- The sensitivity of the amplifier must be high enough to resolve input pulses of 250  $\mu$ V.

### 3. PRACTICAL CONSIDERATIONS

#### 3.1 PCB line studies

Deviations in the width of the transmission lines might degrade the coupling of the amplifier thus affecting to its performance. Different types of transmission lines were considered. All of them can be fabricated in a FR4 laminate, which is inexpensive and widely available. FR4 dielectric permittivity is around 4, which results in reasonably small widths for the 50  $\Omega$  lines and an excellent field confinement, which minimizes the risks of crosstalks [8]. The different types of lines are depicted in Figure 6.2, and the basic characteristics of FR4 laminates are shown in Table 6.2.

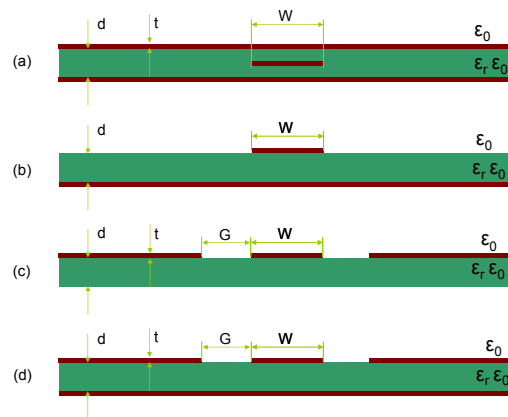


Figure 6.2 Different types of PCB lines: (a) Stripline. (b) Microstrip line. (c) Coplanar line. (d) Coplanar line with ground layer.

<i>Dielectric (Epoxy resin impregnated glass fiber matt)</i>	
Thickness	1.56 mm
$\epsilon_r$	4.3 @ 1 MHz
$\delta$ (dielectric loss tangent)	0.02 (1 MHz) - 0.01 (1 GHz)
Dielectric strength	20 MV/m
<i>Conductor (Copper)</i>	
$\rho_0$ (resistivity normalized to gold)	0.7
Thickness	35 $\mu\text{m}$

Table 6.2 Basic characteristics of the FR4 laminates.

From the transmission line analysis semi-empirical expressions are obtained for microstrip lines [9] [10]. In these expressions, the characteristic impedance of the microstrip line decreases with the line width  $W$ , and increases with the permittivity  $\epsilon_r$  and the dielectric thickness  $d$ .

Under some circumstances, the circuit topology turns to be of a critical relevance. In the integration of the MAGIC PMT preamplifier, for example, it is important the PCB size not to be bigger than the photomultiplier diameter (1"). In these cases it is necessary to reduce to the minimum the line width, keeping the 50  $\Omega$  system impedance. The most practical solution is to design the layouts on very thin substrates, or to use materials with high permittivity. These materials are more expensive, difficult to find and manipulate. Therefore, for test purposes the previously described FR4 laminates have been used.

Coplanar lines have several advantages over microstrip ones. The etched area is smaller, so the time needed for the acid immersion is shorter. This way, the achieved resolution in the copper lines is better (for a long acid immersion lateral etching is produced between the copper and the substrate).

By means of CAD software (APLAC) it is possible to optimize the microstrip line width to perform 50  $\Omega$  characteristic impedance. Figure 6.3 shows the result of minimizing the reflection coefficient as a function of the FR4 PCB line width. The effect of small deviations from the optimum value is also shown.

As can be seen in the simulation, the line width for 50  $\Omega$  impedance is thinner than in the case of microstrip line. This simplifies the implementation of multiple components and the miniaturization of the circuit.

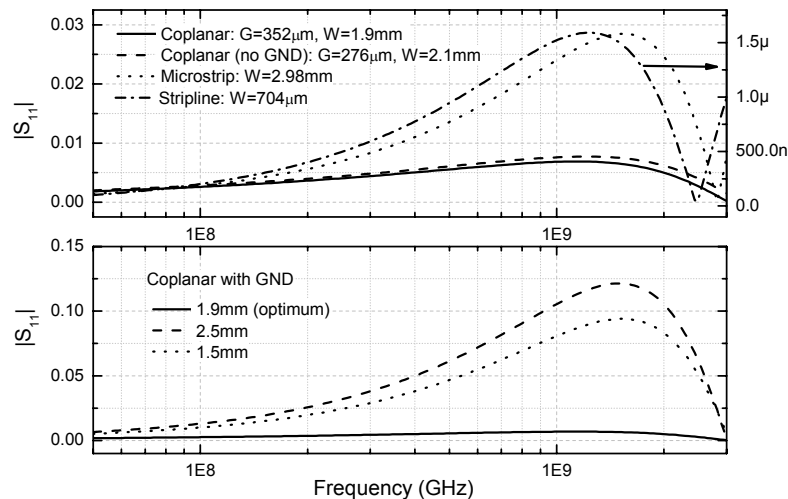


Figure 6.3 Simulation of different 30 mm length PCB transmission lines. *Upper figure:* Reflection coefficient of optimized transmission lines. *Lower figure:* effects of variations in line width in a coplanar (with ground layer) transmission line.

Adding a ground layer has several effects in the performance of the transmission line. The optimum line width increases, but the ground contacts for the components can be made with less parasitics. A ground layer is advantageous from the geometrical point of view, and much more efficient than tracing tracks in a single layer board.

Figure 6.4a shows the total contribution of the transmission lines of an amplifier board to the reflection coefficient. The most important effects are due to the transitions between the  $50\ \Omega$  line and the thin soldering pads of the MMIC. In this case, the width of these pads is limited by the MMIC package dimensions. In order to minimize the impact of these line sections, the circuit components must be placed as close as possible to the MMIC. It is also possible to reduce the reflection coefficient by designing tapered lines connecting the track with the MMIC pads.

Figure 6.4b illustrates the performance of an amplifier before and after drilling via holes to connect the upper and lower grounds. Connecting all the otherwise isolated copper areas not only improves the circuit shielding but also reduces the resonance effects.

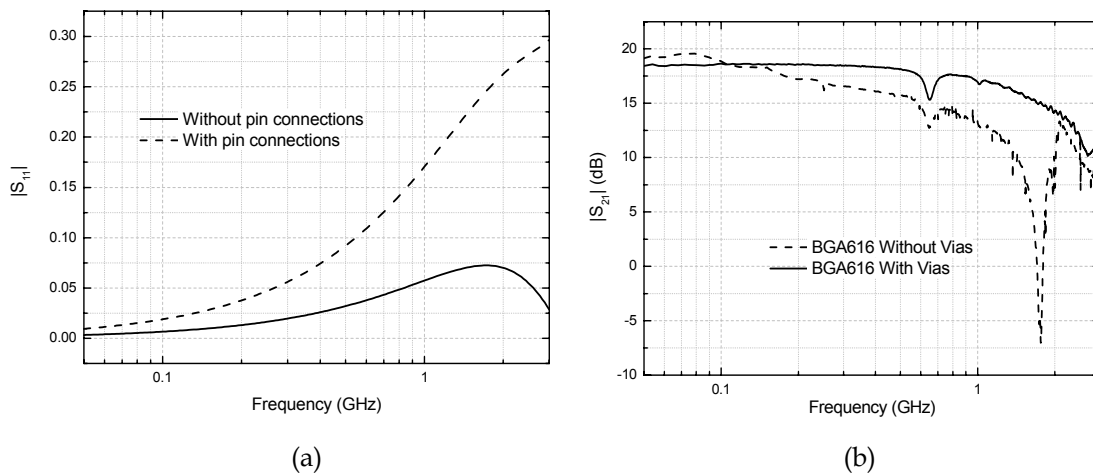


Figure 6.4 (a) Contribution of the PCB lines to the reflection coefficient. The dashed line includes the effects of MMIC connection pads, much thinner than the lines. (b) Effect in the amplifier performance of via holes close to the coplanar lines.

## 3.2 SMD parasitic modelling

At high frequencies component packaging and its combination with pad footprint and PCB layout are sources of parasitic effects, such as resonant



coupling, signal loss, signal distortion, etc. These effects not only make influence in the signal integrity but have also a high potential to be sources of EMI in the circuit. Although axial-lead components, such as air coils and RF chokes used in printed circuits are not strictly SMDs by definition, their performance in the circuit is also affected by board and pad parasitics and can be modelled with similar techniques. In the prototypes fabricated for this thesis, the parasitics of the microHenry-range inductors used in the bias circuits were by far the most problematic ones.

In Table 6.3 the data from some 100  $\mu\text{H}$  commercially available inductors are shown.

Manufacturer	Self-resonance (MHz)	Tolerance (%)	Q	Price (€)
Bourns	15	30	15	2,02
Tyco Electr.	8	10	55	1,65
Epcos	20	20	-	3,26
Panasonic	10	5	20	0,4
Kemet	9	20	-	0,62
Murata	10	10	40	0,4
Vishay Dale	9	10	20	0,43

Table 6.3 Characteristics of some commercially available 100  $\mu\text{H}$  inductors.

One of the most popular models used to characterize inductors is shown in Figure 6.5a [11]. Capacitors can be modelled with simpler circuits, such as the one shown in Figure 6.5b.

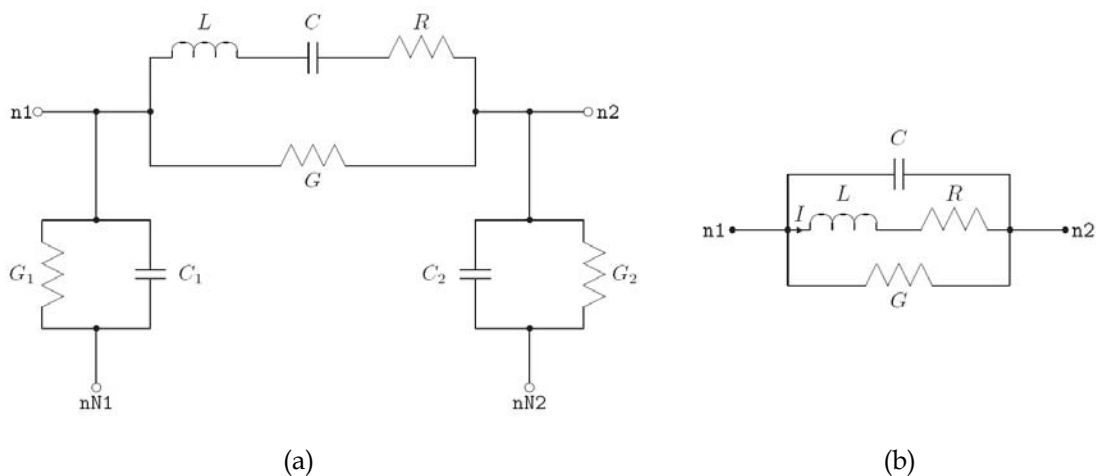


Figure 6.5 High frequency parasitic model for inductors (a) and capacitors (b)

Extraction of equivalent circuits for PCB interconnections and discrete components usually involves either electromagnetic simulations or measurements, followed by curve-fitting the resulting data to the response of a desired circuit, and it is based on a designer's a priori knowledge of the component's physical characteristics. For maximum operating frequencies in the range of 1 or 2 GHz optimization of circuit-based models provides parasitic diagnostics with a reasonable accuracy.

In order to estimate the value of the parasitics, the equivalent model of the component was tested in APLAC. The nominal value of the component and the information given by the manufacturer (usually the series resistance of the inductors) are fixed values in the optimization, the rest of the variables are optimized to fit the scattering matrix measured with a Network Analyzer. The coplanar line used as test-fixture is also included in this parameterisation.

A study of the parasitics of inductors has been done; the values that optimize the model are shown in Table 6.4. Figure 6.6 shows the results of the model fit to the measured reflection coefficient of several components. The modelling has an excellent accuracy for reflection coefficients when these are above -40 dB.

Component	Nominal L, F	Series L	Series R	Shunt C	Shunt R
TDK	10 $\mu\text{H}$	3.192 nH	2.1 $\Omega$	2.342 pF	649 k $\Omega$
EPCOS	1 $\mu\text{H}$	39 nH	0.34 $\Omega$	0.106 pF	4.318 k $\Omega$
MURATA	1 $\mu\text{H}$	86.2 pH	0.328 $\Omega$	1 pF	95 k $\Omega$

Table 6.4 Small signal equivalent circuit values of parasitics. The components with highest operating frequencies were chosen from each manufacturer.

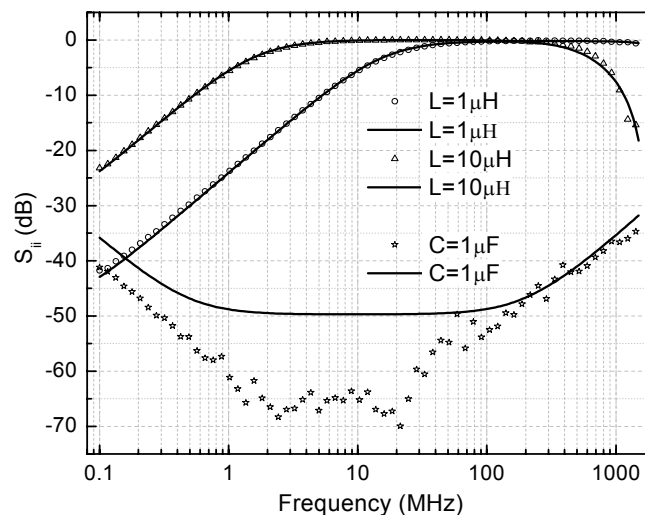


Figure 6.6 Reflection coefficient for some components. *Dots*: measured; *Line*: simulated.

## 4. BIAS CIRCUIT

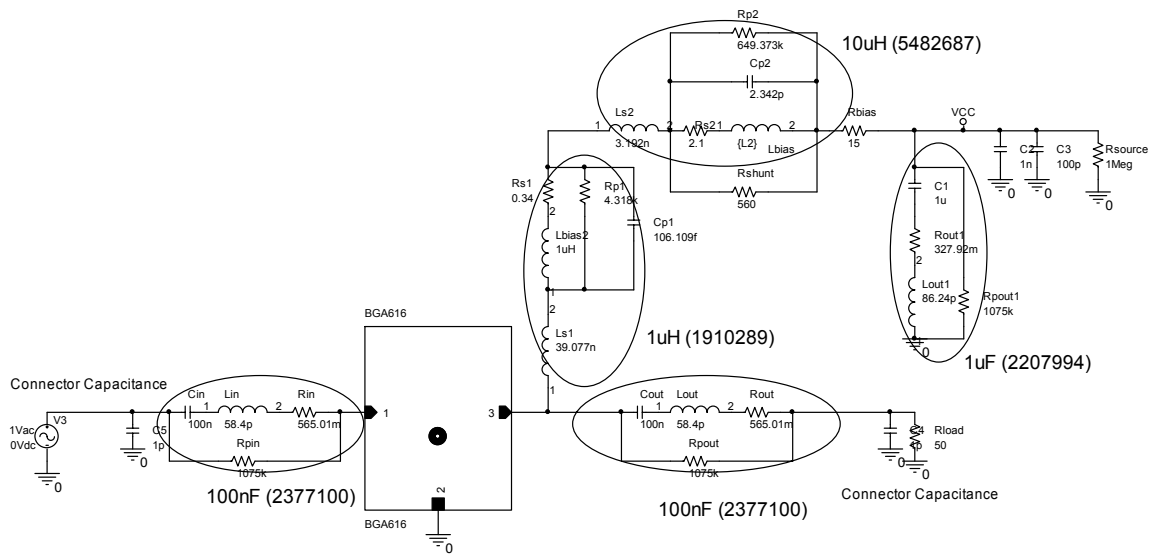
Although compact bias tees are commercially available (either in coaxial or SMD package) [12], it was not possible to find one with suitable characteristics, small size and low cost. Bias networks were therefore specifically designed from discrete SMD components for biasing the amplifiers.

Figure 6.7 illustrates the influence of the bias network and the DC block capacitors on the performance of a pulse amplifier. This simulation has been made taking into account all the parasitics of the components, estimated as commented in the previous section. Even though the amplifier manufacturer guarantees the correct performance of the gain block for low frequencies or even DC (the amplifier SPICE model is shown in Figure 6.7b), there is a low limit imposed to the bandwidth of the amplifier. The DC blocking capacitors, placed at both terminals of the MMIC filter the DC and the lowest frequencies, avoiding the slow variations of the excess current coming from the photodetector to penetrate and damage the MMIC. However, the low frequency cutoff is determined by the performance of the bias network (i.e. the values of the inductances). Figure 6.7c shows the  $S_{21}$  parameter of the entire circuit.

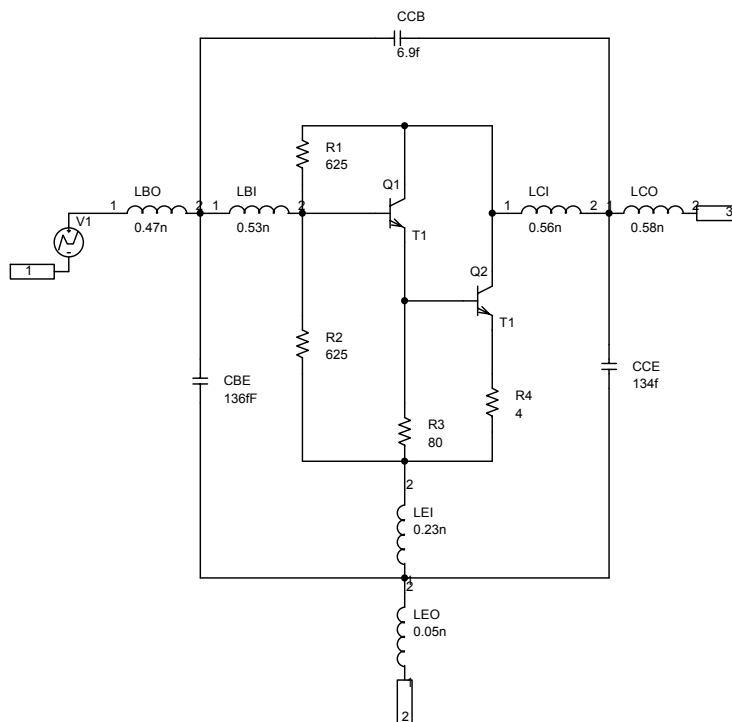
The bias resistor helps in reducing the dependence of the current on the bias voltage and also reduces the current sensitivity to temperature changes. The purpose of the high value bias network inductors is to set an upper limit for the frequency passband of the bias path. The behaviour of these inductors is critical: they must operate at the highest frequencies of the signals but at the same time they must have a high inductance value to cut efficiently the passing of these frequencies to the bias network path. As indicated in Section 3.2, the self resonant frequencies of these components use to be very low for the values needed in a pulse amplifier bias network. In order to alleviate the resonant effects two different procedures have been followed. The first one consists of using two inductors in series, as shown in Figure 6.7a. The one closest to the MMIC has a value of only 1  $\mu\text{H}$ , but works properly at the highest operating frequencies of the MMIC, when the large inductor no more performs a good filtering. The second inductance is 10  $\mu\text{H}$ . Adding a resistor in parallel the inductance  $Q$  is reduced and their resonances are significantly attenuated, as shown in Figure 6.7c. Several simulations determined that the optimum value of this resistor was 560  $\Omega$ .

Figure 6.8 shows the effect of this inductor on the pulse tail width. The effect of filtering the lowest frequencies is to widen the negative pulse tail shown in this figure. A compromise between the low frequency cutoff and the typical pulse tail must be reached. The higher the value of the bias inductor, the shorter the tail is. MAGIC pixel proper performance require a recovery time for the amplifier in the order of several nanoseconds. This way, a pulse rate of several

MHz due to the NSB will not result in a pile-up of the signal and a sensitivity loss.

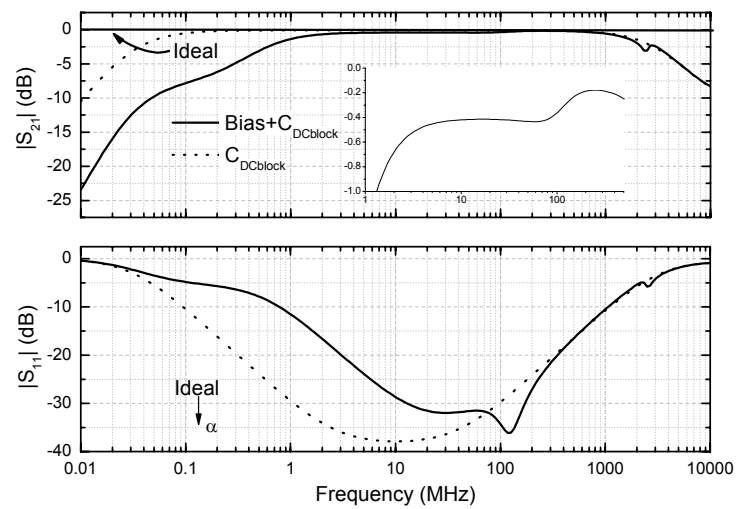


(a)



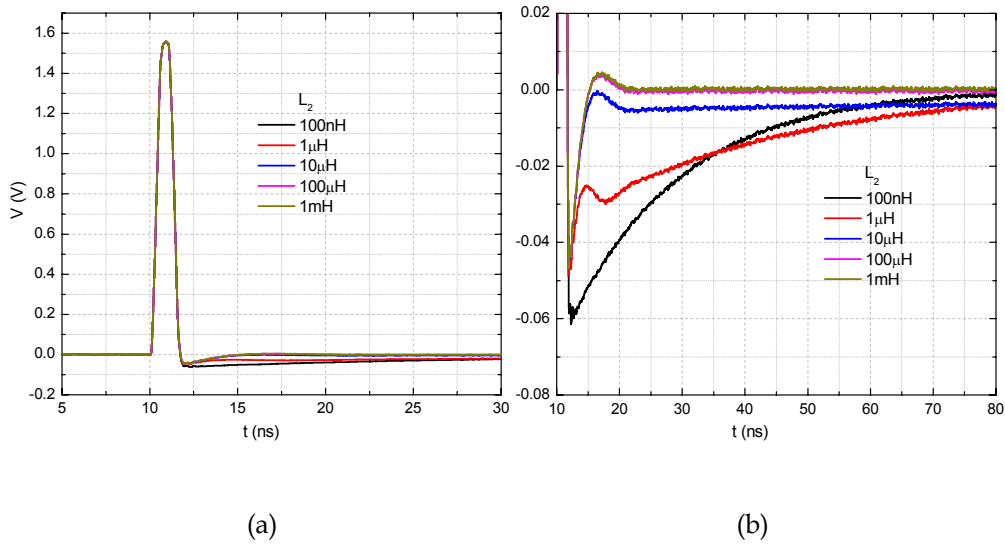
(b)

Figure 6.7 (a) Amplifier schematic, including the bias circuit and the DC block capacitors. (b) SPICE model of the amplifier (BGA616).



(c)

Figure 6.7 (c) APLAC simulation of the  $S_{21}$  of the DC block and bias circuit, including all the parasitics calculated in the previous section. The amplifier has been short-circuited in this simulation.



(a)

(b)

Figure 6.8 (a) Response of an amplifier to a -200 mV input pulse. (b) Detail of the pulse tail as a function of the bias inductor value.

## 5. FREQUENCY-DOMAIN RESPONSE

### 5.1 Scattering matrix

In Table 6.1, several commercial devices were presented. After examining the requirements for the MAGIC II preamplifiers, the following MMICs were selected:

- **Sirenza SGA-4563Z:** both the gain and the 3 dB bandwidth of this device fitted quite well the requirements of the preamplifier. The noise figure is low enough to not to degrade the system sensitivity, and it is well  $50\ \Omega$  matched. The main drawback is the relatively low dynamic range.
- **Sirenza SGA-4586Z:** very similar to the previous one, but better noise figure and dynamic range. It turned out to be less stable.
- **Sirenza SGA-7489Z:** The main advantage of this MMIC was its high dynamic range without the need to perform resistive feedback. The drawbacks were the need of an extra power supply for biasing and the high power consumption.
- **Infineon BGA616:** this device fitted perfectly all the features required for the photodiode preamplifier in the receiver board.

Several other amplifiers were tested, as the versatile **Analog AD8009** operational amplifier or the **Agilent SMA0886**, but were finally discarded because they did not reach the minimum required bandwidth.

In the following sections the main results of the tests performed to these devices are presented.

Figure 6.9a shows the measured gain for the analyzed models. Both SGA4563 and SGA4586 MMICs have been tested in normal (*A* model) and extended dynamic range (*B* model) configurations. For the preliminary tests, a different bias network, simpler than the one presented in Section 4 was used. Figure 6.9b and Table 6.5 describe the circuit. This configuration provides a worse performance at low frequencies, with longer pulse tails (as explained in Section 4); but the parasitics have less influences at high frequencies and the analysis and implementation is easier. Once tested and selected the device, a sample with the adequate bias network is carefully analyzed.

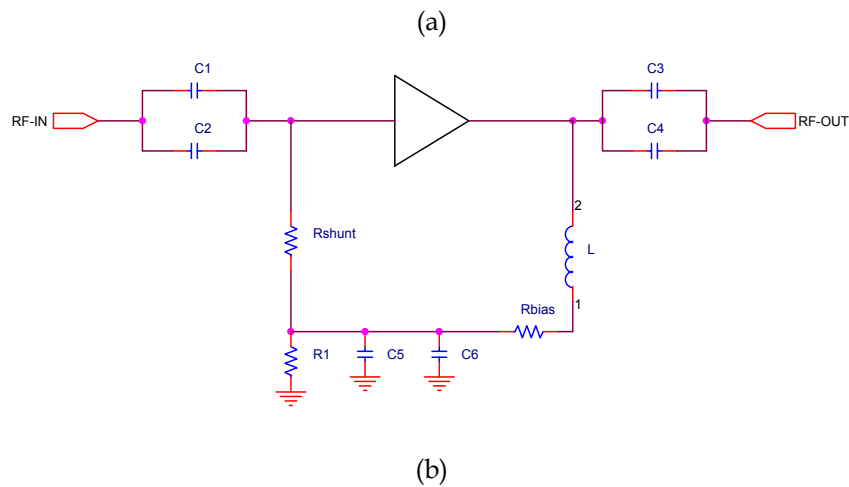
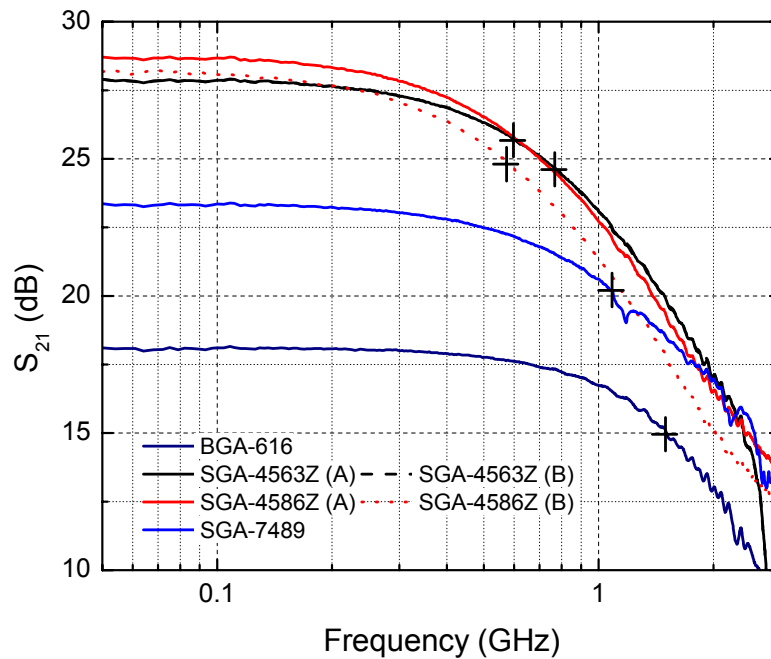


Figure 6.9 (a)  $S_{21}$  of the different analyzed amplifiers. The crosses denote the 3 dB bandwidth. Models noted as 'A' correspond to a standard. Models noted as 'B' correspond to configurations with extended dynamic range. (b) 'A' and 'B' configurations.

Figure 6.10 shows the performance of the final prototype of BGA616, designed to be the preamplifier of the receiver board. The gain has been measured with the network analyzer between 50 MHz and 3 GHz, where the parasitics of the components are more relevant. The simulation, performed with SPICE, includes the parasitics of every component (as described in Section 3), the

transmission lines and the amplifier model given by the manufacturer, as shown in Figures 6.7a and 6.7b.

The effects of the parasitics can be clearly seen in Figure 6.10. The circles are the measured value of the gain for the circuit of Figure 6.7a. The triangles stand for the same circuit, but removing the 560  $\Omega$  shunt resistor.

The black line simulates the circuit without the shunt resistor, and the blue one the complete circuit with all the parasitics. For the simulation represented by the red line, the parasitic capacitance of the SMA connectors was removed.

The peak observed at 100 MHz is the result of the capacitive parasitic of the 10  $\mu\text{H}$  inductor of the bias network. When a shunt resistor is introduced the quality factor of the self-resonance is reduced and the peak disappears. There is a strong dependence on the connector capacitance.

	SGA4563Z A	SGA4563Z B	SGA4586Z A	SGA4586Z B	SGA7489Z	BGA616
$C_1, C_3$	1 mF	1 mF	1 mF	1 mF	1 mF	1 mF
$C_2, C_4$	100 nF	100 nF	100 nF	100 nF	100 nF	100 nF
$R_{\text{SHUNT}}$	$\infty$	3.3 k $\Omega$	$\infty$	3.3 k $\Omega$	$\infty$	$\infty$
$R_{\text{BIAS}}$	33 $\Omega$	33 $\Omega$	33 $\Omega$	33 $\Omega$	10 $\Omega$	$\Omega$
L	1 $\mu\text{H}$	1 $\mu\text{H}$	1 $\mu\text{H}$	1 $\mu\text{H}$	1 $\mu\text{H}$	$\mu\text{H}$
$C_5$	1 $\mu\text{F}$	1 $\mu\text{F}$	1 $\mu\text{F}$	1 $\mu\text{F}$	1 $\mu\text{F}$	$\mu\text{F}$
$C_6$	1 nF	1 nF	1 nF	1 nF	1 nF	nF
V	5 V <sub>DC</sub>	5 V <sub>DC</sub>	5 V <sub>DC</sub>	5 V <sub>DC</sub>	6.26 V <sub>DC</sub>	5 V <sub>DC</sub>
I	45 mA	83.3 mA	47.7 mA	85 mA	115 mA	

Table 6.5 Component values of the Figure 6.9b.

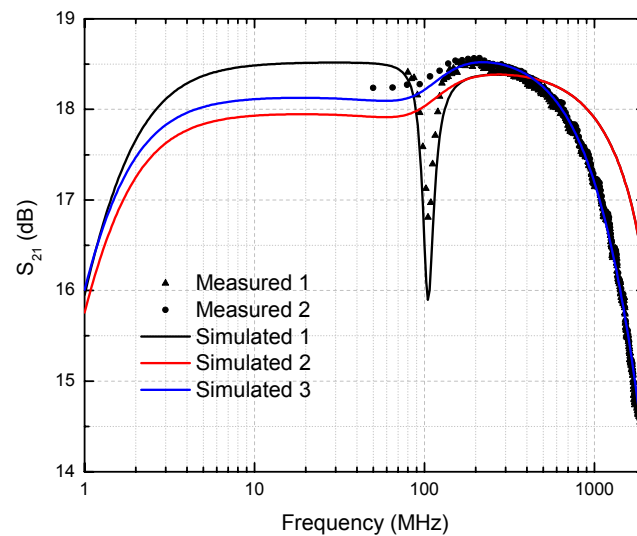




Figure 6.10 Comparison of measured and simulated  $S_{21}$  parameter for BGA616, in order to illustrate the effect of parasitics.

Figure 6.11 shows the  $S_{12}$ ,  $S_{11}$  and  $S_{22}$  parameters of the amplifiers. The measurements have been made between 50 MHz and 3 GHz. In the operating range (up to 1 GHz) all of them show acceptable  $50 \Omega$  matching. The influence of the mismatches on the power transfer can be better observed in Figure 6.12, where the reflection power losses both at the input and at the output of the amplifiers are represented. In the operation range (below 1 GHz) all these losses are below 5 %

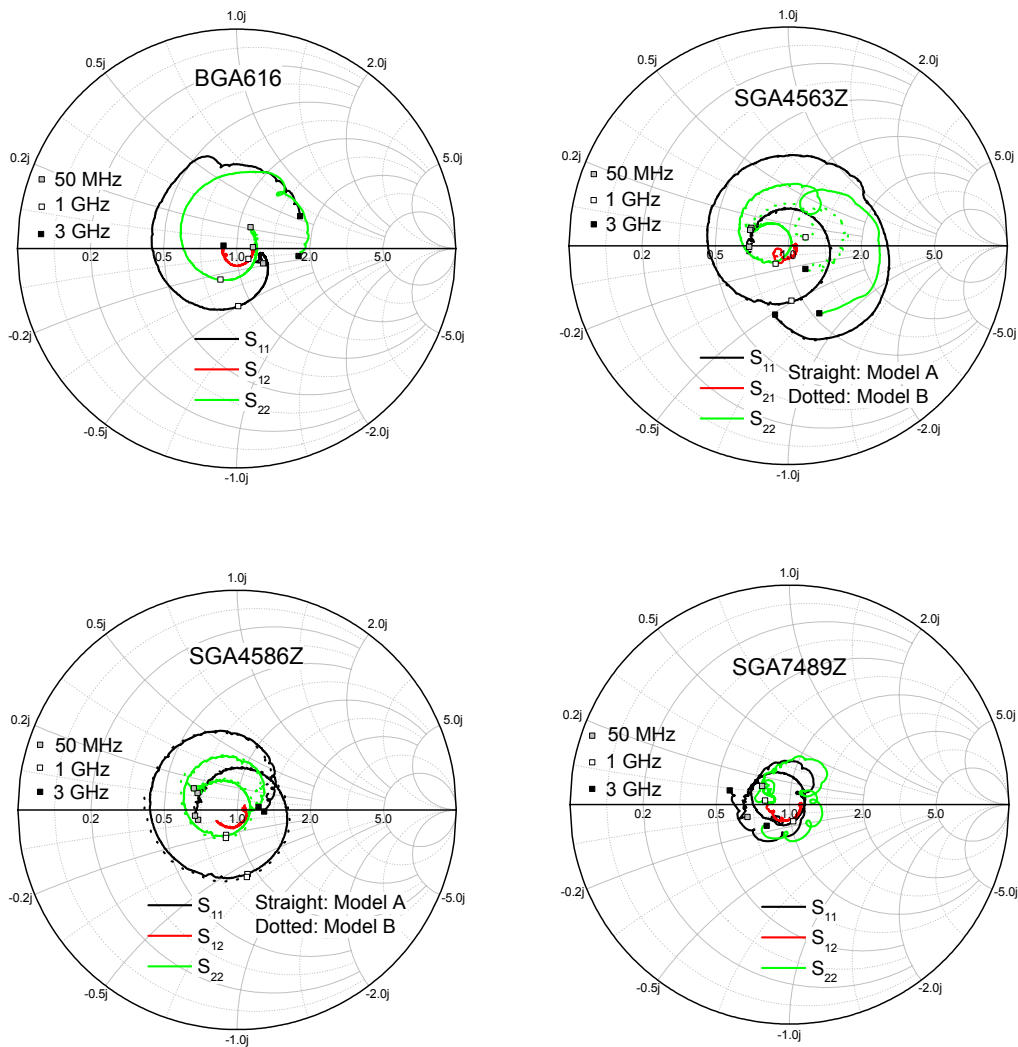


Figure 6.11 Measured scattering parameters. Models noted as 'A' correspond to a standard. Models noted as 'B' correspond to configurations with extended dynamic range.

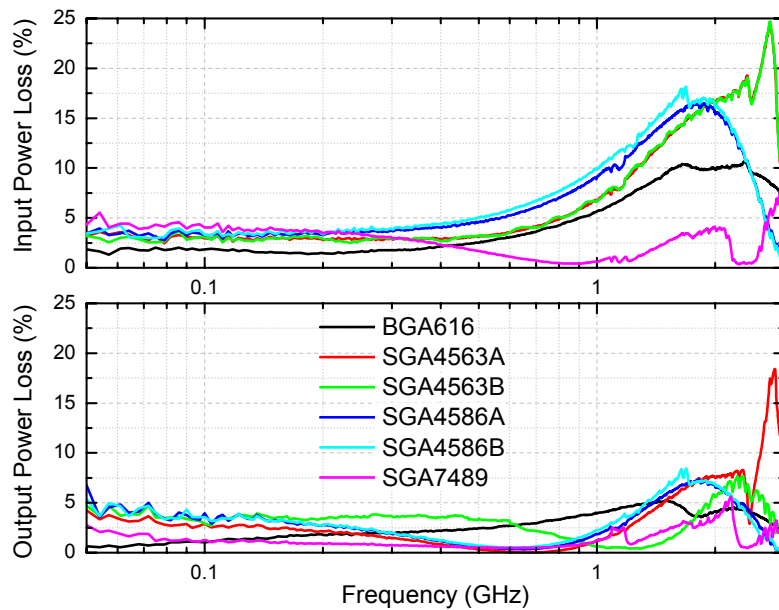


Figure 6.12 Power loss of fabricated prototypes.

## 5.2 Stability

A correct design of the amplifier implies the stability of the system for the operating frequencies and impedances. The feedback resistor of B models has been proven to increase the stability of the amplifier (and the dynamic range) at the expense of increasing the power consumption.

Figure 6.13 shows the stability parameters of the amplifiers, already defined in Chapter 4. As can be seen in the graphs, both selected amplifiers (SGA4563Z and BGA616) are unconditionally stable.

The stability circles determine the impedances which placed at the source or the load of the amplifier would produce reflections coefficients with modula higher than one. In Figure 6.14, source and load stability circles are calculated for both BGA616 and SGA4563 amplifiers. All the circles are outside the Smith chart and the center of this chart is stable in this case. Therefore, the devices will be stable independently of the load and source impedances.

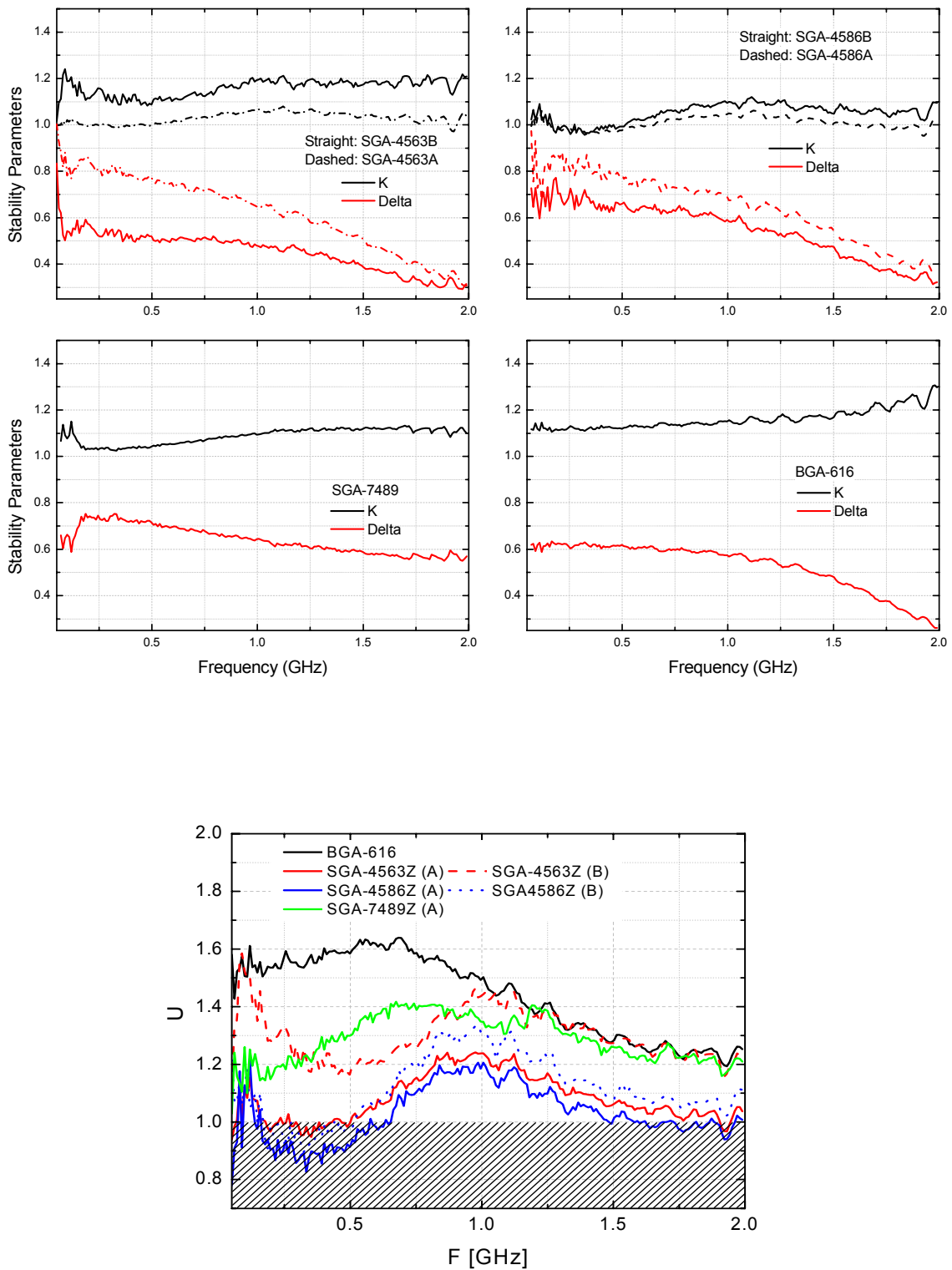


Figure 6.13 Stability parameters of the tested amplifiers. The device is unconditionally stable if  $\kappa > 1$  and  $\Delta < 1$  (or  $U > 1$ ) for every frequency.

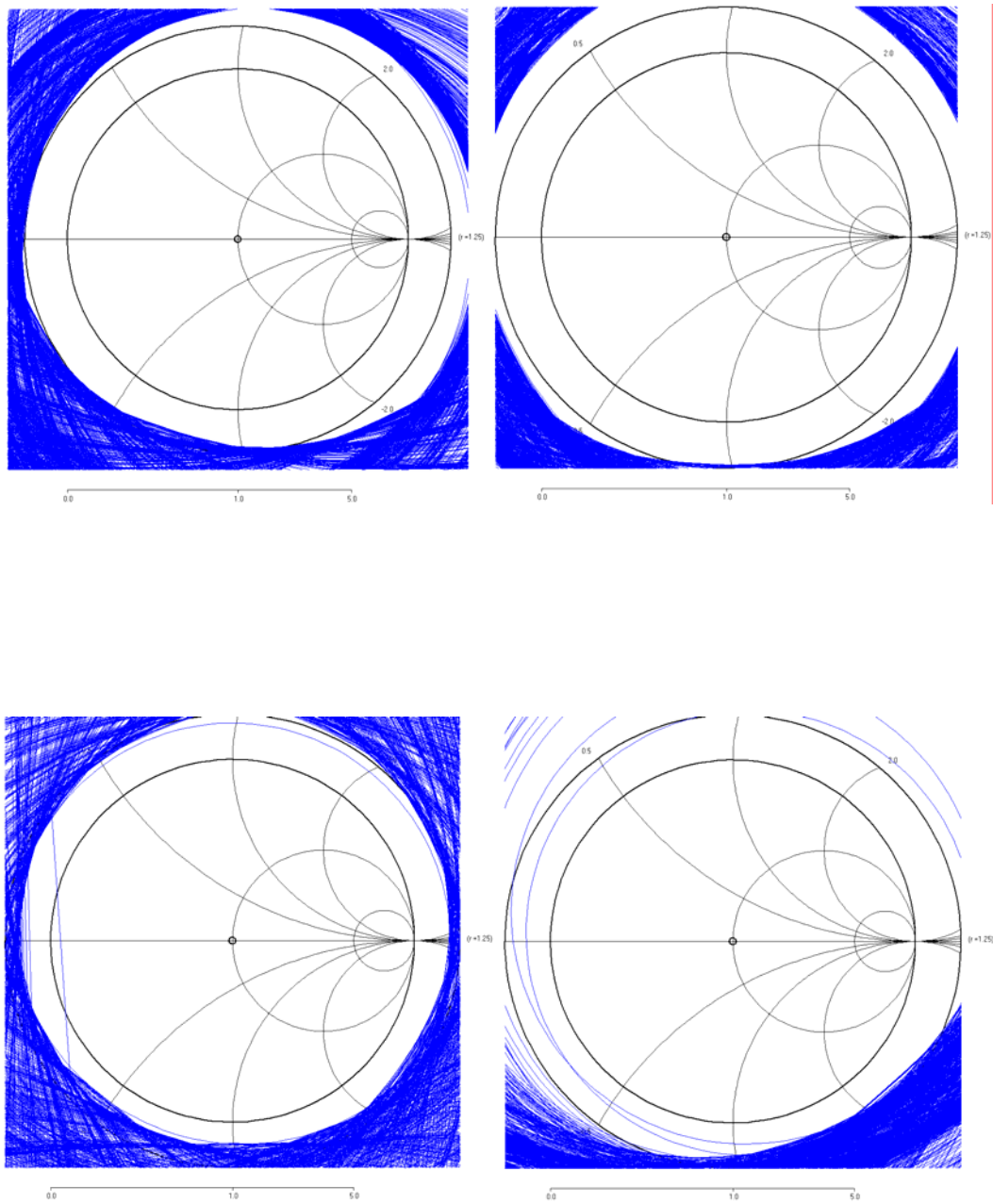


Figure 6.14 Stability circles of the selected amplifiers plotted in the range 50 MHz - 2 GHz. *Upper graphs: BGA616. Lower graphs: SGA4563 (B model). Left: source stability circles. Right: load stability circles. The center of the Smith chart is stable*

## 6. TIME-DOMAIN RESPONSE

### 6.1 Linearity and dynamic range

Linearity and dynamic range have both been measured for the amplifiers under test. The MMIC is DC blocked, and will always be operated in pulse mode, so the input signal applied for these measurements consists of a pulse with 4 ns PWHM, variable amplitude pulse provided by the Tektronix AFG3252 function generator. Both input and output pulses were monitored by the Agilent Infiniium 54855A oscilloscope. The linearity and dynamic range are plot in Figure 6.15, together with the consumed power. Both SGA4563Z and SGA4586Z models have been modified with a 3.3 k $\Omega$  feedback resistor in order to increase the dynamic range. As seen in Section 5.2, this has also positive effects in stability, but the main drawback is the increment in the power consumption and heat dissipation.

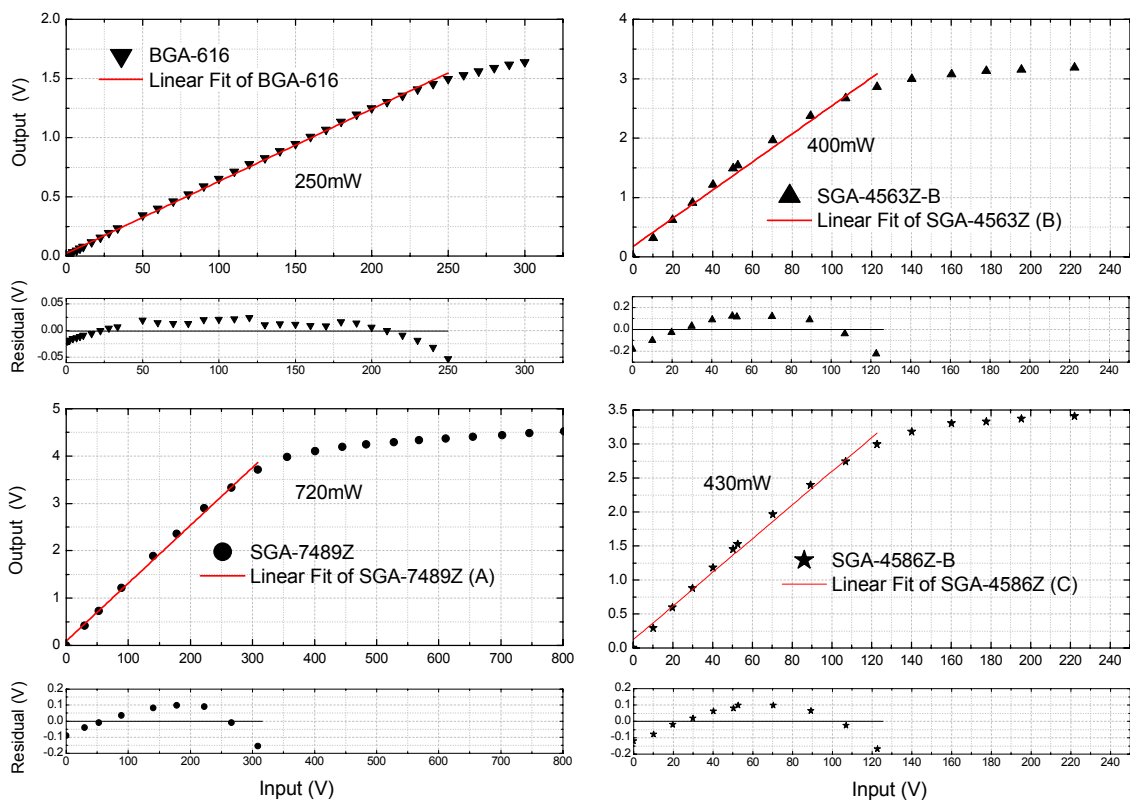


Figure 6.15 Dynamic range and linearity of several MMICs. Models noted as 'B' correspond to configurations with 3.3 k $\Omega$  feedback resistor for extended dynamic range.

Requirements and performance of BGA616 MMIC is represented in detail in Figure 6.16. The lower limit of the dynamic range is given by the noise produced by the receiver photodiode. The upper limit is determined by the dynamic range of the photodiode, which fits well with the 1 dB compression point of the amplifier, producing an overall dynamic range of  $\sim 58$  dB.

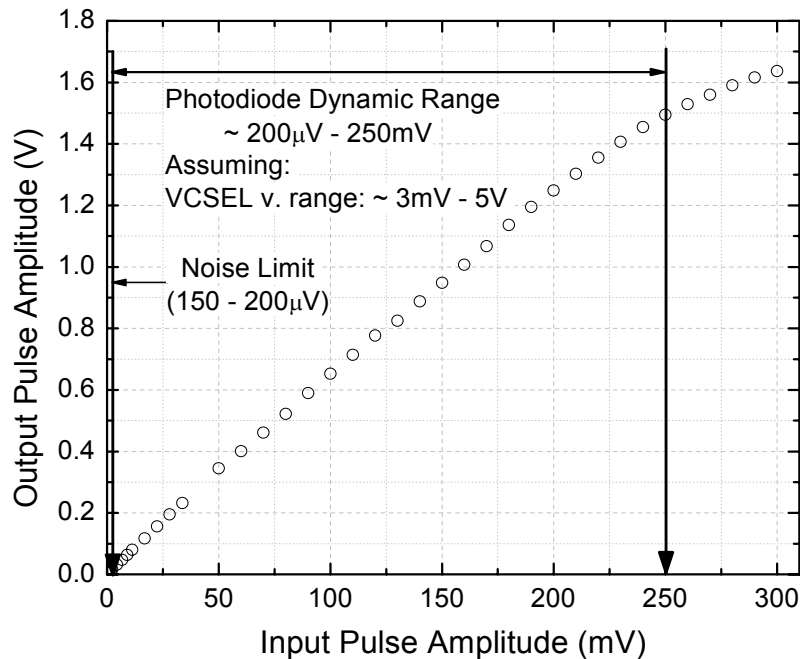


Figure 6.16 Detailed dynamic range of the receiver photodiode - MMIC set.

## 6.2 Amplifier behaviour with the photodiode as source

In order to verify the proper behaviour of the amplifier for photodetector signals, the chain VCSEL - optical fiber - photodiode - preamplifier was tested. Only the results for the BGA616 are shown, since this amplifier was already selected for the receiver boards by the time these measurements were requested. The VCSEL was fed with a 4 ns FWHM pulse with variable amplitude generated by the Tektronix arbitrary signal generator. The results are shown in Figure 6.17 for increasing values of the pulse amplitude. The upper, left plot shows the effects of a hostile environment, in which the signal of a cellular phone (900 MHz, 1800 MHz) is interfering with the measured pulse.

As the maximum output power of the amplifier is reached, the behaviour is no more linear and the pulse starts distorting, as can be seen in the last plot.

Despite this it can be observed that the signal integrity is excellent under working conditions, and for the voltage levels at which the amplifier must operate.

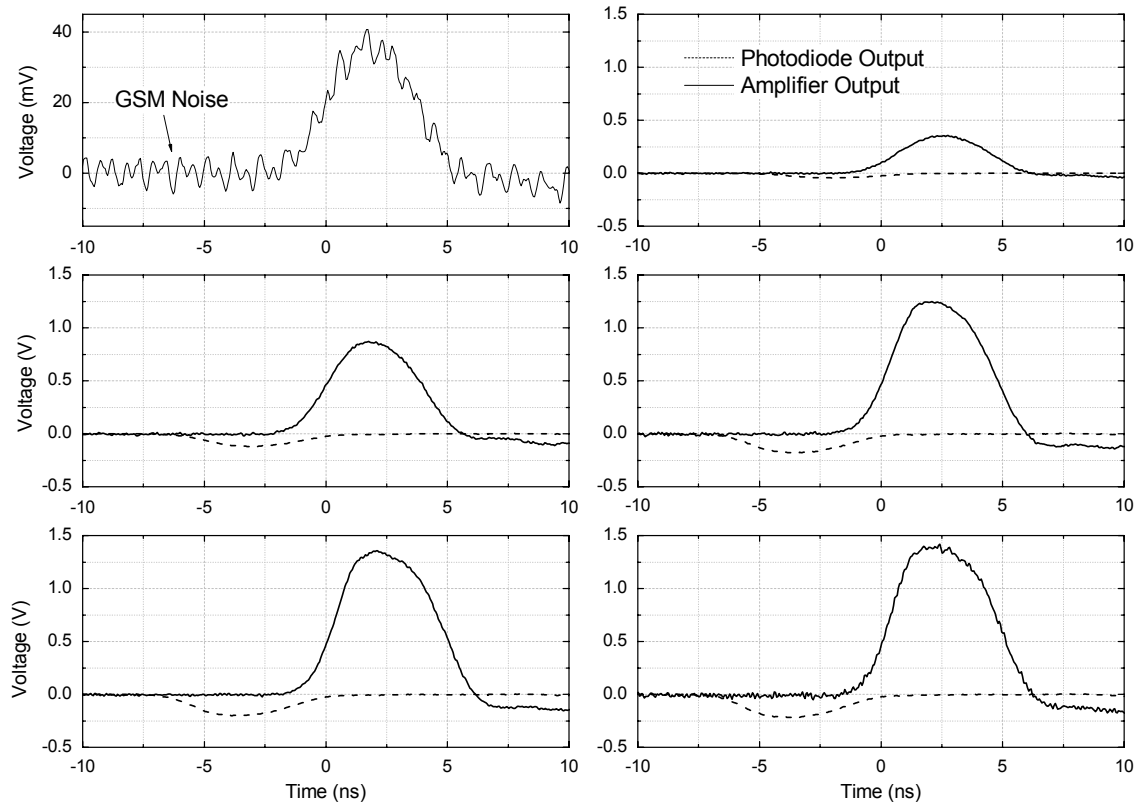


Figure 6.17 BGA 616 response for a 4 ns FWHM, variable amplitude photodiode output pulse.

## 7. NOISE AND SENSITIVITY

The noise figure of the amplifiers has been measured by means of the 'Y Factor Method' [13]. In this procedure, the noise analyzer and calibrated noise source described in Section 3 were used. Figure 6.18 illustrates this method. In the first step, a noise source with pre-calibrated excess noise ratio (ENR) is directly connected to the noise analyzer, which stores in memory several needed parameters.

In the second step, the device under test (DUT) is driven by the noise source and connected to the analyzer, which measures the actual values of the MMIC noise figure.

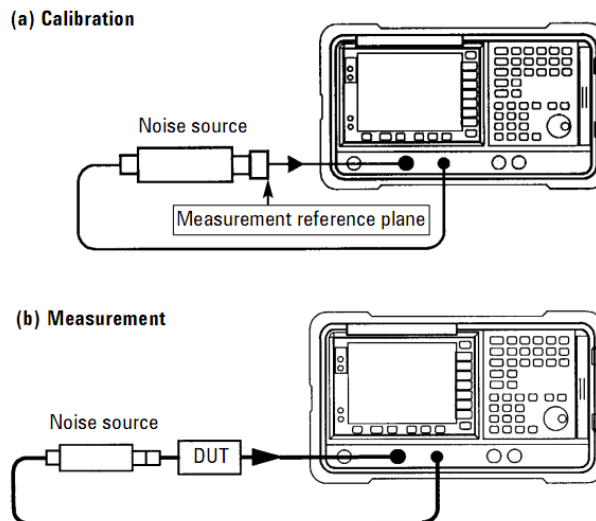


Figure 6.18 The 'Y Factor Method' for noise measurement procedure [14].

The measured noise figures of the amplifiers are plot in Figure 6.19. Once the noise figure of the amplifiers is measured, intrinsic noise produced by the amplifier at the output can be calculated.

All the relevant parameters are listed in Table 6.6. Note that the standard deviation of the output noise is in the order of microvolts, orders of magnitude lower than the noise produced by the VCSELs or the photodiodes. As all the noise components are additive, this means that the intrinsic noise of the MMICs is not a relevant parameter.



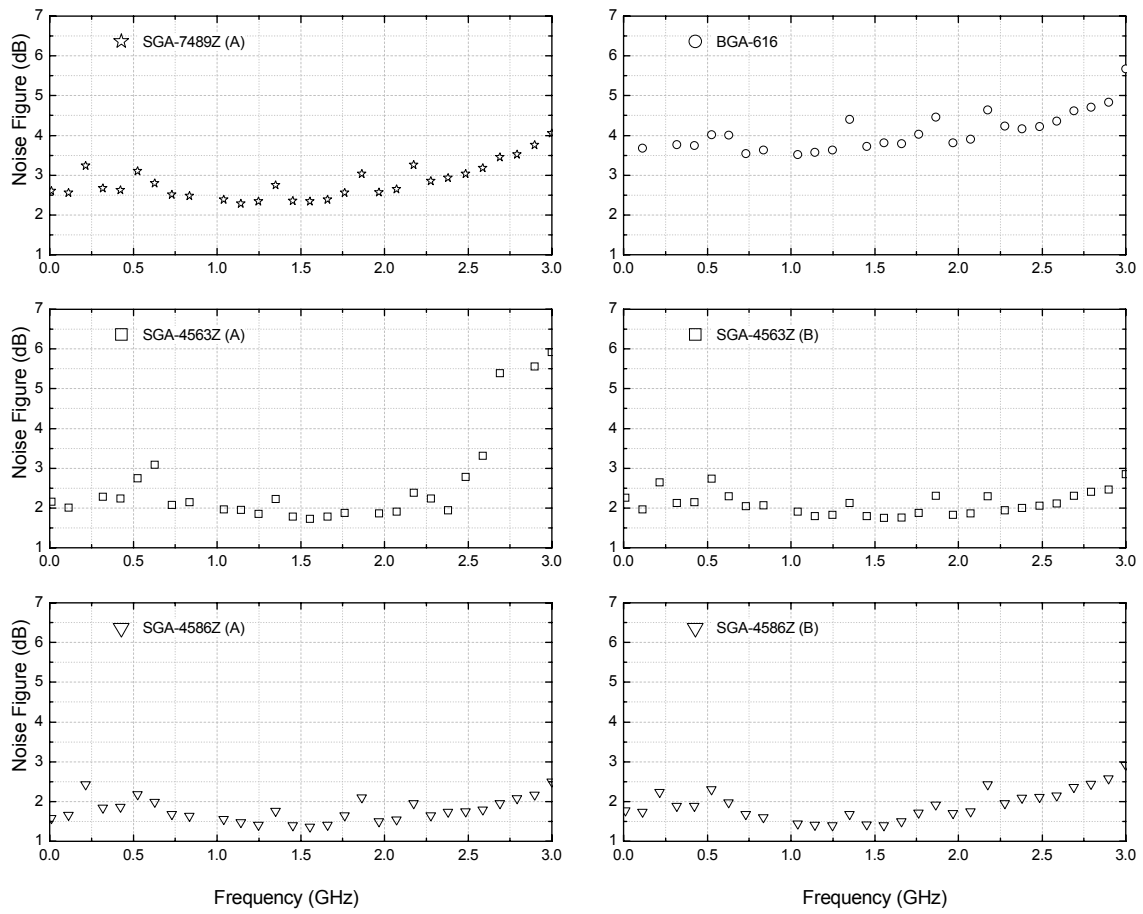


Figure 6.19 Noise figure of the tested MMICs.

MMIC	NF (dB)	Gain (dB)	BW (GHz)	$T_e$ (K)	$\sigma_{50\Omega}$ ( $\mu$ V)
<b>SGA4563Z</b>	2.34	28	0.77	207.05	37.2
<b>SGA4586Z</b>	1.93	28.5	0.60	162.27	29.9
<b>SGA7489Z</b>	2.69	23	1.10	248.76	36.5
<b>BGA616</b>	3.77	18	1.50	400.87	40.6

Table 6.6 Noise parameters of MMICs.

## 8. THERMAL STABILITY

The MAGIC Collaboration has made a special emphasis in the design of cooling systems for the camera of both telescopes. The temperature stability of the electronics plays a very important role in the overall stability of the system and the repeatability of the measurements. In the PMT, the noise due to thermoionic emission increases critically with the temperature. In all passive elements the white (thermal) noise increases with the square root of temperature, and in active devices the dependence is much more compromising. The VCSELs of MAGIC II Camera have a dedicated cooling plate to reduce instabilities due to temperature fluctuations. When the data are analyzed, the system is tagged as OK if the temperature in the center of the camera is in the range between 35 and 38 °C, so that it will be considered as the usual temperature fluctuation [14].

In the counting house, where the receiver boards are located, the ambient temperature is controlled to be between 25 and 30 °C. In the board surface, the temperature can raise up to 50 degrees as maximum.

### 8.1 Bias current stability with temperature

The two amplifiers used in the MAGIC II telescope design have been analyzed for temperature fluctuations. A thermally isolated chamber with a current controlled heater was set. The temperature was measured by means of a calibrated J thermocouple sealed with thermal paste to the MMIC surface.

Figure 6.20 shows the temperature dependence of the bias current of the amplifiers. As can be seen in the plots, variations lower than 3% of the mean value for the BGA616 and 8% for the SGA4563Z are observed, for a ~30 °C range. This approximately linear dependence can be due to the temperature dependence of the semiconductor resistivity. An increase of the temperature produces a decrease of the series resistance and thus the increment of the bias current.

### 8.2 Influence of temperature on the scattering parameters

The analysis of BGA616 scattering parameters for different temperatures shows only small fluctuations. As temperature increases, the gain also slightly increases due to the bias current increment. But, as the MMIC is built to be stable with bias fluctuations, this effect produces only fluctuations in the order of tenths of dB (see Figure 6.21).

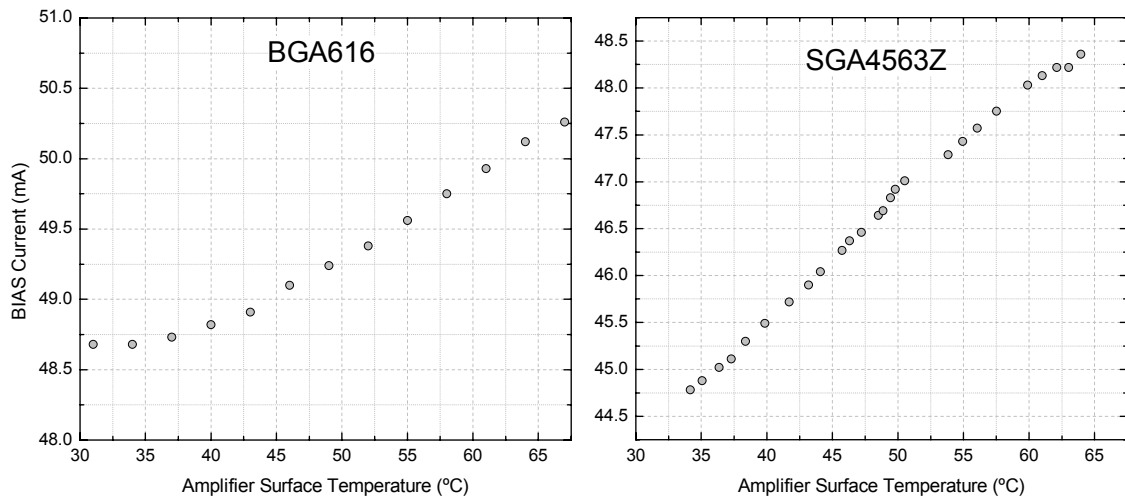


Figure 6.20 Temperature dependence of the BIAS current for BGA616 and SGA4563Z MMICs.

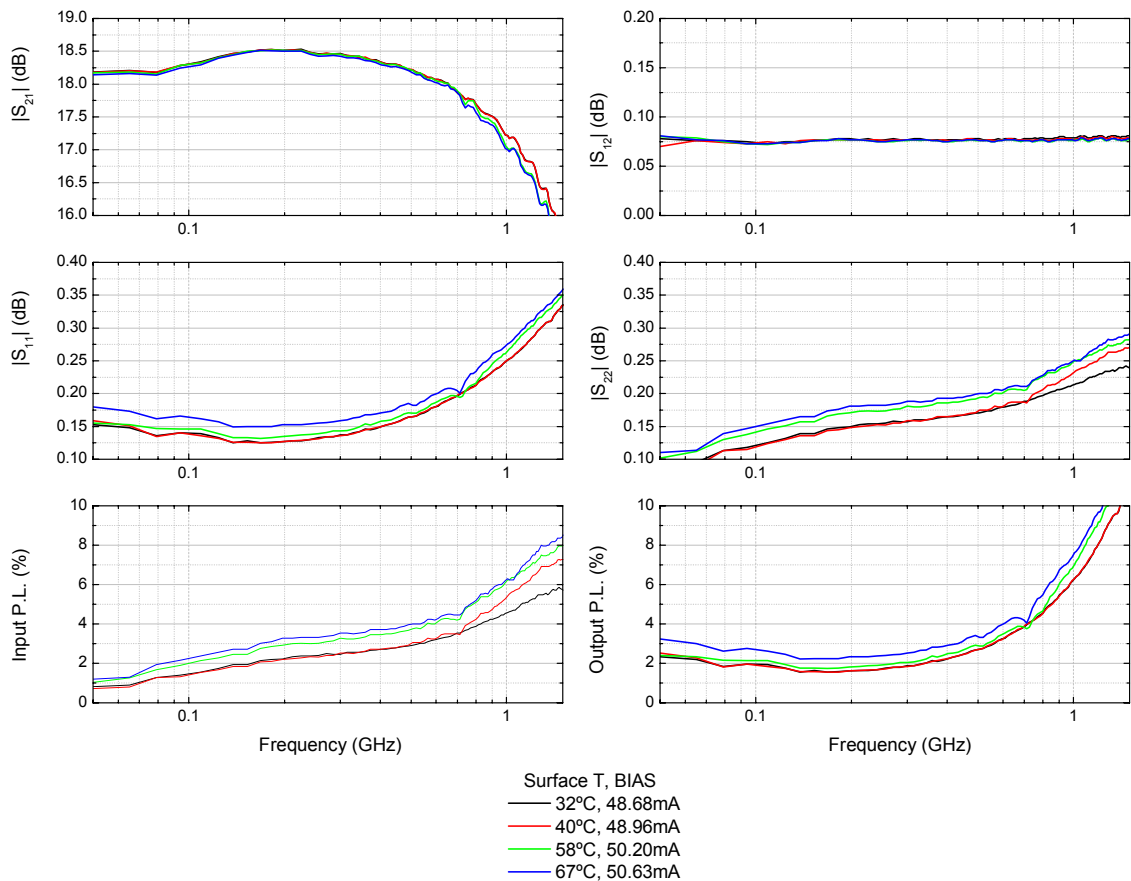


Figure 6.21 Fluctuation of the BGA616 scattering parameters with temperature variations. The lower graphs represent the power loss due to reflections at the input and at the output of the MMIC.

Regarding the amplifier matching, the reflection coefficient increases with the temperature (probably due to the decreasing series resistance of the semiconductor).

The total losses by reflection are below 8% at the input, and 10% at the output for the whole amplifier bandwidth. For frequencies lower than 1 GHz (as will be the signals from PMTs) the losses are under 6%.

If a pulse is applied to the amplifier and the output is monitored for different temperatures, Figure 6.22 is obtained. As expected from the scattering parameters analysis, only small fluctuations in the pulse are produced, and the noise increment is negligible.

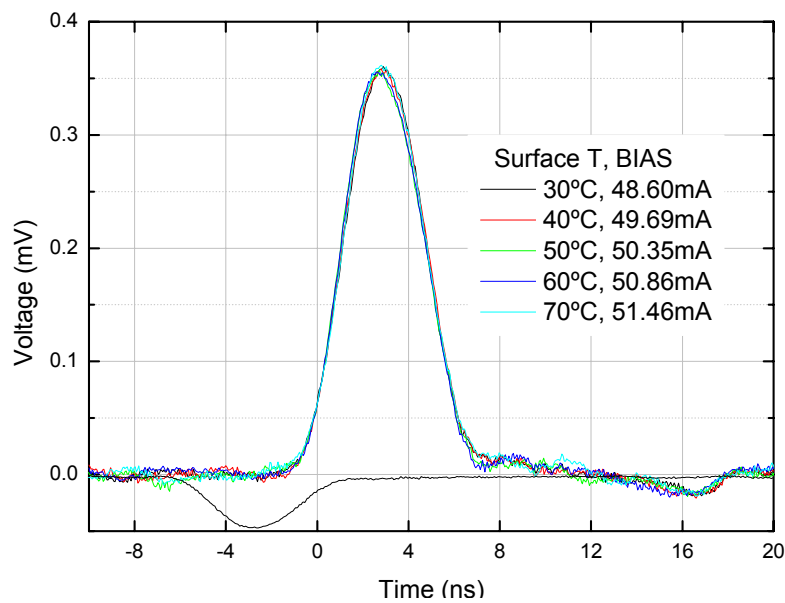


Figure 6.22 Influence of temperature variations on the amplifier output.

## 9. FINAL TESTS

Once the Receiver Boards were finally constructed, a test of the complete system was performed at IFAE laboratories.

The Receiver Board, named 'MONSTER' board, is shown in Figure 6.23a. The highlighted corresponds to the input part of the board. The optical fibers coming from the camera VCSELs are connected to the board input. The orange fiber transmits the signal to the photodiodes connected to the input of the amplifier. Figure 6.23b shows a detail of the amplifying stage, in which all the photodiodes are already connected.

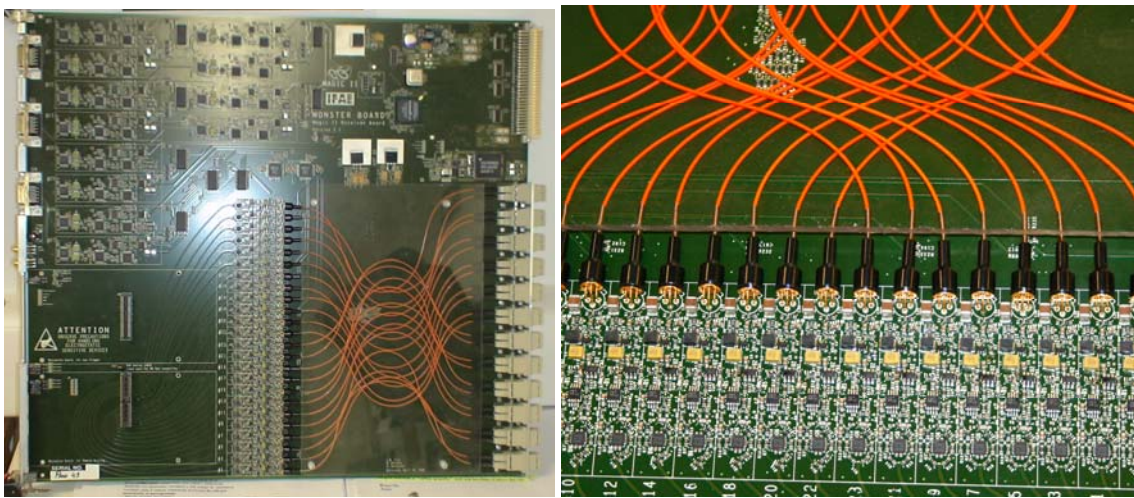


Figure 6.23 (a) Complete view of the 'MONSTER' receiver board for the MAGIC II telescope. (b) Detail: photodiode connection and pre-amplifying stage consisting on BGA616 MMICs and the corresponding bias network. The buffer amplifier for the readout electronics is also seen.

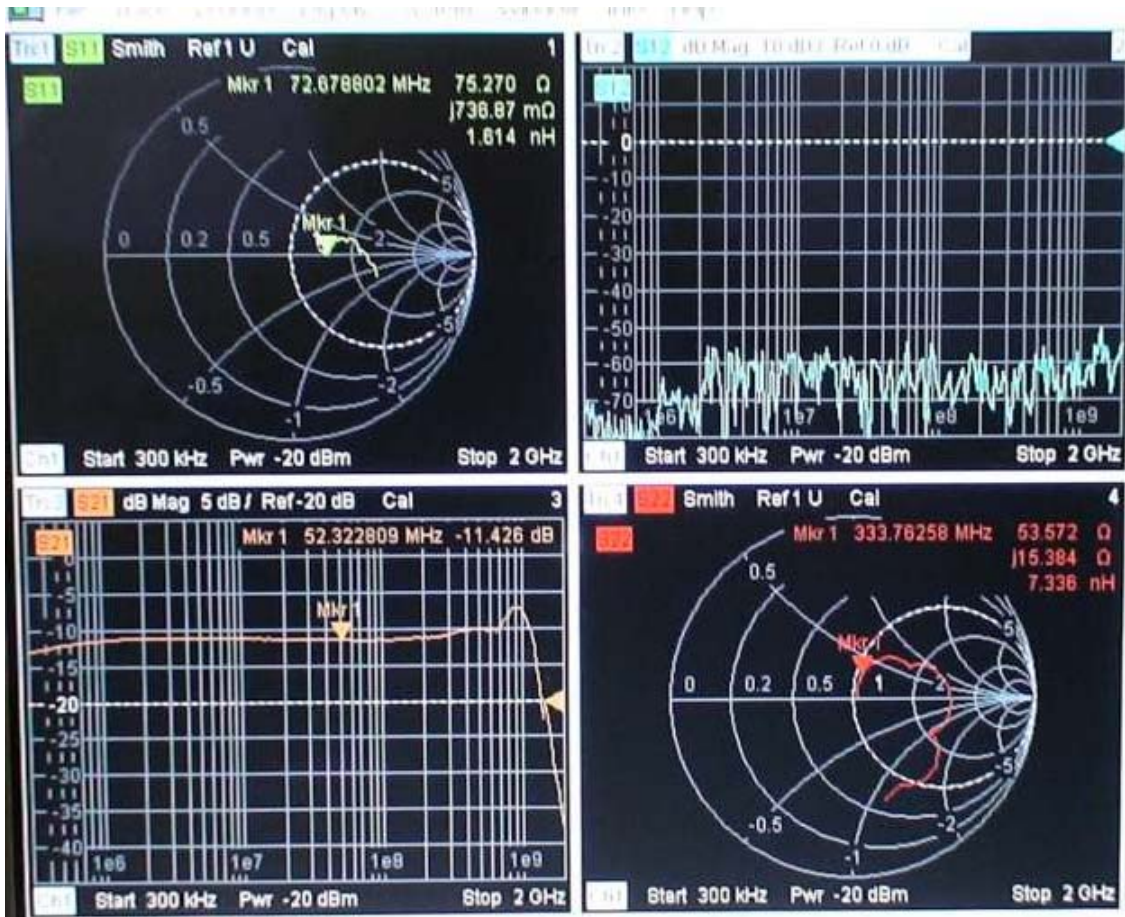
Figure 6.24a shows the setup for the test of the transmission chain. A biased VCSEL is connected to a port of the Network Analyzer. This VCSEL is connected by an optical fiber to the photodiode input, which feeds the amplifier. The other port of the Analyzer is connected to the amplifier output. In Figure 6.24b the scattering parameters of the complete system can be seen. The bandwidth is higher than 1 GHz and both the input and output are well  $50 \Omega$  matched.

When this thesis was close to be finished, some refinements were made to the receiver boards which did not affect to the photodiode preamplifier, and these boards were successfully installed and tested in the MAGIC counting house.





(a)



(b)

Figure 6.24 (a) Setup for the test of the Receiver Board: VCSEL – photodiode – preamplifier connected to a Network Analyzer. (b) Measurement of the scattering parameters. Top left:  $S_{11}$ . Top right:  $S_{12}$ . Bottom left:  $S_{21}$ . Bottom right:  $S_{22}$ . The VCSEL used in these tests had a 75 Ohm input impedance.

## 10. REFERENCES

- 
- [1] *Some Recent Trends in RFIC/MMIC Technology*, July 2005 High Frequency Electronics (p.p. 40-42)
  - [2] P.R. Gray, R.G. Meyer. *Análisis y diseño de circuitos integrados analógicos*. Prentice Hall, 3<sup>a</sup> Edición.
  - [3] D.A. Hodges. *Darlington's Contributions to Transistor Circuit Design*, IEEE Transactions on Circuits and Systems – I: Fundamental Theory and Applications, VOL. 46, NO. 1, January 1999
  - [4] Ching-Cheng Hsu. *PMT Characterization for MAGIC II Telescope*. Proceedings WSPC, October 2007
  - [5] C.C. Hsu et al. for the MAGIC Collaboration. *PMT Characterization for MAGIC II Telescope*. Proceedings of the 30th ICRC. Vol. 3 (OG part 2), pages 1507-1510
  - [6] C.C. Hsu et al. *The Camera of the MAGIC-II Telescope*. Proceedings of the 30TH ICRC. arXiv:0709.2474v1 [astro-ph] 16 Sep 2007
  - [7] *1A446 datasheet*. <http://www.oeca.de>
  - [8] P. Antoranz, J.M. Miranda, J.L. Sebastián, S. Muñoz. *Caracterización de dieléctricos mediante un método basado en la técnica TLM para medida de resistencias semiconductoras*. Proceedings of the 19<sup>th</sup> URSI, Barcelona (2004).
  - [9] J.M. Miranda, J.L. Sebastián, M. Sierra, J. Margineda. *Ingeniería de Microondas. Técnicas Experimentales*. Prentice Hall (2002)
  - [10] David M. Pozar, *Microwave Engineering*, 2nd edition, John Wiley and Sons, (1998)
  - [11] *Aplac 7.70 Reference Manual Vol. 2. Analog components*. 2002 APLAC Solutions Corporation.
  - [12] [http://www.minicircuits.com/products/bias\\_tees\\_main.html](http://www.minicircuits.com/products/bias_tees_main.html)
  - [13] *Noise Figure Accuracy – The Y-Factor Method*. Agilent Application Note 57-2.
  - [14] R. de los Reyes. *MAGIC data check and on-site analysis program*. MAGIC-TDAS 06-11, 060831/RDelosReyes





# Chapter 7

## Development of a testbench for photodetectors

1. Motivation
2. LED modelling
  - 2.1 Circuital model with high frequency effects
  - 2.2 Alternative calculations of  $R_S$  and ideality factors
  - 2.3 Parameter extraction and results
3. Design of the shielding enclosure
  - 3.1 Shielding considerations
  - 3.2 Cabling
  - 3.3 Waveguide below cutoff techniques for optical coupling
  - 3.4 Shielding effectiveness (SE) of the wall
4. Final prototype and measurements
  - 4.1 Design of the test bench
  - 4.2 Results
5. References

## 1. MOTIVATION

**I**N Chapters 3 and 4 we described different prototypes of pulse generators with pulse widths in the order of one nanosecond (and even some hundreds of picoseconds). However, these signals must be converted into light pulses in order to be useful for photodetector testing and characterization. By means of different optical arrangements, it is possible to manipulate the light beams in order to perform different tests on the detectors (time-domain response, single photon detection...). The most suitable device to perform this electro-optical conversion is the Light Emitting Diode (LED).

The fast development experienced by LED technologies in the last ten years have resulted in dramatic improvements on the efficiency, monochromaticity, time response and output power. These advances are especially remarkable in blue LEDs [1], [2], [3], and have been the main motivation for the design of the testbench presented here for photodetector studies.

In order to design a ns LED pulser free from mismatch and ringing effects it is necessary to develop suitable models for the LED impedance, which must be accurate enough up to predict this parameter at both ON and OFF states, and up to frequencies of at least 1 GHz. A model is reported in this thesis which predicts the electrical behaviour of double heterostructure GaN/SiC blue light-emitting-diodes up to microwave frequencies.

A procedure to extract the series resistance ( $R_s$ ) from the reflection coefficient is suggested. This procedure offers the advantage of using measurements at both equilibrium and high bias currents, and therefore it is possible to answer to a key question: are the values of the series resistance strongly influenced by the device heating? In addition, attention has been paid to the standard procedures based on the current-voltage curves to extract key parameters such as the DC series resistance and the ideality factor, in order to validate some key results obtained from the modelling at high frequencies.

The last section of this chapter is devoted to the integration of the LED pulser into a shielded testbench for measurements of low level pulsed signals, and evaluation of pulse distortion and noise. This test bench includes different designs of bias networks for PMTs, HPDs and solid state photodetectors.

## 2. LED MODELLING

### 2.1 Circuital model with high frequency effects

The classical theory of LEDs is based on the p-n homojunction; the new devices, however, often have more complex structures based on single and multiple quantum wells [4]. This has encouraged the development of different simulators based on the self consistent solution of the Schrödinger and transport equations [5].

However, the details of the composition and geometry of commercially available LEDs are not generally known by researchers. In addition, LED devices under usual bias operation are strongly influenced by the device heating [6], [7] and this effect is difficult to be accounted for in the simulations. Finally, the results of these kind of simulations can hardly be integrated in CAD tools for electronic and optoelectronic circuit design such as PSPICE [8], which offer the highest accuracy when they are combined with fitting factors extracted from simple measurements. A simpler, more intuitive DC model of blue LEDs, which is based on direct measurements, is proposed in this thesis.

Most of the research work published up to day in GaN/SiC devices has been addressed to improvements in different steps of the fabrication process, such as GaN doping [9], characterization of interfacial defects [10], DC and low-frequency electrical characterization [11] [12], or efficiency optimisation [13]. However, the high frequency behaviour of blue LEDs has not been yet investigated in such a detail.

With these motivations in mind, we present here a circuital model based on physically meaningful elements that is able to accurately reproduce the electrical behaviour of GaN/SiC blue LEDs in a fairly wide range of frequencies. The model takes into account the parasitic effects of package and bonding wires, the series resistance and the nonlinear behaviour of the junction capacitance and conductance. It has been verified experimentally at frequencies up to 2 GHz. The extraction of the equivalent circuit elements that reproduce the parasitic effects allows to clearly identify what is the limiting factor that affects the high frequency behaviour of the device, and what are the maximum frequencies at which the device impedance is dominated by the intrinsic behaviour of their characteristic elements rather than by parasitics. This information cannot be obtained from conventional I-V or low frequency (<10 MHz) C-V measurements.

Figure 1 shows the equivalent circuit used to simulate the device. It includes two parasitic elements  $C_p$ , and  $L_p$ , which simulate the capacitance of the device package and the inductance of the bonding wires, respectively. The other three

elements are well known and account for the intrinsic behaviour of the LED. The small section of the transmission line simulates the coaxial SMA connector where the devices are mounted.

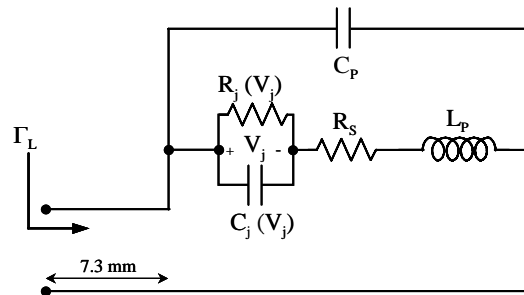


Figure 7.1 Equivalent circuit of the LED.

The series resistance has two main contributions; one is nearly constant and is located at the ohmic contacts, the second contribution accounts for the neutral part of the diodes and depends, in principle, on the bias. However this dependence is usually negligible. The series resistance is typically extracted from the I-V curve, by solving in a self consistent way the diode equation,

$$I = I_0 e^{\frac{q(V - R_s I)}{\eta k T}} \quad (7.1)$$

where the ideality factor  $\eta$  depends on the dominant conduction mechanism.

This procedure has limitations when applied to a number of devices including LEDs, which are derived from the fact that neither  $\eta$  nor  $T$  is really constant. A different approach is adopted here, in which  $R_s$  is extracted by optimization from the reflection coefficient measurements at high frequencies. The measurement is made at 0 V. The high sensitivity of the reflection coefficient to the series resistance is derived from the fact that at high frequencies the junction resistance is almost 'short circuited' by the junction capacitance. This enables an accurate extraction of  $R_s$  without any error derived from the device heating or from inaccuracies in the estimation of the ideality factor.

When a generator of impedance  $Z_0$  feeds the LED with a high frequency small AC signal, a reflected voltage emerges from the device due to the impedance mismatch. The measured reflection coefficient  $\Gamma_L$  at the calibration reference plane is related to the LED impedance  $Z_L$  through the following expression,

$$\Gamma_L = \frac{Z_L - Z_0}{Z_L + Z_0} e^{-2jw\sqrt{\mu_0\varepsilon}\ell} \quad (7.2)$$

where  $\varepsilon$  is the dielectric permittivity of the teflon and  $\ell$  the SMA connector length, which is 7.3 mm in our samples.

The measurement of  $\Gamma_L$  can be made with a network analyzer having the standard characteristic impedance of  $Z_0=50 \Omega$  in a fairly wide range of frequencies.

As shown in Figure 7.1, the device model consists of five different elements. Therefore, a single optimization of all the elements to fit the reflection coefficient measurement to the simulation at all the frequencies is neither effective nor able to provide physically sound values. However, the fairly broad band of the network analyzer enables one to measure the LED impedance  $Z_L$  even at frequencies where this impedance is dominated by parasitics. This makes possible to separately extract  $C_p$  and  $L_p$ , by optimization at the highest frequencies. Accurate initial values for  $C_j$  and  $R_j$  are obtained from conventional G-V and C-V measurements at 10 MHz, and finally  $R_s$  can be obtained by optimizing it together with a slight tuning of  $C_j$  and  $R_j$  to fit the measured reflection coefficient to the simulation at the lowest frequencies measured by the network analyzer. The identification of the ‘high’ and ‘low frequency’ bands of measurement for the optimization can easily be guessed by inspection of the bias dependence of the reflection coefficient.

In order to illustrate the accuracy of the proposed model, a SiC/GaN double heterostructure blue LED, mounted in a standard T-1 3/4 lamp [14] has been tested. The device has a vertical structure with a p-n junction effective area of  $240 \times 240 \mu\text{m}$ , and features a radiant flux of  $1150 \mu\text{W}$  at 20 mA. Other references provide additional details on the device structure [15] and emission spectra [16]. The measured and simulated reflection coefficient for a bias voltage of 0 and 4.5 V are shown in the Smith charts of Figure 7.2. As it can be seen, theoretical and experimental curves can hardly be distinguished at any of the bias points, and the final values obtained for the parasitic elements are fairly not dependent on the bias. In addition, the values for  $C_p$ , rather small in comparison with other RF diodes, and  $L_p$ , relatively large, are in good agreement with the physical structure of the chip mount, which features a significantly long bonding wire at the anode and low capacitive effects between anode and cathode contacts.

The parasitic elements  $C_p$  and  $L_p$  were extracted by optimization of the reflection coefficient from 500 MHz to 2 GHz. The Gradient algorithm [17] was used, and the results were confirmed by repeating the optimization with two additional numerical routines, based on the MinMax and NelderMead techniques [18] [19]. As it can be seen in Figure 7.2, the impedance in this range is nearly insensitive to the bias, and therefore is dominated by parasitics. This

fact was confirmed by the strong variation of the reflection coefficient observed when either of the two elements was 'manually' tuned while keeping constant the other three elements of the model.

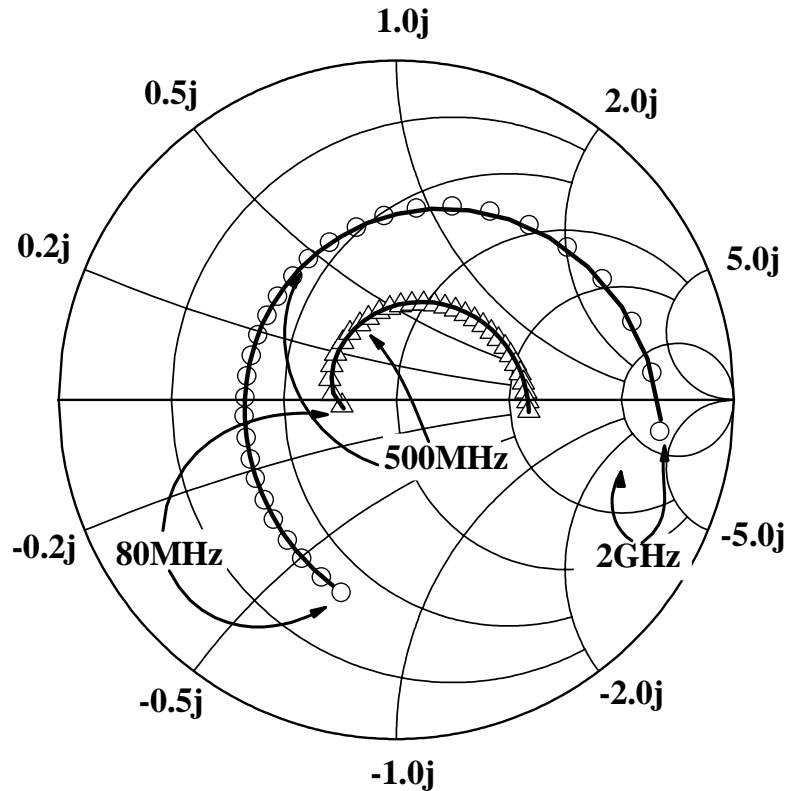


Figure 7.2 Measured (symbols) and simulated (line) reflection coefficient of the diode in equilibrium (circles) and with a forward bias of 4.5 V (triangles).  $|Γ_L|$  for 4.5 V has been divided by 3 in order to differentiate the curves better. The values of the elements used in the simulation are:  $R_j=1371 \Omega$ ,  $C_j=54.92 \text{ pF}$ ,  $R_s=19 \Omega$ ,  $C_p=0.3 \text{ pF}$ ,  $L_p=6.5 \text{ nH}$  (equilibrium), and  $R_j=11.54 \Omega$ ,  $C_j=145 \text{ pF}$ ,  $R_s=19 \Omega$ ,  $C_p=0.3 \text{ pF}$ ,  $L_p=6.5 \text{ nH}$  (bias of 4.5V).

Initial values for the optimization of  $R_j$  and  $C_j$  were obtained from the differential impedance measured at 1 MHz. Then  $R_s$ ,  $C_j$  and  $R_j$  were optimized in the full range of frequencies at which the reflection coefficient was measured.

An ideality factor of  $\eta=8.5$  was estimated by making I-V curves, following the procedure which will be shown in next section. This factor was calculated after estimating the series resistance from the reflection coefficient measurements and extracting the corresponding voltage drop from the total measured voltage.

In order to minimize the effects of the device heating on the calculation, only the lowest current points that fit well to the diode equation were used. The anomalously high value obtained for  $\eta$  agrees well with the reports made by other authors in the characterization of similar devices [4].

Two different arguments have been defended to explain ideality factors above 2 in these devices: the existence of multiple junctions inside the device, and the presence of deep-level-assisted tunnelling effects.

Figure 7.3 shows the differential admittance of the LED, as measured with a HP 4192A Impedance analyzer, the junction capacitance and resistance measured at RF and microwave frequencies and a non linear fit to the measured capacitance for the full range of frequencies. This fit was achieved with the following model

$$C = C_j + \frac{C_1}{1 + (\omega\tau_1)^2} + \frac{C_2}{1 + (\omega\tau_2)^2} \quad (7.3)$$

The presence of several junctions in the device is consistent with the observed dependence of the measured conductance on the frequency below 10 MHz. Although a single frequency dependent junction conductance and capacitance would explain the measurements as well, no tunnelling effects with time constants as high as the ones observed here have been found in the literature.

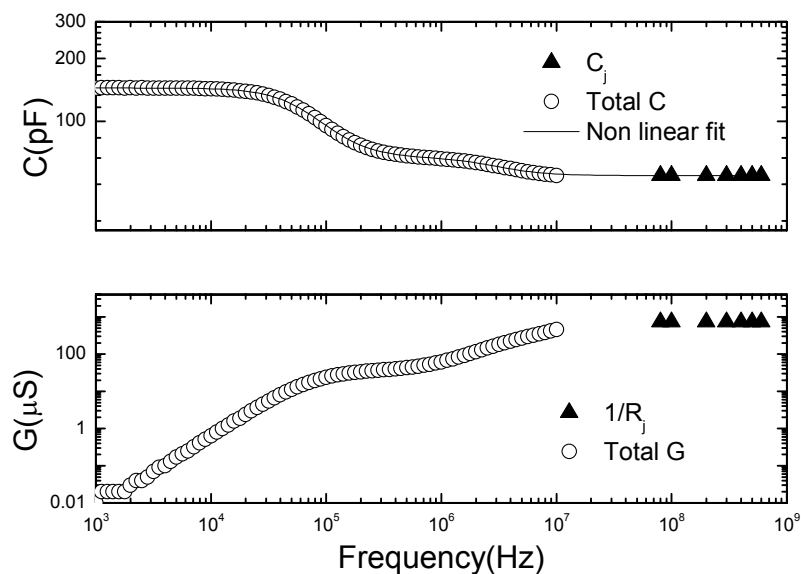


Figure 7.3  $C$ - $f$  and  $G$ - $f$  curves at 0 V. Total low frequency conductance and capacitance (open circles) and high frequency junction conductance and capacitance (stars). The nonlinear fit shown in the capacitance plot was obtained with  $C_1=77.5$  pF,  $\tau_1=2.08$  ns,  $C_2=12$  pF,  $\tau_2=54.9$  ns,  $C_j=54.92$  pF.

It must be pointed out that the three contributions to the frequency dependent capacitance measured here are additive and therefore cannot account for three different capacitances located in different parts of the device and connected in series. Therefore, the lorentzian dependence of the capacitance is an attribute that must be assigned to the full device rather than to individual parts

of it. Nevertheless, the high accuracy of the model given by Figure 7.1 demonstrates that multiple junctions need only be considered below 10 MHz.

In summary, it is worth to mention the following concluding remarks:

- 1) The model proposed here to predict the high frequency behaviour of DH SiC/GaN blue LEDs is able to accurately estimate the device impedance even at frequencies at which this impedance is fully dominated by parasitics. The parasitic inductance of the bonding wire has been identified as the main limiting factor in the high frequency behaviour of the device.
- 2) The admittance measured up to 10 MHz is consistent with the high frequency model presented in this Chapter, by assuming a non linear lorentzian behaviour of the device capacitance with two different time constants.
- 3) The frequency dependence of the conductance measured below 10 MHz could be explained by the presence of multiple rectifying junctions, but at higher frequencies a single junction model is accurate enough.
- 4) An anomalously high value of the ideality factor in the DH SiC/GaN blue LED presented in this work confirm previously reported work in similar structures.
- 5) The high sensitivity of the reflection coefficient at 0 V to the series resistance enables the calculation of this factor without any errors derived from the device heating or from the inaccuracies in the estimation of the ideality factor.

## 2.2 Alternative calculations of $R_s$ and ideality factors

The small signal equivalent circuit of the LED described in the previous section contains a number of different unknowns: the intrinsic elements are bias dependent and nonlinear, and the LED mount contains parasitics that cannot be estimated by theoretical considerations. This has motivated different techniques based on trying to extract some parameters of the equivalent circuit by means of other independent measurements.

On the other hand, the extracted values of the series resistance and ideality factor of the LED which have been reported in the previous section have motivated us to look for an alternative approach in order to confirm whether the optimization of our suggested procedure provides physically sound values or not.



The current-voltage characteristics are typically used to obtain information on diode parameters, including the ideality factor and the series resistance. Although the corresponding procedures are well known and simple when applying to a conventional diode, the modelling of the I-V curves of a LED is not straightforward. Two main difficulties must be addressed: the high series resistance and the thermal effects, since the device is not at room temperature.

This Section aims to study how to obtain a model able to accurately reproduce the current voltage characteristics of light emitting diodes even at the highest operating bias points. This model makes use of a simple, empirical current-temperature dependence, and postulates the presence of two different conduction mechanisms. It accounts for the influence of the series resistance, and for the temperature dependence of the inverse saturation current. The accuracy of the model is illustrated by comparing the simulated and measured I-V curves of different commercially available LEDs.

The considerations described above set a motivation to develop a model for the DC behaviour of LEDs with the following main goals in mind:

- It must be able to accurately reproduce the DC curves even at the highest operating currents, which are in fact the usual ones under common operation of LEDs.
- It must be compatible with the increase of temperature shown by the experimental evidence.
- It must be compatible with the fact that the reverse saturation current is temperature-dependent.
- It must be simple enough to be integrable in conventional circuit theory CAD tools.
- It must not require a detailed knowledge of the internal device composition and structure.

In order to fulfil these objectives we postulate a model for forward bias that accounts for three different conduction mechanisms, leading to a dependence of the measured current  $I_{meas}$  versus measured voltage  $V_{meas}$  given by

$$I_{meas} = I_{or} \left( \exp \left( \frac{q(V_{meas} - R_S I_{meas})}{n_r k T} \right) - 1 \right) + I_{oi}(T) \exp \left( \frac{q(V_{meas} - R_S I_{meas})}{n_i k T} \right) + \frac{V_{meas} - R_S I_{meas}}{R_{sh}} \quad (7.4)$$

where  $I_{or}$ ,  $I_{oi}$  are the reverse saturation currents,  $R_S$  the series resistance,  $R_{sh}$  the parasitic shunt resistance and  $n_r$ ,  $n_i$  fitting factors.  $R_{sh}$  can be originated by any channel that bypasses the ideal junction. This bypass can be caused by surface states or damaged regions of the intrinsic junction. When  $R_{sh}$  is not

negligible, the I-V curve exhibits a linear dependence at reverse bias or even at low forward currents.

After testing the I-V curves under reverse operation, it was found that all the diodes presented in this work have a shunt resistance above 5 GHz and therefore the third contribution to  $I_{meas}$  in (7.4) will be considered negligible. In the following paragraphs, the first contribution to the current shown in (7.4) will be called the 'low current term' (LCT), and the second contribution the 'high current term' (HCT). Since the LCT is dominant at low currents, the temperature dependence of  $I_{or}$  is neglected. However, the influence of the series resistance must be kept in order to avoid an overestimation of this contribution at the highest currents against the HCT.

The proposed model is considered valid only for forward bias since it does not take into account reverse bias conduction mechanisms as avalanche breakdown or tunnelling effects. However, despite what happens in other diodes the modelling of the reverse bias in a LED is of marginal use.

The dependence of  $I_{oi}$  with temperature is assumed to be similar to that of an heterojunction dominated by the thermionic emission mechanism [20],

$$I_{oi}(T) = I_{00}T \exp\left(-\frac{qE_G}{kT}\right) \quad (7.5)$$

where  $I_{00}$  is a constant, and  $E_G$  is the energy GAP in eV of the active layer. This dependence differs from the one expected for a conventional p-n homojunction dominated by the drift-diffusion mechanism [21]. A linear temperature dependence of  $E_G$  can be assumed in the high temperature limit. Therefore,

$$E_G = E_{G00} - \gamma T \quad (7.6)$$

where  $E_{G00}$  and  $\gamma$  are empirical factors which fit the curve  $E_G(T)$  to a straight line within the operating temperature range of a LED, typically from 290 K to 370 K. Substituting (7.6) into (7.5) yields

$$I_{oi}(T) = I'_{00}T \exp\left(-\frac{qE_{G00}}{kT}\right) \quad (7.7)$$

where  $I'_{00}$  is a constant that groups two factors,  $I_{00}$  and  $\gamma$ , that are usually unknown.

The temperature increase at the highest currents can be obtained by means of the thermal resistance concept [22]. If  $R_{TH}$  is the thermal resistance between the junction and a point of the package that can be reached by a thermocouple probe,  $T$  can be obtained from the temperature measured by the probe  $T_P$  with the following equation,

$$T = T_p + R_{TH} P_D = T_p + R_{TH} V_{meas} I_{meas} \quad (7.8)$$

where  $P_D$  is the total power dissipated by the device. All the measurements were made once a constant temperature state was reached. It was observed that in conventional packages such as the T1-3/4 (5 mm) lamps a more useful dependence of  $T$  versus bias can be assumed,

$$T = T_R + \theta I_{meas} \quad (7.9)$$

where  $T_R$  is the room temperature and  $\theta$  is constant. If the thermal resistance is not known,  $\theta$  must be an additional fitting factor. The thermal resistances given by manufacturers were used in the simulations presented here.

An accurate extraction of  $R_S$  can be made by means of RF measurements with a network analyzer [23].  $R_S$  is obtained by optimization of the reflection coefficient measurements at frequencies between 100 MHz and 500 MHz, and at 0 V or moderate bias. The high sensitivity of the reflection coefficient to the series resistance is derived from the fact that at high frequencies the junction resistance is practically 'short circuited' by the junction capacitance. This enables an accurate extraction of  $R_S$  without any error derived from the device heating or from inaccuracies in the estimation of the ideality factor.

### 2.3 Parameter extraction and results

The procedure used to extract the model parameters starts with the analysis at the lowest currents, where the junction temperature can be assumed as the room temperature and the recombination term in (7.4) is dominant. It is assumed that the bias voltage is high enough to neglect the factor '-1' in the recombination term. Therefore, the measured voltage can be written as [24]

$$V_{meas} = \frac{n_r k T_R}{q} \ln \frac{I_{meas}}{I_{0r}} + R_S I_{meas} \quad (7.10)$$

Differentiating with respect to  $I_{meas}$ ,

$$I_{meas} \frac{dV_{meas}}{dI_{meas}} = \frac{n_r k T_R}{q} + R_S I_{meas} \approx \frac{n_r k T_R}{q} \quad (7.11)$$

Equation (7.9) enables us to obtain  $n_r$  and then  $I_{0r}$  is extracted from (7.10), by assuming that  $R_S I_{meas}$  is negligible. Once the recombination part was obtained, the thermal resistance was used to obtain the junction temperature from (7.6), and then (7.7) was used to obtain  $\theta$ .  $R_S$  was extracted from RF measurements [23], and  $n_i$  was approached to  $n_r/2$ . This leaves only one parameter,  $I_{00}$  as a fitting factor for the I-V curve at high currents. Finally, the accuracy was

maximized by performing a slight tuning of  $I'_{00}$ ,  $n_i$  and  $E_{G00}$ , and making a second simulation in an iterative way.

The final simulated values of the theoretical currents at the highest operating points must be obtained by means of a self consistent procedure, especially when the series resistance is high. This is due to the fact that (7.4) is implicit. Therefore, if one uses the measured current as the factor which multiplies to  $R_S$  in (7.4) to obtain a calculated current  $I_{th}$ , the final value of  $I_{th}$  will not verify (7.4) due to the discrepancies between the measurement and the simulation. In order to avoid this problem, a self consistent algorithm was devised. This algorithm starts with an initial guess for the calculated current, which is made by using (7.4) with  $I_{meas}$  as parameter which multiplies to  $R_S$ . Then an array of possible theoretical currents is defined within an interval around this preliminary estimation at each bias point. Equation (7.4) is then used to test the consistency of each current of the array. The final value for  $I_{th}$  is taken as the current  $I$  of the array that minimizes  $\varepsilon$ , where  $\varepsilon$  is defined as

$$\varepsilon = \left| I - I_{0r} \left( \exp \left( \frac{q(V_{meas} - R_S I)}{n_r kT} \right) - 1 \right) - I_{0i}(T) \exp \left( \frac{q(V_{meas} - R_S I)}{n_i kT} \right) \right| \quad (7.10)$$

In order to verify the model described above, measurements of different commercially available LEDs were performed. The main characteristics of the devices are shown in Table 7.1, together with the codes supplied by the manufacturer. In order to investigate the versatility of the proposed model at other wavelengths, a red and an ultraviolet device were also included in our measurements. All the devices have a standard T1-3/4 package.

LED	Peak $\lambda$ (nm)	Spectral line half-width (nm)	Luminosity or output power @ 20 mA
#1 HLMP-EG08-WZ00	635	17	12 Cd
#2 MARL 110106	470	25	3 Cd
#3 HLMP-DB25-B0000	426	60	0.04 Cd
#4 HUVL370-510	370	20	1.5 mW

Table 7.1 Measured Devices

Figure 7.4 shows the measured and simulated I-V curves, and illustrates the influence of neglecting either the temperature increase or the series resistance in the simulation of the UV diode.

The accumulated error of the simulation as a function of the series resistance and  $\theta$  is plotted in Figure 7.5. As  $R_S$  is known by means of RF measurements  $\theta$

can accurately be determined, since only one value of  $\theta$  provides a good fit to the experimental I-V curve for a fixed  $R_S$ .

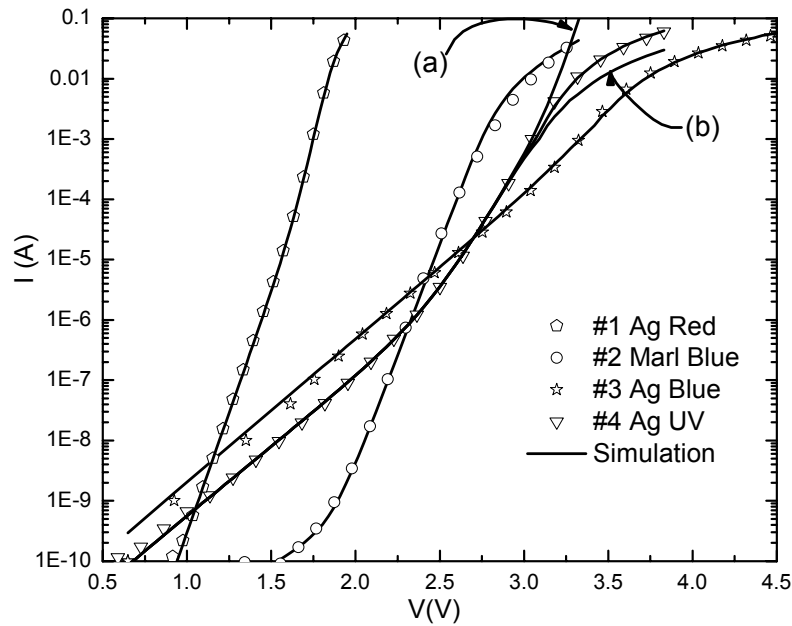


Figure 7.4 Measured and simulated I-V curves. Effect of the neglect of the series resistance [curve (a)] and the heating of the device [curve (b)] in LED# 4 are also shown.

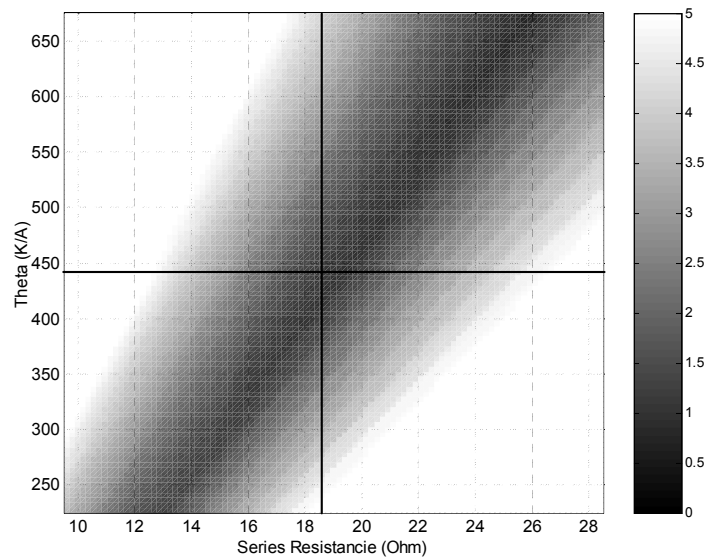


Figure 7.5 Accumulated error of the simulation as a function of  $R_S$  and  $\theta$  (LED # 4). The vertical and horizontal lines indicate the values used in the simulation. This error was calculated as

$$\varepsilon_{Acc} = \sum_{K=1}^N \left| \log(I_{meas_K}) - \log(I_{sim_K}) \right|$$

where  $N$  is the number of measured IV points,  $I_{meas}$  the measured current and  $I_{sim}$  the simulated one.  $N=101$  in all the measurements presented here.

The fact that the simulations reproduce the measurements in samples with different wavelengths, fabricated by different manufacturers and in different test conditions assured that equation (7.4) has a fairly wide margin of applicability.

The extracted model parameters are shown in Table 7.2. As it can be seen in this table,  $n_r$  is nearly equal to  $2n_i$  in all cases. This relationship is not expected to have any physical meaning, since  $n_r$  and  $n_i$  are factors which correspond to independent conduction mechanisms. However, it is a useful empirical relationship that helps to make a preliminar estimation of one factor once the other has been estimated. Furthermore, it was observed that the tuned values for  $E_{G00}$  agree well with the following simple relationship,

$$E_G = 1.02 \frac{hc}{q\lambda_{peak}} \quad (7.11)$$

where  $E_G$  is expressed in eV and  $\lambda_{peak}$  is the peak wavelength. Equation (7.11) is particularly helpful when the active layer material is not known.  $\lambda_{peak}$  is usually provided by the LED manufacturer, or it can be easily measured.

LED	$I_{or}$ (pA)	$I_{oo}$ (A/K)	$R_s$ ( $\Omega$ )	$\Theta$ ( $A^{-1}$ )	$n_r$	$n_i$
#1 HLMP-EG08-WZ00	$3.5 \cdot 10^{-6}$	$1.15 \cdot 10^{-4}$	1.9	340	2.14	1.23
#2 MARL 110106	$1.3 \cdot 10^{-4}$	$3 \cdot 10^{19}$	21	1100	4.7	2.3
#3 HLMP-DB25-B0000	8.65	$1.7 \cdot 10^{29}$	24	500	7.2	3.7
#4 HUVL370-510	1.8	$4.42 \cdot 10^{36}$	18.5	440	7	3.3

Table 7.2 Model Parameters

This model is, therefore, well suited for high currents, where the device performance becomes affected by the thermal heating and the parasitic effect of the series resistance. These influences on the accuracy of the simulations show that an underestimation of the junction temperature can lead to an underestimation of the series resistance. Therefore, it is convenient to obtain either this resistance or the junction temperature by means of an independent measurement, as the RF impedance measurements described in the previous section. Once one of these two parameters is known, the DC curves can be used to avoid multiple solutions in the extraction of the other.

### 3. DESIGN OF THE SHIELDING ENCLOSURE

#### 3.1 Shielding considerations

One of the main issues to address in the testing of photodetector sensitivity and noise is the electromagnetic shielding. In order to illustrate the problem, an experiment was made with a sample of a MAGIC II pixel chain. The output of the PMT was connected to a spectrum analyzer with an internal low noise amplifier working in the 10 kHz - 3 GHz band, as shown in Figure 7.6. The signals coming from mobile phone GSM operators, TDT and analog TV signals could be observed very clearly. In order to minimize the influence of these spurious peaks on the photodetector tests, attention was paid to the design of a suitable metallic enclosure.

The shielding of a conductive wall is usually specified in terms of the shielding effectiveness ( $SE$ ), which is defined as the inverse of the effective transmission factor  $T_{eff}$ ,

$$SE(dB) = 20 \log \frac{1}{|T_{eff}|} \quad (7.12)$$

In the calculation of this transmission factor, the multiple reflections at both sides of the wall are considered. It is in principle easy to get a  $SE$  of over 100 dB from very thin metals at frequencies above 10 MHz, but in practice the  $SE$  is seriously compromised by the fields that leak from even the smallest apertures, and also by cabling. Control of apertures and cable penetrations is in fact the key to achieving good  $SE$  figures - especially at frequencies above 100 kHz - than the type or thickness of the wall.

It is generally assumed that the interferences enter into a shielded box through an aperture in a way similar to a fluid. However, when a field impinges upon a shielding conducting wall, currents flow in its surface. When these currents encounter an aperture, they must divert from their preferred path in order to flow around it. Diverting a current creates an inductance and the  $H$  fields associated with that are in exactly the right orientation to pass straight through the aperture, which means straight through the shield material, and as a result the  $SE$  is degraded.

Furthermore, resonances could occur that greatly amplify the leakages through the apertures at certain frequencies. All apertures in shielded enclosures behave as slot antennas, by radiating/transmitting EM energy through the shield. The lowest resonance of an aperture is the frequency at which its longest dimension equals half of the wavelength ( $\lambda/2$ ). Below this first resonance the

efficiency of the antenna is assumed to reduce at 20 dB per decade. This is shown in Figure 7.7, where the *SE* of a single aperture was calculated under far-field conditions.

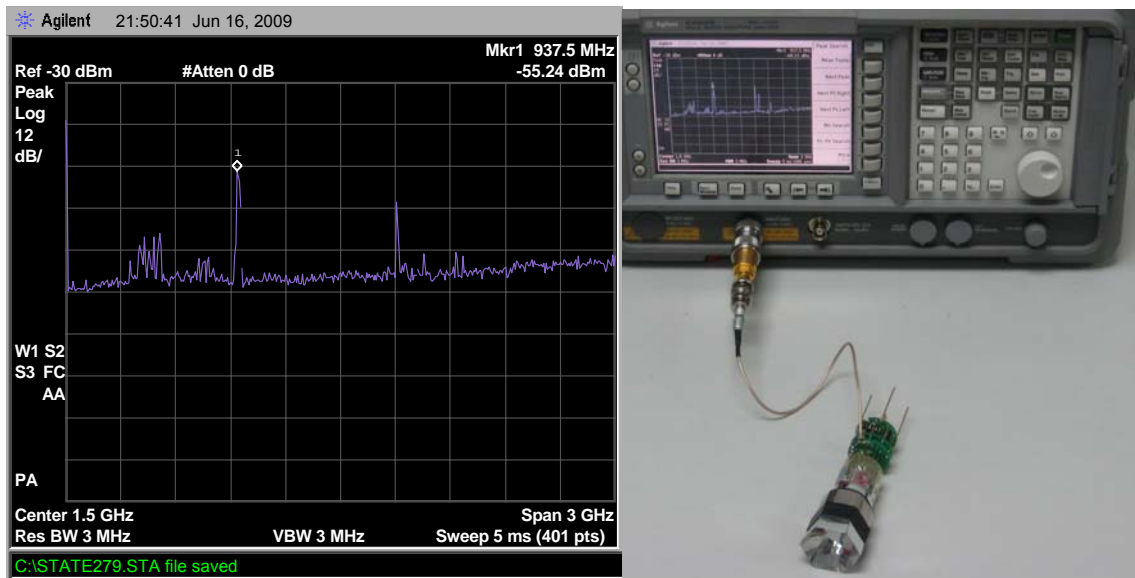


Figure 7.6 Measurement of the antenna effect of a MAGIC II PMT pixel with a spectrum analyzer. The photomultiplier and the preamplifier were both unbiased and the Winston cone is used. Similar values were obtained without the Winston cone, and with a backside shielding.

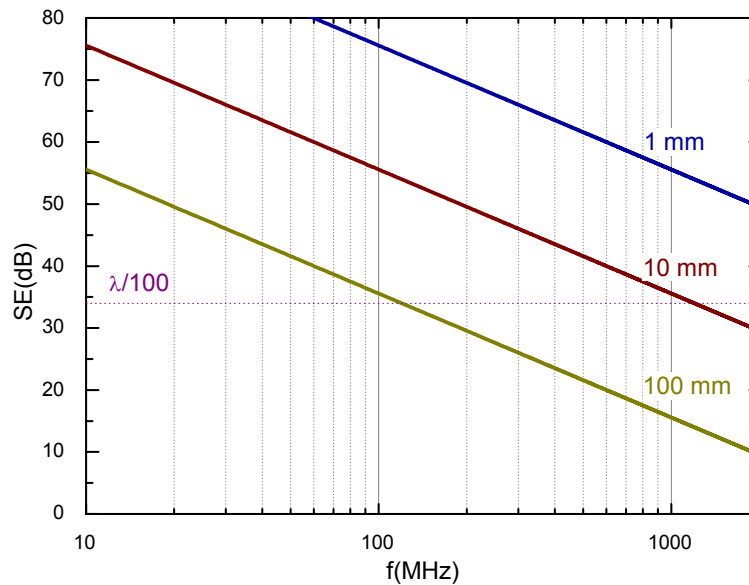


Figure 7.7 Simulation of the degradation of shielding effectiveness of a wall with a single circular aperture as a function of the diameter. Far field conditions are assumed.



## 3.2 Cabling

To obtain the full EM performance able to provide the cable shielding, it is important to electrically bond (360°) the shield correctly at both ends of the cable [25]. When a shield interacts with an EM-field, currents flow in it. 'Skin Effect' makes RF currents travel on the surface of a shield, with current density diminishing with depth into the shield's metal by around 36% for every 'skin depth'.

Ideally the shield should have several skin depths of thickness at the lowest characteristic frequency of the pulses. Figure 7.8 illustrates this situation. With a 360° shield coverage at each joint and enough metal thickness, the skin effect tends to force the external surface currents to flow on the outside of the box, and the internal ones on the inside.

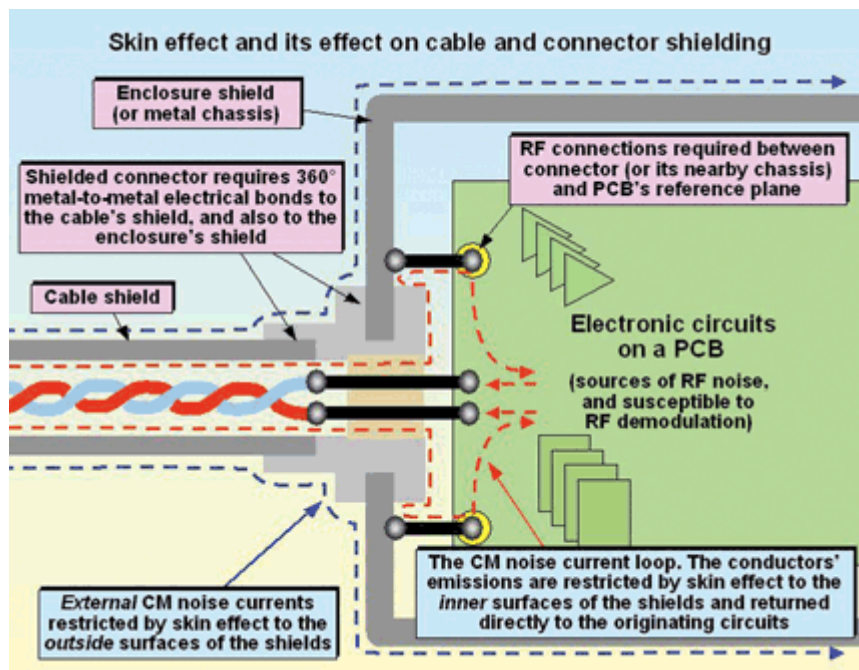


Figure 7.8 Effective cable connection to a shielded box [25].

Finally, it is worth to mention that any unshielded conductor may behave as an antenna, picking any external radiated interference, and coupling it to the inner side. An electromagnetic field solver can simulate accurately these kind of effects. Figure 7.9 shows an example of a single wire radiating field inside a shielded box [26].

Therefore, in the design of our test box, shielded coaxial cables and connectors were used not only for the photodetector signal, but also for the bias and the slow control.

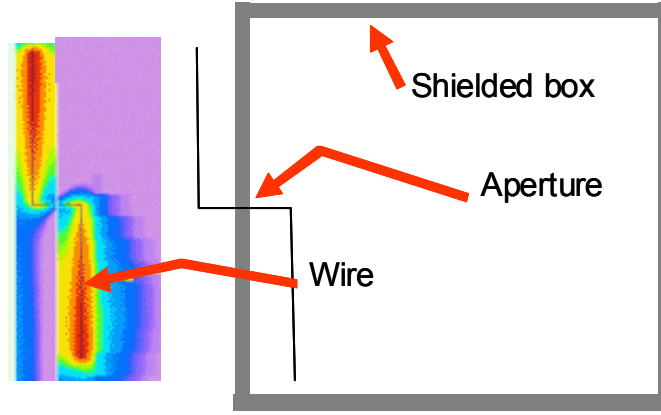


Figure 7.9 Unshielded wire radiation inside a conductive box [26].

### 3.3 Waveguide below cutoff techniques for optical coupling

Hollow waveguides working below cutoff may be used in shielded enclosures to provide access for optical fibers with nearly no risk of electromagnetic interference coupling. In these waveguides it is not possible to transmit transverse electromagnetic field modes (TEM). The transverse electric (TE) and transverse magnetic (TM) mode fields have a dependence along the propagation axis  $z$  given by

$$\vec{\mathbf{H}}(z) = \vec{\mathbf{H}}_0 e^{-j\beta_{mn}z}; \quad \vec{\mathbf{E}}(z) = \vec{\mathbf{E}}_0 e^{-j\beta_{mn}z} \quad (7.13)$$

Where the phase constant for each mode is  $\beta_{mn} = \sqrt{k^2 - k_{cnn}^2} = \sqrt{\mu_0 \epsilon_0 (\omega^2 - \omega_{cnn}^2)}$ , and  $\omega_{cnn}$  is the angular cutoff frequency. In the case of a waveguide with a circular cross section of diameter  $a$ , the lowest cutoff frequency corresponds to the TE<sub>11</sub> mode and is given by

$$\omega_{c11} = \frac{1.84}{a\sqrt{\mu_0 \epsilon_0}} \quad (7.14)$$

Therefore, any interference with a characteristic frequency below  $\omega_{c11}$  cannot be propagated along this waveguide, since the phase constant becomes a pure imaginary number and the fields suffer an exponential attenuation.

This property of waveguides can be used to provide access to a shielded enclosure without the risk of radiated interference pollution. The procedure cannot be applied to wires or cables, since they have conductors able to induce TEM modes inside the waveguide. TEM modes have a null cutoff frequency and therefore could enable transmission to any interference. However, the waveguide below cutoff frequency can be used to provide access for an optical fiber.

The cutoff frequencies can be slightly modified when the waveguide is filled with an optical fiber, since the dielectric permittivity of the fiber is higher than that of the air. However a worst case hypothesis can be made by assuming that the waveguide section is completely filled by the fiber. Dielectric permittivities of optical fibers range between 2 and 5, and therefore it is reasonable to assume that fiber will decrease the cutoff frequency by no more than a factor of  $\sqrt{5}$ . Figure 7.10 shows the attenuation factor corresponding to a circular waveguide for different diameters and lengths of 5 and 10 cm, operating in cutoff mode.

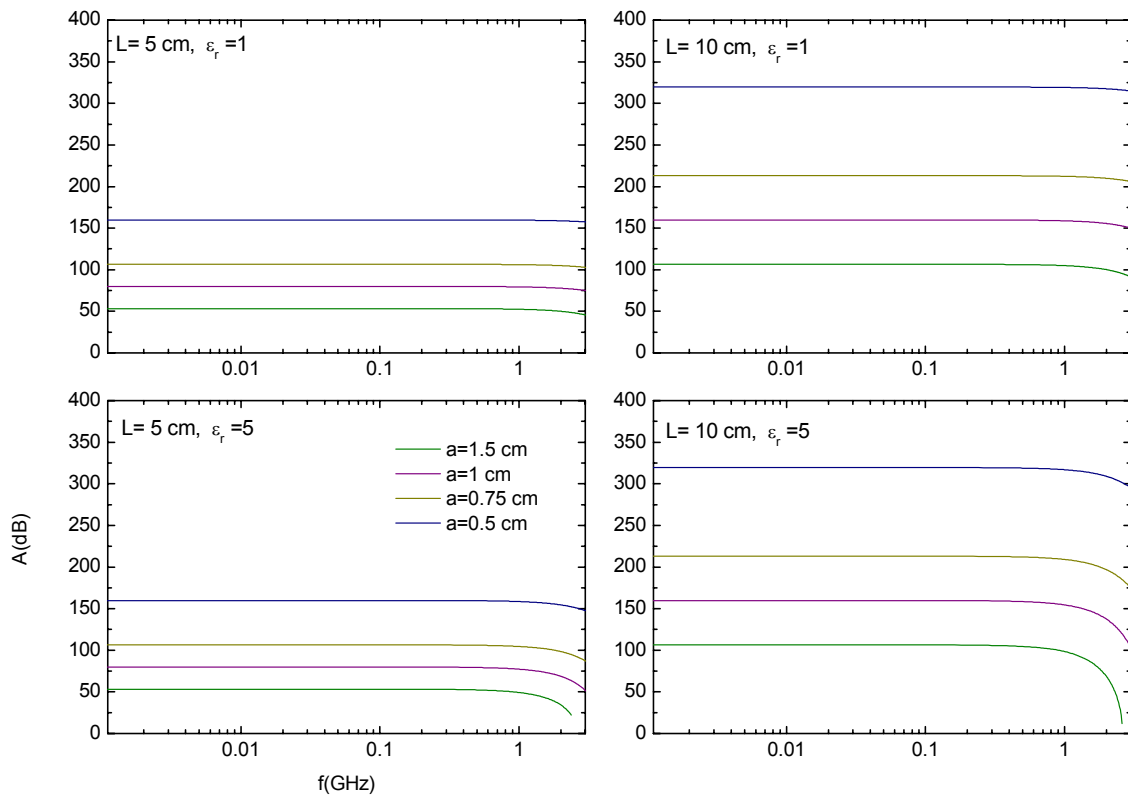


Figure 7.10 Attenuation of a cylindrical waveguide in cutoff mode for two different lengths ( $L$ ) and two different dielectric filling permittivities  $\epsilon_r$ .

### 3.4 Shielding effectiveness (SE) of the walls

The estimation of the wall  $SE$  with a thickness  $L$  can be made with the analysis of multiple reflections in the situation depicted in Figure 7.11 [27]. The total  $SE$  has three major contributions,

$$S = S_A S_R S_{RM} \quad (7.15)$$

where  $S_A$  is the field absorption of a single travelling way between 0 and  $L$ ,  $S_R$  is the contribution to attenuation from a partial reflection and  $S_{RM}$  a contribution from multiple reflections. All three factors can be calculated from the wall electrical properties and the wave impedances inside ( $Z_1$ ) and outside ( $Z_0$ ) the wall.  $S_A$  is given by

$$S_A = \frac{E_1(z=0)}{E_1(z=L)} = e^{\gamma L} = e^{\frac{L}{\delta}} = 8.686 \frac{L}{\delta} \text{ (dB)} \quad (7.16)$$

where  $\delta$  is the skin depth and the assumption of a good conductive wall is made.  $S_R$  is

$$S_R = \frac{E_0(z=0)}{E_0(z=L)} = \frac{1}{T_{12} T_{23}} = \frac{(Z_1 + Z_0)^2}{4Z_1 Z_0} \quad (7.17)$$

Where  $T_{ij}$  are the corresponding transmission coefficients. Finally,  $S_{RM}$  is

$$S_{RM} = 1 - \Gamma_{21} \Gamma_{23} e^{-2\gamma L} \quad (7.18)$$

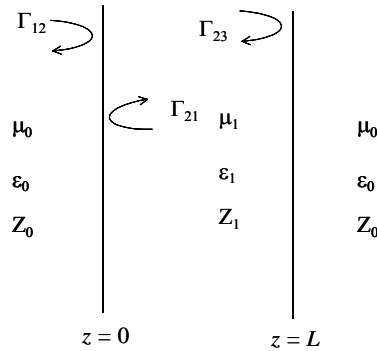


Figure 7.11 Calculation of the SE of a conductive wall.

## 4. FINAL PROTOTYPE AND MEASUREMENTS

### 4.1 Design of the testbench

Figure 7.12 shows the box fabricated to test the PMTs and a comparative measurement showing the influence of the shielding. The spectrum analyzer was configured in this measurement with an internal low noise preamplifier switched on for maximum sensitivity. Each wall was made with two double sided PCB laminates with copper layers of 35  $\mu\text{m}$ . The walls were soldered to mount the box at the inside edges of it. The outside edges were attached with conductive EMC tape. This tape is a 35 micron tin clad aluminium foil coated with an electrically conductive acrylic adhesive and a removable polyester masking tape [28].

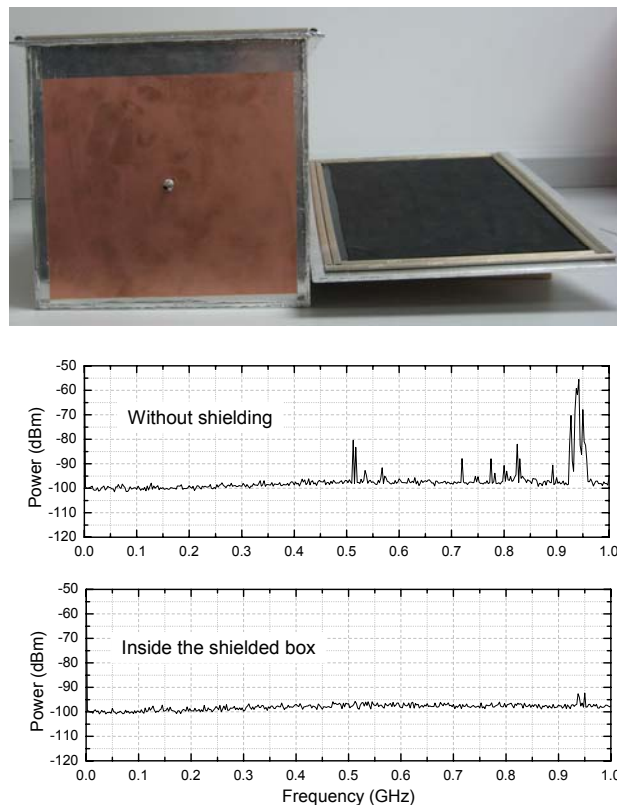


Figure 7.12 (a) Box fabricated for the PMT tests. The front side is shown with the detail of the cylindrical waveguide for optical fiber access. (b) Comparison between the signal detected by an unbiased PMT when located outside (top) and inside (bottom) the box.

The inner walls of the box were covered by a black neopren adhesive layer to avoid both electromagnetic resonances and optical reflections. The box door sealing was made with extruded gasket profiles in soft easy to compress silicone sponge base with a conductive knitted wire mesh over the sponge section [29]. An access to optical fibers was made at the front side with a circular waveguide of 0.5 mm diameter and 7 cm length. The box also has three coaxial thru connectors for bias photodetector signal output and slow control.

By neglecting the influence of coaxial connectors and assuming far field conditions for radiating interferences, the estimated shielding effectiveness is 155 dB at 1 GHz and 60 dB at 1 MHz. It must be pointed out that these estimations would not be accurate for a close interference of a low impedance (magnetic) wave mode, for which the shielding effectiveness of the box would be significantly lower. This would be the case of a close source of low frequency AC magnetic fields, such as those generated by transformers. In this case it would be necessary to keep the box far enough from the source (satisfying the condition  $kr > 10$ , where  $k$  is the phase constant of an equivalent plane wave and  $r$  the distance to the source), or to use an additional shielding of a high magnetic permeability and high magnetic losses, such as Permalloy, HyMu80 or MuMetal. This was unnecessary for the laboratory at which the tests with this box were made.

## 4.2 Results

For the measurements of the PMTs the pulse generator described in Section 1 of Chapter 4 was used. Due to the high asymmetry of the pulse train, it was possible to use commercially available LEDs placed at short distances without damaging the PMT. As a result, a full characterization of the PMT response could be made a very short LED - PMT distance, which was 30 cm with the LED polarized to 50% of its maximum operating voltage during the transmission of the pulse to the LED.

The amount of light due to pulses of the order of ns is very small, therefore a pulse generator of this type can help to measure the sensitivity of the PMT for very low illumination levels. Using light attenuators, it could even be possible to detect single photons. Several tests showed that the lack of stability in the voltage supply can affect not only the efficiency but also the width and duration of the pulse as well as the rise time. To quantify these effects we have made several measurements of the pulses with and without a blocking capacitor.

Figure 7.13a shows a comparison between the simulated pulse and the measured pulse driving the LED without the blocking capacitor. It can be seen that the simulation is able to predict the amplitude and the fall time with a good accuracy. However, the rise time is significantly degraded, as the effective

duration of the pulse is about two times wider than the theoretical value. Figure 7.13b shows a comparison of the generated pulse as measured with and without the blocking capacitor. A 500 MHz digital phosphorus oscilloscope TDS3052 Tektronic was used.

The pulse generator was applied to a high speed GaN LED L7113PBC from Kingbright, with a maximum light intensity of 1 cd for a peak wavelength,  $\lambda_{LED}$  of 468 nm. In this way, very short pulses of 10 ns wide and peaked in the UV band as the typical Čerenkov pulses, were obtained.

The equivalent circuit model for this LED described in Section 2 was used to evaluate the possible mismatches between the generator and the device. The series resistance of these devices, in excess of  $20 \Omega$  matched the generator to the LED very accurately and therefore no coupling networks were needed to avoid pulse distortions.

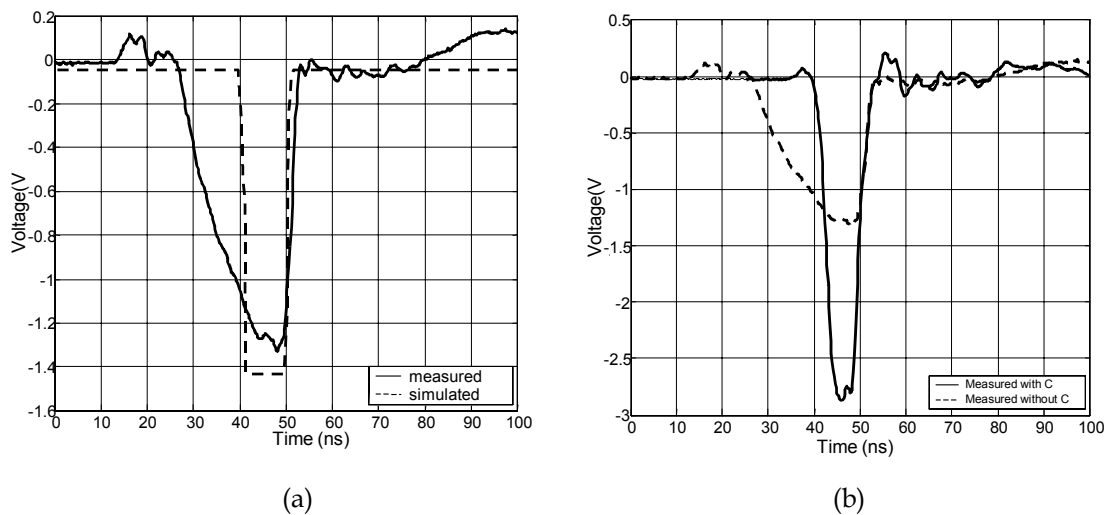


Figure 7.13 Measured and simulated pulse waveforms. Pulse measured without blocking C (a) and (b) influence of the blocking C on the measured pulse.

Figure 7.14a shows one of the pulse attacking the LED (forward voltage  $V_f=2.72 \text{ V}$ ) and the PMT anode pulse in response to the light emitted ( $V_{pulse}=76 \text{ mV}$ ). It can be seen that the device has a good time response, with no significant distortions in the pulse shape. During the time at which the excitation voltage is positive the LED is in reverse mode and it does not emit, therefore the weak ripple generated after the pulse is not transmitted to the photomultiplier. The delay time of PMT response versus the arrival time of the exciting pulse can be estimated from Fig. 7.14. Taking into account that there is a delay of about 15 ns due to the length of the cable used, we have estimated that the transit-time spread is of about 15 ns, which agrees with the specifications given by the manufacturer. The fidelity of the pulse shape evaluation can be better observed

by a comparison with more conventional techniques based in plastic scintillators. Figure 7.14b shows the measured pulse of the same PMT by substituting the pulse generator described in this thesis for a radioactive plastic scintillator. It can be seen that the LED generator enables much better evaluation of the photodetector response.

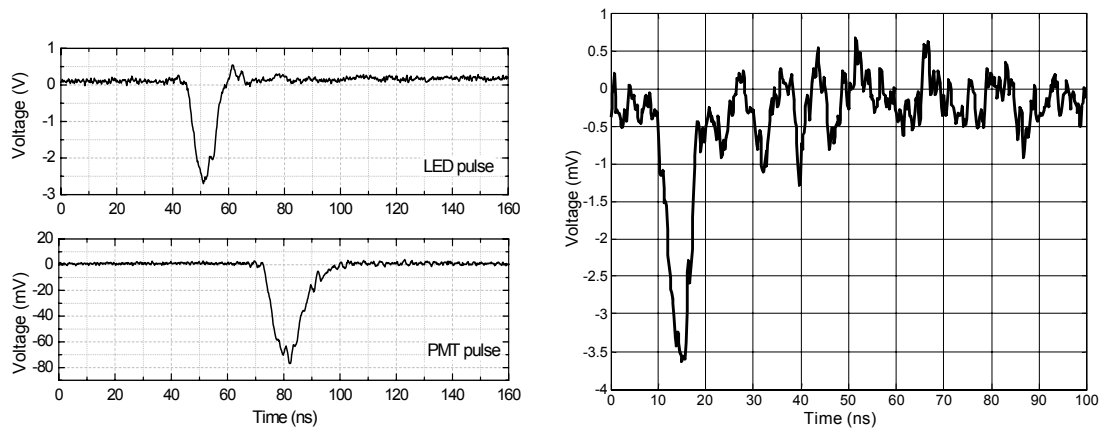


Figure 7.14 (a) Measured pulse waveforms at the output generator (top) and at the output PMT (bottom). (b) Measurement of the PMT with the conventional technique based on a plastic scintillator.

Figure 7.14a was obtained at a fixed LED polarization of 4V. By varying the voltage driven the pulse generator, it is also possible to obtain different light pulse amplitudes from the LED. Figure 7.15 shows the PMT output for different pulse amplitudes. The graph shows the excellent linearity of the PMT response against the light emission.

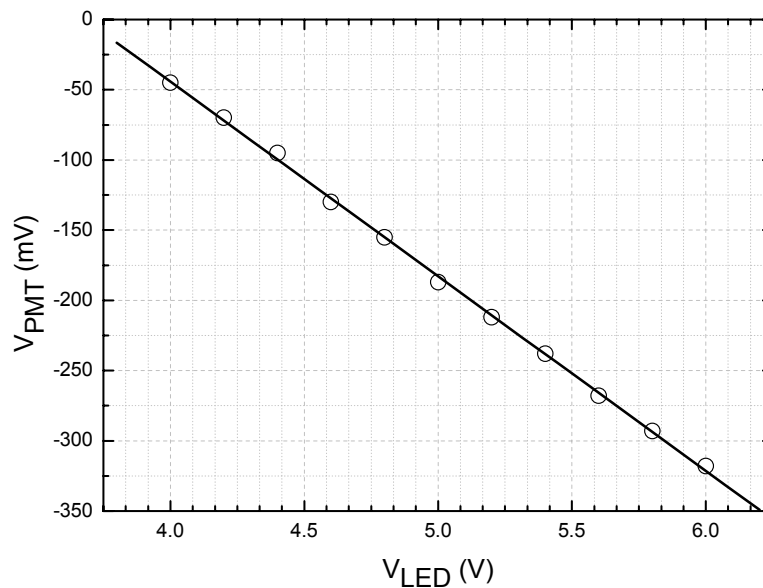


Figure 7.15 PMT anode pulse (peak) as a function of the LED polarization.



In order to test the time response performance of the photodetector, the PicoQuant pulse head model PLS 340-10 was used [30]. The pulse width of this LED is in the order of 500 ps, for a wavelength of 340 nm. Figure 7.16 shows the signal measured by the MAGIC II PMT when excited by this source. The PMT was biased for a gain of 20000. As it can be observed in this figure, the PMT has a bandwidth which is significantly slower than the pulse bandwidth. As a result, the measured pulse is wider than the incident one. The PMT bandwidth is mainly limited by two factors: the first one is the variance of the transit time of the electrons inside the tube, and the second one is the variance in the electron emission in the dynodes.

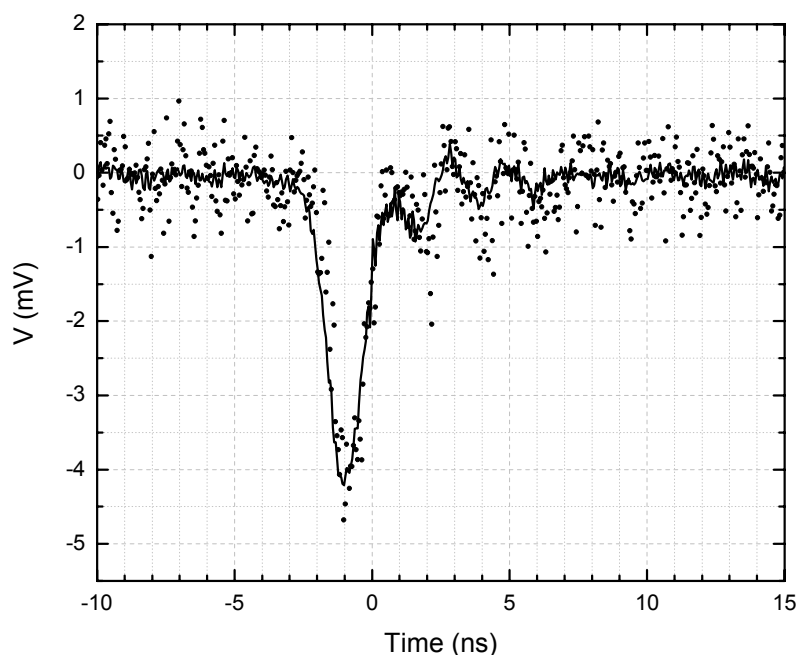


Figure 7.16 Signal from the PMT when excited with the PicoQuant LED. *Circles*: raw signal. *Line*: averaged.

Further tests were performed utilizing the SRD-based pulse generator described in Chapters 3 and 4. The fiber optic introduced into the box through the circular waveguide was illuminated by means of different blue LEDs, which were excited with the 4 V, 1.3 ns pulses. In this case, the amplitude of the pulse is a critical factor, as blue LEDs have much higher threshold voltages than other types of LEDs. Figure 7.17 shows the measured pulse when the PMT was excited by an inexpensive Kingbright LED, model L53MBC, driven by the SRD pulser. As can be seen in the graph, the response of this LED is not fast enough to be used for the test of PMT time-domain response. This is due to the high capacitances presented by these devices, and the long time required to remove

the carriers when switching off. This LED has a nominal capacitance of 100 pF measured at 1 MHz and zero bias. After an exhaustive search among all the blue LED retailers it was observed that this capacitance is rather similar in all of these devices no matter which package (surface mount or standard T-1 3/4 lamp) is used. Slightly lower capacitances, around 45 pF, are usually found in Turquoise LEDs). Inexpensive green LEDs with capacitances of 15-20 pF were also found, but the quantum efficiency of the MAGIC PMTs drops for wavelengths above 500 nm.

Despite the limitations of the inexpensive blue LEDs in terms of time response, the SRD based pulse generator is an attractive alternative to the very expensive commercial devices for the integration in photodetector testbenches. Although the time response of blue LEDs is not fast enough yet to take benefit of the ns range pulses provided by the generator presented in this thesis, the rise flank of this LEDs is very short. In addition, the cost of these LED pulsers is only around 50 euros, while the PicoQuant PLS 340-10 costed 8,500 euros (head and driver). Furthermore, as the manufacturers are constantly developing their products, faster diodes will break into the market soon at very competitive prices. This will enable the production of self-made blue light pulsers in the range of the nanosecond.

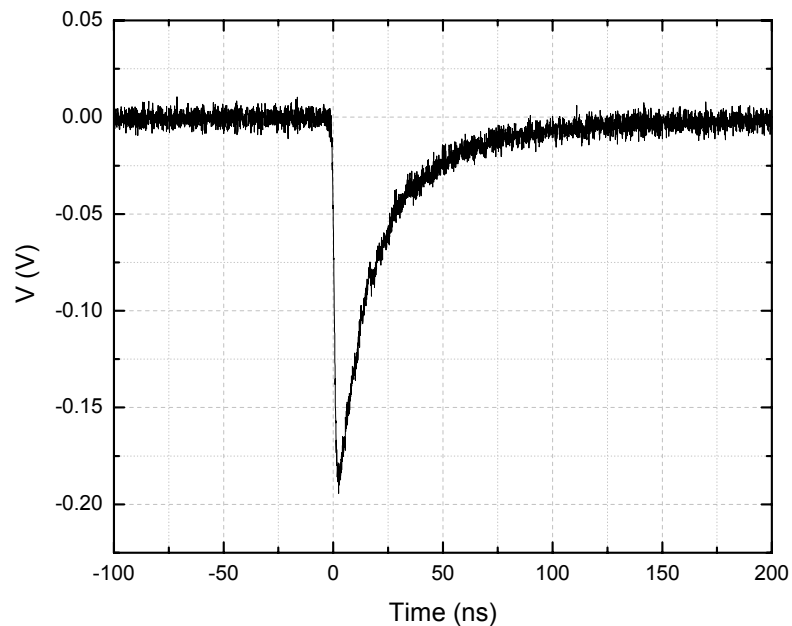


Figure 7.17 Response of a Kingbright L53MBC when mounted on the SRD pulse generator.

## 5. REFERENCES

- [1] S. Nakamura, T. Mukai, M. Senoh, *Candela-class high-brightness InGaN/AlGaIn double-heterostructure blue-light-emitting diodes*, Applied Physics Letters, vol 64 (13), pp 1687-1689, (1994).
- [2] Agilent, *HLMP-CB28-RU000 T-1 3/4 (5mm) Super Bright Precision Optical Performance InGaN LED Lamp*, Datasheet.
- [3] Toyoda-Gosei, *E1L51-xxxxx Series*, Datasheet.
- [4] J.M.Shah, Y.-L.Li, Th. Gessmann, E.F.Schubert, *Experimental analysis and theoretical model for anomalously high ideality factors ( $n \gg 2.0$ ) in AlGaNGaN p-n junction diodes*, Journal of Applied Physics, vol 94 (4), pp. 2627-2630 (2003).
- [5] SILENSE. *Examples of Simulations*, Semiconductor Technology Research Inc., 2004.
- [6] Y. Xi and E. F. Schubert, *Junction-temperature measurement in GaN ultraviolet light-emitting diodes using diode forward voltage method*, Applied Physics Letters, vol 85 (12), pp 2163-2165, (2004)
- [7] X.A. Cao, E.B. Stokes, P.M. Sandvik, S.F. LeBoeuf, J. Kretchmer, D. Walker, *Diffusion and tunneling currents in GaN/InGaIn multiple quantum well light-emitting diodes*, IEEE Electron Device Letters, vol 23 (9), pp 535 – 537 (Sept 2002).
- [8] L. W. Nagel, *SPICE2: A Computer Program to Simulate Semiconductor Circuits*, Berkeley, Univ. of California, Electronic Research Laboratory. ERL-M520 (1975).
- [9] H. Amano, J. Appl. Phys. 28, 2112 (1989).
- [10] S.D. Lester, *High dislocation densities in high efficiency GaN-based light-emitting diodes*. Appl. Phys. Lett. 66, 1249 (1995).
- [11] B.J. Zhang, T. Egawa, G.Y. Zhao, J. Ishikawa, M. Umeno, and T. Jimbo, *Schottky diodes of Ni/Au on n-GaN grown on sapphire and SiC substrates*. Appl. Phys. Lett. 79, 2567 (2001).
- [12] J.T Torvik, M. Leksono, J.I. Pankove, B.V. Zeghbroek, H.M. Ng, and T.D. Moustakas, *Electrical characterization of GaN/SiC n-p heterojunction diodes*. Appl. Phys. Lett. 72, 1371 (1998).
- [13] P. Waltereit, H. Sato, C. Poblenz, D.S. Green, J.S. Brown, M. McLaurin, T. Katona, S.P Den Baars, J.S. Speck, J.H. Liang, M. Kato, H. Takamura, S. Omori, and C. Funaoka, *Blue GaN-based light-emitting diodes grown by molecular-beam epitaxy with external quantum efficiency greater than 1.5%*. Appl. Phys. Lett. 84, 2748 (2004).
- [14] Kingbright L53MBC datasheet.
- [15] M. A. Tischler. *High brightness electroluminescent device, emitting in the green to ultraviolet spectrum and method of making the same*, U. S. Patent N° 5585648 (1996).
- [16] Cree Electronics Technical Report. *G-SiC® Technology Super-Blue™ LEDs C430CB230-S0100*.
- [17] R. Fletcher, *Function minimization by conjugate gradients*. Computer Journal 7, 149 (1964).
- [18] K. Madsen, *Efficient Minimax Design of Networks without Using Derivatives*. Microwave Theory Tech 23, 803 (1975).

- 
- [19] W. Press, B. Flannery, S. Teukolsky, and W. Vetterling. *Numerical recipes in C*. Cambridge University Press, 1990.
  - [20] M Shur, *Physics of Semiconductor Devices*, pg. 225, Prentice Hall, 1990.
  - [21] S.M.Sze, *Physics of Semiconductor Devices* 2nd Edition, pg. 84, Ed. Wiley 1981.
  - [22] *Thermal Resistance Values for LED Lamps*, Application Brief I-002, Agilent, 1999.
  - [23] P.Antoranz, J.M.Miranda, J.L.Sebastián, M.Cámara, M.V.Fonseca, *High frequency modeling of GaN/SiC blue light emitting diodes*, J. Appl. Phys. 97, 096107 (2005)
  - [24] E. F. Schubert, *Light Emitting Diodes*, pg. 60, Cambridge University Press, 2003.
  - [25] K. Armstrong, *Design techniques for EMC*, Cherry Clough Consultants, 1999. Available at <http://www.cherryclough.com>
  - [26] *Flomerics field solver brochure*, (CST recently completed the acquisition of the EM division of flomerics). Available at [www.cst.com/Content/Products/MST/Overview.aspx](http://www.cst.com/Content/Products/MST/Overview.aspx)
  - [27] J.L. Sebastian, *Compatibilidad Electromagnética*, Pearson, 1999.
  - [28] *AT 541 40 Technical datasheet*, available at [www.advancetapes.com](http://www.advancetapes.com)
  - [29] *FAB2210-CN-AC datasheet*, available at [www.warth.co.uk](http://www.warth.co.uk)
  - [30] [http://www.picoquant.com/\\_products.htm](http://www.picoquant.com/_products.htm)

# Chapter 8

## Summary and future prospects

1. Main accomplishments
  - 1.1. Measurements during MAGIC shifts
  - 1.2. Central Pixel electronics
  - 1.3. Nanosecond range pulse generators
  - 1.4. Nanosecond range pulse amplifiers
  - 1.5. High frequency modelling of blue LEDs
  - 1.6. Evaluation boards and testbenches
2. Future work on IACTs: The Čerenkov Telescope Array (CTA)
  - 2.1 Structure and objectives of CTA
  - 2.2 Thesis usefulness for CTA
3. References

## **1. MAIN ACCOMPLISHMENTS**

**T**HIS Thesis has been developed in coordination with more than one hundred researchers working at twenty two institutes and universities. Its main objectives were carefully selected to harmonize them with all these efforts, by keeping in mind that the priority has always been to pursue innovation in those aspects related to high frequency electronics technology that can be more helpful to the collaboration.

The main accomplishments presented in this thesis are summarized below.

### **1.1 Measurements during MAGIC shifts**

During the period of this thesis the author participated as an operator in three shifts periods of 3 to 4 months each one: P33 (September 2005), P46 (September 2006) and P59 (October 2007). These were made under the rules established by the MAGIC collaboration policies. As a result of these measurements a large number of different sources have been observed which have been the subject of numerous peer reviewed publications. In addition the author gained a deep knowledge on the MAGIC telescope operation and subsystems, which helped to clearly identify the most demanding topics of research on hardware work within the collaboration.

### **1.2 Central pixel electronics**

The central pixel of MAGIC I camera was designed by the author of this thesis for optical monitoring. An electro-optical system was developed to transmit through optical fiber the output signal to the counting room, where it is digitized and stored for off-line analysis. During the period of this thesis the author also participated in a technical shift by working on the installation of this pixel. The system was tested by observing the optical pulsation from the Crab pulsar.

### **1.3 Nanosecond range pulse generators**

In this thesis we have presented different prototypes of compact pulse generators suitable for evaluation boards. These prototypes found the following applications: 1) Design of evaluation devices for diagnostics of pixel electronics, 2) Design of a testbench for photodetector testing and 3) Design of a testbench for optical transmission link testing. The prototype based on step recovery diodes (SRD) is especially remarkable. It can provide pulses of 1 ns and more than four volts of peak amplitude, with state of the art jitter figures (less than 8 ps). In addition, a model of a SRD compatible with PSPICE was developed and used to accurately predict the pulse shape of the generator without the need for using complex numerical procedures to estimate the dynamic behaviour of the diode space charge.

### **1.4 Nanosecond range pulse amplifiers**

Nanosecond pulse amplifiers based on monolithic gain blocks have been designed, fabricated and tested. The tests include noise and S parameter measurements, temperature-sensitivity behaviour, dynamic range and pulse shape integrity. Specific software to accurately predict the time domain response and stability from the S parameter measurements has also been developed, which offers the advantage of being user friendly for a researcher without any expertise in high frequency electronics. The most important prototype presented in this work is the one based on the BGA616 chip. It was finally integrated in the receiver boards of MAGIC II, which feature a bandwidth of 1 GHz, three times higher than the bandwidth of MAGIC I. In addition, after the successful installation of the MAGIC II receiver boards it has been confirmed that the design proposed in this thesis offered an excellent degree of repeatability and reliability, with no reported amplifier failures at the first installation, among the more than one thousand pixels.

### **1.5 High frequency modelling of blue LEDs**

Blue light-emitting diodes based on gallium nitride GaN semiconductor compounds represent one of the most important breakthroughs in electronics and optoelectronics of recent years. We also reported on this thesis a model to

accurately predict the electrical behaviour of double-heterostructure GaN/SiC blue light-emitting diodes up to microwave frequencies, which has been helpful in the design of a ns light pulser for the photodetector testbench. Software has been developed which uses a self consistent procedure to extract the series resistance  $R_s$  from the reflection coefficient. This approach offers the advantage of using measurements without any bias current and therefore the obtained values of  $R_s$  are influenced neither by the device heating nor by inaccuracies in the calculation of the ideality factor. In addition, software has been developed to accurately predict the I-V characteristics of the LED, and therefore to extract physically sound values of the LED ideality factor and series resistance, which were used starting values for the optimization analysis needed in the calculation of the high frequency equivalent model.

## 1.6 Evaluation boards and testbenches

The prototypes for evaluation boards and test benches presented in this thesis take benefit from all the accomplishments mentioned above. A testbench for photodetector evaluation has been built and used to measure sensitivity, linearity, pulse shape integrity and single photoelectron response. This test bench features a compact blue/UV LED pulse generator which feeds an optical bench screened from both radiated and conducted interferences. The optical coupling was made with a cylindrical waveguide designed to convert any radiated interference above 10 GHz in an evanescent waveguide mode, thus obtaining good electromagnetic screening figures of merit, which are most suitable for measuring photodetector noise and single photoelectron response. This testbench incorporates the possibility of biasing different photodetectors and has been used to measure PMTs, HPDs and solid state photodetectors.

In addition, a compact four channel VCSEL pulse generator has been designed to test the MAGIC II receiver boards. This device imitates the signals supplied by the pixels of MAGIC II camera to the optical fiber links, by providing four channels with 1.3 ns pulses of 4 V. The design consists of a fast step recovery diode pulser, a 4-output resistive power divider, a 4-channel high power amplification stage and a board with VCSEL biasing circuitry. The modularity has been maximized while minimizing the lengths of the planar transmission lines. This enables an optimum performance in terms of pulse distortion, as well as robustness to interferences and crosstalk. The circuit operates with a single bias supply of 12 V. Pulse jitter measured with a 6 GHz oscilloscope is 6 ps. Pulse Repetition Frequency (PRF) jitter is less than 25 ns for a mean PRF value of 20 KHz.



## 2. FUTURE WORK ON IACTS: THE ČERENKOV TELESCOPE ARRAY (CTA)

The CTA collaboration emerged from different research groups, some of which were largely involved in the design and construction of MAGIC and H.E.S.S. telescopes [1]. The Design Study Phase started in 2007 and it is expected to be concluded in 2010. After that a new preparatory phase (2011 - 2012) will start, consisting in the construction of telescope prototypes. The observatory is expected to be commissioned by 2014.

CTA observatory will be located in two sites, one in the northern hemisphere (emphasized on extragalactic sources) and the other in the southern one (for galactic sources) [2].

### 2.1 Structure and objectives of CTA

The main goal of the CTA project is to unify and improve the different characteristics of both H.E.S.S. and MAGIC telescopes. Currently, H.E.S.S. is building a big telescope to decrease the energy threshold and MAGIC has already commissioned a second telescope to obtain stereoscopic observation, as indicated in Chapter 2.

Figure 8.1 shows the projected layout (a) and the estimated sensitivity for the CTA array (b), both in energy flux and in terms of Crab signal. With a dynamic range from  $\sim 10$  GeV to more than 100 TeV, the array will cover all energies between the satellite observations and one order of magnitude more than current telescopes. This will permit the overlapping and crosscheck with the data from other observatories, such as the Fermi Gamma-ray Space Telescope. The sensitivity of the array will exceed in a factor of ten the sensitivity of MAGIC and H.E.S.S. The array will have, as compared with current detectors, a much higher detection area (and therefore detection rate) and angular resolution.

Monte Carlo simulations, using both MAGIC and H.E.S.S. data have been performed in order to estimate the dimension of the installation. The optimum obtained layout is composed by 50-100 telescopes, divided into three different types, and with a minimum separation of 80-100 m between telescopes. The total expected area could be around 3-4 km<sup>2</sup>. A preliminary study of the expected physical achievements can be found in [3].

The inner section is constituted by the biggest telescopes, with the lower energy thresholds. The second, with mid-size telescopes will peak sensitivity in 100 GeV - 10 TeV range, and the outer ring, with the smallest telescopes, will cover the highest energies.

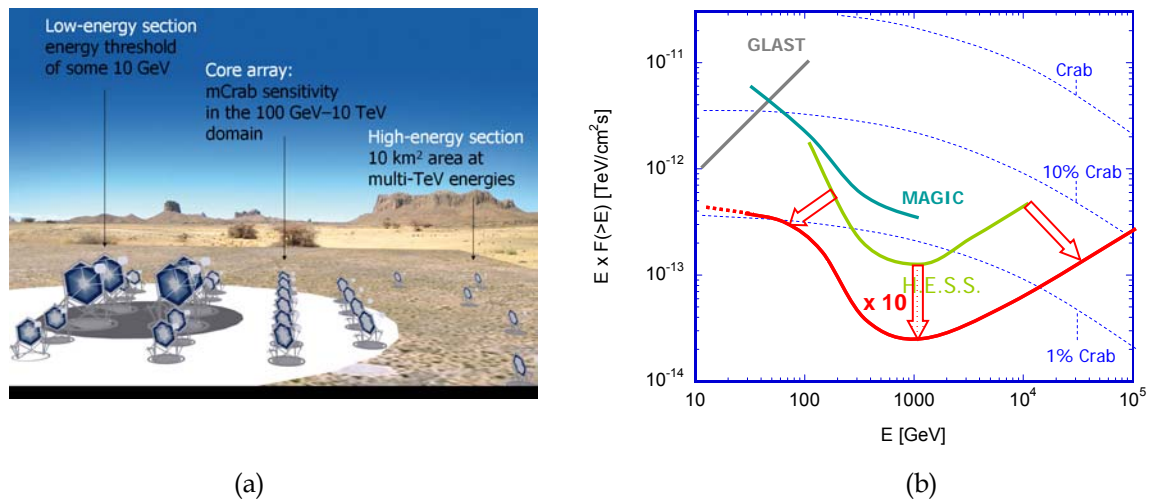


Figure 8.1 CTA layout (a) and projected sensitivity of the CTA Array (b).

A brief description of the possible structures for the projected telescopes is shown in Table 8.1 [4] [5]. In the design of these telescopes, the technology developed for MAGIC and H.E.S.S. will be used. Along these years, the results prove the reliability of the structures and electronics of these experiments. In some fields, however, important R&D is needed in order to achieve the expected performance. This is carefully detailed in the work packages description [6], in which the groups involved are assigned.


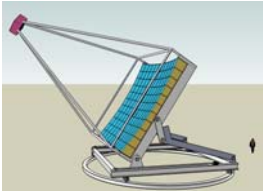
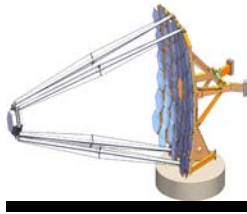
	Low Energy Telescopes	Middle energy telesc.	High Energy Telesc.
<b>Energy range</b>	> 10 GeV	100 GeV – 10 TeV	> 10 TeV
<b>Diameter</b>	24 m	12 m	6 m
<b>Sensitivity</b>	~10 mCrab	~1 mCrab	10 - 100 mCrab
<b># of telesc.</b>	4	~30 - 40	> 50
<b>Example</b>			

Table 8.1 Description of the projected telescopes for CTA [5].

## 2.2 Thesis usefulness for CTA

CTA activities are clasified in different work packages, which have already been specified in the collaboration Memory of Understanding (MoU). These are the following ones:

WP1	MNG	Management of the design study
WP2	PHYS	Astrophysics and astroparticle physics
WP3	MC	Optimization of array layout, performance studies, ...
WP4	SITE	Site evaluation and site infrastructure
WP5	MIR	Telescope optics, mirrors, mirror alignment
WP6	TEL	Telescope structure, drive, control, robotics
WP7	FPI	Focal plane instrumentation, mechanics and photo detectors
WP8	ELEC	Readout electronics and trigger
WP9	ATAC	Atmospheric monitoring, associated science & instrument calib.
WP10	OBS	Observatory operation and access
WP11	DATA	Data handling, data processing, data management and access
WP12	QA	Risk assessment and quality assurance, production planning

The spanish group **UCM-ELECTRONICS** [7], in which the author and the advisor of this Thesis are integrated, will participate in different tasks which have been approved and funded by the spanish government under the project

FPA2009-14226-C05-03, "DESARROLLO DE TECNOLOGIAS CLAVE PARA EL PROTOTIPADO DEL CHERENKOV TELESCOPE ARRAY: ELECTRONICA DE ALTA FRECUENCIA E INVESTIGACION EN FOTODETECTORES DE UV ULTRARRAPIDOS"

The work to be done under this project is mainly grouped in the following goals:

### a) **Development of front-end electronics optimized for low-threshold**

The work described in this Thesis matches to the expertise demand for this task. The development of wideband amplifiers is a milestone for the design of the camera and the signal chain. The modules designed for MAGIC II receiver board constitute a good candidate for the integration in CTA electronics. However, the final version of the camera design will not be available until 2011-2012, so further tests on new commercially available MMICs and RF components will be performed.

The development of simulation software is a very important issue in the design of the front-end electronics. Special emphasis must be done in signal transmission. System characteristics as impedance, gain, stability or noise have a critical role in the integrity of the signal. The analysis and simulation software described in Chapter 5 is a very practical tool for high electronic developers, and further updates of the software are proposed.

**b) Tests and quality control of camera and readout electronics.**

An important feature highlighted in the CTA preliminary study is the reliability of the components. The UCM-ELECTRONICS group accumulates a good expertise in electromagnetic compatibility, and the facilities of the group are about to obtain the ENAC qualification [8], which will enable the group to play a relevant role in the quality assurance work package (WP12).

In cooperation with IFAE and the Spanish company *Fidias* [9], UCM-ELECTRONICS will contribute with their expertise in quality control and failure analysis techniques in the fabrication of CTA camera, and will cooperate in the test of the cluster prototypes. Software for failure analysis and prediction will also be developed. The prototype of multichannel pulse generator described in Chapter 4 and the test setup described in Chapter 7 could be helpful to successfully accomplish these tasks.

**c) Research on new solid state photodetectors.**

The main tasks in which UCM-ELECTRONICS is involved are: 1) Modelling and test of new UV solid state photodetectors; 2) Development of electrical models for signal integrity studies, and 3) creation of testbenches to characterize the detectors and validate the previously defined models. Again, the results presented in chapters 4 and 7 will serve as a good starting point for the experimental work to be done for this goal.

### 3. REFERENCES

- 
- [1] *CTA: An advanced facility for ground-based high-energy gamma ray astronomy*. Presentation to the 2005 European ESFRI sub-committee.
  - [2] *The Two Arrays of the CTA Observatory*. [http://www.cta-observatory.org/CTA\\_arrays.html](http://www.cta-observatory.org/CTA_arrays.html)
  - [3] *The Astronet Infrastructure Roadmap: A strategic plan for European Astronomy*, pg 28-30. <http://www.astronet-eu.org>
  - [4] Eckart Lorenz. *Ongoing developments for 23 m LST design*. CTA General Meeting, Crakow, May 2009.
  - [5] Werner Hofmann, *CTA 2009 Spring Meeting Cracow Opening remarks*. CTA General Meeting, Crakow, May 2009.
  - [6] *CTA Design Study*, [http://www.cta-observatory.org/CTA\\_DS.html](http://www.cta-observatory.org/CTA_DS.html)
  - [7] [http://www.ucm.es/info/electron/personal/miranda\\_archivos/cta/index.html](http://www.ucm.es/info/electron/personal/miranda_archivos/cta/index.html)
  - [8] <http://www.enac.es/web/enac/inicio>
  - [9] <http://www.fidias.es/>









